Distribution Agreement

In presenting this thesis or dissertation as a partial fulfillment of the requirements for an advanced degree from Emory University, I hereby grant to Emory University and its agents the non-exclusive license to archive, make accessible, and display my thesis or dissertation in whole or in part in all forms of media, now or hereafter known, including display on the world wide web. I understand that I may select some access restrictions as part of the online submission of this thesis or dissertation. I retain all ownership rights to the copyright of the thesis or dissertation. I also retain the right to use in future works (such as articles or books) all or part of this thesis or dissertation.

Signature:

_____

Gregory E. Vansuch Date

The Bioinorganic Energy Conversion Puzzle:
Pieces from a [NiFe]-Hydrogenase Ligand Scaffold

By
Gregory E. Vansuch
Doctor of Philosophy
Chemistry

_____

Dr. R. Brian Dyer, Advisor

_____

Dr. Tianquan Lian, Committee Member

_____

Dr. Craig L. Hill, Committee Member

Accepted:

_____

Dr. Lisa A. Tedesco
Dean of the Laney T. James School of Graduate Studies

_____

Date

The Bioinorganic Energy Conversion Puzzle: Pieces from a [NiFe]-Hydrogenase Ligand Scaffold

By
Gregory E. Vansuch
B.A., University of Colorado Boulder, 2014

Advisor: Dr. R. Brian Dyer

An abstract of
A dissertation submitted to the Faculty of the
James T. Laney School of Graduate Studies of Emory University
in partial fulfillment of the requirements for the degree of
Doctor of Philosophy
in Chemistry
2021

The Bioinorganic Energy Conversion Puzzle:
Pieces from a [NiFe]-Hydrogenase Ligand Scaffold

By
Gregory E. Vansuch

The activation and formation of small molecules by metalloenzymes is a critical component of microbial metabolism. It is also relevant to fuel production. Sustainable energy conversion catalysts are often modelled off such enzymes. However, they typically fall short of achieving the rates and/or efficiencies of the enzymes. Advances in (bio)inorganic catalysis have demonstrated the importance of the ligand/protein scaffold for optimal enzyme/catalyst function. Thus, understanding the roles of protein scaffolds in metalloenzymes is critical for refining bioinspired catalyst blueprints. In this thesis, the structure-function relationship of the [NiFe] active site with part of its secondary sphere is probed in the soluble hydrogenase-1 from *Pyrococcus furiousus* (*Pf* SH1) with three enzyme variants that targeted two critical amino acid residues.

The first two enzyme variants targeted a glutamate residue (E17) and changed either side chain functionality or length. The rather conservative mutation E17Q changed side chain functionality. Probing the effects of the mutation provided insight into/verification of a probable efficient proton transfer pathway. Subtle modulation of active site properties under equilibrium and time-resolved conditions were also observed. The less conservative mutation E17D changed the side chain length. Probing the effects of this mutation provided insight into the convoluted role of the [NiFe]-core with the secondary and outer coordination spheres. The third variant targeted an arginine residue above the active site exogenous ligand binding position (R355), which was mutated to a lysine (R355K). This thesis presents the first in depth spectroscopic characterization of the effects caused by this mutation to help determine possible role(s) of R355 during catalysis. In combination with H/D exchange kinetics, it was found a major role of the arginine is to control the reactivity and/or stability of bridging hydrides that are critical catalytic intermediates.

Overall, the results established fundamental secondary sphere interactions with the [NiFe] core in *Pf* SH1, which sets a foundation for more in depth equilibrium, steady state, and time-resolved investigations of *Pf* SH1 enzyme variants.

The Bioinorganic Energy Conversion Puzzle: Pieces from a [NiFe]-Hydrogenase Ligand Scaffold

By
Gregory E. Vansuch
B.A., University of Colorado Boulder, 2014

Advisor: Dr. R. Brian Dyer

A dissertation submitted to the Faculty of the
James T. Laney School of Graduate Studies of Emory University
in partial fulfillment of the requirements for the degree of
Doctor of Philosophy
in Chemistry
2021

Acknowledgements

First, I would like to thank my advisor R. Brian Dyer, who has guided me through all aspects of my projects and who has also been beyond patient with me, especially during my early years of graduate school. He allowed me to explore all aspects of my project freely and encouraged me to collaborate with others outside my direct area of study, which has allowed me to become familiar with a great deal sub-branches in the chemical sciences. He also put up with obnoxious non-stop laughing and has gone out of his way to make sure I never lost sight of the important things in life outside of work. Being mentored by him has made me not just a better scientist, but also a much better person than I was when I joined the department six and half years ago.

I am also indebted to my committee members Dr. Tianquan "Tim" Lian, Dr. Craig Hill, and Dr. Christopher Scarborough, who all brought unique insights to my project and pushed me to think incredibly critically in my early years about ideas I would have never considered on my own. I would also like to thank Dr. Emily Weinert, Dr. Khalid Saliata, and Dr. Michael Heaven for their collaborations and/or support throughout my graduate school years. I would like to thank my collaborators at the University of Georgia: Dr. Michael W.W. Adams, Dr. Michael K. Johnson, Chang-Hao "Perry" Wu, Dominik Haja, and Soshawn Blair. Both Perry and Dominik provided an immense about enzyme for my research without which essentially none of this thesis work would have been possible.

I of course would also like to thank my parents Martha and Gary Vansuch and my sister Mary for their love and support; my parents have always allowed me to choose my own way and have never once pushed me to choose one activity, sport, career path, etc over the other. They always supported my decisions, even if they did not agree with me, and were always there for me whenever I failed or changed paths. I cannot imagine having had a better upbringing. Mary was always with me during our summer moves to new states before we knew anyone else our age; she has been one of the most important parts of my life and I am fortunate to have seen her grow up into the amazing person she has become.

I am grateful to Dr. Brandon Greene for taking me under his wing during my first year of graduate school and patiently teaching me about hydrogenase research and the many experimental techniques utilized in our laboratory. I am also grateful to Dr. Erin Schuler, Dr. Bryant Chica, and Dr. Ban-Seok "Sam" Jeong for their guidance at various stages of my graduate research. I am also thankful for the many friends and other colleagues I have had at Emory University, especially Dan Wildman, Roger Park, Brooke Andrews, Jing Zhao, Wenxing Yang, Morgan Vaughn, Natalie Uhlikova, Louis Groff, Michelle Leidy, Torie Snider, Sara Gebre, Alexia Prokopik, Rong Fu, Michael Reddish, Sarah Narehood, and David White, all of

whom have made the chemistry department a fantastic place to work. The department environment has also always been a welcome place with Steve Krebs, Claire Scott, and Anne Dasher of whom I am lucky to have interacted and worked with.

In Colorado, I am lucky for my amazing high school and college group of friends and being part “team adventure”: Matt Jewett, Alex Bak, Mandy Johnson, Andrea Sobel, Rachel Anderson, Joe Seiger, Parsa Ghasem, Angela Park, and Allison Jewett.

From college and high school, I would also like to thank teachers and coaches that have had a long lasting impact on my life and education: Jeffrey Reiman, Bernard Gillett, Christine Kelly, Molly Larsen, Veronica Vaida, Allyson Robbins, Bradley Newman, Tari Wood, Curtis Bailey, Linda Anderson, David Walba, David Rothman, and Peter Hebert.

I have been surrounded by amazing people throughout my life, and none of this work would have been possible without a single one of the amazing friends, family, mentors, coaches, teachers, and/or colleagues mentioned here.

Table of Contents

List of Figures

Chapter 1

Chapter 2

Chapter 3

Appendix

List of Tables

Appendix

Chapter 1 – Introduction

1.1 – Overview of Pollution, Global Warming, the Need for Renewable Energy, and Renewable Energy Inspirations found in Nature

1.1.1 – Motivation: Fossil Fuel Contributions to Pollution and Climate Change and the Need for Alternative Energy Sources

Much of modern society is indebted to fossil fuels. Scientific and engineering advances from the industrial revolution to present day would have been impossible without such resources.[1,2] However, fossil fuel use has severe consequences because its combustion forms primary pollutants (e.g. nitric oxides, methane and other volatile organic compounds, sulfur dioxide, black carbon), some of which then form secondary pollutants such as ozone via atmospheric photochemical reactions.[2-4] The resultant decline of air quality causes adverse health effects attributed to several hundred thousand to millions of deaths per year.[4,5] To make matters worse, the pollutants have detrimental environmental and climate impacts like ocean acidification, acid rain, and altered weather patterns.[2-4] Perhaps the most common discussion on this topic concerns greenhouse gases, which trap infrared radiation in the atmosphere causing a net positive radiative force (heating of the earth). However, some pollutants do exert negative radiative forces (cooling effects). For example, sulfate aerosols absorb solar radiation that mitigate the amount of infrared radiation from the earth's surface for greenhouse gases to absorb.[4,6] Overall, such negative radiative forces curb increasing temperatures ~ 0.5 °C.[5]

During the pre-industrial era the molecules mentioned above would hardly have classified as pollutants, many naturally appear in the atmosphere from the biogeochemical cycles that formed the current planetary atmosphere over millions of years. But, fossil fuel combustion altered the flux of these molecules on very short time scales leading to problems like those discussed above.[7,8] Measures have of course been taken to combat such issues, with a major factor determining success being the atmospheric lifetime of a given pollutant. For example, nitric oxides have lifetimes only days and typically exert local effects; thus limiting vehicle emissions that produce such compounds yields positive results rather quickly.[2-4] Damage may essentially be reversed.

Other damage is rather permanent and will become worse without additional mitigation. The simplest example here regards carbon dioxide: 50% of such emissions equilibrate with the oceans and biosphere on the order of a few decades, while 50% remains in the atmosphere and distributes evenly over the planet. Rising temperatures, and thus the corresponding consequences, are positively correlated with increasing CO_2 emissions,[6,9] and if CO_2 emissions ceased at this moment it would take hundreds to thousands of years for natural processes to return the atmospheric CO_2 concentration to pre-industrial era levels.[9,10] The scenario is similar for methane which is a far more potent greenhouse gas than CO_2; but, atmospheric reactions of methane and natural methane sinks make long term effects less clear.[4] Nonetheless, increased atmospheric concentrations of pollutants other than CO_2 have long lasting consequences.

Because the demand for fuels will only continue increasing as countries modernize and the global population continues to rise[2,11,12] it is clearly important to transition to nonconventional energy resources to mitigate pollution. The integration of these resources into society will be driven by a variety of factors such as resource locations and the fact that centralized energy grids in developed nations can be directly linked to alternative sources.[13] Developing regions do not have such infrastructure, and implementing decentralized energy systems will be necessary.[14] Another important consideration is that not all scenarios have clear fossil-fuel alternatives like long distance transportation.[13]

1.1.2 – A Brief Overview of Promises and Inherent Challenges in Nuclear and Renewable Energy and the Need for Efficient Alternative Fuel Generation

Alternative energy resources to combat pollution are typically classified as nuclear or renewable, with renewable sources being those that cannot realistically be used up. The problem is how to utilize them cost effectively on a global scale. General prospects and limitations of these resources are summarized below and outlined in **Figure 1.1**, which ultimately set up the broad framework this thesis is founded on:

the need to understand design principles of catalysts for efficient and economical small molecule activation and production.

Nuclear fission is a fantastic energy conversion strategy that generates no CO_2,[15] and for 50 + years has kept CO_2 emissions roughly two years behind what it would otherwise be.[16] But, building and maintaining nuclear plants costs billions of dollars,[16,17] and there are significant dangers like radioactive waste disposal and deadly reactor accidents. These drawbacks place limits on the role nuclear energy will

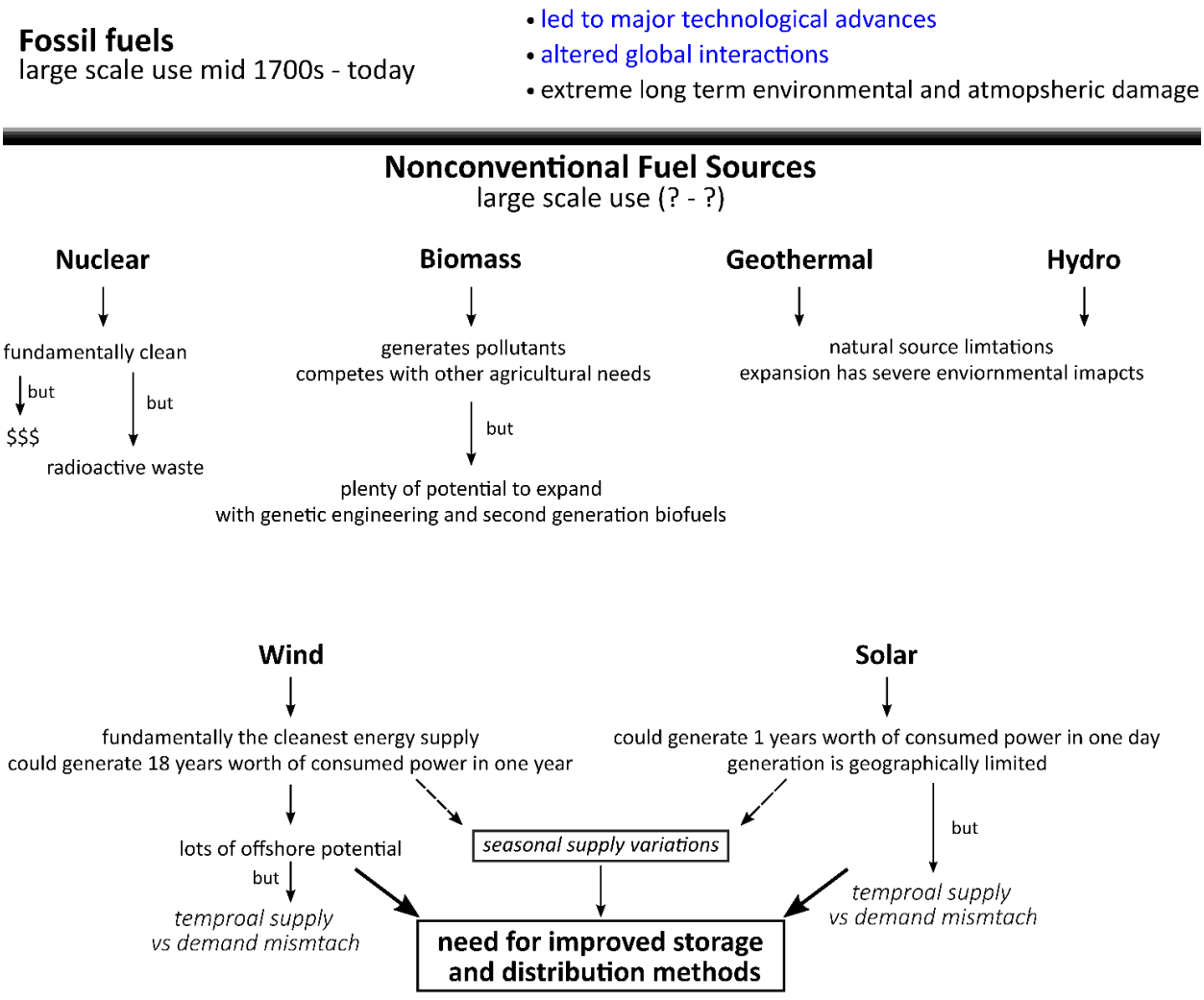

Figure 1.1: (Top): Summary of the broad benefits and disadvantage of fossil fuel use. **(Bottom):** Summary of the benefits, problems, and prospects of various alternative energy sources.

play in many countries,[2,15,17] as already evidenced by its drop in generation from 14% in 2009 to the 10% now[16,18,19] and by the apparent phasing out of nuclear power in some nations via early reactor shutdowns with minimal to no investments in new ones.[9,16-18]

Renewables like hydropower, biomass, geothermal, wind, and solar will thus play a major role for transitioning to widespread nonconventional energy use. Hydropower is a common method for electricity generation, and in 2019 comprised 60 – 95% of domestic electricity generation in some countries.[19] The percentage averages to 16% worldwide,[19] in part because of inherent geographical limitations. Also, while thought to be pollutant free, this is not entirely true because the vegetation growing in reservoirs leads to methane, carbon dioxide, and nitrous oxide emissions, which is one important factor to consider during hydroelectric expansion.[20] Biomass poses unfortunate fundamental issues: burning it in poorly ventilated structures is a health hazard,[3] it diverts from the food supply,[8,11] and large scale production can have severe environmental impacts.[21] Still, a combination of improved infrastructure and advances with second generation biofuels/genetic engineering for microbial fuel generation could cause breakthroughs for large scale use.[8,18,21] Geothermal energy is convenient near locations with natural and accessible sources,[17] and though these are limited, enhanced or artificial sources could make its use more widespread. However, this could result in predictable and unpredictable affects (e.g. environmental) that are not worth the cost. More-so, harnessing geothermal energy accelerates the rate of natural pollutant emissions from these sources, which can cause local health hazards which is problematic regardless of other concerns.[22]

Thus, expansion of the nonconventional energy use will rely on the energy deriving from the wind and sun. Harnessing wind energy is primarily an engineering endeavor and only briefly mentioned here: in 2019 wind generated ~ 5% of domestic electricity worldwide,[19] with values of 17 – 18% in some developed nations.[19] Offshore projects have great potential for increasing the percentages,[23] but require expansion of the energy grid to bring power from inherently remote sources to population centers.

We thus arrive at solar energy. Properly speaking, every type of energy is solar; fossil fuels themselves are just accumulated matter derived from ancient photosynthesis. Their combustion simply completes the cycling of component elements, although at levels not compatible with biogeochemical timescales.[7,8] The solar energy field itself focuses on harvesting sunlight and converting photons into fuels with minimal to no waste generation. This is commonly done with photovoltaics, which only provide ~ 2% of domestic electricity.[19] This is largely because in comparison to methods like nuclear and hydropower, the ability to harness *and* utilize soar energy is several decades behind; but, consider how global energy demand is expected to be ~ 40 – 50 TW by 2100.[10,24] This equates to $1.2 – 1.5 \times 10^{20}$ joules per year. Within one hour, the sun provides Earth about 4.3×10^{20} joules (roughly 119,000 TW). That is, within 3600 seconds, sunlight provides more energy than anticipated yearly consumption by over a factor of 2.[10,24] Capturing all of this energy is not realistic, but even fractional amounts would make an immense impact in a society relying on nonconventional energy resources.

Of course, capturing solar energy is not enough. There are, among other aspects, significant supply vs. demand and supply vs. demand locations differences. The energy must be stored. Common methods to store solar energy include thermal, pumped hydro, batteries, and chemical bonds (fuels).[10,13,14] Fuels are the best storage option on paper from a combination of their large energy density, their ability to store energy for long periods of time (hours to months), and their ability to be utilized at locations lacking centralized energy distribution systems.[14] The fundamental reason fuels have large energy densities is because the energy stored is confined in bonds among low molecular mass elements like hydrogen, carbon, nitrogen, and oxygen. Fuel types may be compared by plotting their gravimetric densities (enthalpy of combustion divided by molar mass) vs. their volumetric densities (gravimetric density multiplied by fuel density) as shown in **Figure 1.2** with select batteries shown for comparison.[13,25-27] Hydrogen gas has the largest gravimetric density but an incredibly small volumetric density unless

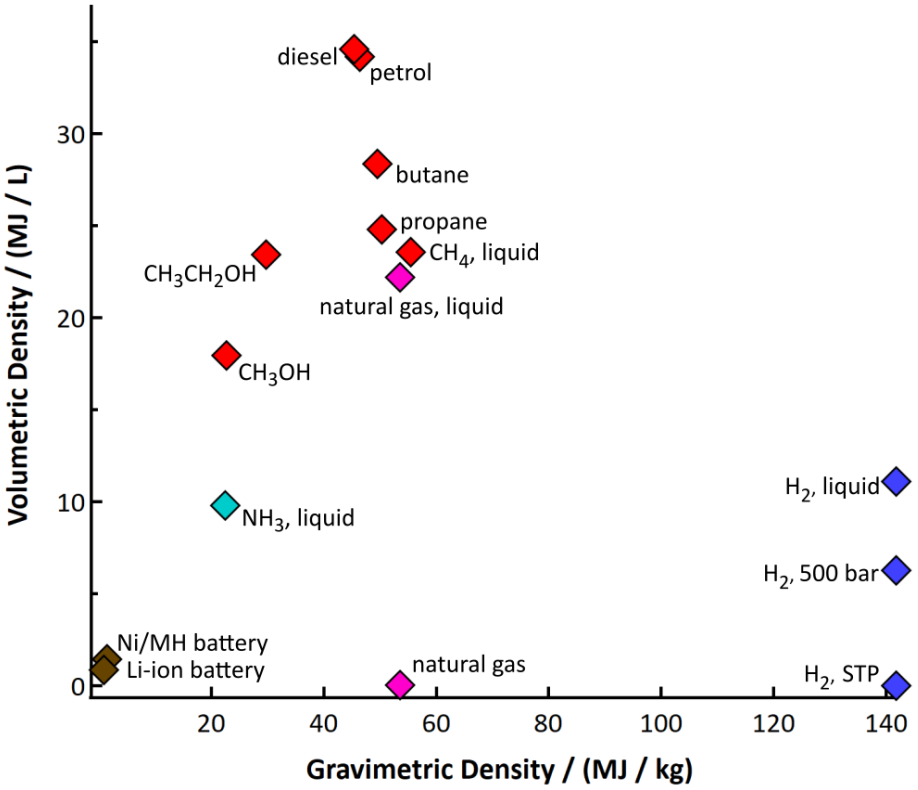

Figure 1.2: Plot of gravimetric density vs. volumetric density of various fuels which color are coded as hydrogen (blue), ammonia (teal), natural gas (pink), and carbon based (red). Ultimately, alternative fuels must 1) have sufficient gravimetric and volumetric densities and 2) be made efficiently and cheaply to rival typical fuels like petrol and diesel. Select batteries are shown for comparison (color coded brown). Though of course useful in modern life for applications such as electronics, the plot demonstrates batteries are currently poor options for large scale alternative energy solutions.

compressed or liquefied. Other alternative generated from energy intensive CO_2 and N_2 reduction processes are more practical from the volumetric perspective, but are no match for fossil fuels.

To become competitive with fossil fuels, alternatives must be generated cheaply and efficiently. A proposed method for this is artificial photosynthesis (**Figure 1.3a**); in natural photosynthesis from which this derives inspiration, energy from solar radiation generates an electron-hole pair to drive water splitting

to oxygen and two protons/electrons (hydrogen), with the protons and electrons ultimately transformed into an organic molecule (energy storage).[8] In an idealized artificial system like the photovoltaic coupled electrolyzer depicted in **Figure 1.3b**,[28] an electric current generated by a light harvesting photovoltaic (PV) is wired to an electrochemical cell. The PV harnesses a solar photon to produce electron-hole pairs to

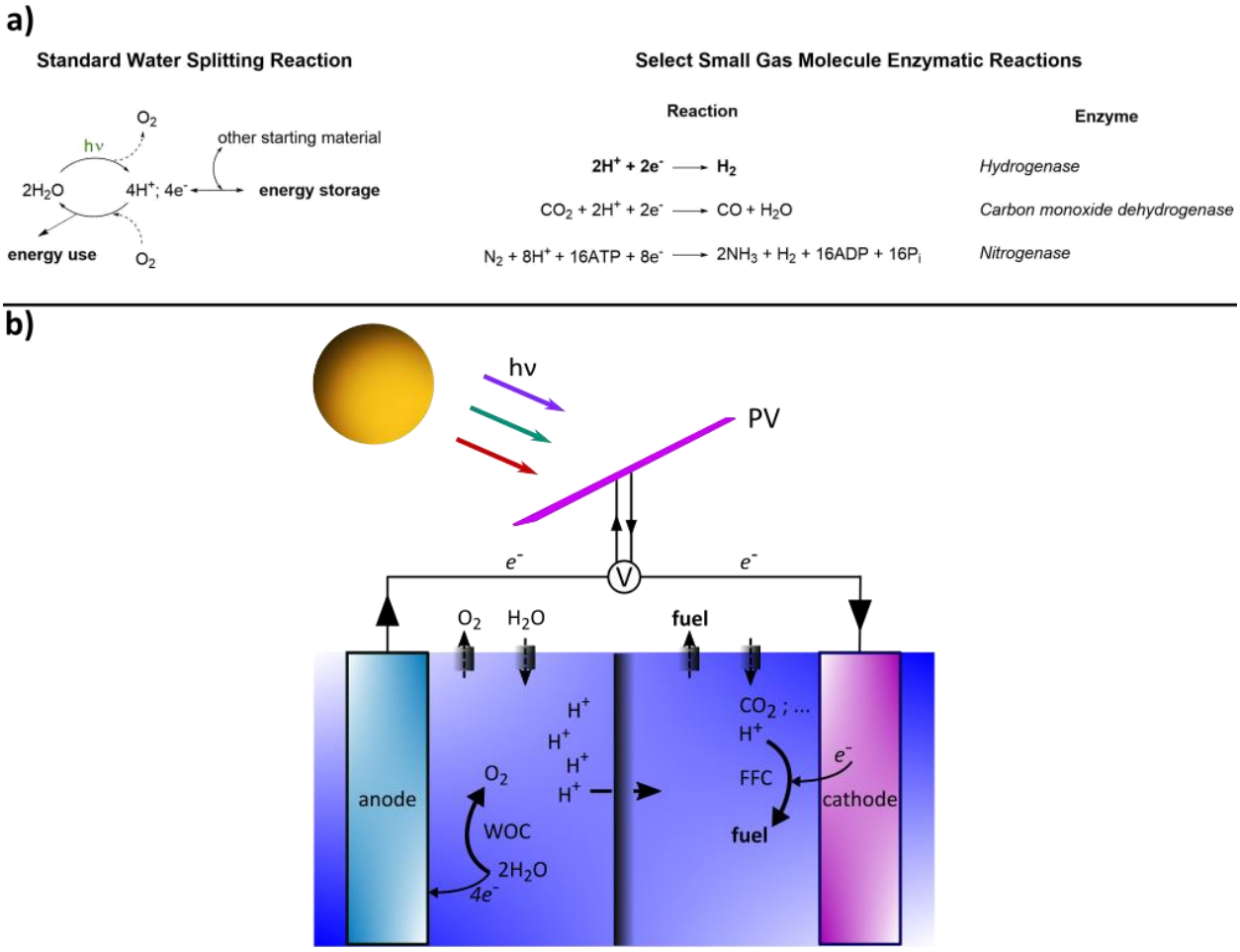

Figure 1.3: a) Schematic of water splitting (adapted from refs 7 and 8) and select enzymes related to energy conversion processes. The hydrogenase reaction, the major focus of this thesis, is bolded. **b)** Illustration of water splitting via a photovoltaic electrolyzer for renewable energy conversion as described in the main text. WOC = water oxidation catalyst; FFC = fuel forming catalyst; PV = photovoltaic device. Adapted from ref 28.

provide a driving force for the fuel cell to operate. Electrons from the conduction band of the anode transverse the electric circuit to the cathode. This results in an oxidizing enough conditions at the valence band to drive water oxidation via a water oxidation catalyst (WOC), which results in just oxygen formation and proton generation. The protons can migrate across the membrane to the fuel generation side of the cell. Here, the electrons along the electrical circuit are reducing enough to drive a reaction with a fuel forming catalyst (denoted here as FFC) to reduce protons (for proton reduction to hydrogen) or other small molecules (such as CO_2 to generate renewable carbon based fuels, which also requires protons). The only byproducts are oxygen, and the only necessary starting material are any required small molecules, water, and the solar photons. Use of the fuel simply regenerates starting materials utilized (e.g. CO_2) and water for net-zero emissions.

Various benchmarks must be achieved for artificial photosynthesis to be practical for large scale use; this includes the development of efficient and cheap catalysts for the fuel forming reactions.[10,14,28] Given that gas processing metalloenzymes, such as those listed in **Figure 1.3a**, catalyze small molecule transformations very efficiently, a fundamental understanding of their reactivity will aid in developing catalyst blueprints.[29-31] Protons, electrons, and often hydrogen gas are required for the reactions in **Figure 1.3a**; hence the bolded reaction in **Figure 1.3a**, the reversible reduction of protons by the hydrogenase enzymes, is thus a minimal model for understanding efficient multi proton transfer, multi electron transfer, and hydrogen reactivity in biological systems that have yet to be realized in efficient and cost effective synthetic catalysts.

1.2 – Enzymatic Catalysis and Gas Processing Metalloenzymes for Energy Conversion: General Considerations

Figure 1.4 shows the classic reaction coordinate of a catalytic vs. non-catalytic transformation of the unimolecular process S → P and the standard transition state theory scheme classically used to describe catalytic rate enhancement.[32,33] The transition state theory explanation of catalytic power is that tighter binding of the transition state to the enzyme leads to a lower activation energy and thus enhanced

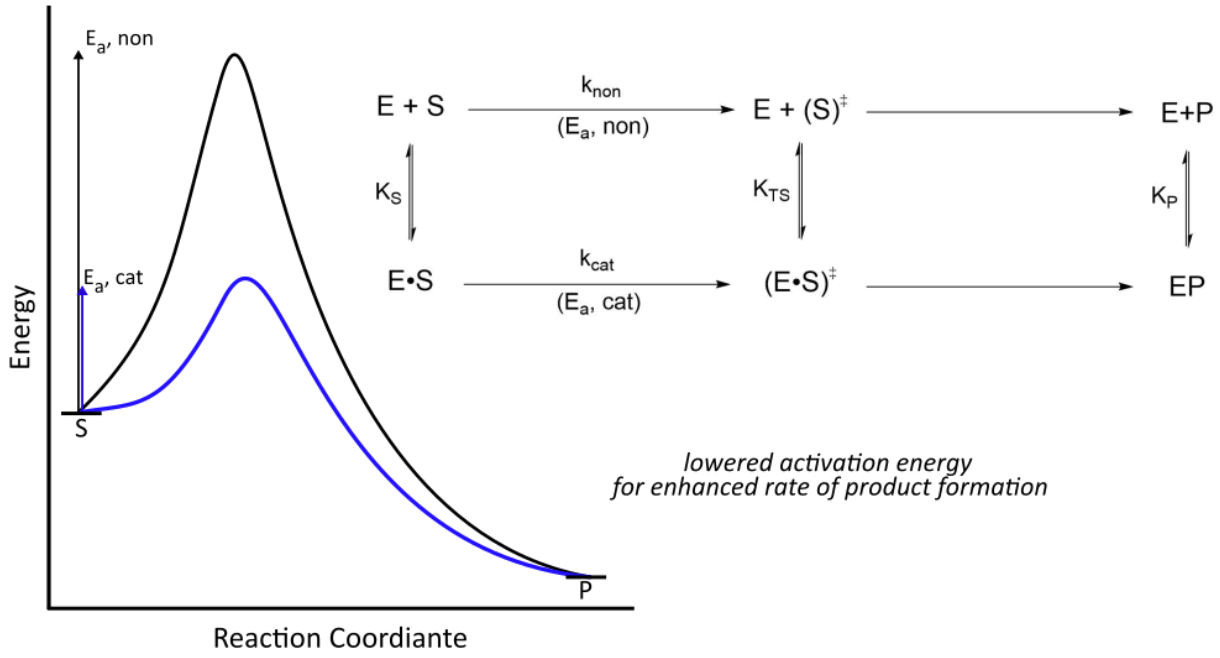

Figure 1.4: Non-enzymatic/enzymatic S→ P reaction coordinate with one activation barrier. The corresponding schematic illustrates the two pathways according to classic transition state theory (TST), which promotes the idea the enzyme lowers the energy barrier because of tighter transition state binding (adapted from refs 32 and 33). TST was critical for developing an understanding of enzymatic reactions; however, it does not capture other important aspects of the reactions like dynamics and electrostatics necessary for reactivity. The energy diagram of course becomes more complicated with more realistic reactions that contain intermediates and that are multi-step; an enzyme must be able to lower all of the barriers relative to a general solution reaction.

turnover rates.[32] However, enzymes are far more sophisticated than initially realized and utilize complex reaction coordinates with convoluted electrostatic and dynamic processes on timescales ranging from femtoseconds to seconds that remain poorly understood.[33-38]

The field of bioinorganic enzymology often focuses on systems with a metal based active sites. A broad subset of these enzymes are gas processing ones like those listed in **Figure 1.3a**, and a general template of these enzymes is depicted in **Figure 1.5a** in which substrate/product molecules transfer between a

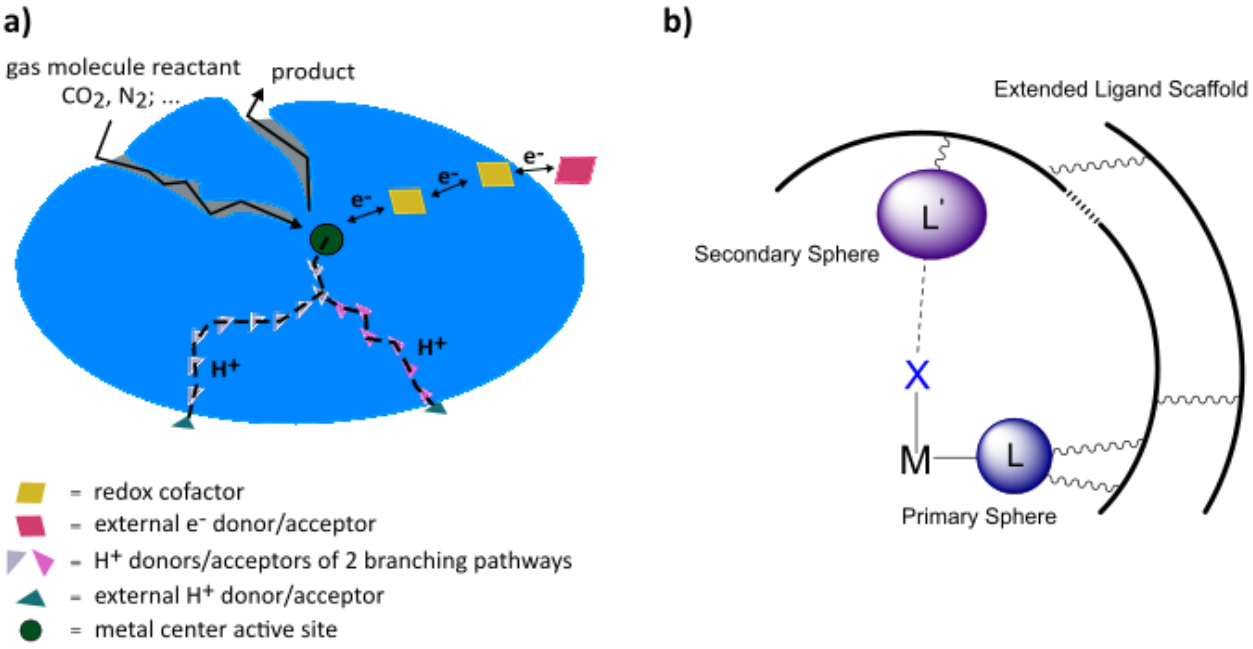

Figure 1.5: a) Generalized framework of a gas processing metalloenzymes with a buried metal center, gas channels that deliver substrate or products, ionizable amino acids for proton transfer, and redox cofactors for electron transfer, all of which are required for small molecule transformations relevant to energy conversion such as CO_2 reduction, H^+ reduction, or N_2 fixation. **b)** Sketch of various aspects of the metal center and primary sphere which forms the building block of the metalloenzymes power, the secondary sphere which influences the primary sphere, and the extended ligand scaffold that influences both.

buried active site and the external environment via gas tunnels;[39] in accord with general enzymology principles, the reducing equivalents transfer along redox active cofactors[40] and protons along ionizable amino acids and water molecules.[41] The heart of the enzyme is the metallic cofactor (depicted as a simple monometallic system in **Figure 1.5b**) where ligands are either protein bound (amino acids of the larger scaffold) or non-protein bound (not connected to the larger protein scaffold).

A critical design component of the primary sphere for enzymes like those in **Figure 1.5a** is the use of cysteine/thiol based ligands,[30,42] which has inter-tangled structural and mechanistic advantages. From a structural standpoint, it allows bimetallic and higher order metals to form as necessary[30] (many of the enzyme based reactions in **Figure 1.5a** occur at active sites with at least two metals[39]). A critical structural/mechanistic feature is the metal-sulfur bond is highly covalent as dictated by hard and soft acid and base theory,[43] which can result in "electronic buffering" between various metal redox states.[30,44] The entire active site behaves as a redox unit instead of just the metals, allowing for multi electron processes to occur within a narrow redox range which can be advantageous in specific physiological and ecological environments (this too can be aided by multiple metal centers, which are often electronically coupled via the connecting ligands).

Though the primary sphere sets the framework for catalysis, it is not enough by itself. There are two instructive examples of this; the first involves the MoFe-cofactor of many nitrogenases, which is likely the site of N_2 reduction to NH_3 in the holoenzyme. Upon isolation from the protein the cofactor itself does not form NH_3, though it can participate in other "side" reactions nitrogenases catalyze.[45] The second example involves a bimetallic iron hydrogenase: a small molecule active site mimic was demonstrated to display no activity; however, when incorporated into the apoprotein the mimic 1) adopted the standard holoprotein active site geometry and connectivity and 2) catalyzed proton reduction with rates nearly identical to the same enzyme isolated from a typical protein expression.[46,47]

Clearly, the secondary and outer sphere environment, like that depicted in **Figure 1.5b**, is critical for efficient catalysis. They provide various covalent and non-covalent interactions that facilitate electrostatic and dynamic processes for efficient and specific selective substrate binding, substrate activation, bond making and breaking, and product removal. The general principles of such cooperativity remain quite elusive in bioinorganic catalysis,[42,48] making it critical to understand such structure-function relationships to further develop or refine synthetic catalyst design templates. The relative simplicity of the catalytic cofactor substrate requirements of [NiFe]-hydrogenases poise them as excellent models to investigate such metal-ligand cooperativity.

1.3 – Hydrogenases, with a Focus on [NiFe]-Hydrogenases

1.3.1 – An Overview of Hydrogenases and Their General Reactivity

The deceptively simple reversible reduction of protons, $2H^+ + 2e^- \leftrightarrows H_2$, occurs in nature by the action of the hydrogenase (H_2ase) enzymes.[49,50] There are three evolutionarily distinct H_2ase classes which are defined by their catalytic cofactor metal content: [NiFe], [FeFe], and [Fe]-only[51] (the [Fe]-only was initially thought to be metal-free; each cofactor is pictured in **Figure 1.6**[52]). The ecologically and physiologically diverse [NiFe] and [FeFe] classes are further divided into groups (and the [NiFe] into subgroups) based on amino acid sequence motifs and the enzyme's cellular environment and function.[51,53,54] Both are distributed in bacteria; the [NiFe] class is also found in archaea while the [FeFe] class is also found in eukarya[51,54] (and tentatively archaea[53]). *In vivo* requirements often poise [NiFe]-H_2ases to function in the direction of H_2 oxidation and the [FeFe]-H_2ases for H_2 production,[51,53] but *in vitro* studies show both often display reversible behavior with minimal overpotential,[55-57] though a clear bias for either H_2 production or oxidation is usually evident for a given enzyme source. Their electrochemical behavior can also be similar to the exceptional Pt based catalysts (per active site)[58,59] and turnover frequencies are quite large, with some being ~ 1,000 – 10,000 s^{-1}.[55,59] The [Fe]-only H_2ases are too very

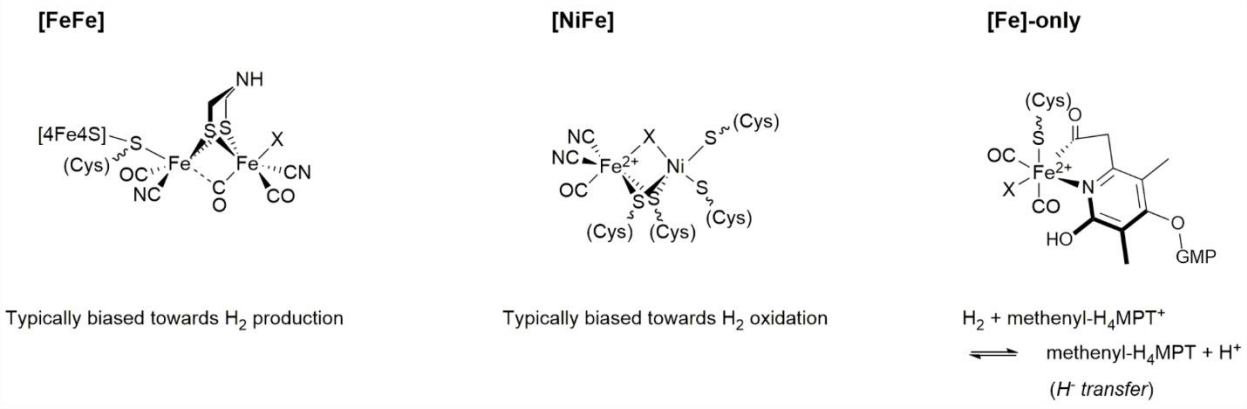

Figure 1.6: The active sites of the three hydrogenase classes. The redox state of formally redox inactive metals are labeled. The other metals formally change oxidation state during turnover (nickel typically adopting redox states of +3, +2, and +1, and iron +2 and +1).

efficient and exhibit large rates.[60] However, they are only found in specific methanogenic archaea under nickel limiting conditions that suppress [NiFe]-hydrogenase expression, and are different in that they are formally redox inactive and specifically function as a reversible hydride transfer agent in the presence of methenyltetrahydromethanopterin (methenyl-H_4MPT).[61]

A common occurrence in the primary sphere of these enzymes are the soft carbon monoxide/cyanide and cysteine/thiolate ligands (**Figure 1.6**) which are expected to tune active site electronics for H_2 activation (and formation) via η-H_2 / σ-complex complex formation via synergistic M(dπ, filled) → $H_2(\sigma^*)$ and/or $H_2(\sigma)$ → M(dσ, empty) electron donation (**Figure 1.7a**).[62,63] There are three possible outcomes following η-H_2 formation: a stable η-H_2 complex, homolytic cleavage of H_2 (oxidative addition), or heterolytic cleavage of H_2 (**Figure 1.7b**); the possible outcomes primarily depend on the metal center properties and donor/acceptor nature of the ligand environment.[62-64] The combination of 3d metal(s), donor/acceptor ligand environment, and plausible nearby proton/donor acceptors highly suggests H_2ases utilize a heterolytic mechanism.[62-64]

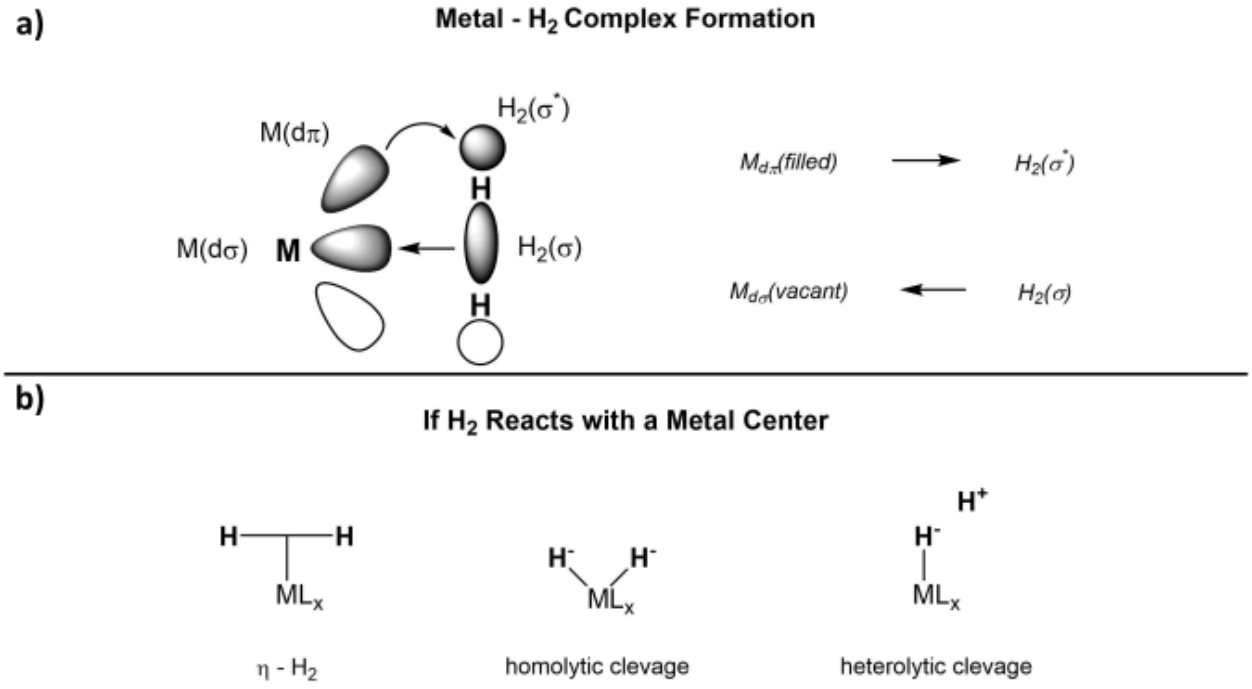

Figure 1.7 a) Representation of dihydrogen activation by a metal complex via synergistic interactions between a metal center and H_2. Adapted from ref 63. **b)** Results of a metal-dihydrogen interaction: sigma complex formation (η-H_2) formation, homolytic cleavage to make a dihydride complex, or heterolytic cleavage to form a metal-hydride complex and a proton, which results in base protonation via an inter- or intramolecular reaction depending on the metal complex and surrounding environment. A η-H_2 sigma-complex may be in an equilibrium with a dihydride complex. Formation of the sigma complex or the mechanism of hydrogen activation (heterolytic or homolytic) depends on a variety of metal and/or ligand properties that effect orbital overlaps and the extent of $H_2(\sigma^*)$ occupation for bond breaking.

Heterolysis is further implied by two classic H_2ase assays 1) the H/D exchange of H_2 or D_2 gas with D_2O or H_2O, respectively, and 2) ortho/para H_2 nuclear spin isomer conversion.[65] Using cells from the H_2ase containing *Proteus vulgaris*, Krasna and Rittenberg demonstrated isotopic exchange between a H_2 gas phase and D_2O solvent. Furthermore, they showed isomer conversion occurred *only* in H_2O; D_2O facilitated

the exchange reaction instead.[66] The conclusion was that hydrogen is heterolytically cleaved to form a hydride and an exchangeable proton. In H_2O there is no isotopic scrambling, and so the hydride ultimately recombines with a proton to form para hydrogen. In D_2O, isotopic exchange of the proton with deuterons with solution facilitates H/D exchange, so even in the presence of ortho hydrogen enrichment of the para spin isomer does not occur[66] (or at least much more slowly depending on the organism[65]). **Figure 1.8a**-**b** illustrates such isotopic H/D exchange and the ortho/para conversion via this hypothesis. In combination with fundamental inorganic aspects of the H_2ase active sites, the bulk evidence points to H_2 heterolysis.

Assuming heterolysis, redox chemistry is absent during ortho/para and H/D exchange; these only require substrate activation/product formation, and in the case of H/D exchange, H^+ and D^+ movement. Redox chemistry is required for complete turnover in the [NiFe] and [FeFe]-H_2ases, which is classically demonstrated by the reduction/oxidation of an external redox mediator like a natural redox partner or redox dye (e.g. methyl viologen, benzyl viologen, methylene blue).[65] The general turnover process with an external electron donor/acceptor is illustrated in **Figure 1.8c** with arbitrary electron and proton transfer orderings (in such assays, protons are transferred to/from an aqueous buffer). The precise ordering of proton and electron transfers here and in any relevant enzymatic reaction (PT/PT, PT/ET, or concerted) depends on the proton coupled electron transfer landscape that is modulated by the protein scaffold.[67]

1.3.2 – [NiFe]-Hydrogenases: General Properties

The [NiFe]-H_2ases are the most diverse[51,53] and probably the most ancient[54] of the hydrogenase classes. The minimal architecture is a heterodimer, with a large subunit harboring the active site and a small subunit harboring electron transfer iron-sulfur clusters.[51,68] The first crystal structure in 1995 with the *Desulfovibrio gigas* (*D gigas*) enzyme[69] and later structures from other enzyme sources showed there

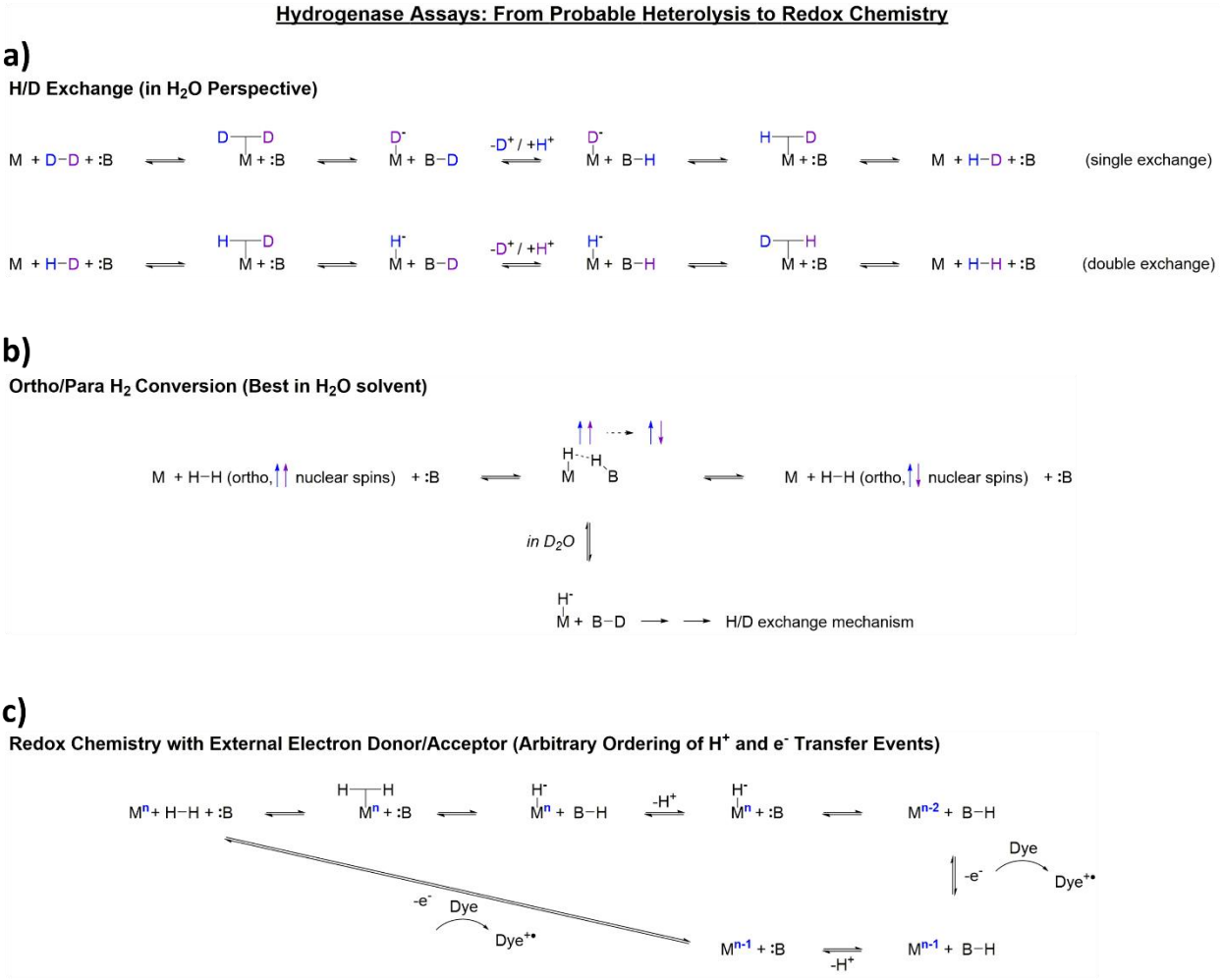

Figure 1.8: The three types of major activity displayed by hydrogenases from the perspective of a metal center, dihydrogen, and a nearby base. **a)** H/D exchange in D_2 gas with H_2O solvent; an essentially identical scheme could be drawn with H_2 gas and D_2 solvent. **b)** Ortho/para hydrogen nuclear spin conversion in H_2O; in D_2O, H/D exchange competes with the nuclear spin conversion. **c)** A very overly simplified mechanism of hydrogen oxidation/proton reduction by a metal center like in hydrogenases, which incorporates dihydrogen complex formation and heterolytic cleavage. Each proton and electron transfer (PT and ET) step is shown as a distinct step with arbitrary ordering. PT and ET steps could also be concerted (that is, one proton and one electron transfer could occur by concerted proton-coupled electron transfer). Note: to date, there is no proof of heterolysis.

are three iron-sulfur (FeS) clusters in a near linear arrangement extending form the active site to the protein surface with edge-to-edge distances of ~ 12Å,[52,70] which is within an optimal distance for electron tunneling for efficient catalysis.[40] Each cluster is termed relative to its location from the active site: proximal (typically $[4Fe4S]^{2+/+}$), medial (typically $[4Fe4S]^{2+/+}$ or $[3Fe4S]^{2+/+}$), and distal (typically $[4Fe4S]^{2+/+}$).[52,69,70] Crystallographic studies, most notably through the use of xenon or argon soaked crystals,[71,72] and computations/simulations showed the presence of hydrophobic gas tunnels for H_2 transfer that converge near the active site nickel atom.[70,73,74] Possible proton transfer pathways from the active site to the protein surface were hypothesized via crystallographic analyses, mutagenesis and computations/simulations,[70,74-79] but such pathway(s) have been notoriously difficult to verify. **Figure 1.9a** provides a pictorial overview of the minimal heterodimeric structure and general midpoint potentials for an energy landscape template at pH = 7.0 (FeS cluster midpoint potentials are from the *D gigas* enzyme[40,80,81]).

The active site itself consists of a $(CN)_2COFe(\mu\text{-}Cys)_2Ni(Cys)_2$ core,[69,73,82-84] which we can consider being constructed from an iron ($Fe(CN)_2CO$) and a nickel ($(\mu\text{-}Cys)_2Ni(Cys)_2$) fragment. The iron stays in the +2 redox state during catalysis[85,86] and the fragment appears to utilize cyanide and carbon monoxide, at a minimum, to 1) maintain a low spin iron redox state via their large ligand field strength and 2) to take advantage of their strong σ-donating properties and the π-accepting ability of CO to fine tune the active site electron density (electronic buffering) during any exogenous ligand binding that may occur trans to the CO ligand as well as for hydrogen splitting/formation.[62] The actual site of H_2 binding is believed to occur at the nickel atom,[87] where the protein scaffold likely keeps the nickel coordination geometries in quite reactive distorted structural/electronic configurations to help facilitate efficient catalysis.[88,89]

Both fragments together and nearby residues (see **Figure 1.9b**) form an ideal electronic buffer to facilitate facile proton reduction/hydrogen oxidation. Paramagnetic resonance studies have shown the nickel atom is formally redox active and can adopt the +3, +2, and +1 redox states;[90-93] however, X-ray

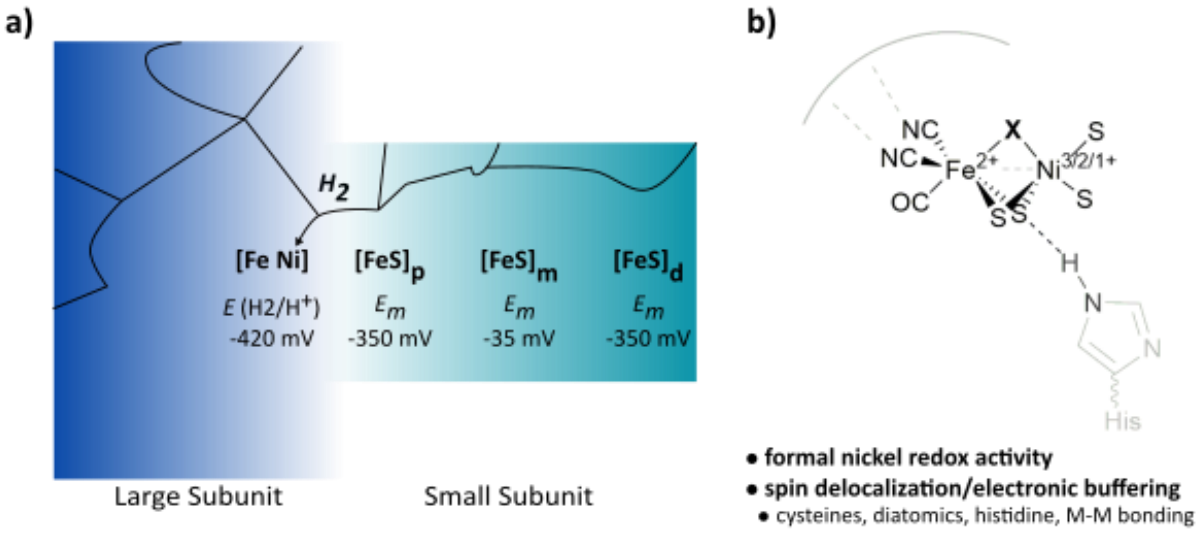

Figure 1.9: a) Representation of the minimal heterodimer [NiFe]-H_2ase architecture. The midpoint potential of the H_2/H^+ couple is provided for a general energetic description of the overall H_2ase reaction at pH = 7.0; this changes by 0.59 mV/pH by the standard Nernst equation. The β-subunit contains the three iron-sulfur clusters of the standard electron transfer chain which are abbreviation as proximal (p); medial (m); and distal (d) based on their proximity to the active site. The general midpoint potentials of the FeS clusters for the extensively studied *D gigas* enzyme are provided at pH = 7.0. These differ with various enzymes. Exactly why the medial cluster has a rather high midpoint potential is not known and beyond the scope of this thesis; but what is evident is it does not seem to hinder catalysis despite the mismatch with the other clusters and active site. **b)** Representation of the active site in the primary sphere along with hydrogen bonding interactions from the conserved histidine and generalized description of hydrogen bonding character of the cyanide ligands. Based on pulsed EPR studies and computational work, the histidine is thought to be protonated throughout catalysis and tune the active site electronics. The iron is believed to be low spin and in the +2 redox state throughout catalysis, and the nickel can formally adopt the +3, +2, and +1 redox states. Below is a brief list of active site properties that make it an electronic buffer system despite the formal nickel redox activity.

absorption spectra indicate minimal perturbation of the 1s → 3d Ni K-edge energy for numerous [NiFe]-H_2ases under various redox poises, which suggests actual redox changes at the nickel atom are minimal.[94] In fact, paramagnetic resonance[95-97] and computations[98-101] have found significant electron density on the cysteine ligands, indicating these are non-innocent and participate in redox events despite the formalized nickel oxidation state changes.[94] One of the bridging cysteines hydrogen bonds to a rather conserved secondary sphere histidine to further delocalize electron density.[98,102-104] The buffering extends to the $Fe^{2+}(CN)_2CO$ fragment via π-backbonding between the formally redox inactive iron and the CN^- and CO ligands as indicated by changes of the infrared ν_{CO} and ν_{CN} bands when the nickel atom formally changes redox state.[105,106] This is further extended to the secondary sphere via hydrogen bonding by the cyanide ligands.[98,107] Furthermore, adoption of the unfavored highly reduced Ni^+ species[94] is aided by formation of a nickel-iron bond.[101,108]

These properties combined poise the active site to operate in a narrow redox window between roughly -300 mV to -450 mV (at least as indicated by *in vitro* studies).[52,106] This range is incompatible with adoption of formal nickel +3, +2, and +1 redox states that would necessitate a much larger potential window,[94] indicating the active site ligands and metals of both the iron and nickel fragment function together as a single redox unit.

1.3.3 – [NiFe]-Hydrogenases: A Mechanistic Outline in the Primary Sphere

With the general structural and electronic framework of the [NiFe] core established, we now turn to how it facilitates turnover. This first requires a few brief remarks. First, our discussion requires mentioning a variety of enzyme "states" which are abbreviated Ni_x^{y+}-Z, where 1) y+ refers to the formal nickel redox state, 2) x = u, r, or a mean a "unready", "ready", or an "active" state, respectively, and 3) Z refers to specific letter(s) historically designated for a specific active site configuration (e.g. electron count, exogenous ligand presence, extent of protonation). Second, distinct hydrogenases have likely adopted

unique properties for optimal function; however, the general belief is that they all utilize the same general active site states from an outline perspective.[52,109] However, kinetic competency of distinct states has only been established in soluble hydrogenase-1 from *Pyrococcus furiosus*, and in this case chemical competency was only demonstrated for electrons (and by consequence protons).[110] Lastly, regarding infrared features, ν_{CO} values are discussed because they red- or blueshift as expected based on changes of active site electron density. This is because carbon monoxide is a strong π-acid[111,112] that allows its extent of π-backbonding with the iron of the $Fe^{2+}(CN)_2CO$ fragment to be systematically correlated to distinct redox/protonation events. The CN ligands are less π-acidic[111,112] and the backbonding changes are not as clearly correlated with redox/protonation events.[52]

[NiFe]-H_2ases are often isolated in oxidized inactive states, especially after aerobic purification. Classic oxidized states are called Ni_u^{3+}-A and Ni_r^{3+}-B; they differ by how long activation is required to obtain maximal catalytic activity. Ni_u^{3+}-A reactivates slowly (on the order of hours) in the presence of a reductant; on the contrary, Ni_r^{3+}-B reactivates quickly (on the order of minutes).[52,68] It is generally accepted both Ni_u^{3+}-A and Ni_r^{3+}-B have a bridging hydroxide ligand, though other differences (e.g. why one takes longer to activate) remains unclear.[52] Broadly speaking, however, distinct [NiFe]-H_2ase groups/subgroups utilize particular methods to adopt to oxidizing conditions and/or oxygen that do not necessarily conform to Ni_u^{3+}-A and Ni_r^{3+}-B;[109,113,114] Ni_u^{3+}-A itself is not typically observed outside of the so-called standard group-1 [NiFe]-H_2ases and often times ambiguity results in Ni_r^{3+}-B being referred to as "Ni_r^{3+}-B like".[52,109]

Activation proceeding from the more common Ni_r^{3+}-B/"Ni_r^{3+}-B like" state first involves a one electron reduction to produce Ni_r^{2+}-S, where "S" indicates it is an EPR silent state (**Figure 1.10**).[52,106] Further activation results in the resting state of the enzyme. Details of the Ni_r^{3+}-B → Ni_r^{2+}-S → resting state are not clear, but it is thought this activation process involves protonation of the bridging hydroxide to form water that is transferred away from the catalytic core via hydrophilic channels. [52] The resting state is called Ni_a^{2+}S (**Figure 1.10**). For some time, was hypothesized that Ni_a^{2+}-S had an empty binding position between

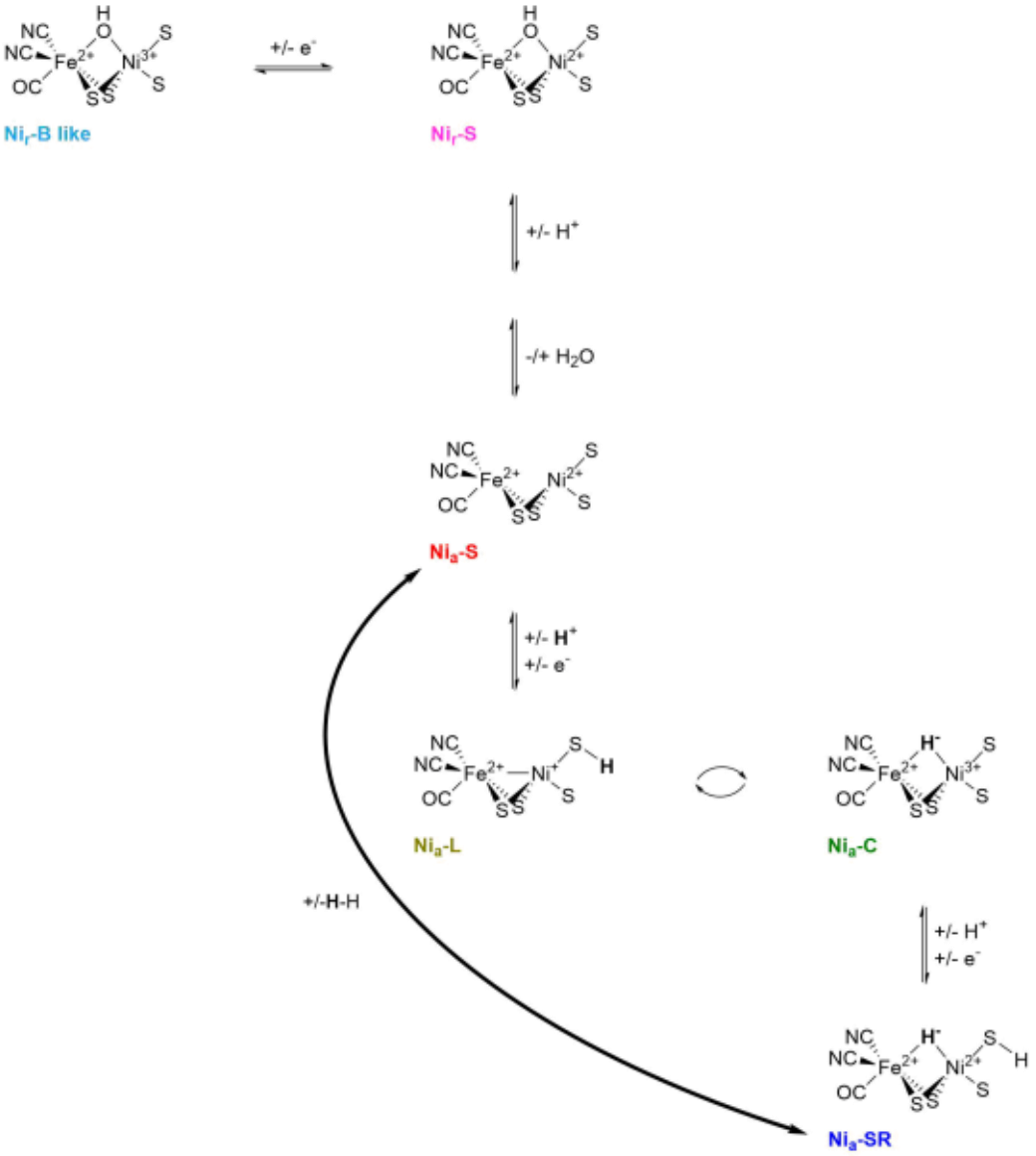

Figure 1.10: An outline of activation and turnover of [NiFe]-H_2ases. Oxidase activity from a Ni_r^{3+}-B like state (top left) forms water that allows the enzyme to form the resting state, Ni_a^{2+}-S. In the direction of proton reduction, a proton-coupled electron transfer event forms Ni_a^{+}-L forms. This state then tautomerizes to form Ni_a^{3+}-C. Afterwards, a proton coupled electron transfer event forms Ni_a^{2+}-SR. The second proton protonates the bridging hydride to form H_2 (which is removed via hydrophobic gas channels to bulk solution) to regenerate the enzyme resting state.

the nickel and iron atoms (consistent with ligand from the inactive state being transformed into water and being removed from the active site),[52,106] but the vacant bridging position was only recently confirmed in the first crystal structure of Ni_a^{2+}-S[88] (the enzyme source being the group 3b[53] *Methanosarcina barkeri* H_2ase).

Moving in the direction of proton reduction, a proton-coupled electron transfer (PCET) event forms the EPR active Ni_a^{+}-L state.[110,115,116] Recent cryogenic FTIR spectroscopy with the enzyme from *Desulfovibrio* v*ulgaris* Miyazaki F (*Dv* MF) provided compelling evidence the proton resides on a terminal cysteine ligand (**Figure 1.10**),[117] which was generally consistent with a former Raman study[118] and a combined computational and paramagnetic resonance study.[101] The same computational work predicted the presence of a nickel-iron bond, which is ultimately protonated by the cysteine bound proton[101] to store two electrons and one proton of H_2 as a bridging hydride in the tautomeric EPR active Ni_a^{3+}-C state (**Figure 1.10**).[98,102,119]

The fact that both Ni_a^{+}-L or Ni_a^{3+}-C have paramagnetic properties in addition to infrared features has led to extensive experimental and computational investigations that arguably making them the most rigorously characterized catalytic states.[93,96-98,101-103,115,116,119] Of note is the $\geq$ 30 cm^{-1} ν_{CO} redshift of Ni_a^{+}-L compared to Ni_a^{2+}-S.[52,115,116] This is consistent with the expectation the $(\mu\text{-Cys})_2Ni(Cys)_2$ fragment would not promote formation of a highly reduced core with a formally monovalent nickel species,[94] thus highlighting the importance of the electronic buffer's $Fe^{2+}(CN)_2CO$ component. The ν_{CO} frequency of Ni_a^{3+}-C is blueshifted from Ni_a^{2+}-S by ~ 17 – 20 cm^{-1},[52,82,105,110,115] signifying a loss of electron density in the $Fe^{2+}(CN)_2CO$ fragment as expected following an oxidation event. However, the shift's magnitude is not as great as with Ni_a^{+}-L, which may stem from the anionic $(\mu\text{-Cys})_2Ni(Cys)_2$ fragment stabilizing the oxidized nickel[94] that could minimize the need for electron density uptake by the iron fragment.

The actual charge differences on the nickel atom in Ni_a^{+}-L and Ni_a^{3+}-C are unclear because both have similar K-edge energies in X-ray absorption spectra.[96,120] However, the rhombic Ni_a^{3+}-C EPR signals have g_z

~ 2.01 ~ g_e as expected for a d_z^2 HOMO; [121] but, the rhombic Ni_a^+-L g_z value is notably greater than g_e (~ 2.05 vs. 2.0) and has a much larger separation of g_x and g_y values than Ni_a^{3+}-C, demonstrating there are much more than just subtle differences between the two states.[122] Indeed, the nickel-iron bond in Ni_a^+-L results in a rehybridization of orbitals to give a nickel based $d_x^2 - _y^2$ HOMO and largely iron centered d_x^2 LUMO that leads to significantly altered electronics and thus orbital energies that are compatible with the observed paramagnetic properties[101] and yet the similar nickel electronics to Ni_a^{3+}-C observed from X-Ray absorption spectra[101] (see refs. 95 and 98 for, to the best of our knowledge, the most comprehensive descriptions and discussions of the electronics and paramagnetic properties of Ni_a^{3+}-C and Ni_a^+-L).

Following Ni_a^{3+}-C formation, a PCET event forms the most reduced state of the enzyme, Ni_a^{2+}-SR (**Figure 1.10**).[110] This state is EPR silent and hence the "R" to distinguish it from the enzyme resting state. A high resolution crystal structure and nuclear vibrational resonance spectroscopy from *Dv* MF indicated Ni_a^{2+}-SR has a bridging hydride, and models of the data support the additional proton resides on a terminal cysteine ligand (**Figure 1.10**),[123,124] although the cysteine protonation remains controversial.[125] The ν_{CO} frequency of Ni_a^{2+}-SR is only slightly blueshifted relative to Ni_a^{2+}-S,[52,82,110] which is probably a consequence of the protonated cysteine ligand despite the same formal redox state. Protonation of the hydride forms hydrogen and returns the enzyme to the resting state.

1.3.4 – A Need to Probe Structure-Function Relationships Between the Active Site and Ligand Scaffold

The H_2ases are of significant interest in the inorganic and organometallic community because they inspire design principles of robust and small footprint catalysts that could be used in practical systems. Furthermore, they provide insight into fundamental proton and electron management in efficient energy conversion, which is important for understanding even more complicated energy conversion systems for reactions like nitrogen and CO_2 fixation that also utilize protons/hydrides, electrons, and sometimes hydrogen.

There are broadly two types of H_2ase inspired systems: 1) those that aim to mimic the active site structure, electronics, and mechanism (biomimetic systems) and 2) those that do not conform to the structures or mechanisms of the H_2ases, but borrow enzyme features such as acid-base functionalities, metals, and general reactivity (bioinspired systems). There are an immense amount of fascinating biomimetic H_2ase complexes.[112,126,127] Unfortunately, the mimics turnover rather slowly (if at all) and/or have rather large overpotentials (η) that so far limit prospects for large scale use. In contrast, bioinspired complexes have provided more promise for developing catalysts for use beyond fundamental organometallic research.

The case point with bioinspired complexes are the nickel diphosphine electrocatalysts investigated by the DuBois', Shaw, and co-workers. [31,128-130] As with H_2ases, the building blocks of these systems are critical for reactivity. Complexes like those shown in **Figure 1.11a** established the importance of structural and electronic effects (e.g. distortions, electron donation, and withdrawing ability) dictated by the pincer ligands that fine tune important reactivity factors, especially the thermodynamic hydricity and pK_a's of metal hydrides.[128,131,132] But, as with the H_2ases, the building blocks are not enough. Any of the complexes of the general $[Ni(diphosphine)_2]^{2+}$ framework that managed to turnover were sluggish with large overpotentials.[128,129]

Installing pendant amines (e.g. a proton relay) in the secondary sphere via the use of PNP and the $P^R_2N^{R'}_2$ ligands modestly improved the catalysts. This is because the PNP ligands and the varied electronics and structural isomers afforded by $P^R_2N^{R'}_2$, can 1) interact with substrate/product H_2, 2) be tuned to closely match the hydricity/pK_a of the metal to lower energy barriers for hydride formation or donation, 3) participate in proton transfer to/from the catalytic core, 4) exchange protons rapidly with external acid/base, and 5) couple proton and electron transfers, all which help lower reaction energy barriers for increased rates or lower overpotentials.[128-130,132-134] **Figure 1.11b** provides generalized $[Ni(PNP)_2]^{2+}$ and $[Ni(P^R_2N^{R'}_2)_2]^{2+}$ structures, and comparison of the thermodynamics and kinetic parameters listed under the

Building Blocks

a)

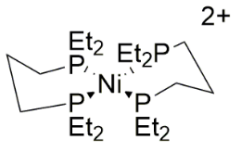

$[Ni(depp)_2]^{2+}$
$TOF_{H2\ ox} < 0.2\ s^{-1}$
Operating Potential = 0.00 V vs $Fc^{2+/+}$

b)

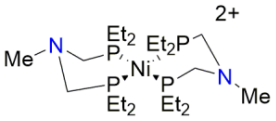

$[Ni(PNP)_2]^{2+}$
$TOF_{H2\ ox} < 0.2\ s^{-1}$
Operating Potential = -0.65 V vs $Fc^{2+/+}$

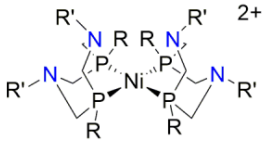

$[Ni(P_2^RN_2^{R'})_2]^{2+}$
$TOF_{H2\ ox} \sim 10\ s^{-1}$
Operating Potential = -0.73 V vs $Fc^{2+/+}$

Toward More Practical Systems

c)

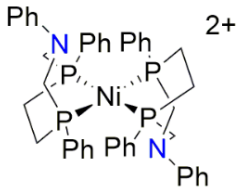

$[Ni(P_2^RN^{R'})_2]^{2+}$
$TOF_{H+\ red} \sim 100{,}000\ s^{-1}$
Operating Potential = -1.16 V vs $Fc^{2+/+}$
$\eta > 0.6$ V

d)

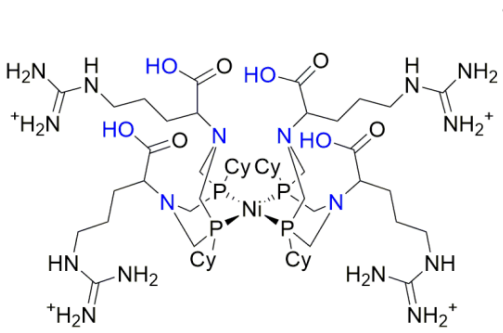

$[Ni(P_2^{Cy}N_2^{Arg})_2]^{7+}$
reversible
$TOF_{H2\ ox,\ opt} \sim 20\ s^{-1}$, 75 °C
$TOF_{H+\ red,\ opt} \sim 403\ s^{-1}$, 75 °C
$\eta \sim 0.2$ V

Figure 1.11: Aspects of H_2 oxidation/proton reduction catalysts evolution using diphosphine ligands. **a)** Mimicking the distorted nickel environment in [NiFe]-H_2ases which affords better reactivity for H_2 activation (see ref. 132, as well as ref 131). **b)** Use of pendant amines within secondary sphere. **c)** A catalyst that obtained an extraordinarily high turnover frequency (see ref 138). **d)** A reversible catalyst at elevated temperatures (see ref 142). Operating potential and TOFs for a) and b) from ref 129; overpotential and TOF for c) from ref 135 and for d) from refs 138 – 139. Pendant amine proton relays components are colored blue.

catalysts in **Figure 1.11a-b**[129] indicate how evolution of the catalysts beyond the primary sphere building blocks provided evident kinetic or thermodynamic benefits.

Overall, the use of the building blocks of the primary sphere with a secondary modifications minimally mimicked key protein features like proton transfer pathways and cooperativity of the ligand(s) and metal center for product activation/substrate release. However, broad issues remained such as the fact that the ligands were rather flexible; this resulted in the catalysts adopting various isomers that may or may not be productive in catalysis, thus slowing the rates and/or increasing the overpotentials (amongst other factors). More-so, the catalysts were typically reported to operate in only one direction.[129,130]

However, one of the faster nickel-diphosphine catalysts to date was generated by minimally mimicking key protein features. It utilized the slightly different $P^{R}_{2}N^{R'}$ ligand scaffold and had a TOF > 100,000 s^{-1} for H^{+} reduction, albeit with an operating potential > 1 V vs. $Fc^{2+/+}$ under optimal conditions (η > 0.6 V, see **Figure 1.11c**).[135]The astounded rate but large overpotential illustrated that generalized TOF-scaling relationships were being seen. These arise from the distinct electronic effects in the primary and secondary sphere that improve TOFs also imposing larger driving forces for redox events to occur at the metal center. In the case of DuBois' catalyst with the large TOF,[135] the large overpotential was at a minimum the consequence of electronic tuning to poise the metal center to be more hydridic for product release, which reduces the tetrahedral distortion of the resting complex and increases its reduction potential.[128,131,135] TOF-scaling relationships (often visualized as a plot of TOF vs η which has a positive slope) can be less drastic or be inverted (TOF vs η with a negative slope) if changes do not directly affect metal center electronics,[136] which is of course advantageous for catalyst design.

In attempt to circumvent various problems like those discussed above, recent generations of the nickel diphosphine catalysts have utilized more elaborate scaffold and solvent effects to 1) minimize isomer conformations via intramolecular interactions of peptide chains and/or interactions with solvent to poise a catalyst in reactive conformations and 2) provided extensions of the proton relay, both of which

can enhance rates and/or minimize overpotentials.[31,130,137-140] Quite notable advances were achieving electrocatalytic reversibility with peptide based complexes[138,139] (reversibility was quite rare beforehand;[129] an example peptide based complex is provided in **Figure 1.11d** along with a typical rate and overpotential for comparison to **Figure 1.11c**) and departure from the typical positive slope of TOF versus η correlations.[137,140]

Clearly, the "evolution" of the nickel diphosphine catalysts to more protein like systems (e.g. use of solvent and extensive scaffolds to control dynamics and electrostatics at the metal center and beyond) led to significant improvements past the fundamental catalyst building blocks. There has yet to be a reversible catalyst breaking the typical TOF-η relationship,[130] and there is clearly a very complex interplay between the building blocks, secondary sphere, and outer sphere that are not trivial to tune in a positive light simultaneously; for example, imparting improved structural dynamic control has been shown to have subtle effects that slow catalysis such as by changing the pK_a of secondary sphere proton relays.[141]

Nonetheless, the advances made with the nickel diphosphine systems indicate promise for even more breakthroughs. There are also related advances in utilizing artificial enzymes/mini-proteins for energy conversion reactions,[31,142,143] which include utilizing specific mutations of a protein scaffold to improve artificial systems.[144,145] Ultimately, an entire small protein scaffold surrounding a catalyst will probably prove most beneficial via ideal control of electrostatics, dynamics and rigidity, the solvent environment near the active site, and stability for precise application conditions.[31,142,143] Much work from protein engineering to catalyst designs will be required to achieve these goals. Our specific focus for contributing to this field is probing how the ligand scaffold in the enzymes provide the ideal macro- and micro-environment for catalysis with a [NiFe]-H_2ase.

1.4 – Hypothesis and Scope of this Thesis

The general catalytic mechanism of [NiFe]-H_2ases from the perspective of catalytic core is well established from a combination of crystallographic, computational, spectroscopic investigations, and information obtained from model compounds. As previously noted though, enzymes like H_2ases and corresponding bioinspired systems rely on far more than the metal center: the surrounding protein/ligand scaffold is incredibly important. Thus, refining design principles in bioinspired systems requires understanding how the protein scaffold contributes to bioinorganic catalysis. However, in bioinorganic enzymology the role(s) of amino acid scaffolds in catalysis are generally very controversial and not well established.

Our laboratory previously constructed an elementary model of [NiFe]-H_2ase catalysis with the soluble hydrogenase-1 from *Pryococcus furiosus* (*Pf* SH1), and the goal of this thesis was to begin mapping out how elementary steps in *Pf* SH1 are facilitated by the larger protein scaffold. We studied three secondary sphere enzymes variants that were previously shown by others to form mature enzyme and that have possible roles in chemical steps involving protons and/or hydrogen. The main portion of this thesis first discusses relevant background regarding native SH1. Then, it discusses results from enzyme variant studies that provided insight into proton transfer dynamics, electrostatics, communication of the primary sphere with the secondary sphere, and probable communication of the secondary sphere with the outer sphere that are required for efficient catalysis. More questions derived from the data than were actually answered, and a foundation for more in-depth structure-function studies of *Pf* SH1 has been set.

1.5 – References

(1) Hartley, H. Man's use of energy. *Nature* **1950**, *166*, 368-376.

(2) Smil, V. Energy in the twentieth century: Resources, conversions, costs, uses, and consequences. *Annu. Rev. Energ. Env.* **2000**, *25*, 21-51.

(3) Armaroli, N.; Balzani, V. The legacy of fossil fuels. *Chem. Asian J.* **2011**, *6*, 768-784.

(4) von Schneidemesser, E.; Monks, P. S.; Allan, J. D.; Bruhwiler, L.; Forster, P.; Fowler, D.; Lauer, A.; Morgan, W. T.; Paasonen, P.; Righi, M.; Sindelarova, K.; Sutton, M. A. Chemistry and the linkages between air quality and climate change. *Chem. Rev.* **2015**, *115*, 3856-3897.

(5) Lelieveld, J.; Klingmüller, K.; Pozzer, A.; Burnett, R. T.; Haines, A.; Ramanathan, V. Effects of fossil fuel and total anthropogenic emission removal on public health and climate. *Proc. Natl. Acad. Sci. U. S. A.* **2019**, *116*, 7192.

(6) Karl, T. R.; Trenberth, K. E. Modern global climate change. *Science* **2003**, *302*, 1719.

(7) Steifel, E. I.: Bioinorganic chemistry and the biogeochemical Cycles. In *Biological Inorganic Chemistry: Structure & Reactivity*; Bertini, I., Gray, H. B., Stiefel, E. I., Valentine, J. S., Eds.; University Science Books: Sausalito, California, 2007; pp 7 - 30.

(8) Barber, J. Photosynthetic energy conversion: Natural and artificial. *Chem. Soc. Rev.* **2009**, *38*, 185-196.

(9) *Intergovernmental Panel on Climate Change (IPCC): Global warming of 1.5 C*, 2018.

(10) Lewis, N. S.; Nocera, D. G. Powering the planet: chemical challenges in solar energy utilization. *Proc. Natl. Acad. Sci. U. S. A.* **2006**, *103*, 15729-15735.

(11) Nocera, D. G. On the future of global energy. *Daedalus* **2006**, *135*, 112-115.

(12) Rosa, E. A.; Dietz, T. Human drivers of national greenhouse-gas emissions. *Nat. Clim. Chang.* **2012**, *2*, 581-586.

(13) Davis, S. J.; Lewis, N. S.; Shaner, M.; Aggarwal, S.; Arent, D.; Azevedo, I. L.; Benson, S. M.; Bradley, T.; Brouwer, J.; Chiang, Y.-M.; Clack, C. T. M.; Cohen, A.; Doig, S.; Edmonds, J.; Fennell, P.; Field, C. B.; Hannegan, B.; Hodge, B.-M.; Hoffert, M. I.; Ingersoll, E.; Jaramillo, P.; Lackner, K. S.; Mach, K. J.; Mastrandrea, M.; Ogden, J.; Peterson, P. F.; Sanchez, D. L.; Sperling, D.; Stagner, J.; Trancik, J. E.; Yang, C.-J.; Caldeira, K. Net-zero emissions energy systems. *Science* **2018**, *360*.

(14) Cook, T. R.; Dogutan, D. K.; Reece, S. Y.; Surendranath, Y.; Teets, T. S.; Nocera, D. G. Solar energy supply and storage for the legacy and nonlegacy worlds. *Chem. Rev.* **2010**, *110*, 6474-6502.

(15) Dresselhaus, M. S.; Thomas, I. L. Alternative energy technologies. *Nature* **2001**, *414*, 332-337.

(16) International Energy Agency (IEA) 2019: nuclear power in a clean energy system. https://www.iea.org/reports/nuclear-power-in-a-clean-energy-system (accessed March 2020).

(17) Armstrong, R. C.; Wolfram, C.; de Jong, K. P.; Gross, R.; Lewis, N. S.; Boardman, B.; Ragauskas, A. J.; Ehrhardt-Martinez, K.; Crabtree, G.; Ramana, M. V. The frontiers of energy. *Nat. Energy* **2016**, *1*, 15020.

(18) Chu, S.; Majumdar, A. Opportunities and challenges for a sustainable energy future. *Nature* **2012**, *488*, 294.

(19) Key world energy statistics 2019; International Energy Agency (IEA).

(20) Gibson, L.; Wilman, E. N.; Laurance, W. F. How green is 'green' energy? *Trends. Ecol. Evol.* **2017**, *32*, 922-935.

(21) Scharlemann, J. P. W.; Laurance, W. F. How green are biofuels? *Science* **2008**, *319*, 43.

(22) Bustaffa, E.; Cori, L.; Manzella, A.; Nuvolone, D.; Minichilli, F.; Bianchi, F.; Gorini, F. The health of communities living in proximity of geothermal plants generating heat and electricity: A review. *Sci. Total Env.* **2020**, *706*, 135998.

(23) International Energy Agency (IEA) 2019: Offshore wind outlook 2019. https://www.iea.org/reports/offshore-wind-outlook-2019 (accessed March 2020).

(24) Hoffert, M. I.; Caldeira, K.; Jain, A. K.; Haites, E. F.; Harvey, L. D. D.; Potter, S. D.; Schlesinger, M. E.; Schneider, S. H.; Watts, R. G.; Wigley, T. M. L.; Wuebbles, D. J. Energy implications of future stabilization of atmospheric CO_2 content. *Nature* **1998**, *395*, 881-884.

(25) *CRC Handbook of Chemistry and Physics*; 100th ed.; CRC Press Taylor & Francis Group, 2019.

(26) Mazloomi, K.; Gomes, C. Hydrogen as an energy carrier: Prospects and challenges. *Renew. Sust. Energ. Rev.* **2012**, *16*, 3024-3033.

(27) Palacín, M. R. Recent advances in rechargeable battery materials: a chemist's perspective. *Chem. Soc. Rev.* **2009**, *38*, 2565-2575.

(28) Zhang, B.; Sun, L. Artificial photosynthesis: opportunities and challenges of molecular catalysts. *Chem. Soc. Rev.* **2019**, *48*, 2216-2264.

(29) Armstrong, F. A.; Hirst, J. Reversibility and efficiency in electrocatalytic energy conversion and lessons from enzymes. *Proc. Natl. Acad. Sci. U. S. A.* **2011**, *108*, 14049-14054.

(30) Sellmann, D.; Sutter, J. In quest of competitive catalysts for nitrogenases and other metal sulfur enzymes. *Acc. Chem. Res.* **1997**, *30*, 460-469.

(31) Laureanti, J. A.; O'Hagan, M.; Shaw, W. J. Chicken fat for catalysis: a scaffold is as important for molecular complexes for energy transformations as it is for enzymes in catalytic function. *Sustain. Energy Fuels* **2019**, *3*, 3260-3278.

(32) Lienhard, G. E. Enzymatic catalysis and transition-state theory. *Science* **1973**, *180*, 149-154.

(33) Cannon, W. R.; Singleton, S. F.; Benkovic, S. J. A perspective on biological catalysis. *Nat. Struct. Biol.* **1996**, *3*, 821-833.

(34) Callender, R.; Dyer, R. B. The dynamical nature of enzymatic catalysis. *Acc. Chem. Res.* **2015**, *48*, 407-413.

(35) Hanoian, P.; Liu, C. T.; Hammes-Schiffer, S.; Benkovic, S. Perspectives on electrostatics and conformational motions in enzyme catalysis. *Acc. Chem. Res.* **2015**, *48*, 482-489.

(36) Klinman, J. P. Dynamically achieved active site precision in enzyme catalysis. *Acc. Chem. Res.* **2015**, *48*, 449-456.

(37) Fried, S. D.; Boxer, S. G. Electric fields and enzyme catalysis. *Annu. Rev. Biochem.* **2017**, *86*, 387-415.

(38) Hammes-Schiffer, S. Catalytic efficiency of enzymes: A theoretical analysis. *Biochemistry* **2013**, *52*, 2012-2020.

(39) Fontecilla-Camps, J. C.; Amara, P.; Cavazza, C.; Nicolet, Y.; Volbeda, A. Structure-function relationships of anaerobic gas-processing metalloenzymes. *Nature* **2009**, *460*, 814-882.

(40) Page, C. C.; Moser, C. C.; Chen, X. X.; Dutton, P. L. Natural engineering principles of electron tunnelling in biological oxidation-reduction. *Nature* **1999**, *402*, 47-52.

(41) Wraight, C. A. Chance and design—Proton transfer in water, channels and bioenergetic proteins. *Biochim. Biophys. Acta, Bioenerg.* **2006**, *1757*, 886-912.

(42) Rees, D. C. Great metalloclusters in enzymology. *Annu. Rev. Biochem.* **2002**, *71*, 221-246.

(43) Glusker, J. P.: Structural aspects of metal liganding to functional groups in proteins. In *Adv. Protein Chem.*; Anfinsen, C. B., Edsall, J. T., Richards, F. M., Eisenberg, D. S., Eds.; Academic Press, 1991; Vol. 42; pp 1-76.

(44) Westcott, B. L.; Gruhn, N. E.; Enemark, J. H. Evaluation of molybdenum−sulfur interactions in molybdoenzyme model complexes by gas-phase photoelectron spectroscopy. The “electronic buffer” effect. *J. Am. Chem. Soc.* **1998**, *120*, 3382-3386.

(45) Bazhenova, T. A.; Bazhenova, M. A.; Petrova, G. N.; Shilova, A. K.; Shilov, A. E. Catalytic reduction of acetylene and dinitrogen with the participation of the iron-molybdenum cofactor of nitrogenase and synthetic polynuclear molybdenum(III) complexes. *Russ. Chem. Bull.* **1998**, *47*, 861-867.

(46) Berggren, G.; Adamska, A.; Lambertz, C.; Simmons, T. R.; Esselborn, J.; Atta, M.; Gambarelli, S.; Mouesca, J. M.; Reijerse, E.; Lubitz, W.; Happe, T.; Artero, V.; Fontecave, M. Biomimetic assembly and activation of [FeFe]-hydrogenases. *Nature* **2013**, *499*, 66-69.

(47) Esselborn, J.; Lambertz, C.; Adamska-Venkatesh, A.; Simmons, T.; Berggren, G.; Noth, J.; Siebel, J.; Hemschemeier, A.; Artero, V.; Reijerse, E.; Fontecave, M.; Lubitz, W.; Happe, T. Spontaneous activation of [FeFe]-hydrogenases by an inorganic [2Fe] active site mimic. *Nat. Chem. Biol.* **2013**, *9*, 607-609.

(48) Wodrich, M. D.; Hu, X. Natural inspirations for metal–ligand cooperative catalysis. *Nat. Rev. Chem.* **2017**, *2*, 0099.

(49) Stephenson, M.; Stickland, L. H. Hydrogenase: a bacterial enzyme activating molecular oxygen. I. The properties of the enzyme. *Biochem. J.* **1931**, *25*, 205-214.

(50) Green, D. E.; Stickland, L. H. Studies on reversible dehydrogenase systems: The reversibility of the hydrogenase system of Bact. coli.1. *Biochem. J.* **1934**, *28*, 898-900.

(51) Vignais, P. M.; Billoud, B.; Meyer, J. Classification and phylogeny of hydrogenases. *FEMS Microbiol. Rev.* **2001**, *25*, 455-501.

(52) Lubitz, W.; Ogata, H.; Rüdiger, O.; Reijerse, E. Hydrogenases. *Chem. Rev.* **2014**, *114*, 4081-4148.

(53) Greening, C.; Biswas, A.; Carere, C. R.; Jackson, C. J.; Taylor, M. C.; Stott, M. B.; Cook, G. M.; Morales, S. E. Genomic and metagenomic surveys of hydrogenase distribution indicate H_2 is a widely utilised energy source for microbial growth and survival. *ISME J.* **2016**, *10*, 761-777.

(54) Peters, J. W.; Schut, G. J.; Boyd, E. S.; Mulder, D. W.; Shepard, E. M.; Broderick, J. B.; King, P. W.; Adams, M. W. W. [FeFe]- and [NiFe]-hydrogenase diversity, mechanism, and maturation. *Biochim. Biophys. Acta, Mol. Cell Res.* **2015**, *1853*, 1350-1369.

(55) Pershad, H. R.; Duff, J. L. C.; Heering, H. A.; Duin, E. C.; Albracht, S. P. J.; Armstrong, F. A. Catalytic electron transport in Chromatium vinosum [NiFe]-hydrogenase: Application of voltammetry in detecting redox-active centers and establishing that hydrogen oxidation is very fast even at potentials close to the reversible H^+/H_2 value. *Biochemistry* **1999**, *38*, 8992-8999.

(56) Hambourger, M.; Gervaldo, M.; Svedruzic, D.; King, P. W.; Gust, D.; Ghirardi, M.; Moore, A. L.; Moore, T. A. [FeFe]-hydrogenase-catalyzed H2 production in a photoelectrochemical biofuel cell. *J. Am. Chem. Soc.* **2008**, *130*, 2015-2022.

(57) Hexter, S. V.; Grey, F.; Happe, T.; Climent, V.; Armstrong, F. A. Electrocatalytic mechanism of reversible hydrogen cycling by enzymes and distinctions between the major classes of hydrogenases. *Proc. Natl. Acad. Sci. U. S. A.* **2012**, *109*, 11516-11521.

(58) Jones, A. K.; Sillery, E.; Albracht, S. P.; Armstrong, F. A. Direct comparison of the electrocatalytic oxidation of hydrogen by an enzyme and a platinum catalyst. *ChemComm* **2002**, 866-867.

(59) Madden, C.; Vaughn, M. D.; Díez-Pérez, I.; Brown, K. A.; King, P. W.; Gust, D.; Moore, A. L.; Moore, T. A. Catalytic turnover of [FeFe]-hydrogenase based on single molecule imaging. *J. Am. Chem. Soc.* **2012**, *57*, 70.

(60) Zirngibl, C.; Van Dongen, W.; Schwörer, B.; Von Bünau, R.; Richter, M.; Klein, A.; Thauer, R. K. Hydrogen-forming methylenetetrahydromethanopterin dehydrogenase, a novel type of hydrogenase without iron-sulfur clusters in methanogenic archaea. *Eur. J. Biochem.* **1992**, *208*, 511-520.

(61) Thauer, R. K.; Kaster, A.-K.; Goenrich, M.; Schick, M.; Hiromoto, T.; Shima, S. Hydrogenases from methanogenic archaea, nickel, a novel cofactor, and H_2 storage. *Annu. Rev. Biochem.* **2010**, *79*, 507-536.

(62) Kubas, G. J. Fundamentals of H_2 binding and reactivity on transition metals underlying hydrogenase function and H_2 production and storage. *Chem. Rev.* **2007**, *107*, 4152-4205.

(63) Gordon, J. C.; Kubas, G. J. Perspectives on how nature employs the principles of organometallic chemistry in dihydrogen activation in hydrogenases. *Organometallics* **2010**, *29*, 4682-4701.

(64) Jessop, P. G.; Morris, R. H. Reactions of transition metal dihydrogen complexes. *Coord. Chem. Rev.* **1992**, *121*, 155-284.

(65) Mortenson, L. E.; Chen, J.-S.: Hydrogenase. In *Microbial Iron Metabolism*; Neilands, J. B., Ed.; Academic Press: New York, New York, 1974; pp 231-282.

(66) Krasna, A. I.; Rittenberg, D. The mechanism of action of the enzyme hydrogenase. *J. Am. Chem. Soc.* **1954**, *76*, 3015-3020.

(67) Migliore, A.; Polizzi, N. F.; Therien, M. J.; Beratan, D. N. Biochemistry and theory of proton-coupled electron transfer. *Chem. Rev.* **2014**, *114*, 3381-3465.

(68) Albracht, S. P. J. Nickel hydrogenases: in search of the active site. *Biochim. Biophys. Acta, Bioenerg.* **1994**, *1188*, 167-204.

(69) Volbeda, A.; Charon, M.-H.; Piras, C.; Hatchikian, E. C.; Frey, M.; Fontecilla-Camps, J. C. Crystal structure of the nickel-iron hydrogenase from *Desulfovibrio gigas*. *Nature* **1995**, *373*, 580-587.

(70) Fontecilla-Camps, J. C.; Volbeda, A.; Cavazza, C.; Nicolet, Y. Stucture/Function relationships of [NiFe]- and [FeFe]-hydrogenases *Chem. Rev.* **2007**, *107*, 4273-4303.

(71) Montet, Y.; Amara, P.; Volbeda, A.; Vernede, X.; Hatchikian, E. C.; Field, M. J.; Frey, M.; Fontecilla-Camps, J. C. Gas access to the active site of Ni-Fe hydrogenases probed by X-ray crystallography and molecular dynamics. *Nat. Struct. Mol. Biol.* **1997**, *4*, 523-526.

(72) Kalms, J.; Schmidt, A.; Frielingsdorf, S.; van der Linden, P.; von Stetten, D.; Lenz, O.; Carpentier, P.; Scheerer, P. Krypton derivatization of an O_2-tolerant membrane-bound [NiFe] hydrogenase reveals a hydrophobic tunnel network for gas transport. *Angew. Chem., Int. Ed.* **2016**, *55*, 5586-5590.

(73) Volbeda, A.; Montet, Y.; Vernède, X.; Hatchikian, E. C.; Fontecilla-Camps, J. C. High-resolution crystallographic analysis of *Desulfovibrio fructosovorans* [NiFe] hydrogenase. *Int. J. Hydrog. Energy* **2002**, *27*, 1449-1461.

(74) Oteri, F.; Baaden, M.; Lojou, E.; Sacquin-Mora, S. Multiscale simulations give insight into the hydrogen in and out pathways of [NiFe]-hydrogenases from *Aquifex aeolicus* and *Desulfovibrio fructosovorans*. *J. Phys. Chem. B* **2014**, *118*, 13800-13811.

(75) Dementin, S.; Burlat, B.; De Lacey, A. L.; Pardo, A.; Adryanczyk-Perrier, G.; Guigliarelli, B.; Fernandez, V. M.; Rousset, M. A glutamate is the essential proton transfer gate during the catalytic cycle of the [NiFe] hydrogenase. *J. Biol. Chem.* **2004**, *279*, 10508-10513.

(76) Szőri-Dorogházi, E.; Maróti, G.; Szőri, M.; Nyilasi, A.; Rákhely, G.; Kovács, K. L. Analyses of the large subunit histidine-rich motif expose an alternative proton transfer pathway in [NiFe] hydrogenases. *PLoS One* **2012**, *7*, e34666.

(77) Teixeira, V. H.; Soares, C. M.; Baptista, A. M. Proton pathways in a [NiFe]-hydrogenase: a theoretical study. *Proteins: Struct., Funct., Bioinf.* **2008**, *70*, 1010-1022.

(78) Galvan, I. F.; Volbeda, A.; Fontecilla-Camps, J. C.; Field, M. J. A QM/MM study of proton transport pathways in a [NiFe] hydrogenase. *Proteins: Struct., Funct., Bioinf.* **2008**, *73*, 195-203.

(79) Sumner, I.; Voth, G. A. Proton transport pathways in [NiFe]-hydrogenase. *J. Phys. Chem. B* **2012**, *116*, 2917-2926.

(80) Cammack, R.; Patil, D. S.; Hatchikian, C. E.; Fernández, V. M. Nickel and iron-sulphur centres in *Desulfovibrio gigas* hydrogenase: ESR spectra, redox properties, and interactions. *Biochim. Biophys. Acta* **1987**, *912*, 98-109.

(81) Teixeira, M.; Moura, I.; Xavier, A. V.; Moura, J. J. G.; Legall, J.; Dervartanian, D. V.; Peck, H. D.; Huynh, B. H. Redox intermediates of *Desulfovibrio-gigas* [Nife] hydrogenase generated under

hydrogen. Mossbauer and EPR characterization of the metal centers. *J. Biol. Chem.* **1989**, *264*, 16435-16450.

(82) Volbeda, A.; Garcin, E.; Piras, C.; de Lacey, A. L.; Fernandez, V. M.; Hatchikian, E. C.; Frey, M.; Fontecilla-Camps, J. C. Structure of the [NiFe] hydrogenase active site: Evidence for biologically uncommon Fe ligands. *J. Am. Chem. Soc.* **1996**, *118*, 12989-12996.

(83) Happe, R. P.; Roseboom, W.; Pierik, A. J.; Albracht, S. P.; Bagley, K. A. Biological activation of hydrogen. *Nature* **1997**, *385*, 126.

(84) Pierik, A. J.; Roseboom, W.; Happe, R. P.; Bagley, K. A.; Albracht, S. P. J. Carbon monoxide and cyanide as intrinsic ligands to iron in the active site of [NiFe]-hydrogenases. $NiFe(CN)_2CO$, biology's way to activate H_2. *J. Biol. Chem.* **1999**, *274*, 3331-3337.

(85) Huyett, J. E.; Carepo, M.; Pampolona, A.; Franco, R.; Moura, I.; Moura, J. J. G.; Hoffman, B. M. ^{57}Fe Q-band pulsed ENDOR of the hetero-dinuclear site of nickel hydrogenase: Comparison of the NiA, NiB, and NiC states. *J. Am. Chem. Soc.* **1997**, *119*, 9291.

(86) Dole, F.; Fournel, A.; Magro, V.; Hatchikian, E. C.; Bertrand, P.; Guigliarelli, B. Nature and electronic structure of the Ni-X dinuclear center of *Desulfovibrio gigas* hydrogenase. Implications for the enzymatic mechanism. *Biochemistry* **1997**, *36*, 7847-7854.

(87) Ogata, H.; Mizoguchi, Y.; Mizuno, N.; Miki, K.; Adachi, S.-i.; Yasuoka, N.; Yagi, T.; Yamauchi, O.; Hirota, S.; Higuchi, Y. Structural studies of the carbon monoxide complex of [NiFe]hydrogenase from *Desulfovibrio vulgaris* Miyazaki F: Suggestion for the initial activation site for dihydrogen. *J. Am. Chem. Soc.* **2002**, *124*, 11628-11635.

(88) Ilina, Y.; Lorent, C.; Katz, S.; Jeoung, J.-H.; Shima, S.; Horch, M.; Zebger, I.; Dobbek, H. X-ray crystallography and vibrational spectroscopy reveal the key determinants of biocatalytic dihydrogen cycling by [NiFe] hydrogenases. *Angew. Chem., Int. Ed.* **2019**, *58*, 18710-18714.

(89) Hugenbruch, S.; Shafaat, H. S.; Krämer, T.; Delgado-Jaime, M. U.; Weber, K.; Neese, F.; Lubitz, W.; DeBeer, S. In search of metal hydrides: an X-ray absorption and emission study of [NiFe] hydrogenase model complexes. *Phys. Chem. Chem. Phys.* **2016**, *18*, 10688-10699.

(90) Moura, J. J. G.; Moura, I.; Huynh, B. H.; Krüger, H.-J.; Teixeira, M.; DuVarney, R. C.; DerVartanian, D. V.; Xavier, A. V.; Peck, H. D., Jr.; LeGall, J. Unambiguous identification of the nickel EPR signal in nickel-61 enriched *Desulfovibrio gigas* hydrogenase. *Biochem. Biophys. Res. Commun.* **1982**, *108*, 1388-1393.

(91) Albracht, S. P. J.; Graf, E. G.; Thauer, R. K. The EPR properties of nickel in hydrogenase from *Methanobacterium thermoautotrophicum*. *FEBS Lett.* **1982**, *140*, 311-313.

(92) Van der Zwaan, J. W.; Albracht, S. P. J.; Fontijn, R. D.; Slater, E. C. Monovalent nickel in hydrogenase from *Chromatium vinosum*. Light sensitivity and evidence for direct interaction with hydrogen. *FEBS Lett.* **1985**, *179*, 271-277.

(93) Foerster, S.; Stein, M.; Brecht, M.; Ogata, H.; Higuchi, Y.; Lubitz, W. Single crystal EPR studies of the reduced active site of [NiFe] hydrogenase from *Desulfovibrio vulgaris* Miyazaki F. *J. Am. Chem. Soc.* **2003**, *125*, 83-93.

(94) Maroney, M. J.; Allan, C. B.; Chohan, B., S.; Choudhury, S. B.; Gu, Z.: Redox metalloenzymes featuring S-donor ligands hydrogenase: A case study. In *Transition Metal Sulfur Chemistry*; ACS Symposium Series 653; American Chemical Society, 1996; Vol. 653; pp 74-100.

(95) Albracht, S. P. J.; Kröger, A.; Van der Zwaan, J. W.; Unden, G.; Böcher, R.; Mell, H.; Fontijn, R. D. Direct evidence for sulfur as a ligand to nickel in hydrogenase: an EPR study of the enzyme from *Wolinella succinogenes* enriched in sulfur-33. *Biochim. Biophys. Acta, Protein Struct. Mol. Enzymol.* **1986**, *874*, 116-127.

(96) Whitehead, J. P.; Gurbiel, R. J.; Bagyinka, C.; Hoffman, B. M.; Maroney, M. J. The hydrogen binding site in hydrogenase: 35-GHz ENDOR and XAS studies of the nickel-C (reduced and active form) and the Ni-L photoproduct. *J. Am. Chem. Soc.* **1993**, *115*, 5629-5635.

(97) Müller, A.; Tscherny, I.; Kappl, R.; Hatchikian, E. C.; Hüttermann, J.; Cammack, R. Hydrogenases in the "active" state: determination of g-matrix axes and electron spin distribution at the active site by 1H ENDOR spectroscopy. *J. Biol. Inorg. Chem.* **2002**, *7*, 177-194.

(98) Kampa, M.; Lubitz, W.; van Gastel, M.; Neese, F. Computational study of the electronic structure and magnetic properties of the Ni-C state in [NiFe] hydrogenases including the second coordination sphere. *J. Biol. Inorg. Chem.* **2012**, *17*, 1269-1281.

(99) Stein, M.; Lubitz, W. The electronic structure of the catalytic intermediate Ni-C in [NiFe] and [NiFeSe] hydrogenases. *Phys. Chem. Chem. Phys.* **2001**, *3*, 5115-5120.

(100) Stein, M.; Lubitz, W. Relativistic DFT calculation of the reaction cycle intermediates of [NiFe] hydrogenase: a contribution to understanding the enzymatic mechanism. *J. Inorg. Biochem.* **2004**, *98*, 862-877.

(101) Kampa, M.; Pandelia, M.-E.; Lubitz, W.; van Gastel, M.; Neese, F. A metal–metal bond in the light-induced state of [NiFe] hydrogenases with relevance to hydrogen evolution. *J. Am. Chem. Soc.* **2013**, *135*, 3915-3925.

(102) Foerster, S.; van Gastel, M.; Brecht, M.; Lubitz, W. An orientation-selected ENDOR and HYSCORE study of the Ni-C active state of *Desulfovibrio vulgaris* Miyazaki F hydrogenase. *J. Biol. Inorg. Chem.* **2005**, *10*, 51-62.

(103) Chapman, A.; Cammack, R.; Hatchikian, C. E.; McCracken, J.; Peisach, J. A pulsed EPR study of redox-dependent hyperfine interactions for the nickel center of *Desulfovibrio gigas* hydrogenase. *FEBS Lett.* **1988**, *242*, 134-138.

(104) Buhrke, T.; Brecht, M.; Lubitz, W.; Friedrich, B. The H_2 sensor of *Ralstonia eutropha*: biochemical and spectroscopic analysis of mutant proteins modified at a conserved glutamine residue close to the [NiFe] active site. *J. Biol. Inorg. Chem.* **2002**, *7*, 897-908.

(105) Bagley, K. A.; Duin, E. C.; Roseboom, W.; Albracht, S. P. J.; Woodruff, W. H. Infrared-detectable group senses changes in charge density on the nickel denter in hydrogenase from *Chromatium vinosum*. *Biochemistry* **1995**, *34*, 5527-5535.

(106) de Lacey, A. L.; Fernández, V. M.; Rousset, M. Native and mutant nickel-iron hydrogenases: Unraveling structure and function. *Coord. Chem. Rev.* **2005**, *249*, 1596-1608.

(107) De Lacey, A. L.; Fernández, V. M.; Rousset, M.; Cavazza, C.; Hatchikian, E. C. Spectroscopic and kinetic characterization of active site mutants of *Desulfovibrio fructosovorans* Ni-Fe hydrogenase. *J. Biol. Inorg. Chem.* **2003**, *8*, 129-134.

(108) Lindahl, P. A. Metal-metal bonds in biology. *J. Inorg. Biochem.* **2012**, *106*, 172-178.

(109) Shafaat, H. S.; Rüdiger, Olaf; Ogata, H.; Lubitz, W. [NiFe] hydrogenases: A common active site for hydrogen metabolism under diverse conditions. *Biochim. Biophys. Acta, Bioenerg.* **2013**, *1827*, 986-1002.

(110) Greene, B. L.; Wu, C.-H.; McTernan, P. M.; Adams, M. W.; Dyer, R. B. Proton-coupled electron transfer dynamics in the catalytic mechanism of a [NiFe]-hydrogenase. *J. Am. Chem. Soc.* **2015**, *137*, 4558-4566.

(111) Cotton, F. A.; Wilkinson, G.: *Advanced Inorganic Chemistry*; 5th ed.; John Wiley & Sons, Inc: New York, New York, 1988. pp. 1021 - 1051.

(112) Darensbourg, M. Y.; Lyon, E. J.; Smee, J. J. The bio-organometallic chemistry of active site iron in hydrogenases. *Coord. Chem. Rev.* **2000**, *206-207*, 533-561.

(113) Kwan, P.; McIntosh, C. L.; Jennings, D. P.; Hopkins, R. C.; Chandrayan, S. K.; Wu, C.-H.; Adams, M. W.; Jones, A. K. The [NiFe]-hydrogenase of *Pyrococcus furiosus* exhibits a new type of oxygen tolerance. *J. Am. Chem. Soc.* **2015**, *137*, 13556-13565.

(114) Shomura, Y.; Taketa, M.; Nakashima, H.; Tai, H.; Nakagawa, H.; Ikeda, Y.; Ishii, M.; Igarashi, Y.; Nishihara, H.; Yoon, K. S.; Ogo, S.; Hirota, S.; Higuchi, Y. Structural basis of the redox switches in the NAD+-reducing soluble [NiFe]-hydrogenase. *Science* **2017**, *357*, 928-932.

(115) Tai, H.; Nishikawa, K.; Suzuki, M.; Higuchi, Y.; Hirota, S. Control of the transition between Ni-C and Ni-SIa states by the redox state of the proximal FeS cluster in the catalytic cycle of [NiFe] hydrogenase. *Angew. Chem., Int. Ed.* **2014**, *53*, 13817-13820.

(116) Greene, B. L.; Wu, C.-H.; Vansuch, G. E.; Adams, M. W.; Dyer, R. B. Proton inventory and dynamics in the Nia-S to Nia-C transition of a [NiFe] hydrogenase. *Biochemistry* **2016**, *55*, 1813-1825.

(117) Tai, H.; Nishikawa, K.; Higuchi, Y.; Mao, Z.-w.; Hirota, S. Cysteine SH and glutamate COOH contributions to [NiFe] hydrogenase proton transfer revealed by highly sensitive FTIR spectroscopy. *Angew. Chem., Int. Ed.* **2019**, *131*, 13419-13424.

(118) Siebert, E.; Horch, M.; Rippers, Y.; Fritsch, J.; Frielingsdorf, S.; Lenz, O.; Velazquez Escobar, F.; Siebert, F.; Paasche, L.; Kuhlmann, U.; Lendzian, F.; Mroginski, M.-A.; Zebger, I.; Hildebrandt, P. Resonance raman spectroscopy as a tool to monitor the active site of hydrogenases. *Angew. Chem., Int. Ed.* **2013**, *52*, 5162-5165.

(119) Brecht, M.; Gastel, M. v.; Buhrke, T.; Barbel, F.; Lubitz, W. Direct detection of a hydrogen ligand in the [NiFe] center of the regulatory H_2 sensing hydrogenase from *Ralstonia eutropha* in its reduced state by HYSCORE and ENDOR spectroscopy. *J. Am. Chem. Soc.* **2003**, *125*, 13075-13083.

(120) Davidson, G.; Choudhury, S. B.; Gu, Z.; Bose, K.; Roseboom, W.; Albracht, S. P. J.; Maroney, M. J. Structural examination of the nickel site in *Chromatium vinosum* hydrogenase: Redox state

oscillations and structural changes accompanying reductive activation and CO binding. *Biochemistry* **2000**, *39*, 7468-7479.

(121) Moura, J. J. G.; Teixeira, M.; Moura, I.; LeGall, J.: (Ni,Fe)Hydrogenases from sulfate-reducing bacteria: Nickel catalytic and regulatory roles. In *The Bioinorganic Chemistry of Nickel*; Lancaster Jr. , J. R., Ed.; VCH Publishers, Inc.: New York, New York, 1988; pp 191-226.

(122) Salerno, J. C.: The EPR spectra of odd-electron nickel ions in biologial systems: Theory for d7 and d9 Ions. In *The Bioinorganic Chemistry of Nickel*; Lancaster Jr. , J. R., Ed.; VCH Publishers, Inc.: New York, New York, 1988; pp 53-71.

(123) Ogata, H.; Nishikawa, K.; Lubitz, W. Hydrogens detected by subatomic resolution protein crystallography in a [NiFe] hydrogenase. *Nature* **2015**, *520*, 571-574.

(124) Ogata, H.; Krämer, T.; Wang, H.; Schilter, D.; Pelmenschikov, V.; van Gastel, M.; Neese, F.; Rauchfuss, T. B.; Gee, L. B.; Scott, A. D.; Yoda, Y.; Tanaka, Y.; Lubitz, W.; Cramer, S. P. Hydride bridge in [NiFe]-hydrogenase observed by nuclear resonance vibrational spectroscopy. *Nat. Commun.* **2015**, *6*, 7890.

(125) Evans, R. M.; Brooke, E. J.; Wehlin, S. A.; Nomerotskaia, E.; Sargent, F.; Carr, S. B.; Phillips, S. E.; Armstrong, F. A. Mechanism of hydrogen activation by [NiFe] hydrogenases. *Nat. Chem. Biol.* **2016**, *12*, 46-50.

(126) Schilter, D.; Camara, J. M.; Huynh, M. T.; Hammes-Schiffer, S.; Rauchfuss, T. B. Hydrogenase enzymes and their synthetic models: The role of metal hydrides. *Chem. Rev.* **2016**, *116*, 8693-8749.

(127) Tard, C.; Pickett, C. J. Structural and functional analogues of the active sites of the [Fe]-, [NiFe]-, and [FeFe]-hydrogenases. *Chem. Rev.* **2009**, *109*, 2245-2274.

(128) Rakowski DuBois, M.; DuBois, D. L. The roles of the first and second coordination spheres in the design of molecular catalysts for H_2 production and oxidation. *Chem. Soc. Rev.* **2009**, *38*, 62-72.

(129) Shaw, W. J.; Helm, M. L.; DuBois, D. L. A modular, energy-based approach to the development of nickel containing molecular electrocatalysts for hydrogen production and oxidation. *Biochim. Biophys. Acta, Bioenerg.* **2013**, *1827*, 1123-1139.

(130) Dutta, A.; Appel, A. M.; Shaw, W. J. Designing electrochemically reversible H_2 oxidation and production catalysts. *Nat. Rev. Chem.* **2018**, *2*, 244-252.

(131) Berning, D. E.; Miedaner, A.; Curtis, C. J.; Noll, B. C.; Rakowski DuBois, M. C.; DuBois, D. L. Free-energy relationships between the proton and hydride donor abilities of $[HNi(diphosphine)_2]^+$ complexes and the half-wave potentials of their conjugate bases. *Organometallics* **2001**, *20*, 1832-1839.

(132) Curtis, C. J.; Miedaner, A.; Ciancanelli, R.; Ellis, W. W.; Noll, B. C.; Rakowski DuBois, M.; DuBois, D. L. $[Ni(Et_2PCH_2NMeCH_2PEt_2)_2]^{2+}$ as a functional model for hydrogenases. *Inorg. Chem.* **2003**, *42*, 216-227.

(133) Wilson, A. D.; Newell, R. H.; McNevin, M. J.; Muckerman, J. T.; Rakowski DuBois, M.; DuBois, D. L. Hydrogen oxidation and production using nickel-based molecular catalysts with positioned proton relays. *J. Am. Chem. Soc.* **2006**, *128*, 358-366.

(134) Fraze, K.; Wilson, A. D.; Appel, A. M.; Rakowski DuBois, M.; DuBois, D. L. Thermodynamic properties of the Ni−H bond in complexes of the type $[HNi(P_2^RN_2^{R'})_2](BF_4)$ and evaluation of factors that control catalytic activity for hydrogen oxidation/production. *Organometallics* **2007**, *26*, 3918-3924.

(135) Helm, M. L.; Stewart, M. P.; Bullock, R. M.; DuBois, M. R.; DuBois, D. L. A synthetic nickel electrocatalyst with a turnover frequency above 100,000 s^{-1} for H_2 production. *Science* **2011**, *333*, 863-866.

(136) Martin, D. J.; Wise, C. F.; Pegis, M. L.; Mayer, J. M. Developing scaling relationships for molecular electrocatalysis through studies of Fe-porphyrin-catalyzed O_2 reduction. *Acc. Chem. Res.* **2020**, *53*, 1056-1065.

(137) Hou, J.; Fang, M.; Cardenas, A. J. P.; Shaw, W. J.; Helm, M. L.; Bullock, R. M.; Roberts, J. A. S.; O'Hagan, M. Electrocatalytic H_2 production with a turnover frequency $>10^7$ s^{-1}: the medium provides an increase in rate but not overpotential. *Energy Environ. Sci.* **2014**, *7*, 4013-4017.

(138) Dutta, A.; DuBois, D. L.; Roberts, J. A. S.; Shaw, W. J. Amino acid modified Ni catalyst exhibits reversible H_2 oxidation/production over a broad pH range at elevated temperatures. *Proc. Natl. Acad. Sci. U. S. A.* **2014**, *111*, 16286-16291.

(139) Boralugodage, N. P.; Arachchige, R. J.; Dutta, A.; Buchko, G. W.; Shaw, W. J. Evaluating the role of acidic, basic, and polar amino acids and dipeptides on a molecular electrocatalyst for H_2 oxidation. *Catal. Sci. Technol.* **2017**, *7*, 1108-1121.

(140) Klug, C. M.; Cardenas, A. J. P.; Bullock, R. M.; O'Hagan, M.; Wiedner, E. S. Reversing the tradeoff between rate and overpotential in molecular electrocatalysts for H_2 production. *ACS Catal.* **2018**, *8*, 3286-3296.

(141) Reback, M. L.; Ginovska, B.; Buchko, G. W.; Dutta, A.; Priyadarshani, N.; Kier, B. L.; Helm, M. L.; Raugei, S.; Shaw, W. J. Investigating the role of chain and linker length on the catalytic activity of an H_2 production catalyst containing a β-hairpin peptide. *J. Coord. Chem.* **2016**, *69*, 1730-1747.

(142) Hemschemeier, A.; Happe, T. The plasticity of redox cofactors: from metalloenzymes to redox-active DNA. *Nat. Rev. Chem.* **2018**, *2*, 231-243.

(143) Le, J. M.; Bren, K. L. Engineered enzymes and bioinspired catalysts for energy conversion. *ACS Energy Lett.* **2019**, *4*, 2168-2180.

(144) Slater, J. W.; Marguet, S. C.; Gray, M. E.; Monaco, H. A.; Sotomayor, M.; Shafaat, H. S. Power of the secondary sphere: modulating hydrogenase activity in nickel-substituted rubredoxin. *ACS Catal.* **2019**, *9*, 8928-8942.

(145) Laureanti, J. A.; Ginovska, B.; Buchko, G. W.; Schenter, G. K.; Hebert, M.; Zadvornyy, O. A.; Peters, J. W.; Shaw, W. J. A positive charge in the outer coordination sphere of an artificial enzyme increases CO_2 hydrogenation. *Organometallics* **2020**, *39*, 1532-1544.

Chapter 2 – Materials, Methods, and Data Analysis

Aspects of this chapter have been reprinted with permission from Vansuch, G. E.; Wu, C.-H.; Haja, D. K.; Blair, S. A.; Chica, B.; Johnson, M. K.; Adams, M. W. W.; Dyer, R. B., *Chem. Sci.* **2020,** *11* (32), 8572-8581. Published by the Royal Society of Chemistry; Greene, B. L.; Vansuch, G. E.; Wu, C.-H.; Adams, M. W. W.; Dyer, R. B., *J. Am. Chem. Soc.* **2016,** *138* (39), 13013-13021. Copyright 2016 American Chemical Society.

2.1 – Introduction

The focus of this chapter is to provide a comprehensive listing and description of the materials and techniques utilized for the experiments in this thesis. We also note, as appropriate, where specific preparations, methodologies, etc are utilized later in thesis. The chapter itself is thus divided into four main parts: 1) a description of the preparation and purification of the native and mutant *Pyrococcus furiosus* soluble hydrogenase-1 (*Pf* SH1) enzyme utilized in this thesis (this was done in the laboratory of Dr. Michael W.W. Adams at the University of Georgia by Chang-Hao "Perry" Wu and Dominik Haja); 2) general materials and methods (with contributions from Bryant Chica, Yughene Liu, Sarah Narehood, and Monica Sanchez at Emory University noted); 3) discussion of the various methods and sample preparations used for probing the structure-function relationship of *Pf* SH1 and; 4) a thorough description of the data analyses.

2.2 – Preparation of Native Soluble Hydrogenase – 1 and the E17Q, E17D, and R355K Variants

All protein expression and purification was performed at the University of Georgia Department of Biochemistry and Molecular Biology in the laboratory of Dr. Michael W.W. Adams by Chang-Hao "Perry" Wu and Dominik Haja.

Native soluble hydrogenase-1 from *Pyrococcus furiosus* (*Pf* SH1) was expressed and purified as described previously.[1] The plasmid encoding the E17Q, E17D, or R355K variant was prepared using the QuikChange Site-Directed Mutagenesis Kit (Agilent Technologies). The site directed mutated gene was amplified from the sequence confirmed plasmid and assembled with the *pyrF* selection marker, P_{slp} as the promoter, a 9x-His tag at the N-terminus, and upstream (UFR) and downstream (DFR) flanking regions by overlapping PCR as previously reported.[1] The flanking regions were targeted to the intergenic space between PF0574 and PF0575. By homologous recombination, the linear knock-in cassette was transformed into MW0015 (Δ*pyrF* Δ*shI*$\beta\gamma\delta\alpha$ Δ*shII*$\beta\gamma\delta\alpha$), which does not contain any cytoplasmic

hydrogenase activity. The sequence-confirmed clone (MW0530) was used for large scale fermentation, protein purification, and characterization.[2] Briefly, cells were harvested from a 20L fermenter and lysed in 25 mM sodium phosphate, pH = 7.5, containing 1 mM dithiothreitol (DTT) and 50 µg/mL DNAse I with a cell to buffer ratio of 1:5 (g, wet weight : mL) in an anaerobic chamber. The cytoplasmic fraction obtained after ultracentrifugation was directly loaded on a Ni-NTA column and the bound protein was obtained by gradient elution. The hydrogenase was further purified by QFF chromatography and used for subsequent activity assays and spectroscopic characterization discussed herein. The purified enzyme was stored in 50 mM phosphate buffer containing 2 mM DTT and 300 mM NaCl (pH = 8.0) in an anaerobic atmosphere (~4% H_2 and 96% nitrogen or argon atmosphere). These storage conditions allowed for standard EPR and FTIR sample preparations to exhibit activated forms of the enzyme at the Ni_a^{2+}-S level and further reduced states. The molecular weight of *Pf* SH1 used for calculations in this thesis was 153 kDa.[3]

2.3 – Materials

2.3.1 – General Considerations

All purchased chemicals were from Sigma Aldrich, or Fisher Scientific/Alfa Aesar unless otherwise noted and were used as received. Synthetic procedures were carried out using standard Schlenk techniques. All infrared and UV-Vis sample preparations were carried out in an anaerobic glove box or glove bag (Coy Laboratory Products, Inc.) containing a ~ 4% +/ - 1% hydrogen and ~ 95% nitrogen atmosphere, with only gas exchange occurring outside the glove box or bag (e.g. CO incubation). EPR sample preparations at the University of Georgia in the laboratory of Dr. Michael W.W. Adams were carried out similarly in an anaerobic glove bag (Coy Laboratory Products, Inc.) containing an ~ 3% +/ - 1% hydrogen and ~ 97% argon gas mix.

2.3.2 – Buffers

General buffers (usually 45 mL volumes for compact storage in the glove box or glove bag) were prepared by dissolving the appropriate amount of monobasic/dibasic potassium phosphate, MES, MOPS, Tris/TrisHCl, HEPPS, HEPES, or glycine in deionized water and the pH adjusted with concentrated hydrochloric acid (HCl) and/or sodium hydroxide (NaOH). The buffers were passed through a 0.2 µm filter to remove any bacteria after the pH adjustments and purged with the glove box or glove bag atmosphere prior to use for at least 30 – 40 minutes with a fish/air pump; dust that could be introduced from the purge was avoided with a 0.2 µm filter attached to the purge needle. Buffers for EPR measurements at the University of Georgia were prepared similarly. The values reported have errors of +/- 0.05 pH units.

Buffers used for photochemical reduction experiments were prepared in the same manner except that buffer solution included 50 mM of the sacrificial electron donor 3-mercaptopropionic acid (MPA).

2.3.3 – Synthesis of 1,1'-trimethylene-2,2'-bipyridine dibromide

1,1'-trimethylene-2,2'-bipyridine dibromide (abbreviated PDQ) was synthesized by myself, Bryant Chica, or Monica Sanchez at Emory University based on a reported procedure with minor modifications.[4,5] For a general synthesis, 3.0 g of 2,2'-bipyridine was heated to 100 ˚C in 20 mL of 1,3-dibromo propane and stirred for 16 hours (within a short amount of time pale yellow solid product was evident in the reaction mixture). Afterwards, the pale yellow powder product was collected via vacuum filtration and washed with pentanes. Yields were roughly ~ 58 % (see **Figure 2.1a** for the synthesis schematic). Crude product purity (presence of no evident side products) was confirmed via NMR by Cameron Pratt at Emory University in the laboratory of Dr. Nathan Jui.

For purification, the crude product was hot filtered and crystallized in methanol and then washed with pentanes (we did try using ethanol for crystallization because of its minimal toxicity, but this was less successful). The crystals were of yellow color with a rod like morphology. Aliquots of the product were

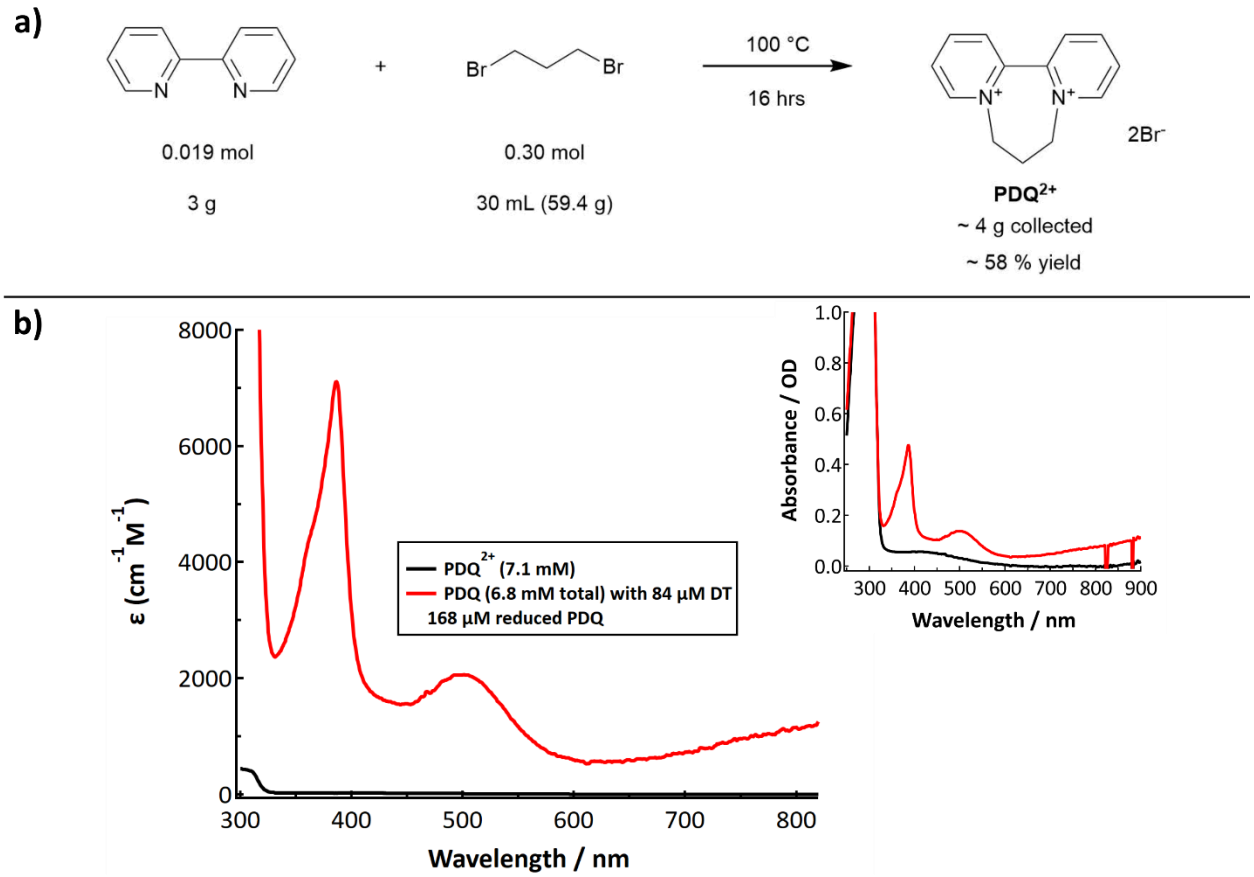

Figure 2.1: a) Synthetic scheme of 1,1'-trimethylene-2,2'-bipyridine dibromide (PDQ^{2+}). **b)** UV-Vis of PDQ as isolated (PDQ^{2+}) and after dithionite reduction to $PDQ^{+\bullet}$ (this assumes one dithionite molecule reduces two PDQ molecules). Inset: absorption spectra after offset subtraction but before conversion to extinction coefficients. Collected with the Ocean Optics spectrometer setup described in this chapter with a 70 ms integration time and 20 scans averaged.

then dissolved to concentrations of 0.5 - 1.0 M in deionized water and stored as stock solutions in the anaerobic glove box/glove bag. A UV-Vis of as isolated and dithionite reduced product (PDQ^{2+} and $PDQ^{+\bullet}$, respectively) are provided in **Figure 2.1b**, which are similar to other reports.[6-8]

2.3.4 – CdSe/CdS Dot-in Rod Nanocrystal Synthesis, Ligand Exchange, and Purification

CdSe/CdS dot-in-rod nanocrystals (NCs) were synthesized by Yughene Liu and exchanged with 3-mercaptopropionic acid (MPA) ligands and buffer exchanged into storage solution by Bryant Chica or Monica Sanchez at Emory University using previously described methods.[5,6] The dot-in-rod NC lengths as measured by transmission electron microscopy (TEM) were ~ 50 nm.[5,6] Exchanged NCs were stored in the dark in an anaerobic glove box with no noticeable aggregation for one month.

2.3.5 – CdSe Rod Nanocrystal Synthesis, Ligand Exchange, and Purification

CdSe NCs of rod like morphology were synthesized based on 1) general synthetic procedures of NCs[9] and 2) modifications of literature protocols for synthesizing CdSe NCs.[10,11] The modifications were developed by Sarah Narehood at Emory University. For a typical synthesis, 0.08 g CdO (98.9 %, Alfa Aesar), 0.80 g n-hexyl phosphonic acid (HPA, ~ 98%, Alfa Aesar), and 4.8 g trioctylphosphine oxide (TOPO, 99%, Sigma Aldrich) were dissolved in a 25 mL three neck round bottom flask by heating under reflux and vacuum at 150 °C for 3 – 4 hours with a slow stir rate. The resultant solution was a dark brown to near transparent color (the exact color was not reproducible batch to batch, but did not appear to affect the results). Afterwards, the reaction was put under N_2 and the temperature increased to ~ 260 – 280 °C. During the temperature ramp, the solution turned a pale yellow or completely transparent color indicating complete dissolution of Cd^{2+} (once again, the color was not reproducible batch to batch, but this did not appear to affect the results).

Following temperature stabilization, the stirring rate was increased and a solution of 0.2 g of selenium dissolved in 3.6 mL of trioctylphosphine (TOP, STREM Chemicals, 97%) was rapidly injected into the flask (to dissolve the selenium in the selenium/TOP mixture, the mixture should be sonicated for about 30 minutes). After ~ 15 – 30 seconds the solution would begin to turn red, at which point it was quickly removed from the heating mantle and cooled with air (the stir bar was kept near the stir plate so that

continued stirring would ensure uniform cooling). Depending on exactly how long the reaction proceeded, the solution visually looked dark orange to dark red in color at room temperature. UV-Vis spectra of select crude solutions in hexanes are shown in **Figure 2.2a**. The crude solutions were stored in a spark-proof freezer until later use (e.g. TEM imaging and ligand exchange).

To obtain TEM images (collected by Monica Sanchez at Emory University), small aliquots of crude solution (~1 – 2 mL) were "purified" by removing excess ligand: the NCs were precipitated by centrifugation at ~ 4,000 rpm in excess ethanol for 8 – 10 minutes (> 3:1 of EtOH: crude solution ratio). Then, the supernatant was removed and the precipitated NCs were dissolved in a minimal amount of hexanes and excess EtOH (> 3:1 EtOH : NC solution ratio) and re-precipitated via centrifugation at ~ 4,000 rpm for 8 minutes. This process was repeated at least three times. The NCs were then dissolved in ~ 1 – 2 mL of hexanes, drop cast onto a carbon supported copper grid (Electron Microscopy Sciences), and allowed to dry. Unfortunately, we have been unable to obtain crisp images of these particular types of NCs; however, the images suggested they were primarily of rod like morphology with lengths no greater than ~ 20 nm (see **Figure 2.2b** for an example).

Ligand exchange to from HPA to MPA (for solubility in aqueous solution) was based on a procedure from a previous report[12] and from Monica Sanchez at Emory University.[7] First, a batch of crude NCs was "purified" in a manner similar to the TEM preparation: NCs were precipitated by centrifugation at ~ 4,000 rpm in excess EtOH for 8 – 10 minutes (~2:1 of EtOH: crude solution ratio). Then, the supernatant was removed and the precipitated NCs were dissolved in a minimal amount of hexanes and excess EtOH (> 3:1 EtOH : NC solution ratio) and re-precipitated via centrifugation at ~ 4,000 rpm for 8 minutes. This process was repeated at least three times.

The NCs were then dissolved in a solution of 15 mM MeOH and 10 mM MPA at pH ~ 8 – 9 (the pH initially adjusted by addition of tetramethylammonium hydroxide and estimated with standard pH paper). The solution was vigorously stirred with a magnetic stir bar and heated under reflux at 70 °C for 2 hours.

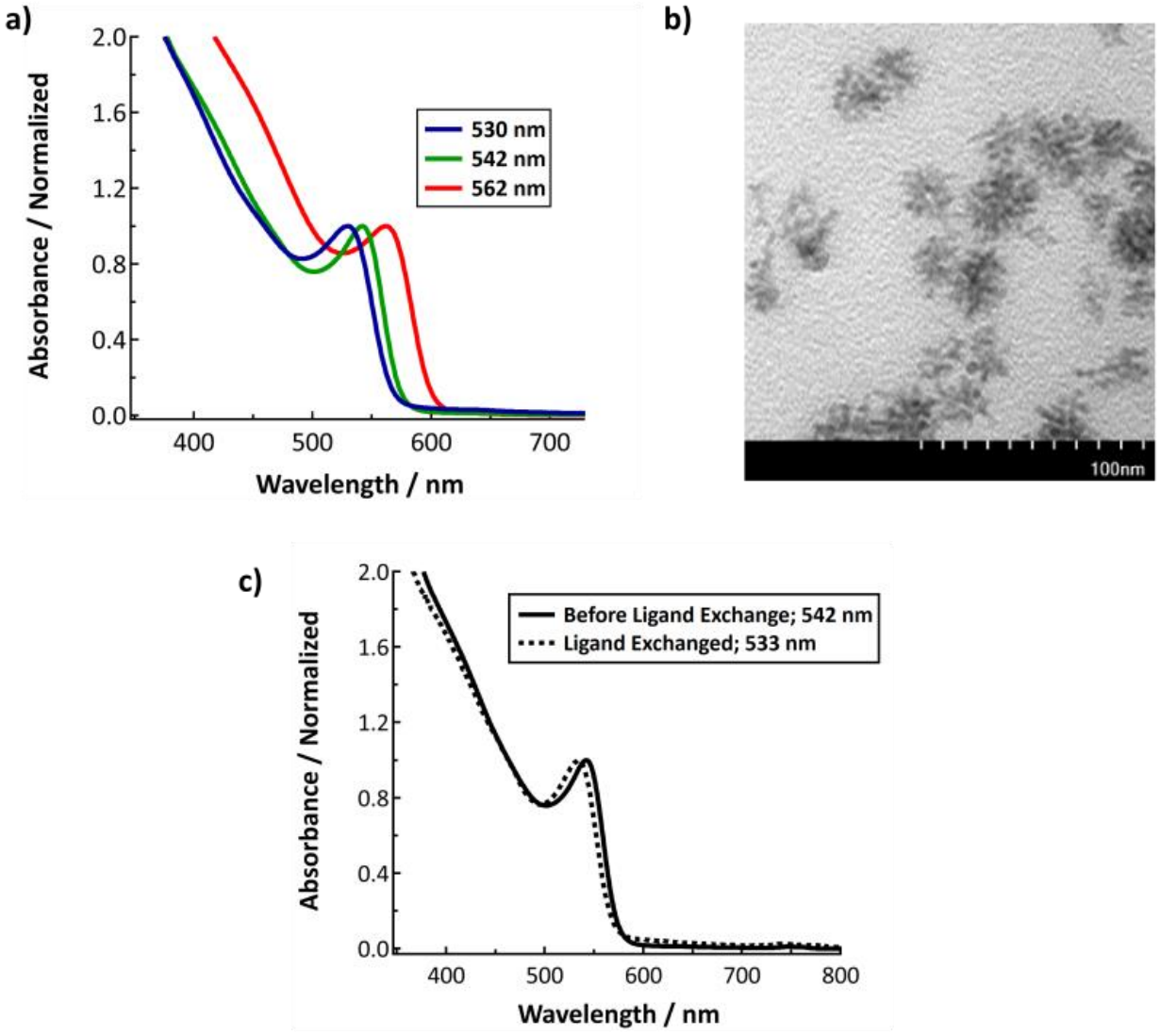

Figure 2.2: a) UV-Vis spectra of select as synthesized CdSe rod NC batches in hexanes that are normalized at the first exciton peak for comparison. **b)** Rough TEM images of a select batch. **c)** UV-Vis spectra of one batch before and after ligand exchange from n-hexylphosphonic acid to 3-mercaptopropionic acid.

Afterwards, the solution was divided into two separate Eppendorf tubes and the NCs precipitated in excess toluene via centrifugation at ~ 5500 rpm for 8 – 10 minutes (> 3:1 toluene : NC solution ratio). After discarding the supernatant, the precipitated NCs were buffer exchanged into 10 mM borate, 10 mM MPA,

and 10 mM tris(2-carboxyethyl)phosphine (TCEP) storage solution via centrifugation in a 50 kDa filter for 8 – 10 minutes at ~ 4,000 rpm. The buffer exchange process was repeated 3 – 4 times (this ensured removal of any residual MeOH exchange solution). Afterwards, the NC/storage buffer solution was passed through a 0.2 µm filter, brought into a glove bag, purged with the bag atmosphere for ~ 15 minutes, and stored in the dark until use. The NCs remained stable for at least one month. A UV-Vis comparison of a NC batch before and after ligand exchange is provided in **Figure 2.2c**.

2.4 – Methodology

2.4.1 Standard Hydrogen Oxidation and Proton Reduction Activity

Proton reduction activity and hydrogen oxidation activity of native, E17Q, E17D, and R355K *Pf* SH1 were routinely measured at the University of Georgia in the laboratory of Michael W.W. Adams by Chang-Hao "Perry" Wu and Dominik Haja. Briefly, hydrogen production assays utilized 8 ml glass vials containing 2 ml of 100 mM anaerobic HEPPS buffer containing 10 mM dithionite as the electron donor and 1 mM methyl viologen as the electron mediator (pH = 8.4; this pH ensures a high reduction potential of dithionite and helps increase the amount of the methyl viologen radical present in the solution[13]). The sample vials were incubated at 80 ˚C for 1 minute and the assay was initiated by the addition of the enzyme. The amount of hydrogen in the headspace was monitored for 6 minutes using a 6580 Network Gas Chromatography (GC) system from Agilent Technologies. Hydrogen oxidation activity was measured by incubating the enzyme in hydrogen-saturated 100 mM EPPS buffer (pH = 8.4) in an anaerobic cuvette for ~ 5 minutes. The reaction was initiated by the addition of 1 mM benzyl viologen as the electron acceptor. The rate of hydrogen oxidation was determined by the rate of benzyl viologen reduction, which was monitored at 580 nm ($\varepsilon \approx 8800\ cm^{-1}\ M^{-1}$). The activities are reported as specific activity, U/mg, where 1 U = µmol of H_2 produced or oxidized min^{-1}.

2.4.2 Standard UV-Vis Spectroscopy

UV-Vis Spectra of CdSe solutions and native and E17Q *Pf* SH1 CO incubated samples were collected at room temperature with a Perkin Elmer Lamba 35 UV-Vis spectrometer utilizing a 1 nm slit width.

Other UV-Vis spectra unless noted otherwise were collected with a Xenon lamp source controlled by an Oriel power supply. The light was attenuated with a neutral density filter and sent through a fiber optics cable that focused the light through onto the cuvette and then sent to a second fiber optics cable connected to an Ocean Optics spectrometer; data were collected with the Spectra Suite software. Integration times and scans averaged are noted elsewhere throughout this chapter. Of general note, the raw signal intensity was perfectly acceptable to be set rather high (though below saturation, which occurs at roughly 60,000 counts); however, for photochemical reduction the raw signal intensity was kept low to avoid probe excitation of the CdSe NCs ($\leq$ 8,500 counts from 300 – 550 nm; power output from the source drops at energies above 300 nm).

2.4.3 Electron Paramagnetic Resonance Spectroscopy of Native and R355K *Pf* SH1

EPR spectra were collected in the Department of Chemistry at the University of Georgia by Soshawn Blair in the laboratory of Dr. Michael K. Johnson. Samples were prepared in the laboratory of Dr. Michael W.W. Adams at the University of Georgia with Dominik Haja.

A stock of native or R355K enzyme was exchanged x 5 into 25 mM MOPS (pH = 6.7) or 25 mM glycine (pH = 9.3) in an ~3% hydrogen / 97% argon atmosphere. The final volumes were adjusted to 250 µL which resulted in enzyme concentrations of ~ 0.13 mM for native and 0.80 mM for R355K SH1. Samples were transferred to EPR tubes and flash frozen in liquid N_2. Low temperature EPR spectra were recorded using an EMXplus spectrometer and an ER4112HV-11 cryostat mated to a cryogen-free Stinger F70L closed cycle refrigeration system (Bruker BioSpin). The temperature was 70 K except for the pH = 6.7 R355K sample that was run at 50 K (we were unable to observe signals at 70 K). The modulation frequency was 100 kHz,

the modulation amplitude was 0.4 mT, and the microwave power was 10 mW. For native SH1, 100 scans were averaged at pH = 6.7, and 500 scans were averaged at pH = 9.3. For R355K, 225 scans were averaged at pH = 6.7, and 100 scans were averaged at pH = 9.3. Data for native enzyme are shown in both **Chapter 3** and **Chapter 4**. Data for R355K enzyme is shown in **Chapter 4.**

2.4.4 Preparation of Samples for Infrared Spectroscopy

FTIR sample preparations were similar to those described previously.[6,14,15] All IR cells for Fourier Transform Infrared (FTIR) spectroscopy and time resolved measurements were two copper plates that housed two CaF_2 windows vertically split by a 76.2 µm Teflon spacer. Samples and references were loaded through small port holes drilled on one of the CaF_2 windows (front face) with a gas tight syringe. The ports sealed with set screws on one of the copper plates (front face) to maximize the amount of time the sample remained anaerobic outside of the glove box/bag.

2.4.4.1: Native, E17D, and R355K *Pf* SH1 Photochemical Reduction Samples

For native *Pf* SH1, enzyme stock was buffer exchanged at least x 5 into pH = 7.19 50 mM KP_i/50 mM MPA buffer with a low volume 50 kDa molecular weight cut off filter (Millipore) at ~ 14000 x g for 8 – 10 minutes; the final exchange was longer to bring the final protein volume to ~ 11 – 12 µL. A batch of CdSe NC rods was buffer exchanged in a similar manner using a 10 kDa filter. The final volume of rods was ~ 20 µL with targeted absorbance values for the final sample (following dilution, see next paragraph) of ~ 0.5 – 1 OD between 400 - 532 nm (based on a UV-Vis absorption spectrum of a known volume of purified rods and corresponding back calculations).

The hydrogenase was transferred to a low volume vial (Verex™). 5 µL of the rods was added and gently mixed with a pipette. Then, an aliquot of PDQ^{2+} (electron mediator) was added to bring the total volume to ~ 17.5 µL; this diluted the buffer concentration by about 6 – 7% and resulted in a working protein

concentration of 200 – 300 µM and a working PDQ^{2+} concentration of ~ 30 mM. The reference side was prepared similarly with an ~ 10 mM working concentration of metmyoglobin (metMb)

The E17D sample preparation was done with Bryant Chica and was overall similar. CdSe/CdS dot-in-rod NCs were buffer exchanged and concentrated in a 50 kDa filter such that the anticipated working OD would be ~ 0.3 at 405 nm. About 1.65 mg of E17D from a 2.2 mg/mL stock was brought to a working concentration of ~ 490 µM. The reference was metMb and 30 mM working concentrations of PDQ^{2+} were used. The buffer was pH= 7.2 30 mM KP_i/50 mM MPA.

Again, the R355K sample preparation was similar to that of the native enzyme; 1 mL of a 4.8 mg/mL R355K stock was exchanged x 5 into pH = 7.23 30 mM KP_i/50 mM MPA buffer to a volume of ~ 10 µL. CdSe/CdS dot-in-rods NCS were exchanged similarly and brought to a final volume of ~ 8 – 9 µL such that the working absorbance near 405 nm would be ~ 0.15 - 0.3. The H_2ase and 4 µL of rods were then gently mixed followed by the addition of 1 µl of PDQ^{2+} with a working concentration of 30 mM. The final volume was ~ 15 µL (the addition of PDQ again diluted the buffer by ~ 6 – 7 %). The R355K SH1 concentration was ~ 2 mM. The reference was prepared similarly with a ~ 1.73 mM working concentration of metMb.

2.4.4.2: Native, E17Q, and R355K *Pf* SH1 CO Incubated Samples

To prepare CO incubated WT and E17Q *Pf* SH1 for photolysis experiments, ~ 560 µL of a 6.4 mg /mL native stock and ~ 450 – 470 µL of a 5.12 mg / mL E17Q stock were exchanged into freshly prepared 50 mM pH = 8.0 HEPES buffer. Each sample was brought to a final volume of 20 – 25 µL and transferred to a gas tight, low volume vial (Verex™) and incubated under a CO atmosphere for 10 – 15 minutes outside of the anaerobic chamber (the volume was kept higher than usual to account for evaporation, which was typically ~ 5 µL). The enzyme was quickly transferred to the anaerobic chamber and loaded into the IR cell. Enzyme concentrations were ~ 1 mM. This is relevant to data in **Chapter 3**; data from the same E17Q preparation is reused for a plot in **Chapter 4.** The reference was just buffer because for these particular

measurements wavenumbers where no dynamics occurred with the SH1 sample were used to account for cooling (see **section 2.5.5**).

CO incubated R355K samples were prepared similarly with, ~ 1 mL of 4.2 mg/mL of enzyme stock and 50 mM, pH = 8.0 HEPPS buffer. The final enzyme concentration was ~ 1 mM. Buffer was used as the reference. This relevant to data in **Chapter 4**; for a plot in this chapter, a separate CO incubated WT sample was used that was prepared with ~ 450 – 470 µL of 6.4 mg /mL WT enzyme stock and 50 mM pH = 8.0 HEPES buffer; the final concentration was ~ 1 – 2 mM. Buffer was used as the reference.

2.4.4.3 E17Q *Pf* SH1 pH Dependent Samples

For pH dependent FTIR (and UV-Vis) characterization, samples in **Chapter 3** were prepared by exchanging ~ 1 mg of E17Q stock into the desired buffer (10 mM MES pH 6.5, 100 mM Tris pH 7.5, and 100 mM HEPPS pH 8.5) at least 5 times in a 50 kDa filter. The final volume was 15 – 20 µL resulting in enzyme concentrations of ~ 300 – 400 µM. The references were ~ 1 – 4 mM deoxymyoglobin.

The transient absorption pH = 6.5 and 8.5 samples for **Chapter 3** were prepared with the same buffer compositions with an anticipated working concentration of 1 mM. The reference for each sample was ~ 5 mM deoxymyoglobin (to match the optical density of the sample at the 532 nm pump for transient absorption measurements for subtraction of cooling[15]).

The temperature dependent FTIR sample was 2.3 mg exchanged in pH = 8.50 50 mM HEPES to a final volume of 15 – 20 µL (~ 750 µM). The reference was buffer.

2.4.4.4 E17D *Pf* SH1 pH Dependent Samples

Samples (for **Chapter 3**) were prepared with 0.25 mL of 8 mg/mL or 1.5 mL of 2 mg/mL enzyme stock exchange at least 4 times into pH 7.2 (30 mM KP_i/50 mM MPA), pH 7.7 (20 mM KP_i), or pH 9.03 (50 mM glycine) buffer to ~ 15 – 20 µL (~ 0.50 – 1.3 mM). The references were 2 – 8 mM deoxymyoglobin.

2.4.4.5 R355K *Pf* SH1 pH Dependent Samples

Samples (for **Chapter 4**) were prepared with 1 – 2 mL of 4.2 or 4.8 mg/mL enzyme stock was exchanged at least 4 times into pH 6.71 (25 mM MOPS); pH 7.51 (50 mM Tris); pH 8.00 (50 mM HEPPS), pH 8.51 (50 mM HEPPS); or pH 9.27 (25 mM glycine) buffer in a 50 kDa filter. The volume of enzyme after the final exchange was 15 – 20 µL for a given pH (~ 1 – 3 mM). The references were corresponding buffer. While monitoring it's oxidation over the course of thirty-two days, the pH = 9.27 sample was stored in a 4 ℃ refrigerator or in the regular lab environment (~ 20℃).

2.4.5 Equilibrium Photochemical Reduction of PDQ^{2+} with CdSe NCs and Quantum Efficiency

Quantum efficiency measurements of PDQ^{2+} reduction by the CdSe NCs was performed in a manner similar to the original procedure developed in our lab for PDQ^{2+} generation with CdS/CdSe dot-in-rod NCs.[5,6] First the setup of the 532 nm diode pump (Thor Labs, Inc) and the 1 cm x 0.4 cm quartz cuvette (Starna Inc.) was optimized on the UV-Vis setup. The cuvette was placed where the probe beam passes along the 1 cm path length and where a stir bar is controlled along the 0.4 cm path length side. The pump was focused tightly near the center of the cuvette with a cylindrical lens, with care taken to make sure it did not hit the stir bar. The power of the pump was measured with a thermal power meter (Thor Labs, Inc.) at three locations along its path: 1) after the diode source; 2) after the cylindrical lens but before the empty cuvette, and 3) after the empty cuvette. Assuming identical scatter off of the front and back face of the cuvette, the incident power that passed through the sample was ~ 4.05 mW.

Samples were prepared in an anaerobic glove bag. An aliquot of CdSe NC stock (targeted final OD > 0.25) was buffer exchanged into pH = 7.2 50 mM KP_i/50 mM MPA buffer in a 10 kDa molecular weight cutoff Amicon filter (Millipore) via centrifugation at least three times. A gas tight syringe was used to measure the volume of CdSe stock after the final exchange and to transfer it to the cuvette containing 1 mL of buffer. Afterwards, an aliquot of PDQ^{2+} stock was added along with additional buffer such that the

final volume was 1.4 mL and the PDQ^{2+} working concentration was 30 mM. The amount of PDQ^{2+} stock used diluted the buffer KP_i and MPA concentrations by ~ 6%. The cuvette was then sealed with a rubber septum and further sealed with Teflon tape.

Afterwards, the cuvette was removed from the glove bag. The 1 cm path length was placed in the path of a focused Xenon lamp probe (the general UV-Vis setup is described in **section 2.4.2**). Magnetic stirring was controlled along the 0.4 cm path length. Dark spectra (the 532 nm pump was blocked by a beam block) were collected for at least one minute to verify no obvious probe excitation of the CdSe NCs.

Photochemical reduction was initiated by manually removing the beam block to allow excitation of the CdSe NCs. Data collection was subsequently initiated at almost the same time. Data were collected with a 100 ms integration time with 20 scans averaged per data point for 8 – 10 minutes.

2.4.6 Fourier Transform Infrared Spectroscopy Measurements, Including Temperature Dependent Measurements

FTIR spectra of the pH dependent E17Q samples were recorded in the internal compartment of a Varian 660 FTIR spectrometer purged with dry air equipped with a liquid nitrogen cooled MCT detector (Kolmar, Inc).

All other FITR data was collected by placing each sample in a dry air purged, home built-external beam compartment of the Varian 660 Fourier Transform Infrared (FTIR) spectrometer equipped with a copper block sample holder, a translation stage controlled by a stepping motor drive (Mark-102, Sigma Koki), and a liquid nitrogen cooled MCT detector (Kolmar, Inc.). In the box, one gold parabolic mirror focused the IR beam to the sample location, which was re-collimated by a second parabolic gold mirror, and then focused onto the detector elements by a third parabolic gold mirror. The IR cell sample or reference side could be selectively set in the path of the IR beam with the translation stage. During typical measurements the

temperature was the lab temperature (~ 20 +/- 1 ̊C), though sometimes a recirculating water bath connected to the sample stage was set to 20 °C.

Temperature dependent FTIR measurements were carried out in the external Varian 660 sample compartment similarly to a previously described method from our laboratory.[16] Briefly, the temperature was controlled and read via a thermocouple with a previously written in-house LabView program. Measurements were generally taken every 5 °C in the range specified on both the sample and reference side of a given IR cell.

The resolution for all measurements was 2 cm^{-1}. The number of scans averaged for a given/sample reference for native, E17Q, and E17D *Pf* SH1 were typically 1024 or 2848 scans; 4096 scans were always averaged for a given sample/reference for R355K *Pf* SH1.

2.4.7 Equilibrium Photochemical Reduction Coupled to Fourier Transform Infrared Spectroscopy with Native, E17D, and R355K R355K *Pf* SH1

Data was collected similarly to standard FTIR measurements from the previous section in the external sample compartment of a Varian 660 FTIR spectrometer. Prior to initiation of the photochemical reduction, 4096 scans of the sample and reference were obtained with a 2 cm^{-1} resolution at lab temperature (~ 20 +/- 1 ̊C) for native and R355K enzyme. 512 scans were used for E17D enzyme. E17D data was collected with Bryant Chica.

The sample was then illuminated with a 405 nm (E17D and R355K enzyme) or 450 nm (native enzyme) laser diode (~ 4 mW, Thor Labs, Inc.); the beam was defocused by a plano-concave lens to allow for uniform illumination of the sample. The illumination times were 30 seconds – 8 minutes for native enzyme, 20 s – 27 minutes for E17D, and 1 – 20 minutes for R355K enzyme. After each illumination period the sample was allowed to equilibrate to the new reducing conditions and then 4096 scans of the sample

were obtained for native and R355K enzyme and 512 scans for E17D enzyme. The last illumination period was constant for E17D enzyme (that is, the pump light was kept on during data collection).

2.4.8 Time Resolved Infrared Spectroscopy

Time resolved IR spectroscopy was performed on a setup described previously.[14,15,17] The 1064 nm fundamental of a Surelite Nd:YAG (Continuum) operating at 10 Hz was frequency double/tripled in a harmonic generator to provide a 532 nm pump (for hydride photolysis) or 355 nm pump (for CO photolysis). A harmonic separator was used to pick the desired pump wavelength, which was then focused to an ~ 1.0 mm spot on the sample. The probe was an infrared beam from a quantum cascade laser (Daylight Solutions) that was tunable in the ~ 1900 – 1975 cm^{-1} range needed. The probe beam was focused to an ~ 100 µm spot on the sample with 80 mm focal length plano convex CaF_2 windows (the positioning of the focal lenses for the IR were optimized for general wavelength range of interest based on specs from ThorLabs). The probe beam was then focused onto to a fast rise time liquid nitrogen cooled MCT detector (Kolmar Technologies, Inc) with a 50 mm focal length plano convex lens. Data collection was triggered with the pump beam with a photodiode either after back reflection off of a lens or after a beam splitter (the beam splitter itself used to help attenuate the pump power).

During measurements, a low intensity visible diode beam was used to keep track of the IR beam location. The sample stage consists of translation stages for x, y, and z dimension control with the sample mounted on a copper block (the x and y stage allow for up-down and side-side control for sample movement as need during the measurements; the z direction is only used for ensuring the setup has the sample at the IR focus).

The pump and probe were overlapped by ensuring the temperature jump of the sample and reference side were of maximum intensity, which in the 1900 – 1975 cm^{-1} is an induced absorbance/voltage decrease The temperature jump is the result of solvent heating from dissipation of excess energy

absorbed by iron heme of the myoglobin or cofactors of the hydrogenase that absorb at the pump wavelength.

Data was collected as the average of 1000 simultaneous shots (for temperature dependent measurements, two separate measurements of 500 shots averaged together) on a home-built LabView program[17] with a 100 MHz sampling rate (for hydride photolysis) or 25 MHz sampling rate (for CO photolysis). One million data points were collected that were binned to the order of 10^4 points prior to actual saving of the data.

For hydride photolysis measurements with native and E17Q *Pf* SH1, data were collected on the sample side of the IR cell from 1900 – 1975 cm^{-1} every wavenumber (e.g. 1900, 1901, …,1975) and every ten wavenumbers on the reference side (1900, 1910,…,1970).[15] Dark spectra (noise) were also collected every ten wavenumbers on the reference side. The pump power was ~ 260 µJ/pulse for the pH = 8.5 sample and ~ 450 µJ/pulse for the pH = 6.5 sample (the power for pH = 6.5 was higher because of an unfortunately low protein concentration).

For CO photolysis measurements with native *Pf* SH1, data were collected on the sample side of the IR cell from 1910 – 1970 cm^{-1} roughly every wavenumbers. Because the the 1910 – 1914 cm^{-1} region only showed cooling behavior and were well removed from observed dynamics, these were utilized as reference wavenumbers. CO photolysis with E17Q was similar, with data collected about every two to three wavenumbers. The probe/pump spot was changed between roughly every other wavenumber measurement by translating the sample stage in the x or y direction. The pump power was ~ 85 – 100 µJ/pulse.

For temperature dependent measurements with hydride photolysis, the temperature of the sample stage was controlled with a recirculating water bath and the temperature measured at the sample with a thermocouple (error of ~ +/- 0.2 °C). Prior to such measurements the temperature was ensured to be

stable for at least five minutes. Data were collected at specified wavenumbers for both the sample and reference side of the IR cell.

2.4.9 H/D Exchange of Native and R355K *Pf* SH1

Samples of native *Pf* SH1 were prepared by diluting an enzyme stock to 222 nM in a quartz cuvette (1 cm x 1 cm, FireflySci) in pH = 6.3, 50 mM potassium phosphate buffer. A stock dithionite was then added to the cuvette (working concentration of 1.5 mM). The cuvette was sealed with a rubber stopper and Teflon tape, and the headspace was then purged with D_2 gas (99.8 % atom D, Sigma Aldrich) for ~ 15 minutes while the solution was vigorously stirred with a magnetic stir bar. The R355K sample preparation was identical except the enzyme concentration was 412 nM and the cuvette was purged with D_2 gas for 70 minutes because we typically observed larger incubation times are required for optimal activity with SH1 variants.

A given sample was then placed in the path of a continuous 532 nm excitation beam from a Verdi laser (Coherent, Inc) operating at 0.9 W. The Raman scatter was collected as described previously with minor modifications.[18] Briefly, scatter was focused, collimated, and sent to a 0.275 m focal length spectrograph (Acton Research Corporation). The spectrograph grating was set to disperse the region of the Q branches of D_2, HD, and H_2 (~ 3000 – 4000 cm^{-1})[19] onto a CCD Camera (Acton/Princeton Research Corporation) operating at - 75 °C. Data were collected using a home-built LabView program designed by Bryant Chica. The camera exposure time was set to 4 minutes per data point. The solution was stirred with a magnetic stir bar to ensure transfer of HD into the headspace and continual transfer of D_2 to solution. Native *Pf* SH1 data were collected for 800 minutes and R355K data were collected for 1200 minutes.

Standards of H_2 (Nexair), D_2 (99.8% atom D; Sigma Aldrich), and HD (96 % mol HD, 98% atom D; Sigma Aldrich) for calibration were measured using an identical camera exposure time in an otherwise empty cuvette with the Verdi operating at 0.85 W.

2.4.10 Methyl Viologen Oxidation Reduction of Native and R355K *Pf* SH1 under 5% H_2 monitored via UV-Vis Spectroscopy

An aliquot of 2.8 mg/mL of native SH1 or 4.2 mg/mL of R355K SH1 was exchanged into pH = 7.2, 50 mM potassium phosphate buffer x 6. The given hydrogenase sample and a stock of methyl viologen were then diluted in a 1 x 1 cm quartz cuvette (containing a magnetic stir bar) to working concentrations of 50 nM hydrogenase and 330 µM methyl viologen. In both cases the immediate appearance of blue from methyl viologen reduction was noted because of the ~4% H_2 gas composition of the buffer. The cuvette was then sealed with a rubber septum and removed from the anaerobic chamber and purged with a 5% H_2 / 95% N_2 gas mix for at least 50 minutes to ensure both samples had identical gas compositions. The septum was sealed with Teflon tape. Temperature dependent UV-Vis data were collected using the absorbance mode of a Horiba Scientific Dual Fluorimeter that was equipped with a Peltier temperature controller and magnetic stir control. A 7 minute equilibration time was set for each point during the temperature ramp for a total collection time of ~ 1.5 hours. When the temperature was returned from 75 ˚C to 15 ˚C, spectra were measured until no change was observed. The reference was a buffer spectrum.

2.4.11 Sequence Alignments

Sequence alignments of the large subunits of various [NiFe(Se)]-H_2ases to demonstrate select conserved motif regions were conducted with FASTA formatted sequences retrieved from UniProt,[20] aligned with Jalview[21]/ClustalOmega,[22] and visualized with Jalview. The sequences used for large subunits were: **1)** *Pf* SH1, UniProt entry: E7FI44; **2)** *Desulfovibrio vulgaris Miyazaki F (Dv MF)*, UniProt entry: P21852; **3)** *Desulfovibrio fructosovorans (Df)*, UniProt entry: P18188; **4)** *Escherichia Coli* Hyd-1 (*Ec* Hyd-1), UniProt entry: P0ACD8; **5)** *Escherichia Coli* Hyd-2 (*Ec* Hyd-2), UniProt entry: P0ACE0; **6)** *Thiocapsa roseopersicina Hyn (Tr Hyn)*, UniProt entry: A0A0U5DZM2; ***7)*** *Desulfovibrio gigas (Dg),* UniProt entry: P12944; **8)** *Allochromatium vinosum* (*Av*), UniProt entry: D3RV26; **9)** *Ralstonia eutropha H16 (membrane*

bound H_2 sensor; Re H16 MBH), UniProt entry: Q79IP6; ***10)*** Methanosarcina barkeri MS F *F_{420}-reducing enzyme (MbFRH)*, UniProt entry: A0A0E3LNA9; ***12)*** *Methanothermobacter marburgensis F_{420}-reducing enzyme (MmFHR)*, UniProt entry: D9PYF9; ***13)*** ***Hydrogenophilus thermoluteolus*** TH-1^T soluble hydrogenase (*Ht*SH), UniProt entry: A0A077LAI5; **13)** *Desulfovibrio vulgaris Hildenborough (DvH)*, UniProt entry: Q72AS3; *and* ***14)*** *Desulfomicrobium baculatum (Dmb)*, UniProt entry: C7LN88. The latter two are [NiFeSe]-H_2ases.

The sequences used for the standard small subunits were: **1)** *Pf* SH1, UniProt entry: E7FHU4; **2)** *Thermococcus kodakarensisi* (*Tk*), UniProt entry: Q8NKS3; **3)** *Mycolicibacterium smegmatis* (*Ms*), UniProt entry: A0A2U9PT23 (supposed sequence as noted in the database); **4)** *Re H16 MBH*, UniProt entry: Q79IP7; **5)** *Ralstonia eutropha H16 (soluble hydrogenase; Re H16 SH)*, UniProt entry: P22319*;* **6)** *Ec* Hyd-1, UniProt entry: P69739; **7)** *Ec* Hyd-2, UniProt entry: P69741; **8)** *Df*, UniProt entry: P18187; **9)** *MbFRH, U*niProt entry: P80491; **10)** *MmFHR*, UniProt entry: D9PYF7; **11)** *Ht*SH, UniProt entry: A0A2Z6DYQ5; **12)** *DvH*, UniProt entry: Q06173; **13)** *Dmb*, UniProt entry: P13063. The latter two are [NiFeSe]-H_2ases.

2.5 – Data Analysis

FTIR absorbance spectra, difference spectra, and corresponding baseline corrections used the Resolutions Pro software. Unless noted otherwise, other data analysis utilized Igor Pro (Wavemetrics, Inc.; Lake Oswego, Oregon). All second derivative FTIR spectra are computed from the corresponding "raw" absorbance spectrum (that is, the spectrum prior to baseline correction).

2.5.1 Quantum Efficiency of Photochemical Reduction of PDQ^{2+} with CdSe NCs

The quantum efficiency of PDQ^{2+} reduction with CdSe NCs were calculated as the number of moles of $PDQ^{+\bullet}$ generated versus the number of moles of photons absorbed at 10 seconds with **equation 1** (this time point is before $PDQ^{+\bullet}$ absorbance at the pump wavelength begins to contribute to an inner filter

effect that unavoidably decreases the ability of the NCs to absorb the pump light uniformly in the sample, which thus decreases the efficiency of $PDQ^{+\bullet}$ generation):

$$\text{Quantum efficiency} = \frac{moles\ of\ radical\ generated\ after\ 10\ s}{Power\ (eV) * photons\left(\frac{1}{eV}\right) * (1-10^{-AbsCdSe,532\ nm}) * (\frac{1}{N_A})}$$

$$= \frac{moles\ of\ radical\ generated\ after\ 10\ s}{0.00405\ W * 10\ s * \frac{eV}{(1.602\ x\ 10^{-19}) W * s} * \frac{photon\ (532\ nm)}{2.332\ eV} * (1-10^{-AbsCdSe,532\ nm}) * (\frac{1}{N_A})} \quad (1)$$

where N_A is Avogadro's number and $1 - 10^{-Abs,CdSe,\ 532\ nm}$ accounts for the fraction of incident photons from the 532 nm pump absorbed by the CdSe NCs. The CdSe NC absorbance at 532 nm was determined from a dark spectrum and accounted for a baseline offset estimation (the baseline primarily a result of scattered probe light off the cuvette).

Estimated solution potentials for a proof of concept of the photochemical reduction method were calculated by the Nernst equation, **equation 2**:

$$E = E^0\ (PDQ^{+\bullet}) + \frac{RT}{nF} ln\left(\frac{[PDQ^{2+}]}{[PQD^{+\bullet}]}\right) \quad (2)$$

where $E^0(PDQ^{+\bullet})$ ~ -550 mV,[4,7] n = 1, R is is the gas constant (8.314 $Jmol^{-1}K^{-1}$), T is the temperature of the lab (~ 20 °C), F is Faraday's constant (96485 $Cmol^{-1}$), and $[PDQ^{2+}] + [PDQ^{+\bullet}]$ = 30 mM. The radical concentration for each time point was calculated using the average absorbance between 808 – 810 nm with Beer's Lambert law. The extinction coefficient used for $PDQ^{+\bullet}$ was 1500 cm^{-1} (**Fig 2.2b** and ref 8). The absorbance for each time point was also corrected by the dark "offset"/scatter in the same region ((Absorbance (used for calculations) = $\text{Absorbance (time x)}_{measured,808\text{-}10nm} - \text{Absorbance(dark)}_{offset,808\text{-}810nm}$).

2.5.2 EPR Spectroscopy

A minimal baseline correction was applied to each spectrum. Using the MATLAB EasySpin toolbox (Pepper function),[23] rhombic fits were applied to the paramagnetic nickel region (g > ~ 2); however, a given spectrum also consisted of a strong axial contribution(s) from additional cofactors such as the [2Fe2S] cluster in the γ-subunit, which has previously been observed in native SH1.[24] The axial signal(s) overlap and effectively mask the typical Ni^{3+} and Ni^{1+} g_z features near g = 2.01 and 2.05, respectively.[25] Thus, the value of g_z was fixed as 2.01 for all native SH1 spectral features and 2.045 for all R355K spectral features. Along with carefully selected g-strain (peak widths), these allowed for a proper baseline prior to the g_y region (in the work with *Pf* SH1 by Silva and co-workers regarding paramagnetic nickel species, g_z had been fixed to 2.0 for all spectral fits (tentative oxidized features and Ni_a^{3+}-C)).[24] The fits were conducted between 2500 - ~ 3400 Gauss. The raw spectra and fits for native and R355K and are provided in **Appendix A**. The g-values and g-strains obtained from the fits are tabulated in **Appendix A**.

For visual clarity in the main text, the maximum value of g_y for the data as fit in EasySpin were scaled/normalized to 1, and the corresponding fits scaled by the same value. For native SH1, the scaling values were 7 (pH = 6.7) and 24 (pH = 9.3). For R355K SH1, the scaling values were 205 (pH = 6.7) and 352 (pH = 9.3).

2.5.3 Fourier Transform Infrared Spectroscopy, Equilibrium Photochemical Reduction of Native, E17D, and R355K SH1

FTIR difference spectra from the equilibrium photochemical reduction were obtained by subtracting the dark sample spectrum from each illuminated sample spectrum ($\Delta A = -\log(I_{light}/I_{dark})$). A minimal baseline spline correction was applied between ~ 1860 – 1907.5, 1980 – 2030, and 2110 - 2200 cm^{-1} for native and R355K enzyme because we observed a small baseline drift. The baseline corrected spectra were then vertically offset to 0 O.D. at 1880 cm^{-1}.

FTIR absorbance spectra from the photochemical reduction were obtained by subtracting the reference solution from each illuminated spectrum ($A = -\log(I_{sample}/I_{reference})$). Because of significant water content differences between the sample and reference, a minimal spline correction was applied between ~ 1860 – 1910; 1970 – 2030; and 2100 – 2200 cm^{-1}; the exact region was enzyme/mutant dependent. The baseline corrected spectra were vertically offset to 0 O.D. at 1880 cm^{-1}.

2.5.4 Standard Fourier Transform Infrared Spectroscopy

FTIR absorbance spectra were obtained by subtracting a given reference spectrum from the sample spectrum ($A = -\log(I_{enzyme}/I_{reference})$). For temperature dependent measurements the reference spectrum for a given temperature was subtracted from the sample spectrum of the same temperature ($A = -\log(I_{sample,\ temperature\ X}/I_{reference,\ temperature\ X})$). A minimal baseline spline correction was typically applied between ~ 1860 – 1910; 1970 – 2030; and 2100 – 2200 cm^{-1} (not overlapping with the ν_{CO} or ν_{CN} region as determined from second derivative spectra; 4 to 6 points were generally used in each region). The exact region was enzyme/mutant sample dependent. For CO incubated samples the 1972 – 2030 region was adjusted accordingly to avoid distorting the exogenous ν_{CO} peaks. Native, E17D, and R355K baseline corrected spectra were then offset to 0 OD at 1880 cm^{-1}.

The absorbance spectra of E17D and R355K enzyme were often normalized to have the area of the curve (AOC) between 1880 – 2000 cm^{-1} equal to 1. For E17Q spectra that were normalized, normalization was based maximum data point of the Ni_a^{3+}-C region.

Spectra (either normalized or not normalized as evident on graph y – axes) were fit using a multipeak pseudo-Voigt function, **equation 3**:

$$f(\nu) = y_o + \sum_i A_i * g_i * e^{\left(\frac{\nu-\nu_i}{w_i}\right)^2} + A_i * (1-g_i) * \frac{1}{1+\left(\frac{\nu-\nu_i}{\frac{w_i}{2}}\right)^2} \quad (3)$$

where y_0 is the linear offset, A_i is the amplitude, g_i is the Gaussian character (0 – 1), v_i is the center frequency, and w_i the peak width at full width half maximum (FWHM) of the i^{th} peak. The peak widths were always fixed for a given fit (native SH1 spectra and the pH dependent E17Q spectra in **Chapter 3** being an exception, peak widths were typically constrained between 3 and 5 cm^{-1} for native enzyme and constrained appropriately in the 2 – 5 cm^{-1} range for E17Q to allow good fit to unfortunately noisy spectra).

2.5.5 Transient Absorption Infrared Absorption CO Photolysis and Hydride Photolysis

Transient absorption workups for both CO photolysis and hydride photolysis are similar. The reference transient trace (a wavenumber in the 1910 – 1914 cm^{-1} from the sample for CO photolysis or and deoxymyoglobin for hydride photolysis) was ratioed on the ms time scale to match the inherent cooling signature of the raw sample trace (for H_2ase primarily from FeS clusters and other cofactor absorbance at the pump wavelength for 532 nm, as well as protein absorbance that is more pronounced with the 355 nm pump; for myoglobin primarily heme absorbance at 532 nm). The resultant transient trace and reference trace was subtracted to generate the transient absorption trace. Dark spectra collected from the reference was also subtracted for hydride photolysis. An example workup from CO photolysis with E17Q *Pf* SH1 is shown in **Figure 2.3** which shows separate traces that have no dynamics, a bleach, and an induced absorbance.

Because the raw traces are actually ΔA measurements (light – dark voltage converted to absorbance by the LabView program), the units are technically ΔΔA (or ΔΔΔ A when noise from the dark spectra are subtracted). For clarity, we just plot transient absorption amplitudes as ΔA.

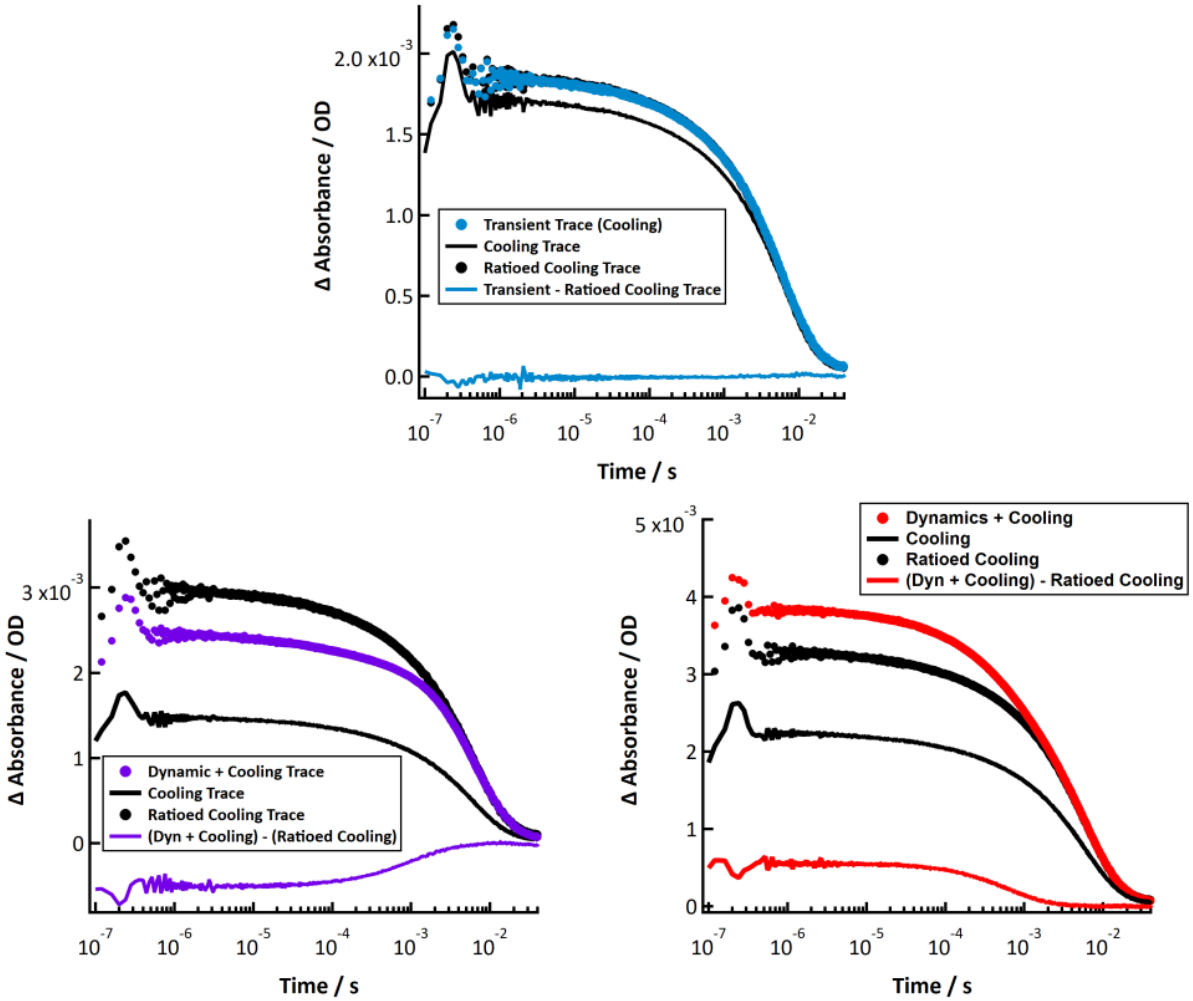

Figure 2.3: Example raw transient traces and corresponding workups from E17Q *Pf* SH1 CO photolysis. **Top:** A trace from 1932 cm^{-1} that is only cooling. **Bottom left:** A trace that from 1947 cm^{-1} is a bleach as indicated after subtraction of the raw transient (labeled as "Dyn + Cooling") from the radioed trace that only contains cooling (labeled as "Cooling"). **Bottom right:** A trace from 1951.9 cm^{-1} that is an induced absorbance as indicated after subtraction of the raw transient (labeled as "Dyn + Cooling") from the ratioed trace that only contains cooling (labeled as "Cooling").

2.5.6 IR Spectroscopy Analysis Specific to R355K *Pf* SH1

Peak widths were held constant for the peaks detected between 1900 – 1954 cm^{-1} as w_i = 4 cm^{-1} for fits to **equation 3**. One (perhaps two) peaks was consistently detected at ν_{CO} > 1955 cm^{-1} that was incredibly broad and difficult to define even in the second derivative spectra, and this width was constrained below 7 cm^{-1}.

In our prior work with native *Pf* SH1, analysis of FTIR data primarily focused on well-defined peak positions; specifically the Ni_a^{3+}-C state that appears in a spectrally uncongested region between ~ 1960 – 1970 cm^{-1}.[15,26] Unfortunately, the extreme spectral congestion in the R355K spectra precluded an analysis based primarily on peak positions. As previously noted for the peak position of Ni_a^{2+}-S in native SH1 following sample preparation under the same conditions used here,[15] exact peak positions are not well defined in spectrally congested regions, especially for shoulder peaks. This is further complicated by the pH dependent peak position shifts that are the results of deprotonation of amino acid residues near the active site and increased population of reduced proximal iron-sulphur clusters as pH increases.[14,15,26] Thus, there is some significant error/variability in peak positions depending on pH and if a given feature is a shoulder or more a well-defined feature (see **Appendix F**). We thus further analysed the FTIR data based on a peak areas at full width half maximum.

The population of each state at a given pH was estimated by integrating the intensity of each spectral feature using **equation 4**:

$$Population\left(Ni_{a/x}-state\right)=\int_{\nu_i-w_i}^{\nu_i+w_i} A_i * g_i * e^{\left(\frac{\nu-\nu_i}{w_i}\right)^2} + A_i * (1-g_i) * \frac{1}{1+\left(\frac{\nu-\nu_i}{\frac{w_i}{2}}\right)^2} \quad (4)$$

where all terms are determined from the fits to **equation 3**, and *Ni_a-state* corresponds to an active state of the enzyme, while *Ni_x-state* corresponds to what we believe to be an inactive state of the enzyme. These populations are presented in **Appendix F**. The populations were then scaled relative to the Ni_a^+-L

states to account for the decreased ν_{CO} oscillator strength as frequency increases; the scaling factors were based on the work of Alben and co-workers.[27] The scaled populations are presented in **Appendix F**.

The estimated H_2/H^+ redox couple for a given pH value was calculated with **equation 5**[28] assuming a 4% hydrogen composition (the precise gas composition depends on how much time has passed between sample removal from the anaerobic chamber and how tight the ports of the infrared cell are sealed, both of which contribute to hydrogen escaping from the cell prior to a measurement):

$$E = 0\,V - \left(\frac{2.303 * R * T}{F} * pH\right) - \left(\frac{2.303 * R * T}{2F} * \log\left(\frac{\rho_{H2}}{\rho_{0)}}\right)\right) \quad (5)$$

where 0 V is the H_2/H^+ couple at pH = 0, F is Faraday's constant (96,485 Coulombs/mol), T is the lab temperature (assumed to be the typical value of ~ 20 °C (293.15 K) in the specific location where the measurements are made as indicated by past measurements of the air temperature with a thermocouple), R is the gas constant 8.314 J/molK, and ρ_{H2} is the partial pressure of hydrogen and ρ_0 is standard pressure.

The day dependent spectra for the pH = 9.27 sample were normalized and processed in the same manner as described above, except more oxidized samples were normalized between 1880 – 2030 cm^{-1} to account for the peak that appeared near 2012 cm^{-1}. Because of the appearance of additional peaks near 2012 and perhaps 2000 cm^{-1}, the spline region typically used between from 1972 – 2030 cm^{-1} was broken into two components: 1978 – 1990 and 2020 – 2030 cm^{-1}. Broad peaks between 1950 – 1975 often required peak widths to be fixed at 5.5 cm^{-1} in this region. The second derivative spectra, normalization values, and peak positions are provided in **Appendix H.**

2.5.7 H/D Exchange

To calibrate the H/D exchange measurements, standards were utilized to observe where H_2, HD, and D_2 appeared on the CCD camera with the instrumental parameters utilized. For each standard, cosmic ray spikes were manually removed by replacing each spike with the average of two adjacent background points. An empty cuvette spectrum (blank) was analyzed identically and then subtracted from each standard. The baselines were then corrected with a spline function. The center pixel for each scatter spectrum was determined by a one component Voigt function and were assigned to the known Raman detectable stretching frequencies of H_2 (4160 cm^{-1}), HD (3632 cm^{-1}) and D_2 (2989 cm^{-1}).[19] A linear correlation of wavenumber vs. pixel was then determined (**Appendix D**). The center pixel of H_2 (determined to be pixel 219) was manually set to 4160 cm^{-1}, and the remaining pixels were assigned a wavenumber relative to this value using the slope of the calibration curve (**Appendix D**).

Each time point for a kinetics measurement was analyzed identically with cosmic ray spike removal, cuvette subtraction, and a spline baseline correction; an example is provided in **Appendix D**. Representative spectra for both native and R355K *Pf* SH1 between 4 – 800 minutes of data collection are provided in **Appendix D**. The relative amount of H_2, HD, and D_2 in the headspace for a given time point were determined by integrating the peak area for each gas in the full width half maximum region as determined by the standards. Plots of the integrated areas versus time are shown for native and R355K *Pf* SH1 in **Appendix D**. The summed total areas under the curve (D_2 + HD + H_2) for each time point averaged to 40000 +/- 1700 for native and 40000 +/- 1600 for R355K SH1, and thus there was no obvious gas loss during the measurements.

For a conservative analysis of the data, we applied the method of initial rates to the first 60 minutes of the measurements of D_2 consumption and HD production for native enzyme. This was also applied to D_2 consumption for R355K. Because of weak signals from HD production at early time with R355K SH1 and the inherent noise of the measurements, the method of initial rates was applied to the first 180 minutes.

Otherwise, rates that varied by up to a factor of two could be obtained at earlier times depending on the exact time point range. Furthermore, exponential fits were applied to the first 668 minutes of native *Pf* SH1 HD production and to the entire data set of R355K, which did not display a notable HD decay (the observed HD decay from native enzyme is from HD in the gas phase eventually reacting the enzyme to form H_2 within the time course of the experiment at a detectable level). The fits and fit parameters are provided in **Appendix D**. The maximum amount of HD produced by native enzyme was determined by the average of the data points between 500 and 600 minutes (**Appendix D**). The maximum amount of HD produced by R355K was determined by the average of the final two data points (**Appendix D**). We also provide the value of HD produced by the R355K enzyme at 800 minutes by averaging the data points at 796, 800, and 804 minutes.

We also estimated the amount of D_2 consumed. It was assumed the total scatter area of starting D_2 was 40,000. The final area (proxy for amount) of D_2 for the native enzyme was estimated as the average of the final five data points, and were divided by 40,000 (and multiplied by 100 and subtracted from 1) to get the percentage of D_2 consumed. The amount of D_2 consumed by R355K was estimated similarly. We also provide the percentage of D_2 consumed by R355K SH1 at 800 minutes by averaging the data points at 796, 800, and 804 minutes for the calculation.

The data for R355K was also scaled to account for concentration differences versus native SH1 (a factor of 0.54) in **Chapter 4 (Figure 4.3b**) and in estimating the amounts of D_2 consumed/HD formed, which assumes a concentration linearity regarding the rates D_2 cleavage and HD and H_2 formation.

2.6 References

(1) Chandrayan, S. K.; Wu, C.-H.; McTernan, P. M.; Adams, M. W. W. High yield purification of a tagged cytoplasmic [NiFe]-hydrogenase and a catalytically-active nickel-free intermediate form. *Protein Expres. Purif.* **2015**, *107*, 90-94.

(2) Wu, C.-H.; Ponir, C. A.; Haja, D. K.; Adams, M. W. W. Improved production of the NiFe-hydrogenase from Pyrococcus furiosus by increased expression of maturation genes. *Protein Eng., Des. Sel.* **2018**, *31*, 337-344.

(3) Ma, K.; Adams, M. W. W.: Hydrogenases I and II from *Pyrococcus furiosus*. In *Method Enzymol.*; Academic Press, 2001; Vol. 331; pp 208-216.

(4) Homer, R. F.; Tomlinson, T. E. Stereochemistry of the bridged quaternary salts of 2,2'-bipyridyl. *J. Chem. Soc.* **1960**, 2498-2503.

(5) Chica, B.; Wu, C.-H.; Liu, Y.; Adams, M. W. W.; Lian, T.; Dyer, R. B. Balancing electron transfer rate and driving force for efficient photocatalytic hydrogen production in CdSe/CdS nanorod–[NiFe] hydrogenase assemblies. *Energy Environ. Sci.* **2017**, *10*, 2245-2255.

(6) Chica, B. C. Semiconductor nanoparticle-protein hybrid systems for solar hydrogen production and photo-triggered mechanistic studies. Ph.D. Thesis, Emory University, 2017.

(7) Sanchez, M. L. K.; Wu, C.-H.; Adams, M. W. W.; Dyer, R. B. Optimizing electron transfer from CdSe QDs to hydrogenase for photocatalytic H_2 production. *ChemComm* **2019**, *55*, 5579-5582.

(8) Yang, W.; Vansuch, G. E.; Liu, Y.; Jin, T.; Liu, Q.; Ge, A.; Sanchez, M. L. K.; K. Haja, D.; Adams, M. W. W.; Dyer, R. B.; Lian, T. Surface-Ligand “Liquid” to “Crystalline” Phase Transition Modulates the Solar H_2 Production Quantum Efficiency of CdS Nanorod/Mediator/Hydrogenase Assemblies. *ACS Appl. Mater. Interfaces* **2020**, *12*, 35614-35625.

(9) Peng, Z. A.; Peng, X. Formation of high-quality CdTe, CdSe, and CdS nanocrystals Using CdO as precursor. *J. Am. Chem. Soc.* **2001**, *123*, 183-184.

(10) Peng, X.; Manna, L.; Yang, W.; Wickham, J.; Scher, E.; Kadavanich, A.; Alivisatos, A. P. Shape control of CdSe nanocrystals. *Nature* **2000**, *404*, 59-61.

(11) Manna, L.; Scher, E. C.; Alivisatos, A. P. Synthesis of Soluble and Processable Rod-, Arrow-, Teardrop-, and Tetrapod-Shaped CdSe Nanocrystals. *J. Am. Chem. Soc.* **2000**, *122*, 12700-12706.

(12) Zhu, H.; Song, N.; Lv, H.; Hill, C. L.; Lian, T. Near unity quantum yield of light-driven redox mediator reduction and efficient H_2 generation using colloidal nanorod heterostructures. *J. Am. Chem. Soc.* **2012**, *134*, 11701-11708.

(13) Mayhew, S. G. The redox potential of dithionite and SO−2 from equilibrium reactions with flavodoxins, methyl viologen and hydrogen plus hydrogenase. *Eur. J. Biochem.* **1978**, *85*, 535-547.

(14) Greene, B. L.; Wu, C.-H.; McTernan, P. M.; Adams, M. W.; Dyer, R. B. Proton-coupled electron transfer dynamics in the catalytic mechanism of a [NiFe]-hydrogenase. *J. Am. Chem. Soc.* **2015**, *137*, 4558-4566.

(15) Greene, B. L.; Wu, C.-H.; Vansuch, G. E.; Adams, M. W.; Dyer, R. B. Proton inventory and dynamics in the Nia-S to Nia-C transition of a [NiFe] hydrogenase. *Biochemistry* **2016**, *55*, 1813-1825.

(16) Maness, S. J.; Franzen, S.; Gibbs, A. C.; Causgrove, T. P.; Dyer, R. B. Nanosecond temperature jump relaxation dynamics of cyclic beta-hairpin peptides. *Biophys. J.* **2003**, *84*, 3874-3882.

(17) Greene, B. L. Proton, electron and proton-coupled electron transfer dynamics in the catalytic mechanism of [NiFe] and [FeFe] hydrogenases. Ph.D. Thesis, Emory University, 2015.

(18) Zhao, C.; Glass, E. N.; Chica, B.; Musaev, D. G.; Sumliner, J. M.; Dyer, R. B.; Lian, T.; Hill, C. L. All-inorganic networks and tetramer based on Tin(II)-containing polyoxometalates: Tuning structural and spectral properties with lone-pairs. *J. Am. Chem. Soc.* **2014**, *136*, 12085-12091.

(19) Ferraro, J. R.; Nakamoto, K.; Brown, C. W.: *Introductory Raman Spectrosocpy*; 2 ed.; Academic Press: Cambridge, MA, 2002.

(20) Consortium, T. U. UniProt: a worldwide hub of protein knowledge. *Nucleic Acids Res.* **2018**, *47*, D506-D515.

(21) Waterhouse, A. M.; Procter, J. B.; Martin, D. M. A.; Clamp, M.; Barton, G. J. Jalview Version 2—a multiple sequence alignment editor and analysis workbench. *Bioinformatics* **2009**, *25*, 1189-1191.

(22) Sievers, F.; Wilm, A.; Dineen, D.; Gibson, T. J.; Karplus, K.; Li, W.; Lopez, R.; McWilliam, H.; Remmert, M.; Söding, J.; Thompson, J. D.; Higgins, D. G. Fast, scalable generation of high-quality protein multiple sequence alignments using Clustal Omega. *Mol. Syst. Biol.* **2011**, *7*, 539.

(23) Stoll, S.; Schweiger, A. EasySpin, a comprehensive software package for spectral simulation and analysis in EPR. *J. Magn. Reson.* **2006**, *178*, 42-55.

(24) Silva, P. J.; De Castro, B.; Hagen, W. R. On the prosthetic groups of the NiFe sulfhydrogenase from *Pyrococcus furiosus*: topology, structure, and temperature-dependent redox chemistry. *J. Biol. Inorg. Chem.* **1999**, *4*, 284-291.

(25) Lubitz, W.; Ogata, H.; Rudiger, O.; Reijerse, E. Hydrogenases. *Chem. Rev.* **2014**, *114*, 4081-4148.

(26) Greene, B. L.; Vansuch, G. E.; Wu, C.-H.; Adams, M. W. W.; Dyer, R. B. Glutamate gated proton-coupled electron transfer activity of a [NiFe]-hydrogenase. *J. Am. Chem. Soc.* **2016**, *138*, 13013-13021.

(27) Alben, J. O.; Moh, P. P.; Fiamingo, F. G.; Altschuld, R. A. Cytochrome oxidase (a3) heme and copper observed by low-temperature Fourier transform infrared spectroscopy of the carbon monoxide complex. *Proc. Natl. Acad. Sci. U. S. A.* **1981**, *78*, 234-237.

(28) Vincent, K. A.; Parkin, A.; Armstrong, F. A. Investigating and exploiting the electrocatalytic properties of hydrogenases. *Chem. Rev.* **2007**, *107*, 4366-4413.

Chapter 3 – Native *Pf* SH1 and Investigating the E17Q and E17D Variants

---

Aspects of this chapter have been reprinted with permission from Vansuch, G. E.; Wu, C.-H.; Haja, D. K.; Blair, S. A.; Chica, B.; Johnson, M. K.; Adams, M. W. W.; Dyer, R. B., *Chem. Sci.* **2020,** *11* (32), 8572-8581. Published by the Royal Society of Chemistry; Greene, B. L.; Vansuch, G. E.; Wu, C.-H.; Adams, M. W. W.; Dyer, R. B., *J. Am. Chem. Soc.* **2016,** *138* (39), 13013-13021. Copyright 2016 American Chemical Society; Greene, B. L.; Vansuch, G. E.; Chica, B. C.; Adams, M. W. W.; Dyer, R. B., *Acc. Chem. Res.* **2017,** *50* (11), 2718-2726. Copyright 2017 American Chemical Society.

Abstract

Interactions of a metal center with the ligand scaffold are critical in bioinspired systems, though the nature and control of such interactions are not well understood. It is thought that better understanding how the secondary and outer sphere contribute to biological catalysis will aid in developing better bioinspired catalyst blueprints. Hydrogenases are model systems for understanding fundamental proton/hydride and electron transfers that most bioinspired systems utilize, and with the elementary mechanism of [NiFe]-H_2ases moderately well-established we have begun focusing on how the secondary sphere contributes to efficient catalysis in soluble hydrogenase-1 from *Pryococcus furiosus*. A highly conserved glutamate residue (E17) adjacent to a terminal cysteine residue is thought to be the proton donor/acceptor to the outer sphere. Here, we mutated E17 to a glutamine (E17Q, conserving side chain length but not conserving side chain functionality) and to an aspartate (E17D, conserving side chain functionality but not side chain length). Each enzyme variant illustrated significantly different pieces of information. E17Q provided insight into proton transfer and hydride recombination timescale/barrier modulation by the E17 position and functionality, while E17D provided more insight into how probable fine-tuned interactions of the glutamate with the outer sphere influence not only catalytic rates, but also active site properties.

3.1 – Introduction

Metalloenzymes active stable small molecules (e.g. H_2, CO_2, N_2) for rapid, specific, and efficient redox chemistry,[1,2] characteristics that are necessary to incorporate into their bioinspired counterparts. Consequently, searching for design principles of metalloenzymes has been an area of significant interest. It has long been apparent that cooperative interactions between a metal center and the protein scaffold are critical to enzyme function,[2-5] but such interactions have proven difficult to reproduce in bioinspired systems,[6-10] partly because a detailed understanding of structure-function relationships of metal centers with their corresponding protein scaffold are largely unclear. Because of the simple substrate

requirements of the seemingly simple $H^+ + 2e^- \leftrightarrow H_2$ carried out by [NiFe]-hydrogenases (H_2ases), these H_2ases are poised as model bioinorganic systems for structure-function (metal-ligand cooperativity) studies.

A well-established method in enzymology to probe such structure-function relationships is to make mutations to the protein scaffold (the mutated enzyme being termed a "variant") and to link changes in enzymatic activity, structure, and spectroscopic changes to perturbations near the active site. Extreme caution must be taken with conclusions drawn directly from activity assays, because the assays do not indicate what change(s) are caused by a mutation. Crystal structures are of course indispensable in general and can help determine changes; however, care must be taken because a mutation may have drastic or subtle effects not necessarily evident from a given structure, highlighting the importance of structural resolution (if plausible/practical) and additional information from other methods.[11,12]

We have focused on structure-function studies of the hyperthermophile soluble hydrogenase-1 from *Pyrococcus furiosus* (*Pf* SH1),[13,14] which is a member of the group 3b cytoplasmic and (hyper)thermophilic [NiFe]-H_2ases that use NADP(H) as an external electron donor/acceptor during cellular metabolism.[15-18] *Pf* SH1 has the heterotetramer architecture displayed in **Figure 3.1**.[13,19] The α and δ subunit are analogous to the large and small subunits of the minimal heterodimeric structure of all [NiFe]-H_2ases.[18] The native enzyme has been well studied with various spectroscopic techniques under equilibrium, steady state, and time-resolved conditions[19-23] which provide ample baseline information for *Pf* SH1 variant studies.

Structure-function studies of the [NiFe] catalytic core with its surroundings typically focus on conserved amino acid residues/motifs.[24-28] A residue of particular interest is the highly conserved glutamate (E17 *Pf* SH1 numbering) that is part of the large subunit "L0"motif.[25] **Figure 3.2a** shows this motif from sequence alignments of enzymes from various groups/subgroups.[15,29] What is of specific

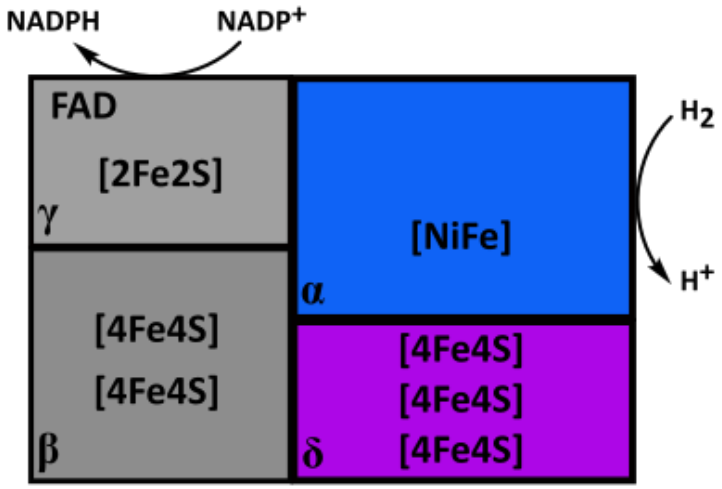

Figure 3.1: Heterodimeric structure of Pf SH1, with the α and δ subunits being the typical large and small subunits utilized by all [NiFe]-H_2ases. Adapted from refs 17 and 86.

interest with the residue is the proximity to an active site terminal cysteine residue, C418 (see **Figure 3.2b**[30]). The cysteine residue has been concluded to be protonated in the Ni_a^+-L state from a combination of cryogenic infrared,[31] cryogenic Raman,[32] and paramagnetic/computational studies.[33] Computations[34,35] further support C418 protonation in the Ni_a^+-L state. The cysteine residue is also believed to be protonated in the standard Ni_a^{2+}-SR state from the results of a high resolution crystal structure, nuclear vibrational resonance, and corresponding models of the data.[36,37] The results are also supported by other computational studies.[34,35] A QM/MM study also suggests C418 is rather flexible,[38] which agrees with rather large temperature factors (disorder) that have been observed in crystal structures[39,40] which imply a dynamic role in catalysis (though such studies were with oxidized/inactive states. Also, radiation damage and heterogeneity of states could also result in such disorder[40]).

Overall, the evidence mentioned above highly suggests C418 is part of proton transfer during catalysis, with the ionizable E17 well poised to exchange protons with the active site during turnover. E17 itself has been shown to likely undergo conformational/protonation changes during the Ni_a^{3+}-C → Ni_a^+-L →Ni_a^{2+}-S

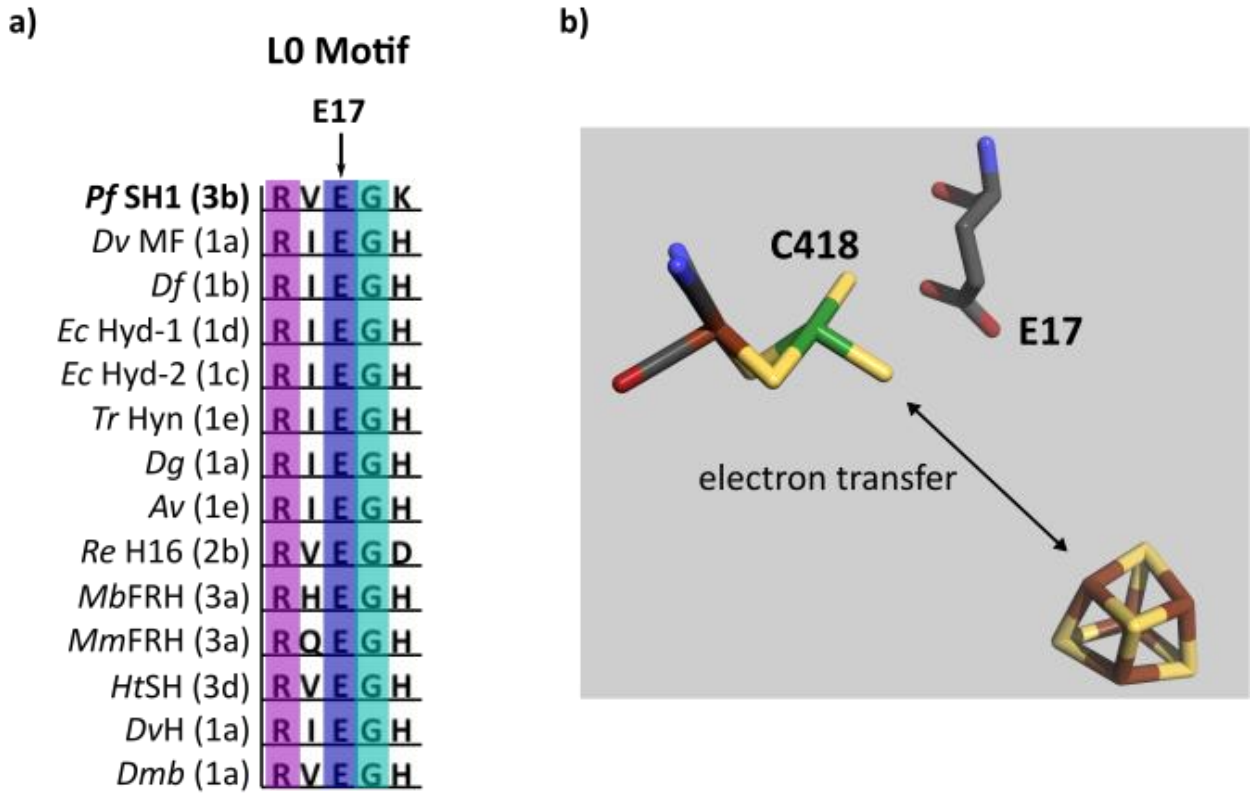

Figure 3.2: a) Sequence alignments of the L0 motif from various [NiFe]-H_2ases. **b)** Representation of the proximity of E17 to the active site terminal cysteine, C418. Also pictured is the proximal FeS cluster, which has a role in ET that is also relevant to this chapter. Pdb code: 4U9I.

transition from a cryogenic IR study.[31] It also has been reported to have high crystallographic temperature factors[41] and simulations indicate it is likely the end/beginning part of plausible proton pathways that extend to/from the protein surface.[42,43] Thus, a reasonable hypothesis from such studies alone that E17 and C418 are part of a proton transfer network during catalysis. However, cryogenic conditions are not directly relevant to catalysis, and from a crystallographic analysis alone one could envision other reasonable H^+ pathways that do not utilize E17.[41]

More convincing evidence was found from a mutagenesis study with E17 variants with the *Desulfovibrio fructosovorans* (*Df*) enzyme. Mutation to aspartic acid (E17D), which maintained overall side chain functionality but with one less carbon in the side chain, resulted in ~ 50% activity relative to the

native enzyme.[26] Mutation to a glutamine (E17Q), which changed the ionizable carboxylate side chain to the nonionizable glutamine side chain (but preserving side chain length), resulted in 0% activity.[26] Hence, it appeared the distance and side chain functionality were critical to turnover, presumably from a proton transport perspective. Interestingly though, the E17Q variant from the membrane bound *Thiocapsa roseopersicina* Hyn enzyme showed ~ 50% activity.[28]

Given these contradictory activity assay results and also the availability of preliminary spectroscopic work with E17 variant(s) with the *Df*[26] and *Roslstonia eutropha* H_2 sensor enzymes,[27] we decided a logical start to our structure-function studies would target E17, which is the focus of this chapter. The next section of the chapter is setup as follows: first, we provide necessary background with native enzyme studies.[22,23] We then present and discuss results of investigations with E17Q followed by E17D *Pf* SH1, which answer some questions about cooperativity in *Pf* SH1, but also raise various questions that set groundwork for further studies. Of important note here too is that despite extensive efforts over at least three decades, it has not been possible to crystallize *Pf* SH1; however, its similar spectroscopic behavior compared to other [NiFe]-H_2ases implies a similar active site structure to those studied by X-Ray crystallography.[20,21] Thus, we often support conclusions with structural studies (and electronic/computational studies) of other [NiFe]-hydrogenases. However, conclusions in this chapter (and chapter 4) should only be directly applied to *Pf* SH1.

3.2 – Results and Discussion

3.2.1 – Native *Pf* SH1 Equilibrium Photochemical Reduction, Electron Paramagnetic Resonance, and Time Resolved Exogenous Carbon Monoxide and Hydride Photolysis

In this section, we present spectroscopic background information of native *Pf* SH1 that is necessary for understanding enzyme variant studies. Standard mechanistic enzymology tools for studying H_2ases are electron paramagnetic resonance (EPR) and infrared (IR) spectroscopy. Regarding EPR spectroscopy, the

[NiFe] active site is known to display rhombic features corresponding to low symmetry S = ½ Ni^{3+} and Ni^{+} paramagnetic electronic configurations.[33,44] Regarding IR spectroscopy, π-backbonding between the iron and the carbon monoxide and cyanide ligands of the active site $(CN)_2(CO)Fe^{2+}$ fragment is sensitive to the delocalized electron density on and nearby the core. Thus, a specific ν_{CO} and ν_{CN} symmetric/antisymmetric pair[45] report on a distinct active site electron count and extent of protonation. Because of the greater π-acidity of the CO ligand,[46,47] ν_{CO} is a more reliable marker of distinct electronics (states) because it shifts in a predictable manner with formal nickel redox chemistry and active site protonation events.[44] **Figure 3.3** shows a general diagram of the EPR energy level diagrams of paramagnetic active states[33] and a general visualization of π-backbonding with the iron and CO ligand for visualization.

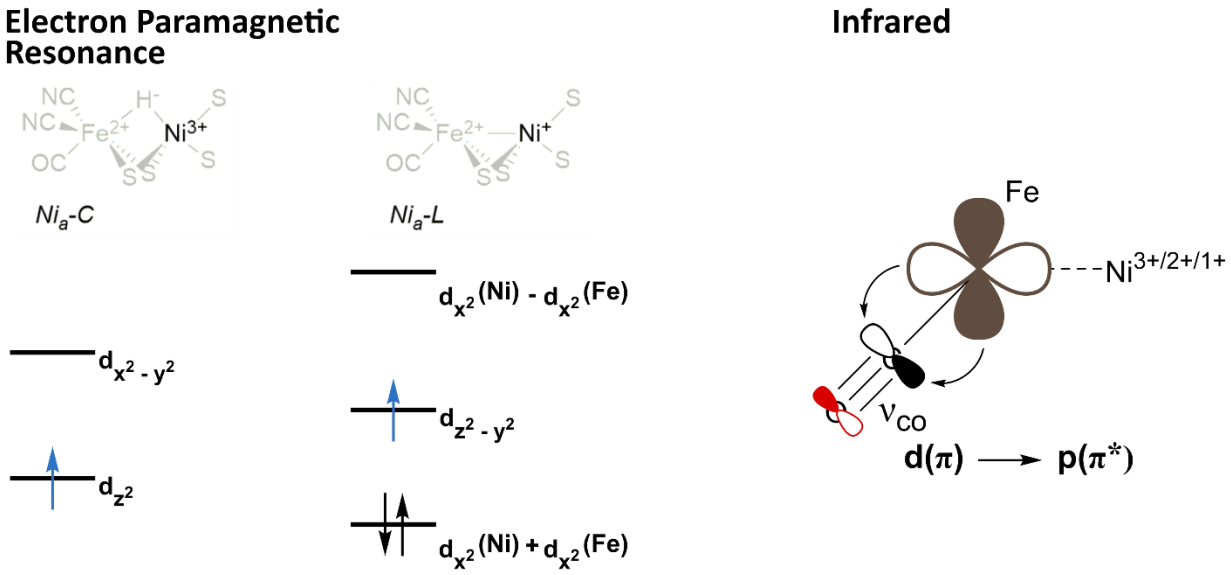

Figure 3.3: Left: Qualitative diagrams of d orbitals energies used to visualize [NiFe]-H_2ase active states that are paramagnetic and that are thus observable via EPR spectroscopy (adapted from ref 33). Right: Illustration of π-backbonding between the active site iron and the π-acid CO ligand that gives rise to infrared features that shift in a predictive manner with active site electron density changes from formal nickel redox state changes and/or active site protonation events.

EPR spectra of native *Pf* SH1 conducted at pH = 6.7 and 9.3 under ~3% H_2 at 70 K are shown in **Figure 3.4**. The main EPR feature was a signal with g_y ~ 2.13 and g_x ~ 2.22 for both pH values (g_z is unable to be

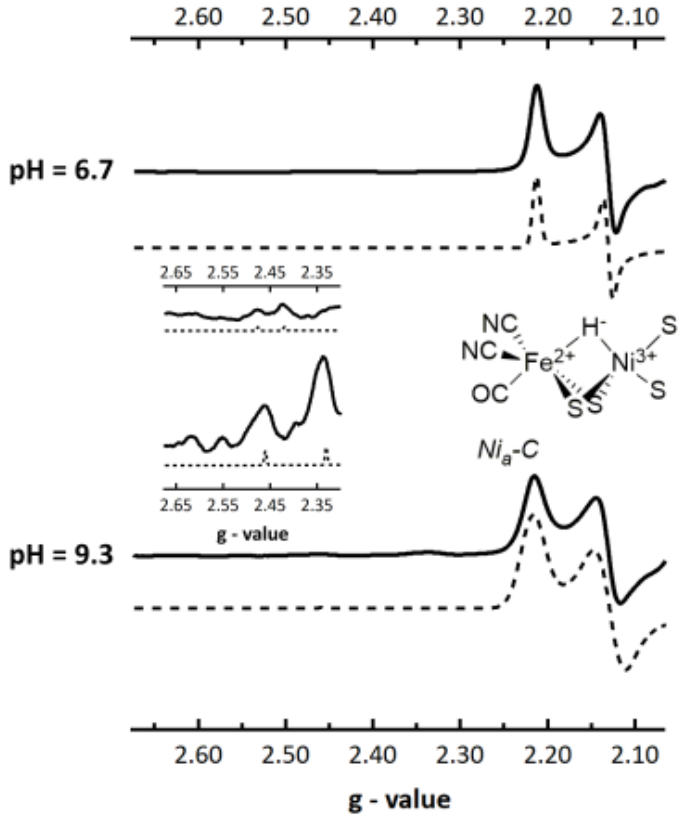

Figure 3.4: X-Band EPR spectra of native *Pf* SH1 (microwave power = 10 mW, temperature = 70 K). The g_z region is not shown because of an overlapping signal due to [2Fe2S] cluster (or other cofactors). The maximum value of g_y was normalized to 1 for each data set for visual clarity. Fits are located below the data and were scaled by the same factor as the respective spectra. Individual plots of raw spectra, fits, and tabulated g-values and g-strains from the fits are provided in **Appendix A**. The protein was isolated under anaerobic conditions and stored under 3 – 4% hydrogen at least one week prior to sample preparation in 25 mM MOPS (pH = 6.7) or 25 mM glycine (pH = 9.3) buffer. The protein concentration was ~ 0.13 mM. The inset shows weak signals in the region g > 2.3 that probably correspond to a small presence of “Ready” and/or “Unready” states as mentioned in the text.

assigned because the [2Fe2S] and/or the flavin in the γ-subunit (**Figure 3.1**) exhibit a strong axial signal that overlaps with and masks the typical [NiFe]-hydrogenase g_z ~ 2.01 – 2.05 features[19,44]). Small amplitudes with g > 2.3 were also observed (**Figure 3.4**). We assigned the main feature to Ni_a^{3+}-C because the g-values corresponded closely to the Ni_a^{3+}-C feature reported in *Pf* SH1 by Silva and co-workers[19] and because the difference between g_y and g_x was not consistent with oxidized/inactive paramagnetic states.[19,44] The states of residual amplitude probably correspond to the "ready" and/or "unready" states previously observed by Silva and co-workers in *Pf* SH1.[19]

An infrared spectrum of native *Pf* SH1 at pH = 7.2 is shown in **Figure 3.5**. The sample was allowed to auto-oxidize under an N_2 atmosphere, leading to a slightly different distribution of states than we typically observe.[21] As seen in the ν_{CO} and ν_{CN} region (~ 1900 – 1980 and 2060 – 2100 cm^{-1}),[20-22] there is a distribution of states with peaks near 1966, 1960, 1950 (including a shoulder) and 1940 cm^{-1} (including a shoulder). To determine which states are which, we utilize photochemical reduction to generate a redox difference infrared spectrum. This method uses a photosensitizer to rapidly reduce a redox mediator to reduce the

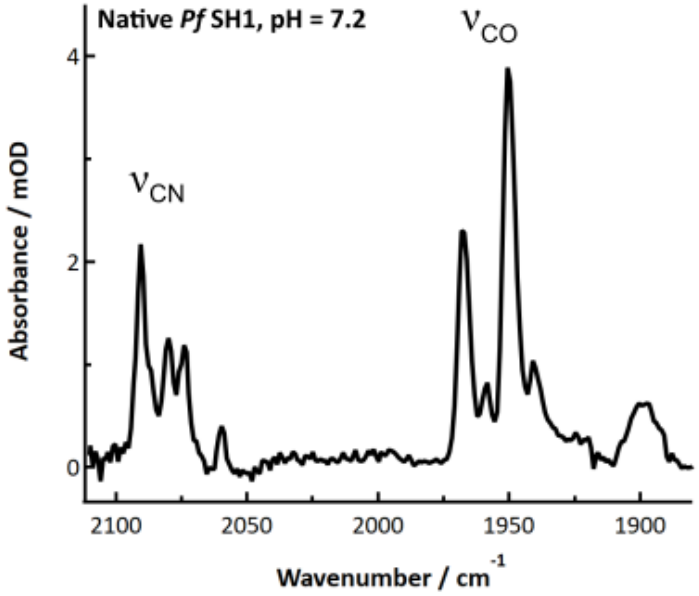

Figure 3.5: Infrared spectrum of the ν_{CO} and ν_{CN} region of an auto-oxidized *Pf* SH1 sample.

solution potential. The enzyme can then equilibrate with the more reducing conditions. This causes active site redox state and protonation changes and thus causes some infrared bands to decrease in intensity and others to increase in intensity.[48] The schematic in **Figure 3.6a** demonstrates the general steps of a photochemical reduction. *Note*: the assignment of states in native *Pf* SH1 by IR nothing new,[20,21,23] but is provided for relevant background information.

Figure 3.6b-c demonstrates a proof of concept experiment with the reaction initiation step from photochemical reduction utilizing CdSe nanocrystal photosensitizers (abbreviated CdSe NCs) and the redox mediator (1,1'-trimethylene-2,2'-bipyridine dibromide (E^0 = -550 mV[49], abbreviated PDQ^{2+}). Illumination of a cuvette containing CdSe NCs and PDQ^{2+} near the first exciton peak of the NC photosensitizers with 532 nm light results in absorption of incident photons by the NCs. The absorption causes charge separation (electron hole-pair formation) via a Se HOMO (p-orbital) → Cd LUMO (s-orbital) band gap transition.[50] "Productive processes"[51] lead to hole filling (via a sacrificial electron donor, e.g. MPA) and the production of $PDQ^{+\bullet}$ in our case. This can be monitored via UV-Vis because PDQ^{2+} itself does not strongly absorb in the visible region while the radical does (see **Figure 2.1b**). Thus, as the solution is illuminated the radical UV-Vis signature becomes apparent, which is best visualized with a difference spectrum that does not include overlapping absorbance from the CdSe NCs (**Figure 3.6b**, inset). As shown in **Figure 3.6c**, the reduction potential of the solution increases over time as the concentration of $PDQ^{+\bullet}$ in the solution builds up (the concentration of $PDQ^{+\bullet}$ over time is shown in the inset). A calculation of the quantum efficiency at 10 s, before any major inner filter effect by the $PDQ^{+\bullet}$ absorbance at the pump wavelength, indicated an efficiency of ~ 60 – 70 % for $PDQ^{+\bullet}$ generation by the CdSe NCs. Probably because of the lack of a core-shell structure,[51] this value is somewhat lower than the ~ 89% efficiency the with CdSe/CdS dot-in-rod NCs/PDQ^{2+} system previously reported by our lab.[23]

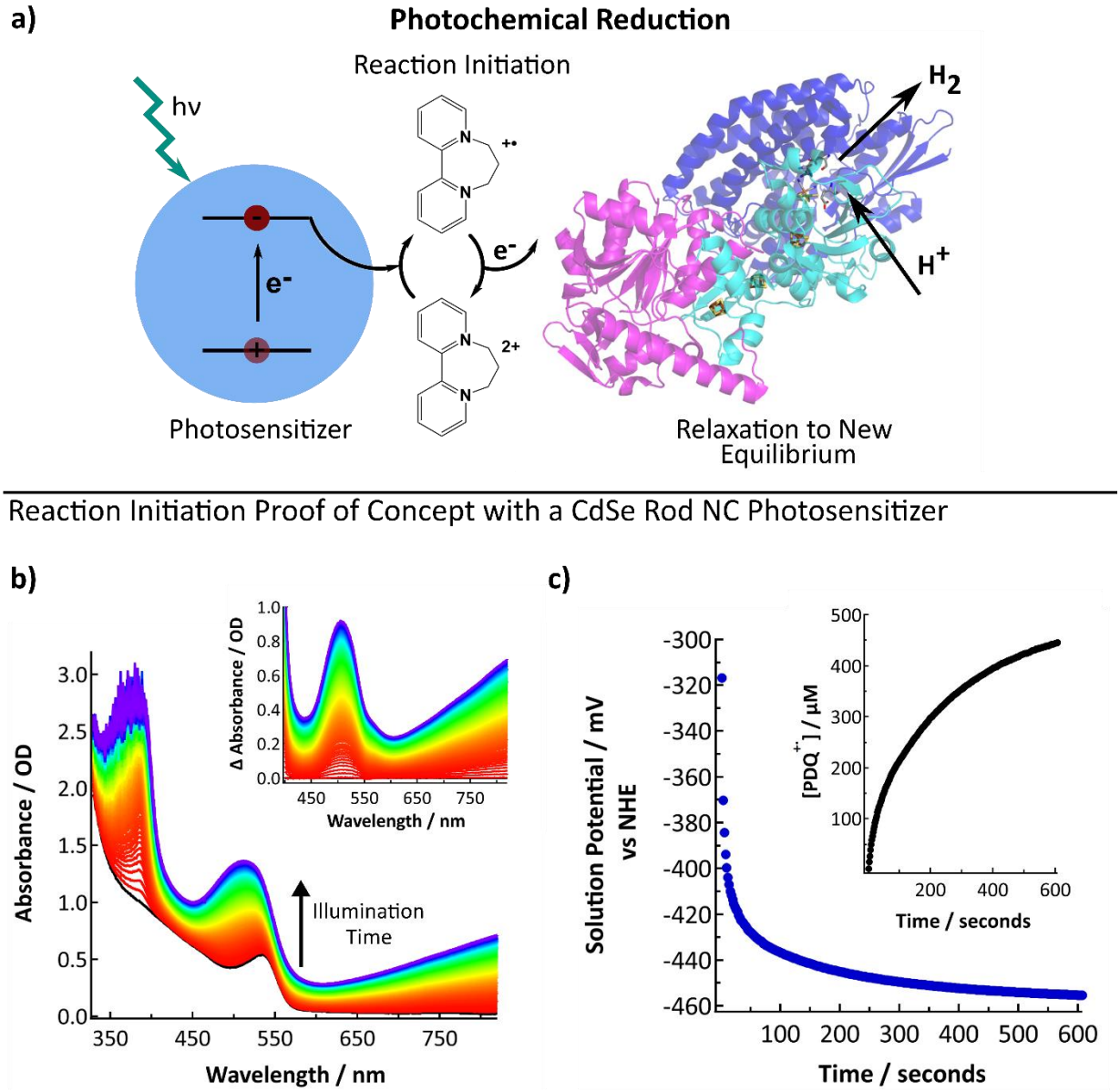

Figure 3.6: a) Concept of photochemical reduction with NCs, a redox mediator, and an enzyme. **b)** Demonstration of CdSe NC photosensitizers reducing a redox mediator, PDQ^{2+} to $PDQ^{+\cdot}$ as monitored by UV-Vis spectroscopy during illumination with ~ 4.05 mW 532 nm light. Inset: Difference spectra that only show reduced $PDQ^{+\cdot}$ signatures. Conditions: pH = 7.2 50 mM KP_i/50 mM MPA buffer, 30 mM PDQ. **c)** Corresponding change of the solution potential over time from the spectra in **b** as more PDQ^{2+} is reduced. Inset: plot of the $PDQ^{+\cdot}$ concentration increase during the illumination calculated near 808 nm, which was used to calculate the solution potential (see **Chapter 2**). Pdb code: 4OMF.

Application of the CdSe NC/PDQ^{2+} system with auto-oxidized *Pf* SH1 gave the results in shown in **Figure 3.7a-b** (absorbance spectra and corresponding difference spectra, respectively) which allows us to assign infrared bands to specific states (the illumination wavelength in this case was 450 nm, which is blue shifted from the first exciton peak of the CdSe NCs). As expected, decreasing the solution potential caused some infrared bands to decrease in intensity bleach (oxidized states) and others to increase in absorbance (reduced states). The sharp peak near 1950 cm^{-1} in the dark spectrum (**Figure 3.5** and **Figure 3.7a**) bleached during the photochemical reduction, suggesting it was the most oxidized active state, Ni_a^{2+}-S.[52-54] A band that has an induced absorbance at early illumination times and a bleach as the conditions become more reducing is located near 1966 cm^{-1} (**Figure 3.7b**), indicating it was the mid-redox level intermediate Ni_a^{3+}-C.[52-54] The state that increased in absorbance near 1954 cm^{-1} during the photochemical reduction is consistent with the most reduced form of the enzyme, Ni_a^{2+}-SR.[52-54] Induced absorbances near 1940 and 1930 cm^{-1} were consistent with Ni_a^{2+}-SR subforms[23,53,54] Ni_a^{2+}-SR' and Ni_a^{2+}-SR'' (**Figure 3.7b**). The feature near 1960 cm^{-1} in the dark spectrum was consistent with a Ni_r-B like state.[23,52-54] Enzyme in this state undergoes expected photochemical reductive activation[23,55] as seen in the absorbance spectra in **Figure 3.7a** where the feature was no longer evident following the first illumination period; the bleach is apparently masked by stronger features from flanking regions in the difference spectra (**Figure 3.7b**). A shoulder in the difference spectra near 1942 cm^{-1} that is also evident in the dark absorbance spectrum might correspond to Ni_r^{2+}-S.[21,54]

Regarding active states, there is ample evidence supporting assignment of Ni_a^{3+}-C and Ni_a^{2+}-SR in *Pf* SH1. Both have induced absorbances at some point as the reduction potential increases in a photochemical reduction experiment shown here and elsewhere,[23] and both have kinetic behavior under time-resolved conditions supporting their role as mid-level and more reduced catalytic intermediates.[21] Unambiguous assignment of Ni_a^{2+}-S is aided by binding of exogenous carbon monoxide (CO). CO is known to binding terminally to the active site nickel atom to form the Ni^{2+}-SCO state.[56,57] The CO ligand is

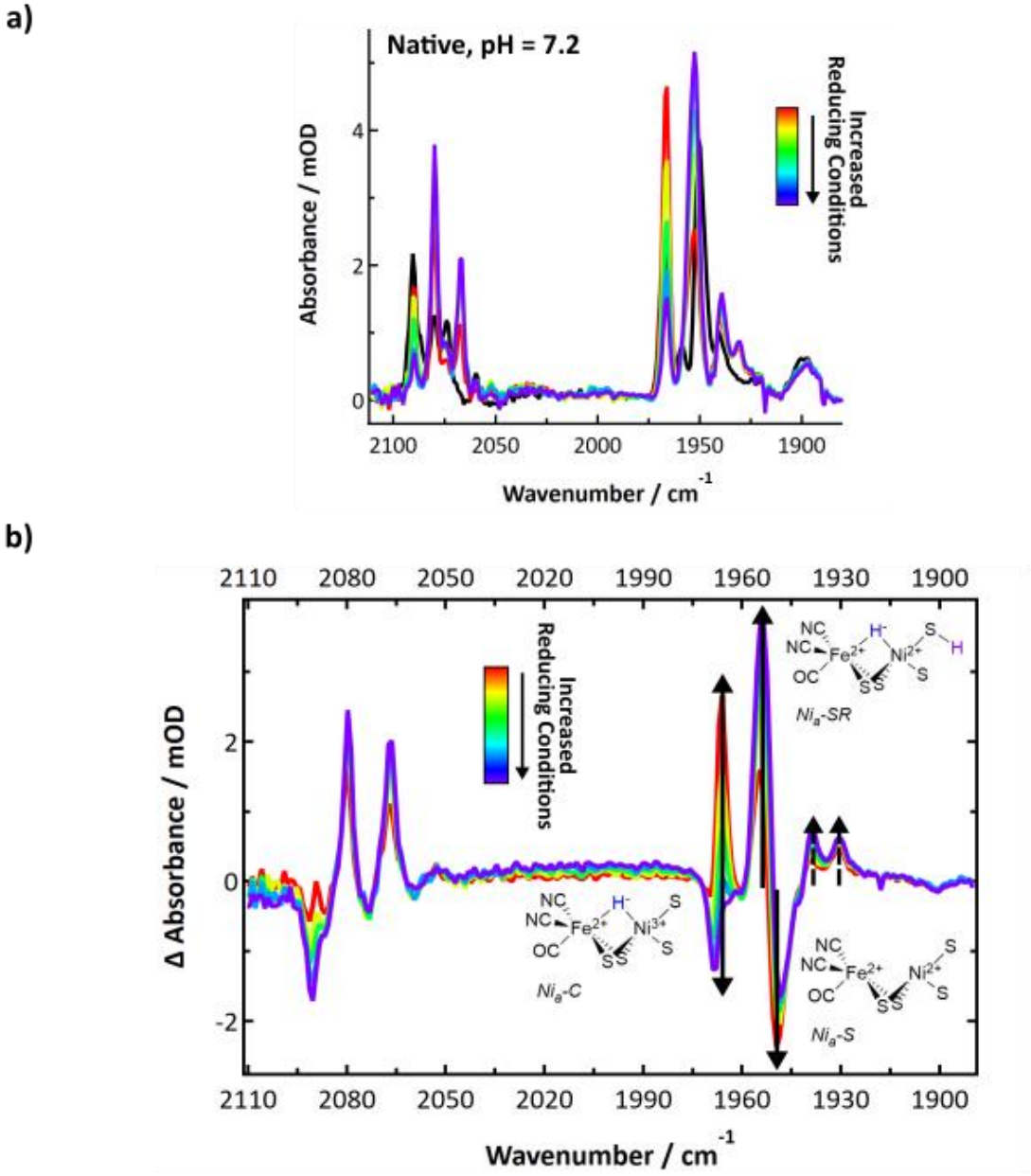

Figure 3.7: a) Infrared absorbance spectra of auto-oxidized native *Pf* SH1 during the photochemical reduction (the dark spectrum is colored black). **b)** Corresponding difference spectra from **a**, with Δ A = (illuminated spectrum – dark spectrum). State assignments based on ν_{CO} peaks indicated by solid black arrows are shown with the corresponding active site structure for Ni_a^{2+}-S, Ni_a^{3+}-C, and Ni_a^{2+}-SR. Dashed arrows correspond to Ni_a^{2+}-SR' and Ni_a^{2+}-SR''.

photosensitive, with illumination under cryogenic conditions showing a bleach of the Ni-SCO signal and formation of Ni_a^{2+}-S.[58-60]

Incubation of *Pf* SH1 under CO yields a general spectrum like that shown in **Figure 3.8a** (pH = 8.0) with an exogenous ν_{CO} peak near 2044 cm^{-1} and an endogenous ν_{CO} peak near 1947 cm^{-1}. A UV-Vis spectrum of the same sample from **Figure 3.8a** showed broad absorbance features from 350 nm to energies below 500 nm (**Figure 3.8b**) that correspond the FeS cluster cofactors,[61] the flavin cofactor,[62] and the nickel carbonyl.[56]

We performed CO photolysis with time-resolved IR spectroscopy with this sample. A study of time-resolved CO photolysis has not been reported before for a [NiFe]-H_2ase, although it has been for the *Chlamydomonas reinhardtii* [FeFe]-H_2ase.[63] We monitored endogenous CO peaks given their stronger intensity and the ability to see photolysis products (e.g. Ni_a^{2+}-S) in this region. Photolysis of the nickel carbonyl with a 10 ns 355 nm pulse yielded a bleach of the 1947 cm^{-1} peak (**Figure 3.8c**, purple trace). The actual breaking of the Ni-CO bond and bleach occurs before the time resolution of the instrument and is thus on the ultrafast time scale (e.g. picoseconds), similar to carbon monoxide photolysis in hemoglobin[64] and myoglobin.[65] An induced absorbance was also seen in the region of the proposed Ni_a^{2+}-S feature from **Figure 3.7** (**Figure 3.8c**, red trace).

A plot of the transient absorbance amplitudes, relative to early and late time, versus wavenumber indicated a negative band with a minimum near 1947 cm^{-1} (corresponding to the endogenous Ni^{2+}-SCO feature from the FTIR spectrum in **Figure 3.8a**) and an induced absorbance with a maximum near 1951 cm^{-1} (**Figure 3.8d**). Both features decayed time back to zero (**Figure 3.8c-d**), indicative of photolyzed CO rebinding at the active site, thus causing Ni^{2+}-SCO to reform (similar again to recombination in heme proteins like myoglobin[66]). The decay rate of Ni_a^{2+}-S (1951 cm^{-1}) and recovery of Ni_a^{2+}-SCO (1947 cm^{-1}) were biphasic with average lifetimes ~ 2 ms and 5 ms, respectively. The biphasic kinetics cannot be interpreted too much without more in-depth investigations; this includes ridding of residual Ni_a^{3+}-C signal near 1966 cm^{-1} that was evident in the FTIR spectrum, because the Ni_a^{3+}-C state itself photosensitive as discussed later. However, the Ni_a^{3+}-C signal equilibrium absorbance was rather small that it probably

contributed negligibly to Ni_a^{2+}-S dynamics on the µs timescale and *does not* account for the induced absorbance of Ni_a^{2+}-S observed on the ns time scale[21,22] (also, no evident photochemistry corresponding

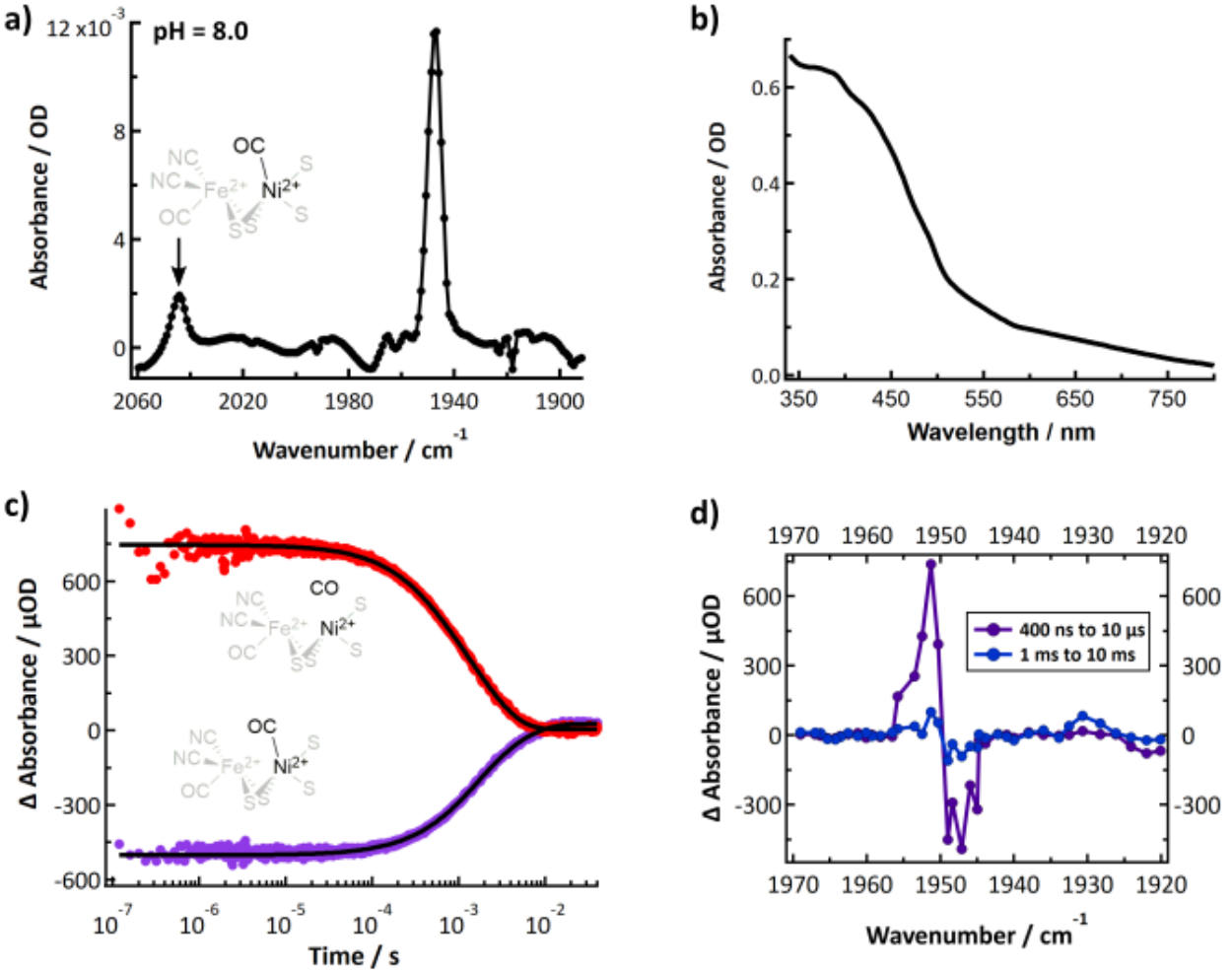

Figure 3.8: a) Infrared spectrum of CO incubated *Pf* SH1; the concentration of protein was ~ 1 mM in 50 mM pH 8.0 HEPES buffer. A structure of Ni-SCO is shown with an arrow pointing to the carbonyl stretch of the Ni-CO species. **b)** Corresponding UV-Vis spectrum. **c)** Transient absorption traces from 1951 cm^{-1} (red) and 1947 cm^{-1} (purple) and the double exponential fits. The active site structures that correspond to each trace are shown with an emphasis on the nickel and exogenous CO, although endogenous ν_{CO} bands were monitored for the transient absorption experiments. **d)** Transient absorption amplitudes at early time and later time that, together with **c** show the decay of the Ni_a^{2+}-S species state and reformation of Ni^{2+}-SCO.

to Ni_a^{3+}-C was observed).[21,22] The main point though is that the results are qualitatively identical to the cryogenic IR CO photolysis with the *Allochromatium vinosum* enzyme[58] and cryogenic IR photolysis and recombination experiments with the *Dv* MF[59] and the O_2 tolerant *Aquifex aeolicus*[60] enzymes, indicating the feature near 1951 cm^{-1} is indeed Ni_a^{2+}-S in *Pf* SH1.

Our laboratory further studied the pH dependence of the infrared features of native *Pf* SH1 as prepared under similar conditions to the EPR samples from **Figure 3.3**, albeit studies in this case were at room temperature. A plot of pH dependent spectra are shown in **Figure 3.9**.[22] The main FTIR signature at all pH values was the Ni_a^{3+}-C state, which underwent a small redshift from moderately low to high pH. A fit to a monoprotic Henderson-Hasselbalch relationships indicated the shift could be, in part, attributed to an acid-base equilibrium with an apparent pK_a of ~ 6.6.[22]

The shift could also be attributed to iron-sulfur cluster cofactor behavior. Such cofactors are known to have decreased intensity of broad a UV-Vis absorbance signature upon reduction because of decreased probability of 3p (sulfur) → 3d (Fe^{3+}) charge transfer.[61,67,68] Thus, it is likely that under more reducing conditions (which for our purposes is at higher pH values that decrease the H_2/H^+ couple) the iron sulfur clusters are more reduced, including the proximal FeS cluster to the active site (**Figure 3.2b**). The proximal cluster's oxidation state has been shown to affect the endogenous ν_{CO} peak position in CO incubated [NiFe]-H_2ases, in which a shift to lower wavenumber is observed with iron-sulfur cluster reduction[59,69] and in native SH1 we have observed a reduced intensity of UV-Vis absorbance under ~ 4% H_2 as pH is increased, indicating an increased population of reduced FeS clusters.[22] Clearly, a probable increase of reduced proximal iron-sulfur clusters population likely contributes to the redshift wavenumber shift of Ni_a^{3+}-C as pH is increased.[22]

The Ni_a^{3+}-C hydride is exchangeable in D_2O solvent to a deuteride[70-72] (formally a proton/deuteron exchange). In conjunction with the Ni_a^{3+}-C state being a catalytic intermediate,[21] this indicates the hydride stores a proton and two electrons of an H_2 molecule. Additionally, the hydride is photosensitive[71-75] with

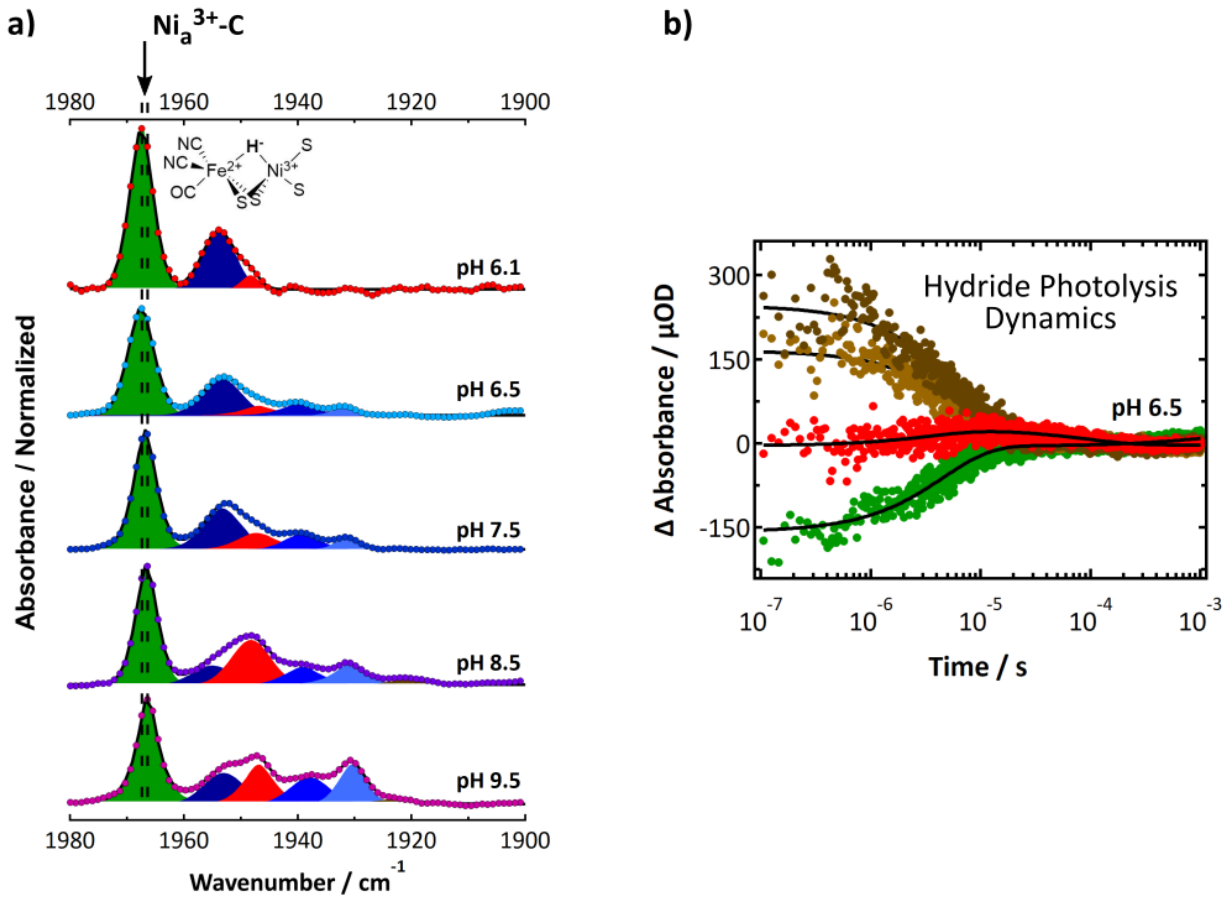

Figure 3.9: a) pH dependent FTIR spectra of native *Pf* SH1 prepared under ~ 4% H_2. States left to right are Ni_a^{3+}-C (green); Ni_a^{2+}-SR (dark blue); Ni_a^{2+}-S (red); Ni_a^{2+}-SR' (blue); and Ni_a^{2+}-SR''/Ni_r^{2+}-S (light blue); a weak Ni_a^{+}-L feature near 1920 cm^{-1} one is present but not visible on the graph at pH = 8.5 and 9.5. Emphasis is placed on the pH dependent shift of the Ni_a^{3+}-C state. **b)** Kinetic traces following Ni_a^{3+}-C hydride photolysis at pH = 6.5; color scheme: Ni_a^{3+}-C (green, 1967 cm^{-1}); photoproducts Ni_a^{+}-L1 (tan, 1917 cm^{-1}) and Ni_a^{+}-L2 (brown, 1922 cm^{-1}); and Ni_a^{2+}-S (red, 1948 cm^{-1}). Adapted with permission from Greene, B. L.; Wu, C.-H.; Vansuch, G. E.; Adams, M. W.; Dyer, R. B., *Biochemistry* 2016, 55 (12), 1813-25. Copyright 2016 American Chemical Society.

the photoproduct(s) previously observed under cryogenic temperatures formally being a Ni^{+} species (termed Ni_a^{+}-L).[76] Recent in depth hydride photolysis studies with the *Dv* MF enzyme from Tai and co-

workers under cryogenic conditions with EPR and FTIR spectroscopy have provided two very important results: 1) the general Ni_a^+-L photoproduct has a protonated terminal C418,[31] and 2) hydride photolysis can result in proton migration out of the active site (that, Ni_a^{2+}-S can form) only if the proximal iron-sulfur cluster is oxidized (that is, if it acts as an electron acceptor).[75]

Our lab monitored hydride photolysis under more catalytically relevant conditions with time-resolved infrared spectroscopy using a 532 nm pump for initiation of photolysis (the photolysis yield has been previously been demonstrated to be highest between 500 – 600 nm[68]). **Figure 3.9b** shows kinetic traces of Ni_a^{3+}-C hydride photolysis (colored green) and hydride recombination, the decay of two observed photoproducts (termed Ni_a^+-L1 and Ni_a^{2+}-L1, colored shades of yellow/brown), and also the observed formation of Ni_a^{2+}-S (colored red) on the μs timescale at pH = 6.5.[22] Like with CO photolysis, time resolution of the hydride photolysis and formation of the photoproducts is not accessible on the time scales of typical time-resolved infrared spectroscopy (this would require ultrafast infrared spectroscopy to directly observe). Because there is no perturbation of the solution conditions with hydride photolysis, the system relaxes back to where it started pre-photolysis, and thus all the transient absorption signals decay back to zero (for example, see **Figure 3.9b**).

A plot of transient absorption amplitudes on the microsecond timescale where all photoproducts and other states were observed is shown in **Figure 3.10** (the state colored grey at pH = 6.1 is not understood and not discussed here).[22] Regardless of pH, photolysis of the bridging hydride and two photoproducts were observed. Ni_a^{3+}-L and Ni_a^+-L are tautomeric species and the proton resides on the a terminal cysteine in the active site in at least one Ni_a^+-L state,[31,33] and the small ν_{CO} differences between the two photoproducts observed indicated the proton remains in the active site primary sphere for both states.[77] However, only Ni_a^{2+}-S formation was observed in the pH = 6.5 – 7.5 range[22] (Ni_a^{2+}-S formation following hydride photolysis has also been observed in *Pf* SH1 at pH = 6.3, 7.0, and 7.7, although the conditions were differnet[21]).

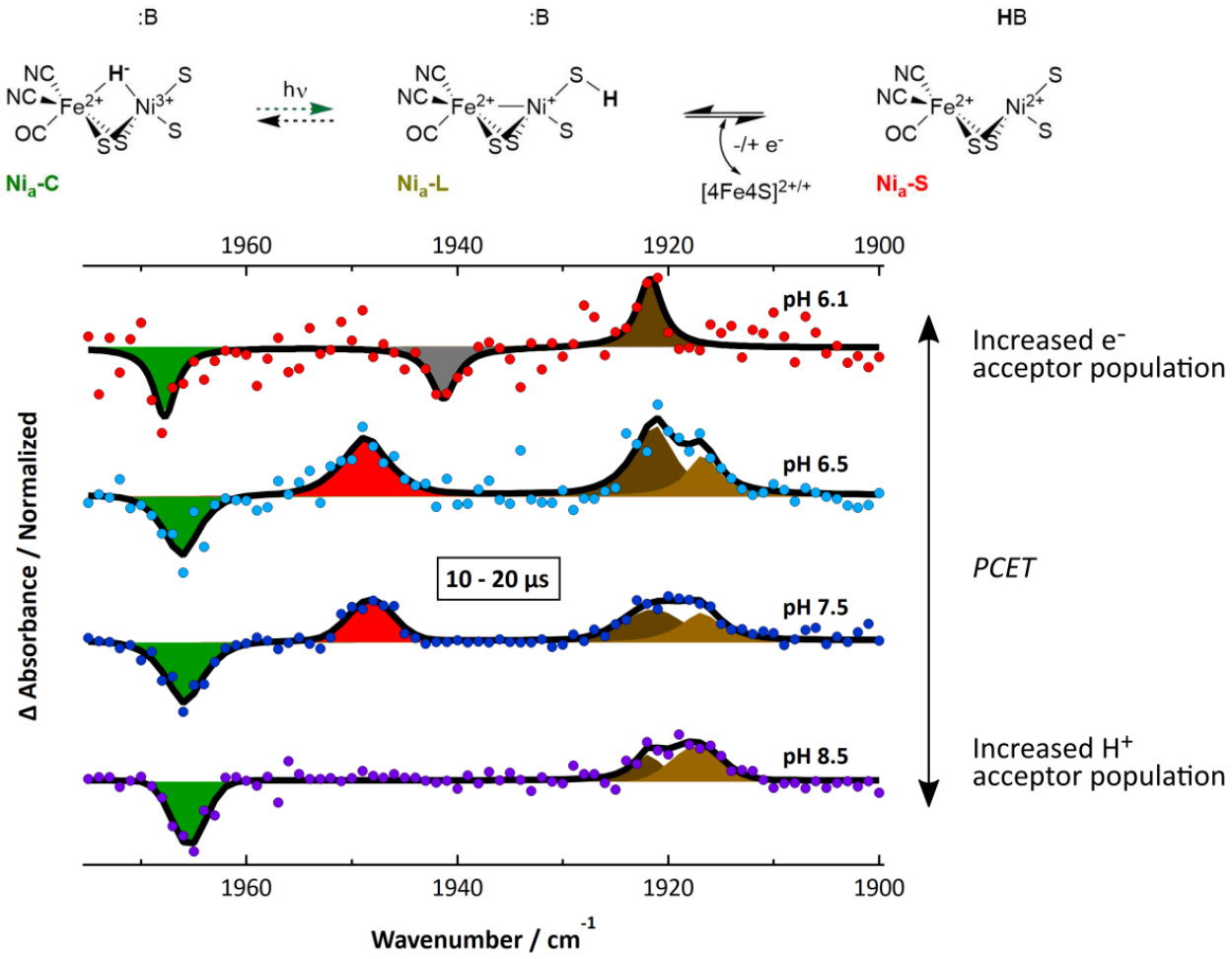

Figure 3.10: Transient absorption amplitudes on the µs timescale from pH dependent hydride photolysis experiments with native *Pf* SH1. Sufficient electron acceptor populations (oxidized proximal FeS clusters) and sufficient proton acceptor populations (depicted here as a base, :B. Proton acceptor(s) would be more protonated at lower pH values) allowed Ni_a^{2+}-S dynamics to be observed at pH = 7.5 and 8.5. The overall reaction and PCET requirements are in the top schematic and side text, respectively. Adapted with permission from Greene, B. L.; Wu, C.-H.; Vansuch, G. E.; Adams, M. W.; Dyer, R. B., *Biochemistry* 2016, 55 (12), 1813-25. Copyright 2016 American Chemical Society.

The overall results summarized in **Figure 3.10** matched those of the *Dv* MF enzyme studies from Tai and co-workers[31,75] quite well and provided additional information; that is, in *Pf* SH1 1) there is an increased population of oxidized FeS clusters as pH is lowered, which provided an electron acceptor during PCET. This means that as pH is raised, the population of electron acceptors *decreases* and PCET is not observed and 2) PCET was not observed at moderately low pH values, which can be readily explained by a decreased population of proton acceptors at more acidic conditions (where they would more likely be protonated). Hence, PCET is only observed in an intermediate pH regime where there is a sufficient population of both oxidized proximal FeS clusters and deprotonated proton acceptors (schematically demonstrated at the top of **Figure 3.10**).

No Ni_a^+-L → Ni_a^{2+}-S signal was observed in D_2O, suggesting hydride recombination was faster than deuteron migration out of the active site (at least at a detectable level).[22] However, a kinetic isotope effect observed for the Ni_a^{2+}-S → Ni_a^{3+}-C transition suggested a tunneling mechanism during proton migration to/from the active site, which necessitates a Ni_a^+-L intermediate.[21] More-so , kinetic modeling suggested the Ni_a^+-L1 and Ni_a^+-L2 states formed in a serial mechanism, Ni_a^{3+}-C ←→ Ni_a^+-L2 ←→ Ni_a^+-L1, and the temperature dependent decay rates of Ni_a^+-L1 and Ni_a^+-L2 larger at pH = 6.5 (where PCET occurs) versus pH = 9.5 (where Ni_a^{2+}-S does not form) indicated a two-step process occurs during their decay when PCET occurs (proton transfer back to the active site during Ni_a^{2+}-S decay followed by reformation of the bridging hydride).[22] However, identity of the proton donor/acceptor in the Ni_a^{2+}-S state could not be determined from these data alone.

The tools (and corresponding analyses) discussed in this section included electron paramagnetic resonance spectroscopy, FTIR spectroscopy, equilibrium photochemical reduction coupled to FTIR spectroscopy, and time resolved hydride and exogenous CO photolysis. All of these methods are used in either the remaining sections of this chapter or in next chapter, which is why we have introduced both published and unpublished data from our lab regarding these methodologies in this section with native *Pf*

SH1. We now turn to the main focus of this chapter, which is probing the E17Q and E17D variants in *Pf* SH1.

3.2.2 – Investigations of E17Q *Pf* SH1: Equilibrium FTIR, Time Resolved Hydride Photolysis, and Exogenous CO Photolysis

As isolated and stored E17Q *Pf* SH1 displayed proton reduction kinetics and hydrogen oxidation kinetics with rates that were ~ 20 % and 30% of native enzyme for standard hydrogen oxidation and proton reduction assays relative to native *Pf* SH1, respectively, at pH = 8.4 with benzyl viologen as an electron acceptor/donor and T = 80 °C (near T_{opt} ~ 100 °C[14,16]). These results are fairly consistent with those of Szőri-Dorogházi and co-workers with the E17Q variant from *Tr* Hyn where the activity was ~ 50 % versus the native enzyme.[28] Overall these measurements indicated E17 is evidently important for turnover in *Pf* SH1. However, there is no obvious reason as to how based off the mitigated, but not insignificant, activity.

To gain further insight, we turned to analysis of spectroscopic signatures for further investigation. A FTIR absorbance spectrum of E17Q at pH = 8.5 under ~4% H_2 and nitrogen is shown in **Figure 3.11a** at T = 20°C**.** Multicomponent Voigt fits to the CO region indicated a peak at ~ 1966 cm^{-1} we assigned to Ni_a^{3+}-C given the almost identical position to Ni_a^{3+}-C in native SH1 and known lack of other features being obseved near 1966 cm^{-1} native SH1.[22,23] Minor state(s), which appeared to be more than noise, were seen at ~ 1919 and 1923 cm^{-1}; we tentatively assigned these to Ni_a^{+}-L(1/2) because measurements with native *Pf* SH1 at pH = 8.5 and 9.5 had shown minor poulations of Ni_a^{+}-L1[22] and thus observation of Ni_a^{+}-L states is not without precedent at pH = 8.5 in SH1. Other states appeared near 1957, 1951, 1943, and 1931 cm^{-1} that were not possible to identify with any confidence based on the spectrum alone.

For further analysis, we performed a “temperature induced” auto-oxidation with the sample: the temperature was ramped from 14 – 54 °C and FTIR spectra recorded roughly every 5 °C. During the ramp, enzyme consumption of H_2 and/or loss of H_2 from the IR cell resulted in oxidation of the sample. In native

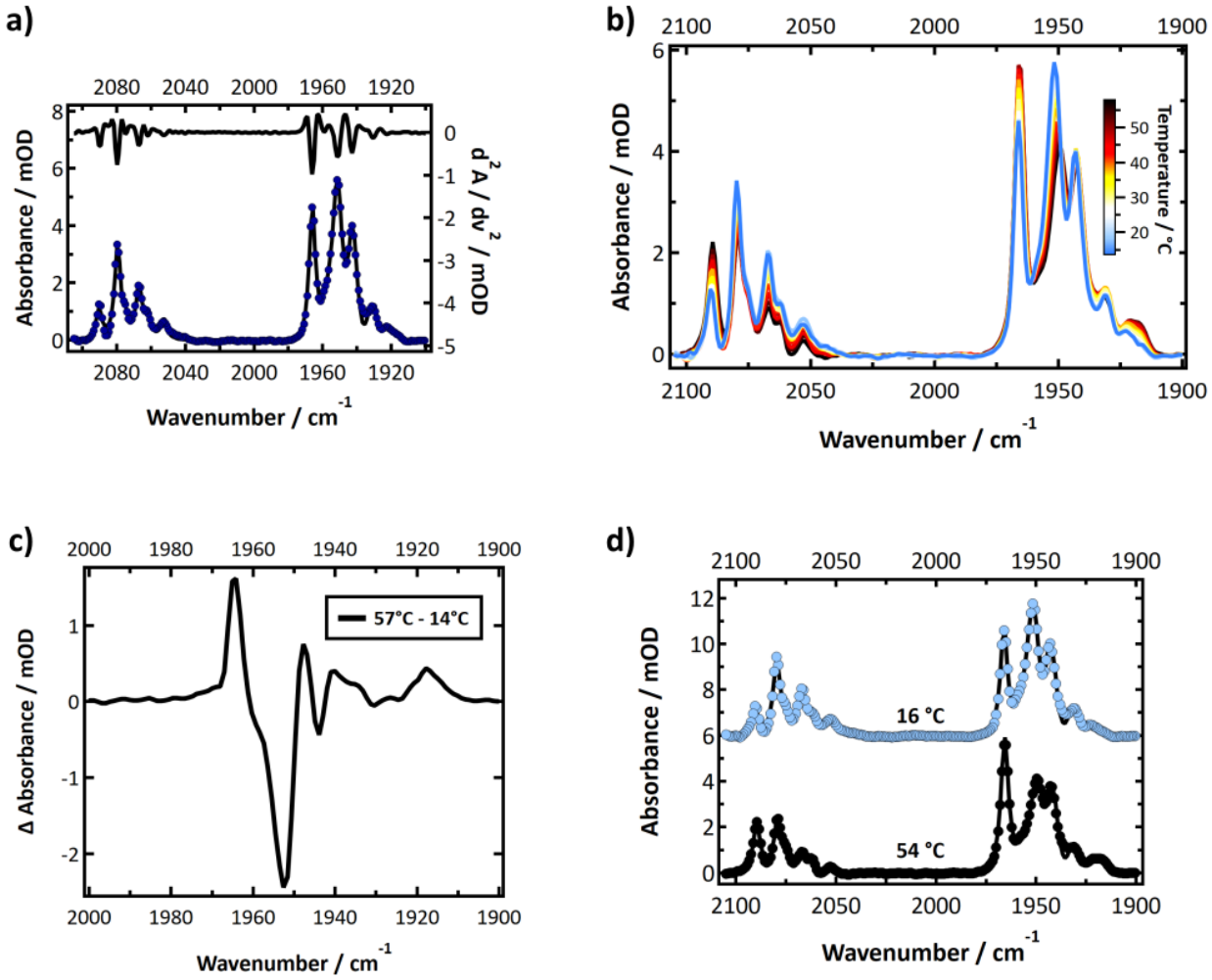

Figure 3.11: a) FTIR spectrum of ~ 750 µM E17Q *Pf* SH1 in pH = 8.5 50 mM HEPPS buffer, T = 20°C; the corresponding fit used 4 cm^{-1} peak widths. The second derivative spectrum corresponds to the right hand axis. **b)** Temperature dependent FTIR spectra of the sample from 14 – 54 °C. **c)** Difference spectrum of the lowest minus the highest temperature. **d**) Display of T = 16 °C and T = 54 °C spectra with corresponding fits; peak widths were 3. 7 cm^{-1}. An offset of 6 mOD added for clarity to the T = 16 °C spectrum.

enzyme, this causes a bleaching of Ni_a^{2+}-C and Ni_a^{2+}-SR state(s) intensities and primarily a growth of the Ni_a^{2+}-S state, as would be expected for oxidation over a short period of time with little to no oxygen exposure (see **Appendix B**). The temperature ramp FTIR spectra with E17Q are shown in **Figure 3.11b**;

Figure 3.11c shows the difference spectrum between the highest and lowest temperature. From both the absorbance and difference spectra there was a clear bleach of a state near 1951 cm^{-1} we assigned to Ni_a^{2+}-SR (most reduced) and a growth of the Ni_a^{3+}-C state near 1966 cm^{-1} (more oxidized/less reduced than Ni_a^{2+}-SR). There was also a clear bleach near 1943 cm^{-1} we attributed to Ni_a^{2+}-SR' and a small bleach near 1931 cm^{-1} attributed to Ni_a^{2+}-SR'' (assignment of Ni_a^{2+}-SR'' is complicated by probable overlap with Ni_r^{2+}-S,[21-23,53] although Ni_r^{2+}-S would only be expected to bleach under highly oxidized conditions not achieved in the temperature ramp). The Ni_a^{2+}-SR position is slightly redshifted relative to native enzyme while the Ni_a^{2+}-SR' state is slightly blueshifted relative to native enzyme (within 2 – 3 cm^{-1}). The Ni_a^{2+}-SR'' position is essentially unchanged. The nature of the 1957 cm^{-1} state is uncertain, but it might be a redshifted Ni^{3+}_r-B like state.[23]

Less obvious in the difference spectrum but more evidenced in the absorbance spectra was a small shift of the CO band(s) near 1950 cm^{-1} (further visualized by selected second derivative and absorbance spectra shown in **Appendix B**). At the low temperature extreme, T = 16 °C, band fit to a species with ν_{CO} = 1951.4 (+/- 0.08) cm^{-1}; one feature was assumed in this region to avoid over fitting/over analysis of the data given there was no obvious shoulder. At the high temperature extreme, T = 54 °C, the band fit to a species with ν_{CO} = 1949.6 (+/- 0.09) cm^{-1}. The shift of the Ni_a^{3+}-C peak was less pronounced in going from 1966 (+/- 0.04) cm^{-1} at T = 16 °C to 1965.6 (+/- 0.03) cm^{-1} at T = 54 °C; the same was true with the native enzyme temperature ramp (see **Appendix B**) where the Ni_a^{3+}-C state went from ~ 1966.2 to 1965.8 cm^{-1} between T = 16 – 49 °C. Thus, it appeared the shift of the band(s) near 1950 cm^{-1} would be more than just because of proximal FeS cluster oxidation that could also occur during the temperature ramp and thus cause a small redshift of ν_{CO} as seen with the Ni_a^{3+}-C in native and E17Q during temperature ramps. We hypothesized the ~ 1951.5 and 1950 cm^{-1} features corresponded to overlapped Ni_a^{2+}-SR and Ni_a^{2+}-S, respectively.

To show where Ni_a^{2+}-S appears in E17Q, we incubated an E17Q sample with carbon monoxide. **Figure 3.12a** shows the FTIR spectrum of the sample; like native enzyme (**Figure 3.8a**) there was an endogenous CO peak near 2044 cm^{-1} that corresponded to a Ni-CO species, and an endogenous CO peak near 1947 cm^{-1}. The corresponding UV-Vis spectrum is shown in **Figure 3.12b**; like native enzyme, the spectrum consists of contributions from FeS clusters, other cofactors, and the Ni-CO species. Time-resolved IR spectroscopy of CO photolysis/recombination initiated with a 10 ns 355 nm pulse showed a bleach near 1947 cm^{-1} (Ni^{2+}-SCO) and an induced absorbance near 1952 cm^{-1} (Ni_a^{2+}-S); transient traces for these two wavenumbers are shown in **Figure 3.12c**. The Ni_a^{2+}-S decay and Ni^{2+}-SCO recovery fit to double exponentials with average amplitude weighted lifetimes of 1.5 ms and 2.6 ms, respectively; the rebinding lifetime is different from native enzyme (~ 5 ms). **Figure 3.12d** shows a plot of transient absorption amplitudes at early and later time. Because E17 is near the gas channel bottleneck at the active site,[78] mutation to glutamine could result in different overall rebinding dynamics to form Ni^{2+}-SCO relative to native SH1; although, again, actual kinetics of CO photolysis and rebinding at the [NiFe] site still require an in depth investigation and should not be interpreted too much at this stage. The photolysis and rebinding data with native and E17Q *Pf* SH1 do, however, suggest CO rebinding is not a simple process involving only two states, which is consistent with observations from CO rebinding with the *Cr* HydA [FeFe]-H_2ase.[63,79] The transient absorption experiment here also showed that Ni_a^{2+}-S has a ν_{CO} feature near 1952 cm^{-1} (exact determination is complicated by overlap with the opposite amplitude of the Ni^{2+}-SCO feature that would result in apparently seemingly lower transient absorption amplitudes closer to 1950 cm^{-1}). Still, it confirms our hypothesis that both Ni_a^{2+}-SR and Ni_a^{2+}-S have CO bands in similar regions from the spectra in **Figure 3.11**.

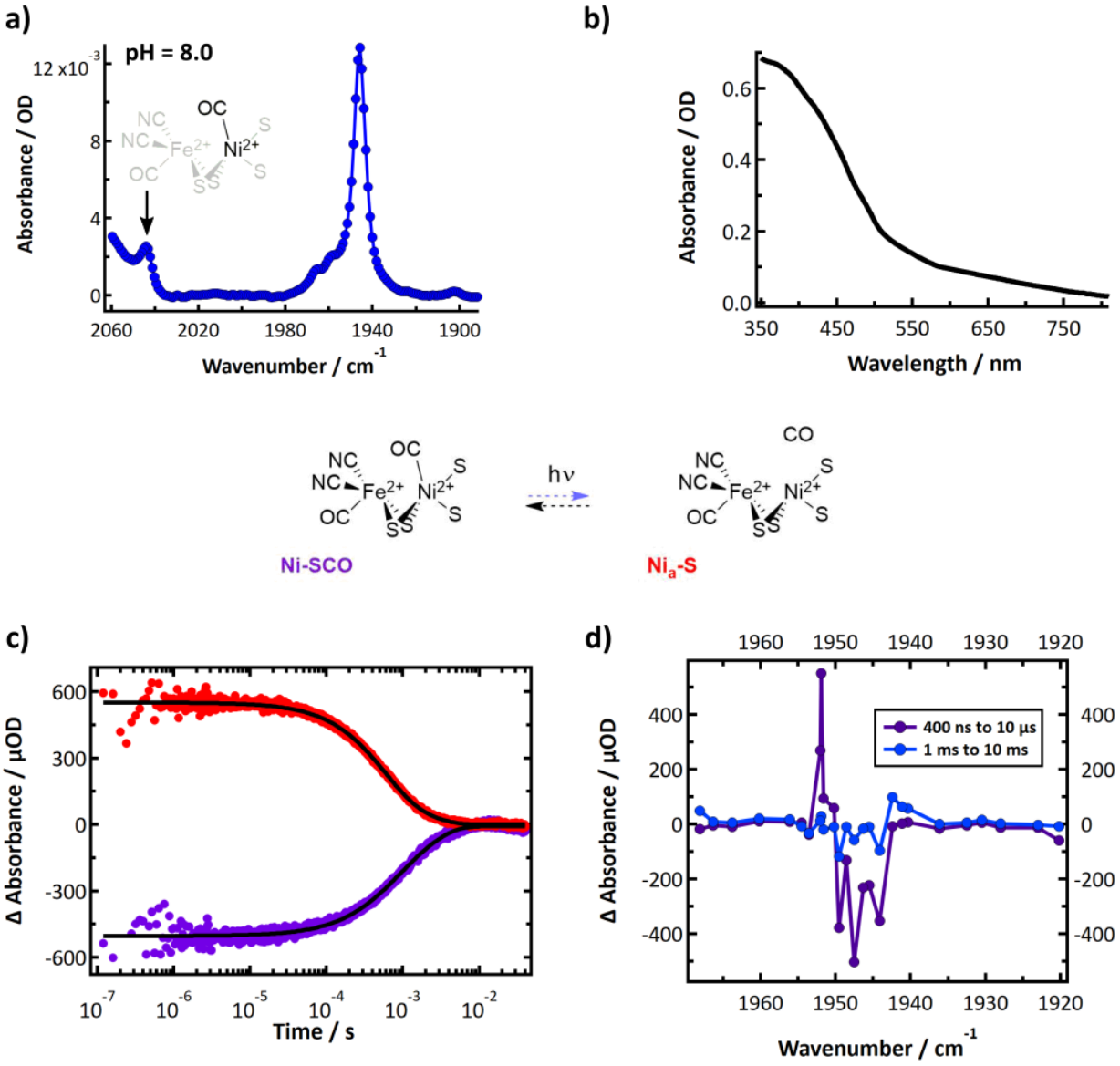

Figure 3.12: a) Infrared spectrum of CO incubated E17Q *Pf* SH1; the concentration of protein was ~ 1 mM in 50 mM pH 8.0 HEPES buffer. A structure of Ni-SCO is shown with an arrow pointing to the carbonyl stretch of the Ni-CO species. **b)** Corresponding UV-Vis spectrum. **c)** Transient absorption traces from 1952 cm^{-1} (red) and 1947 cm^{-1} (purple) and double exponential fits. **d)** Transient absorption amplitudes at early time and later time that, together with **c** show the decay of the Ni_a^{2+}-S species state and reformation of Ni^{2+}-SCO. The middle scheme shows an over simplified process of CO photolysis/recombination.

We also investigated the general pH dependence behavior of E17Q *Pf* SH1. **Figure 3.13** shows FTIR spectra from pH = 6.5 – 8.5. The major features were typically Ni_a^{3+}-C (colored green) and Ni_a^{2+}-SR (colored dark blue, with some probable Ni_a^{2+}-S overlap). In accord with assignments from the temperature dependent spectra in **Figure 3.11**, a state near 1942 cm^{-1} was assigned to Ni_a^{2+}-SR' (blue). States with peaks at wavenumbers < 1930 cm^{-1} were not included in the curve fitting procedure because of an unfortunately noisy baseline. However, **Figure 3.13** has evident features of a state near 1930 cm^{-1} (probably Ni_a^{2+}-SR'' as assigned from the less noisy temperature dependent data). It is interesting to note that in native enzyme the Ni_a^{3+}-C state is the dominant feature in as prepared samples under 100% N_2[21] or ~ 4% H_2 (see **Figure 3.9** for example); however, as evident in **Figure 3.13**, this is no longer the case where Ni_a^{2+}-SR states appear to have near equal populations to that of Ni_a^{3+}-C, if not greater populations. The discrepancy of the 1950 cm^{-1} versus 1966 cm^{-1} band intensity in **Figure 3.11a** versus **Figure 3.13** at identical pH and nearly identical buffering conditions is not clear, but probably has to do with precise sample history. There was consistently a small population of the state near 1957 cm^{-1} (albeit very weak for pH = 6.5 and not included in that fit) that may correspond to the Ni_r^{3+}-B like state (colored grey).[23]

There was a small redshift of the Ni_a^{3+}-C state with increasing pH. The shift appeared less pronounced (1.2 – 1.4 cm^{-1} for native enzyme depending on the exact analysis[22] versus ~ 1 cm^{-1} for E17Q based on the somewhat noisy peak position in **Figure 3.13** for pH = 6.5 and the peak position for the pH = 8.5 sample in **Figure 3.11**). It is very tempting to imply the smaller shift is the result of the E → Q mutation because glutamine is nonionzable, and that the apparent acid-base equilibrium from the Ni_a^{3+}-C shift is from the protonation state of E17. However, the peak position in both native and E17Q *Pf* SH1 is probably a very complicated convolution of the proximal FeS cluster oxidation state and any nearby acid-base equilibrium making it very difficult to assign to a subset of distinct redox or acid-base equilibrium. However, a glutamate residue could reasonable have pK_a ~ 7 – 8 in buried protein environment like H_2ase based on a study from staphylococcal nuclease.[80] Thus, it would be reasonable to assume E17 has an acid/base

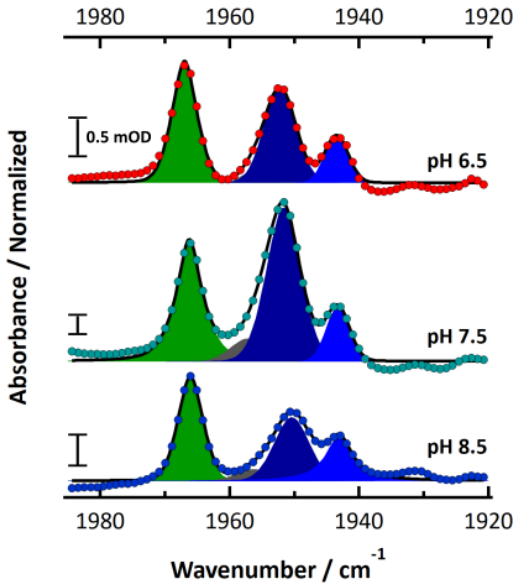

Figure 3.13: pH dependent FTIR spectra of E17Q *Pf* SH1 (10 mM MES pH 6.5, 100 mM Tris pH 7.5, and 100 mM HEPPS pH 8.5) that were normalized relative to the Ni_a^{3+}-C state maximum from the baseline corrected absorbance spectra. Color coding: Ni_a^{3+}-C (green); Ni_x-X (grey), Ni_a^{2+}-R (dark blue, which is probably overlapped with Ni_a^{2+}-S), and Ni_a^{2+}-SR' (light blue). Ni_a^{2+}-SR'' is probably present as evident by a small peak near 1930 cm^{-1}, but a noisy baseline for these measurements did not allow for detailed analysis in this region; similarly, Ni_a^{+}-L state(s) were probably present too at pH = 8.5, but the < 1920 cm^{-1} region was too noisy for any analysis (unlike in **Figure 3.11**). A state that might be Ni_r^{3+}-B like is colored grey.

equilibrium in the pH = 6.5 – 8.5 range in native *Pf* SH1 that contributes to the Ni_a^{3+}-C pH dependent peak position. Thus, the shift would be somewhat smaller in E17, which is what we appeared to observe.

Given the proximity of E17 to C418, our analysis suggested E17 is the proton/donor acceptor during the Ni_a^{3+}C ←→ Ni_a^{2+}-S transition. To probe this, we investigated Ni_a^{3+}-C hydride photolysis dynamics of concentrated E17Q samples at pH = 6.5 and 8.5 samples prepared under conditions similar **Figure 3.12**. Transient absorption traces and transient absorption amplitude plots at pH = 6.5 (where Ni_a^{2+}-S should be

observed based on native SH1 studies[22]) and pH = 8.5 (where Ni_a^{2+}-S should not be observed based on native SH1 studies[22]) are presented in **Figure 3.14a**. At both pH values, we observed hydride photolysis and two photoproducts (Ni_a^{+}-L species) that recovered and decayed, respectively, with kinetics adequately described by a single exponential. At pH = 6.5 the decay rate of the photoproducts were (1.08 – 1.5 $\pm$ 0.02 – 0.03) x 10^5 s^{-1} and (1.36 $\pm$ 0.04) x 10^5 s^{-1} as measured at 1918 – 1920 cm^{-1} and 1926 cm^{-1}, respectively. The recovery rate of Ni_a^{3+}-C was (1.37 $\pm$ 0.015) x 10^5 s^{-1} as measured at 1967 cm^{-1}. At pH = 8.5 the decay rate of the photoproducts were (1.00 – 1.24 $\pm$ 0.013 – 0.017) x 10^5 s^{-1} and (1.59 $\pm$ 0.05) x 10^5 s^{-1} as measured at 1917 – 1919 cm^{-1} and 1923 cm^{-1}, respectively. The recovery rate of Ni_a^{3+}-C was (1.69 $\pm$ 0.016) x 10^5 s^{-1} as measured at 1967 cm^{-1}.

Hence, the rates of photoproduct decay and Ni_a^{3+}-C recovery were essentially identical at a given pH value and consistent at pH extremes where Ni_a^{2+}-S could probably be formed and probably not be formed based on native enzyme studies (see **Figure 3.10** for example).[21,22] As seen in the transient absorption amplitude plots in **Figure 3.14b**, no Ni_a^{2+}-S was actually detected in the E17Q variant at these pH extremes (nor was it seen in pH = 7.5 data collected by Brandon Greene in our laboratory). Temperature dependent dynamics (T = ~ 12 – 55°C) of photoproduct recovery monitored near 1920 cm^{-1} at pH = 6.5 and pH = 8.5 were also investigated. The kinetic traces and corresponding Arrhenius plots are shown in **Figure 3.15** (fits were to the linear region up to about 40 °C, which is prior to the known break point from linear behavior at higher temperatures[14,22] that is probably related to the hyperthermophilic nature of *Pf* SH1; exact causes of the break point are not understood). The nearly identical barrier at both pH values suggested the photoproduct decay occurs by an identical mechanism, in contrast to native SH1 where there was higher barrier when Ni_a^{2+}-S formation occurred because photoproduct decay was linked to proton transfer back to the active site. That is, recombination involved Ni_a^{2+}-S → Ni_a^{+}-L → Ni_a^{3+}-C when PCET occurred and only involved Ni_a^{+}-L → Ni_a^{3+}-C when PCET did not occur). It is interesting to note the photoproduct decay/hydride recombination barrier of 36 – 37 kJ/mol in E17Q is in an intermediate value between the

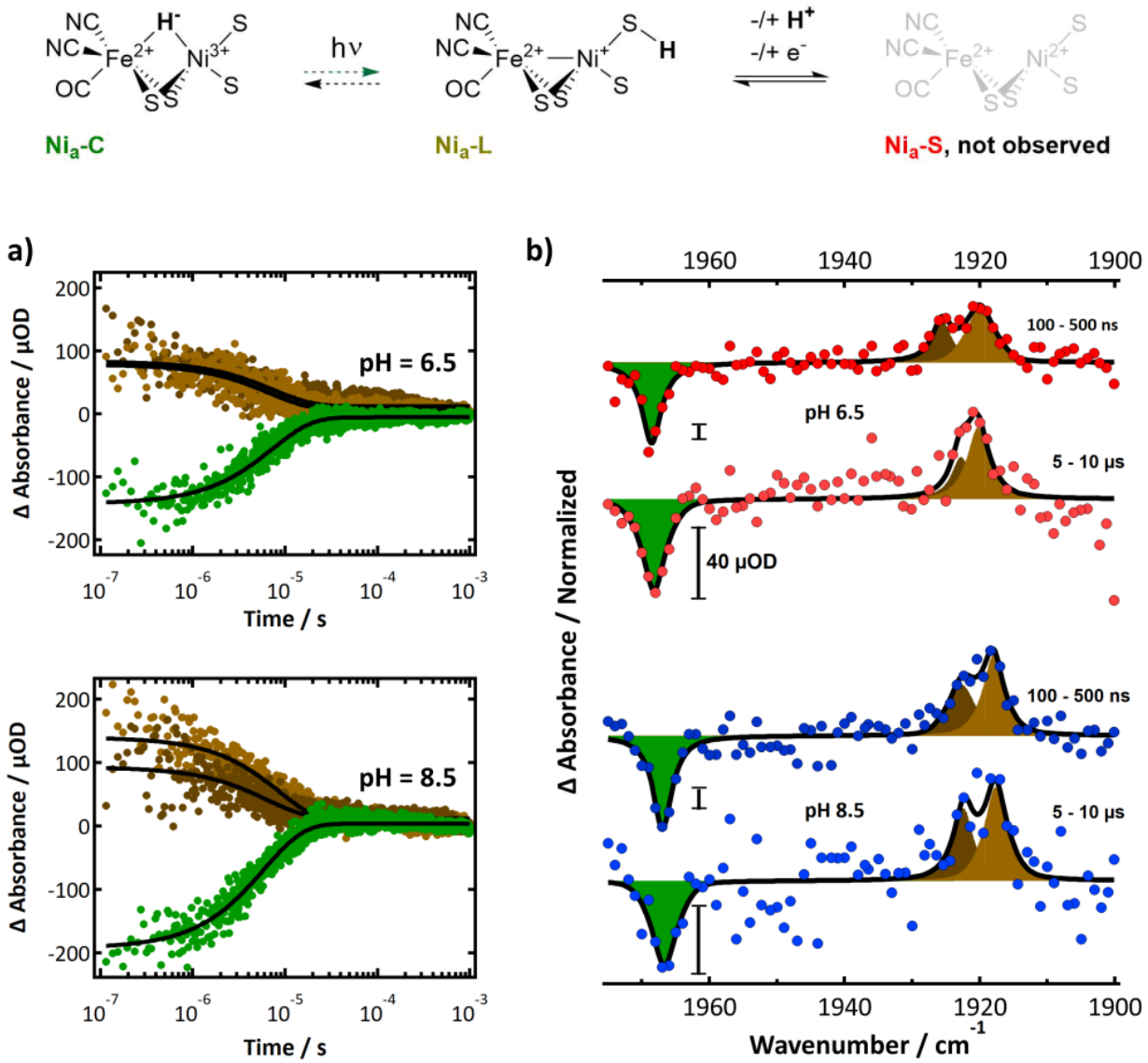

Figure 3.14: a) Kinetic traces and exponential fits from photoproduct decay and Ni_a^{3+}-C recovery after Ni_a^{3+}-C hydride photolysis at pH = 6.5 (1918, 1926, 1967 cm^{-1}) and pH = 6.5 (1918, 1923, 1967 cm^{-1}) with E17Q SH1. **b)** Plot of transient absorption amplitudes from 100 – 500 ns and 5 – 10 µs at pH = 6.5 and pH = 8.5. The Ni_a^{3+}-C bleach and induced absorbance of two photoproducts were observed, but no Ni_a^{2+}-S was detected. The top schematic summarizes the dynamics observed hydride photolysis experiments with E17Q Pf SH1.

extremes measured in native enzyme, which were ~ 32 kJ / mol when PCET did not occur and ~ 40 kJ /

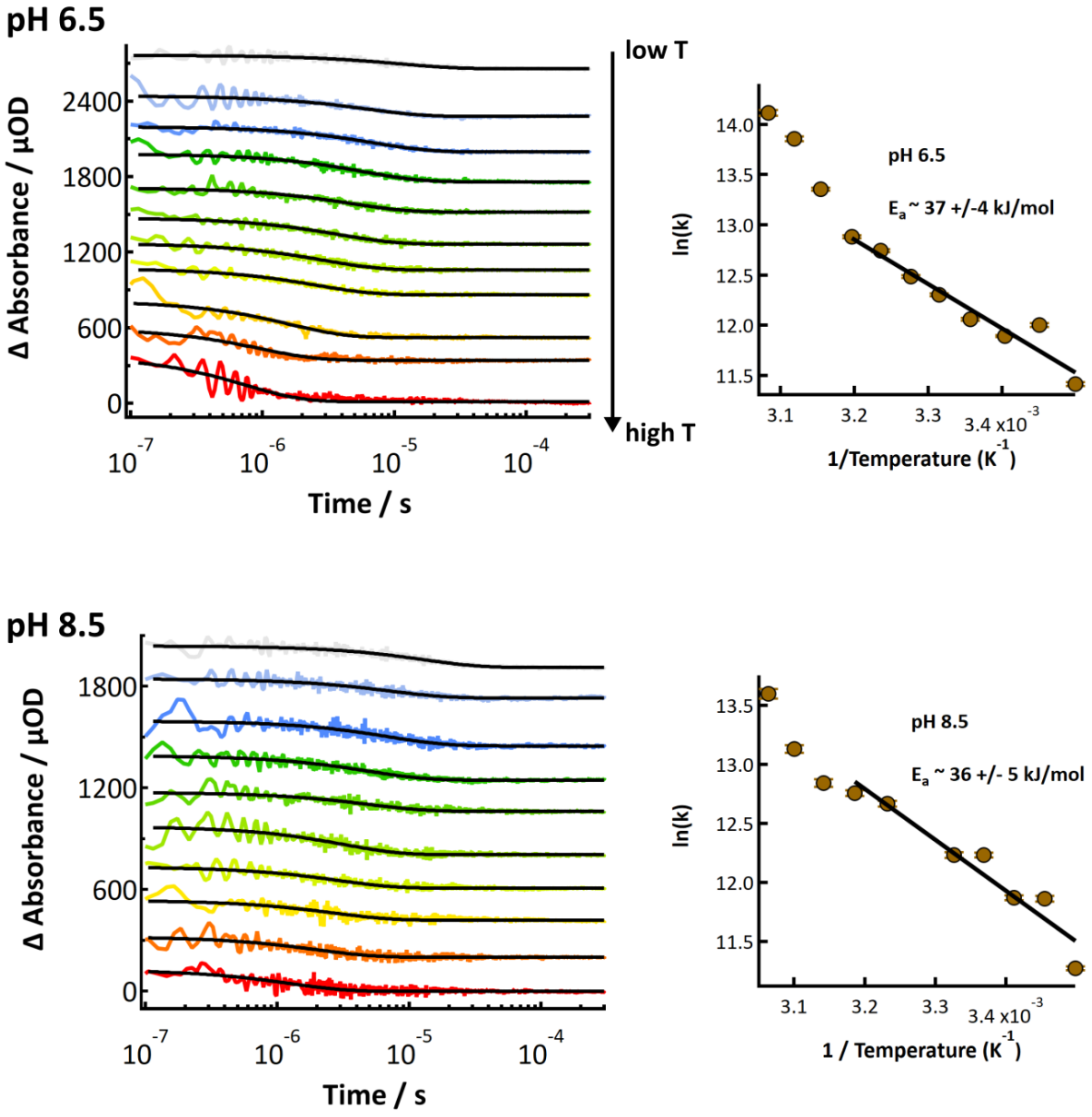

Figure 3.15: Temperature dependent kinetic traces of a Ni_a^+-L photoproduct decay (the lowest wavenumber photoproduct, ~ 1920 cm^{-1}) and corresponding Arrhenius plots fit in the linear region between ~ 12 – 40 °C. Exponential fits to the decay kinetics are shown in black. The fits to went from ~ 100 ns out to 300 µs, which is prior to baseline fluctuations caused by the water bath.

mol when PCET did occur.[22] Because we did not observe PCET, we believe the elevated value relative to 32 kJ / mol is a consequence of subtle structural/environmental differences that affect photoproduct

decay, such as the introduction of a water molecule between C418 and Q17 as observed in the E17Q variant in *Escherichia Coli* Hyd1.[81] This requires further investigation.

Overall, the evidence pointed to the process illustrated in the **Figure 3.14** schematic in which Ni_a^{3+}-C photolysis formed photoproducts (broadly termed Ni_a^{+}-L in the scheme) followed by their decay and recovery of Ni_a^{3+}-C without the formation of Ni_a^{2+}-S at pH = 6.5 where PCET should be observed. The data highly support E17 as the proton donor/acceptor during the Ni_a^{3+}-C ←→ Ni_a^{2+}-S given that the transient absorption traces in **Figure 3.14** did not resolve Ni_a^{2+}-S and the temperature dependent dynamics suggested a process of only hydride photolysis/recombination with no additional factor from proton migration back to the activate site contributing to the Ni_a^{+}-L decay. The conclusion is further supported by the recent cryogenic work with *Dv* MF,[31] which observed a change of hydrogen bonding character of E17 during the Ni_a^{2+}-C → Ni_a^{+}-L → Ni_a^{2+}-S transitions at cryogenic temperatures that included forming a hydrogen bond with C418, which also highly suggests E17 plays a role in proton movement.

We now shift our focus to the nature of the two photoproducts, both of which are seen in native and E17Q *Pf* SH1 at nearly identical locations within error of the noise of transient absorption measurements. Based on our prior assignments, we refer to the lowest wavenumber photoproduct as Ni_a^{+}-L1 (~ 1919 cm^{-1}; color coded light brown in **Figure 3.14**) and the higher wavenumber photoproduct as Ni_a^{+}-L2 (~ 1923 cm^{-1}; color coded dark brown in **Figure 3.14**).[22] Ultrafast investigations to resolve the Ni_a^{3+}-C hydride photolysis process and photoproduct formation have yet to be realized, but as mentioned before kinetic modeling of the data from native enzyme had suggested a serial formation of the photoproducts, that is: Ni_a^{3+}-C → Ni_a^{+}-L(1 or 2) → other Ni_a^{+}- L(1 or 2).[22] The remaining analysis assumes the serial mechanism, but it is important to acknowledge a parallel mechanism has not been disproved. That is, the difference between Ni_a^{+}-L1 and Ni_a^{+}-L2 could be the proton acceptor. Reasonable distinction between a probable serial versus parallel between the two mechanism regarding the photoproducts will require successful

ultrafast investigations and/or neutron scattering[82] or high resolution crystallography[36] of distinct Ni_a^+-L states.

Based on the serial mechanism model, we hypothesized the major differences between the two photoproducts was hydrogen bonding character (presumably protonated C418[31] hydrogen bonding to E17).[22] The small wavenumber difference between Ni_a^+-L1 and Ni_a^+-L2 and their relative positions to Ni_a^{3+}-C and Ni_a^{2+}-S were too small to signify proton from the active site in either state[77,83] The hydrogen bond (protonated C418, presumably with E17) would introduce electron density to the active site relative to no hydrogen bond. Thus, we assigned Ni_a^+-L1 to be the hydrogen bonded species (Cy418SH- - -OE17) and Ni_a^+-L2 to not be hydrogen bonded to E17.[22] Based on the recent cryogenic studies with *Dv* MF,[31] the hydrogen bond is probably with the carboxylate oxygen of E17.

The similar location and behavior of the photoproducts in the E17Q variant relative to native SH1 indicate the same photoproducts are observed in the variant and native enzyme. However, the crystal structure of E17Q that has been solved for the oxygen tolerant *Escherichia Coli* Hyd1 (*Ec* Hyd1) would indicate hydrogen bonding is different from in native enzyme. The structure of reduced Hyd1 variant showed the amide group pointing away from the active site to make room for a water molecule. The water molecule was not observed for the oxygen sensitive Hyd2, but Hyd2 still showed the amide group oriented away from the active site and the carboxylate group oriented toward the active site.[81] Thus, the hydrogen bond of Ni_a^+-L1 in E17Q *Pf* SH1 would probably involve the carbonyl of Q17 or a water molecule; as suggested earlier, such a difference in hydrogen bonding character versus native enzyme be a reason for the somewhat different activation barrier for hydride recombination in E17Q versus native enzyme even in the absence of PCET. **Figure 3.16** shows the proposed structures of the Ni_a^+-L states both native and E17Q *Pf* SH1 and emphasizes their tautomeric relationship with Ni_a^{3+}-C.

Hydride photolysis with E17Q indicated that under non-equilibrium perturbation conditions proton migration out of the active site (Ni_a^+-L → Ni_a^{2+}-S) occurs on timescales slower than hydride recombination

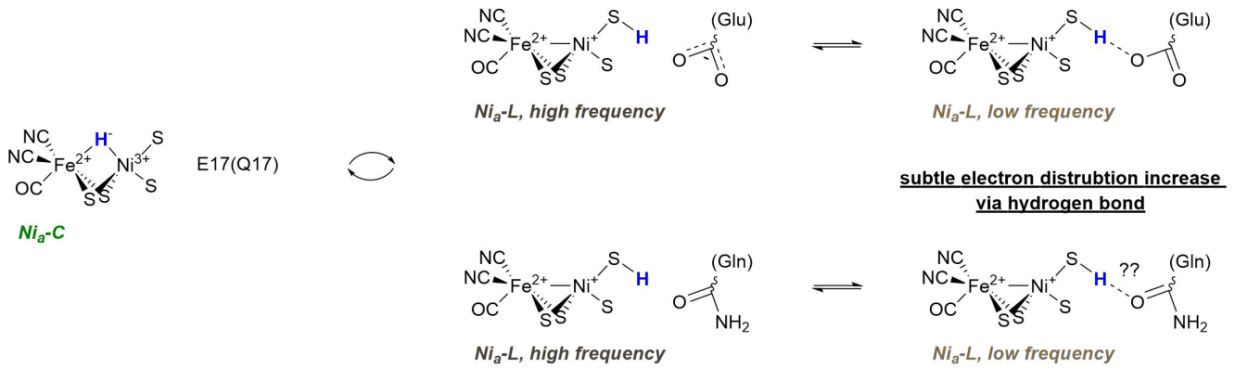

Figure 3.16: Structure of the Ni_a^+-L states in native and E17Q *Pf* SH1. As discussed in the main text, the hydrogen bonding with the low frequency state is probably different in native and E17Q enzyme. Emphasis is also placed on how the Ni_a^+-L states are also just tautomers of Ni^{3+}-C because is no overall active site protonation or electron count difference between them.

(timescale of ~ 10 μs based on the kinetic traces and fit lifetimes). But, the residual activity of E17Q and CO photolysis experiments indicated that Ni_a^{2+}-S is accessible; indeed the resting state itself must be formed at some point for turnover to occur.

In prior work from our lab, the hydride photochemistry coupled to an equilibrium perturbation allowed for the Ni_a^{2+}-S state to form and allowed an entire turnover (Ni_a^{2+}-S → Ni_a^{3+}-C → Ni_a^{2+}-SR) process to be resolved. That is, Ni_a^{3+}-C → Ni_a^{2+}-S photochemistry occurred from hydride photolysis, followed by Ni_a^{2+}-S → Ni_a^{3+}-C → Ni_a^{2+}-SR dynamics from the equilibrium perturbation.[21,23] It is unlikely photochemical reduction equilibrium perturbation would help resolve this issue with E17Q under the conditions used here because the photolysis aspect of the experiment itself does not perturb an equilibrium, and so the same hydride recombination dynamics/rates should occur (e.g. Ni_a^{2+}-S would not form from photolysis prior to the photochemical reduction dynamics). In the *Df* enzyme, the Ni_a^{2+}-S state from the E17Q variant was accessible via reactivation from more oxidized inactive states.[84] We anticipate that proper redox posing of E17Q *Pf* SH1 primarily in the Ni_a^{2+}-S state (e.g. re-oxidation from inactive states or by chemical

oxidation to poise in the enzyme in the Ni_a^{2+}-S state) should allow time-resolved equilibrium perturbation experiments[21,23] to resolve an entire turnover of E17Q and provide insight into the Ni_a^{2+}-S ←→ Ni_a^{3+}-C dynamics with the variant.

3.2.3 – Investigations of E17D *Pf* SH1: Equilibrium FTIR and FTIR Photochemical Reduction

When E17 was altered by one carbon in the E17D variant the resultant activity is ~ 4% of native enzyme for both hydrogen oxidation and proton reduction at pH = 8.5 with benzyl viologen as an electron acceptor/donor and T = 80 °C. This low residual activity significantly is different than the variants studied in *Df*[26] and *Ec* Hyd1[81] which retained 50% and 40% of activity versus the corresponding native enzyme, respectively. FTIR spectra at pH = 7.2, 7.7, and 9.0 are shown in **Figure 3.17a** as prepared under ~ 4% H_2. The major state observed at all pH values had a ν_{CO} ~ 1936 cm^{-1} (colored purple). Based on fits to non-normalized spectra the most intense CN bands were ~ 2071 and 2056 cm^{-1} (see **Appendix C**) and it is reasonable to assume they correspond to the 1936 cm^{-1} CO feature. Other major features were seen at ~ 1952 – 1953 cm^{-1} (dark blue, similar location to Ni_a^{2+}-SR and Ni_a^{2+}-S in native enzyme), 1944 (colored dark purple), and 1956 – 1958 cm^{-1} (colored teal). Additionally, small amplitudes were observed near 1919 – 1921 (colored dark yellow; less pronounced in the pH = 9.0 data and not included in that fit) and 1929 cm^{-1} (colored grey). Ni_a^{+}-L was observed in the *Ec* Hyd1 E17D variant[85] and probably in the *Df* variant,[26] and so the 1919 – 1921 cm^{-1} feature is probably Ni_a^{+}-L. Except for the ~ 1952 – 1953 cm^{-1} feature, no other states were readily assigned based on comparison to native enzyme.

An equilibrium photochemical reduction experiment at pH = 7.2 with CdS/CdSe dot-in-rod NCs and PDQ^{2+} showed the 1936 cm^{-1} feature bleach and the 1952 – 1953 cm^{-1} feature intensity increase with reducing conditions (**Figure 3.17b**). This supported the conclusion 1952 – 1953 cm^{-1} feature was Ni_a^{2+}-SR (though weak and noisy, induced absorbance features in the CN region were similar to that of native enzyme for Ni_a^{2+}-SR, see **Appendix C**; the band could always include some Ni_a^{2+}-S) and indicated the 1936

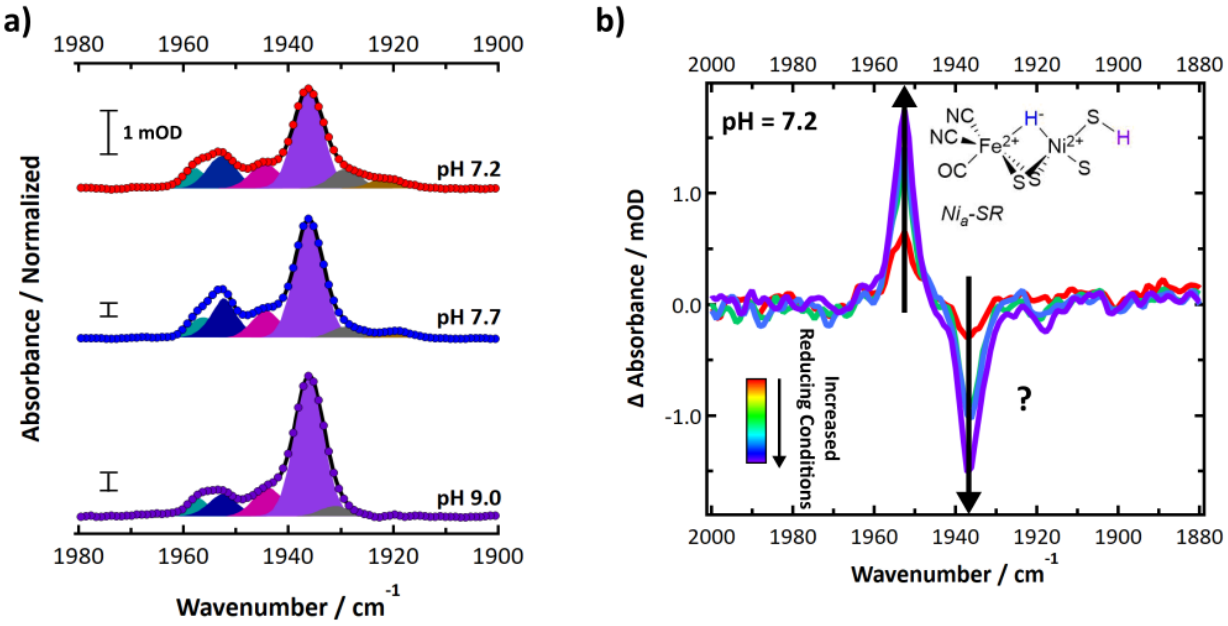

Figure 3.17: a) pH dependent FTIR spectra of E17D *Pf* SH1 at pH 7.2 (30 mM KP_i/50mM MPA), pH 7.7 (20 mM KP_i), and pH 9.0 (50 mM glycine). The corresponding fit used 4 cm^{-1} peak widths. **b)** Difference sepctra from photochemical reduction of a pH = 7.2 sample with CdS/CdSe dot-in-rods and PDQ^{2+}. The question mark indicates the nature of the state near 1936 cm^{-1} that bleaches is unclear. The induced absorbance near 1952 cm^{-1} probably corresponds to Ni_a^{2+}-SR given the amplitude of the state increases with reducing conditions, although it may also correspond to a mix of Ni_a^{2+}-SR and Ni_a^{2+}-S.

cm^{-1} band correspond to an oxidized form of the enzyme. Due to the signal-to-noise other bleaches/induced absorbances were not readily assigned, although there was a hint of a shoulder in the 1936 cm^{-1} bleach corresponding to the 1944 cm^{-1} feature.

A temperature ramp from 13 – 56 °C with the pH = 9.0 sample (auto-oxidation) provided little additional information, although it further alluded to the complicated and unclear nature of the E17D variant. **Figure 3.18a** shows select second derivative spectra and **Figure 3.18b** shows the FTIR spectra at all temperatures. As evidenced in both, there is a slight redshift of the main band near 1936 cm^{-1}. This is

further indicated in the difference spectrum of the lowest minus highest temperature indicated a bleach of a feature near 1938 cm^{-1} (**Figure 3.18c**). Spectral fits of the lowest, a medium, and the highest temperature (**Figure 3.18d**) indicated peak positions of the main band to be 1936.2 (± 0.04), 1936.0 (± 0.04), and 1935.2 (± 0.04) cm^{-1}. Based on **Figure 3.18c** and the spectral fits, the 1936 cm^{-1} probably corresponds to two highly overlapped oxidized features. Though largely speculative, it could be form(s) of blueshifted Ni_r-S states, which is believed to appear near 1931 cm^{-1} in native enzyme based off a typical ~ 35 – 40 cm^{-1} shift to lower energy relative to Ni_a^{3+}-C.[22,44]

The difference spectrum in **Figure 3.18c** also showed a shoulder feature near 1947 cm^{-1}, which is probably somewhat distorted by significant spectral overlap in this region with the 1938 cm^{-1} feature and features near 1950 cm^{-1} (in the FTIR absorbance spectra it corresponds to the 1944 cm^{-1} peak colored dark purple. Conversely, significant overlap in the FTR absorbance spectra could cause the exact location from those spectral fits to be somewhat misleading). We anticipate this shoulder consists of two components: 1) a bleach of the Ni_a^{2+}-SR state as would be expected from auto-oxidation; this probably contributes to the shoulder of the 1947 cm^{-1} shoulder marked with a grey asterisk in **Figure 3.18c** and 2) the state near ~ 1944 cm^{-1}; though speculative, this state may correspond to an inactive state that is known to be on the same redox level as Ni_a^{3+}-C[86] that appears near 1947.5 cm^{-1} in native SH1.[23]

There was also a bleach near 1923 cm^{-1} marked with a grey asterisk in **Figure 3.11c** that supposedly corresponds to Ni_a^{+}-L states. Their bleach during oxidation would not be surprising given they are mid-level redox catalytic intermediates. Interestingly, though not evident in the difference spectrum, was the growth of a feature near 1966 cm^{-1} as the temperature increased (marked with an asterisks in the **Figure 3.18a** and **Figure 3.18d**). This supposedly corresponds to Ni_a^{3+}-C. Although Ni_a^{3+}-C would not be expected to increase/appear during oxidation, there is no reason it could not necessarily if the combination of: 1) the Ni_a^{2+}-SR bleach led to some Ni_a^{3+}-C formation and 2) if the increased temperature somehow favored formation of Ni_a^{3+}-C in the Ni_a^{3+}-C ←→ Ni_a^{+}-L tautomeric equilibrium.

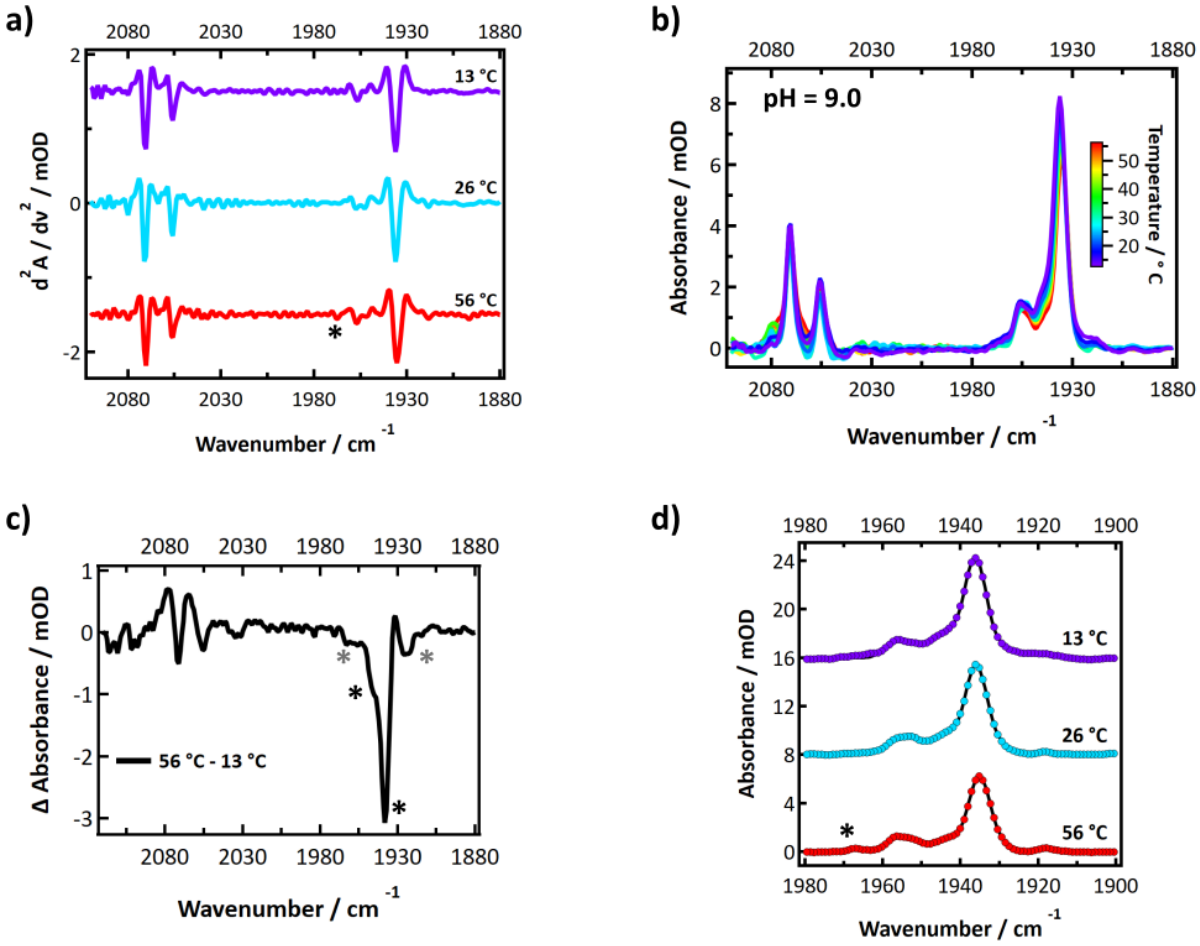

Figure 3.18: a) Selected second derivative spectra of temperature dependent E17D FTIR spectra at pH = 9.0 between 1880 – 2100 cm^{-1}. An asterisk shows a possible feature corresponding to Ni_a^{3+}-C at higher temperatures. **b)** Absorbance spectra as collected from 13 – 56 °C; the sample is identical to the one used in **Figure 3.17**. **c)** Difference spectrum of the lowest and highest temperature. Bolded asterisk mark clear features, which grey asterisk mark probable difference features based on the FITR analysis as discussed in the text. The CN region includes two probable absorbance/difference features that are severely overlapped that are probably associated 1935 and 1938 cm^{-1} CO feature (discussed in the main text) given their similar locations/overlap and the major differences in the absorbance spectra occurring in the 1935 – 1938 cm^{-1} region. **d)** Select individual absorbance spectra and spectral fits in the CO region.

We are unable to provide a good explanation or hypothesis for the CO bands near 1957 cm^{-1} and 1930 cm^{-1} based on the E17D data we have thus far obtained. Given its similar position to an inactive state in native SH1 near 1960 cm^{-1}, the 1957 cm^{-1} band might correspond to an oxidized inactive state.[23] From sheer speculation the 1930 cm^{-1} band may be another sub-state of the broader 1936 cm^{-1} peak. Clearly more data is needed for a good analysis of these peaks (and the other peaks as well).

It has been shown before that E → D mutations can have drastic effects on (metallo)enzymes,[87,88] so is it not surprising how much different the behavior of E17D is relative to native and E17Q *Pf* SH1: the extra carbon matters! The major question still remains: how does the variant change activity? Thus far, with our data and that from others,[26,81,85] there is no good answer. It also appears SH1 handles the mutation differently than the H_2ases from *Df* and *Ec* Hyd1: both of those variants had much larger residual activity (~ 40 – 50 % versus 4 % with SH1).[81] So far a crystal structure has only been solved for the as-isolated (oxidized) E17D variant from *Ec* Hyd1.[81] A comparison of the native and E17D crystal structures of as isolated Hyd1 is shown in **Figure 3.19a**.[30] Two major things are clear just upon inspection: 1) C418 is oxygenated in E17d and 2) D17 and nearby amino acids are oriented differently.[81] Not shown in the figure is a water molecule between D17 and C418 in a manner similar to the E17Q variant from Hyd1.[81] Oxygenation and thus the need for extensive reactivation that has not been accounted for with *Pf* E17D is a possible reason for the mitigated activity and/or altered spectroscopic signatures. However, oxygen inactivation/reactivation studies in native SH1 have shown a ~ 1936 – 1938 cm^{-1} CO band (as of this writing).[23] Given the Ni_a^{2+}-SR feature of E17D has similar CO and CN features, it is unlikely the inactive states have locations that are significantly different from native enzyme, although this cannot be ruled out.

More probable is that a different interaction of the aspartate vs. glutamate with the tertiary sphere (and any resultant cascade affect) cause the mitigated activity. Of the residues shown in **Figure 3.19a**, the ones labeled (other than E17/D17) are not conserved in *Pf* SH1. The isoleucine and he histidine on the

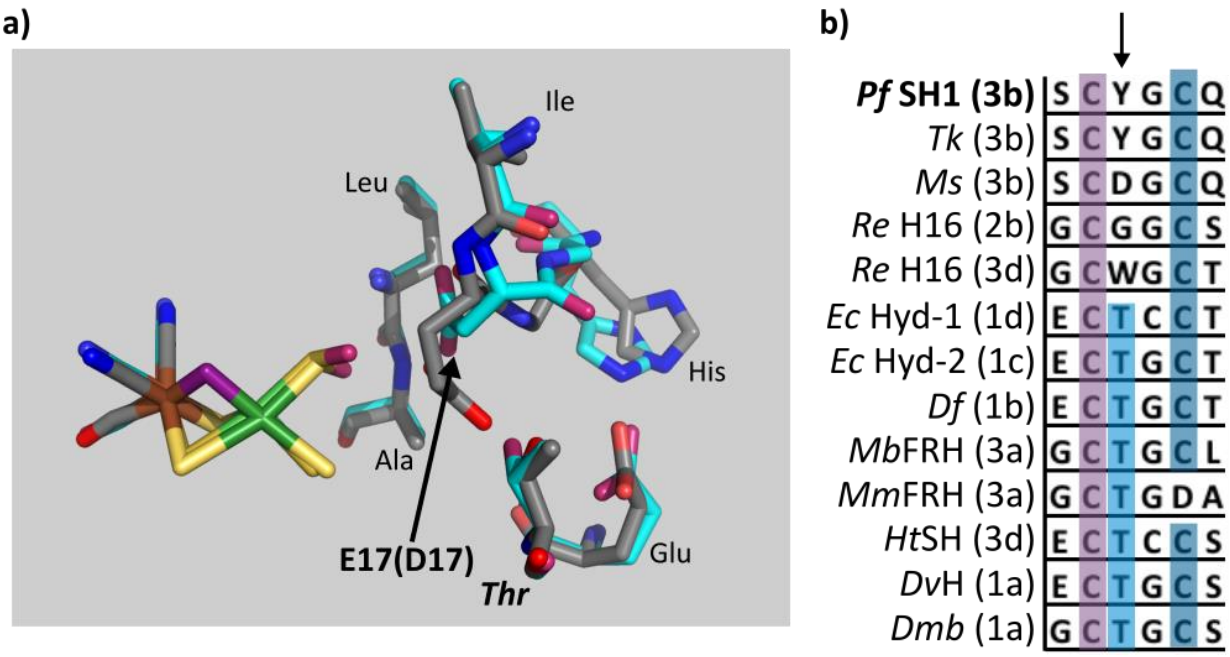

Figure 3.19: a) Overlay of native and E17D (Pf SH1 numbering) *Ec* Hyd-1. Native enzyme has grey carbons and red oxygens; E17D enzyme has blue carbons and light red oxygens. Pdb codes: 5A4M (native) and 5LRY (mutant). Amino acids (aside from E/D17) that are labeled are not conserved in *Pf* SH1. **b)** Sequence alignment near the threonine residue (bolded Thr in **a**), the arrow points to the column corresponding to the threonine.

right side of the picture are part of the L0 motif (see **Figure 3.2**; the isoleucine is not strictly conserved in general); the leucine and alanine shown on the left that interact differently overall with E28 vs. D28 are also not terribly conserved either based on large subunit sequence alignments.

In the Hyd1 E17D variant the interaction of D28 with an outer sphere threonine in **Figure 3.19a** (bold italicized label) is significantly different (if not abolished) relative to native enzyme;[81] in native Hyd1 E17 could reasonably form a hydrogen bond with the threonine, which is consistent with crystal structures from *Dv* MF[36] and *Df*.[89] The threonine is part of the gas channel converging near the nickel site[41,78] and is also known to contribute to the stabilization distinct active states via interaction with E17.[89] The threonine is generally conserved[41,89] but there are exceptions including *Pf* SH1 (**Figure 3.19b**).

Given the overall lack of conserved residues in the outer sphere beyond E17/D17, it is likely the E17D mutation in SH1 causes significantly different changes than in Hyd1, especially because the critical threonine tertiary sphere residues is naturally replaced by a tyrosine in SH1. Regardless, the E17D Hyd1 structure shows shortening the side chain E17 by one carbon has significant outer sphere conformation affects, and this probably does happen in SH1 as well. Such changes could alter 1) gas channel access, 2) observation of distinct active states, and 3) given the proximity of the tyrosine/threonine to the proximal cluster, redox properties of the proximal cluster. Gas channel access and/or alterations of the proximal cluster redox properties could explain why E17D has only 4% activity of the native enzyme and why an apparently quite oxidized state(s) near 1936 – 1938 cm^{-1} appear to dominant the FTIR spectra at all pH values under 4% H_2. However, this does not explain observation of states not seen in native SH1 (e.g. the main 1936 – 1938 cm^{-1} states). The appearance of different states is likely a consequence of how D17 interacts with the outer sphere compared to E17.

3.3 – Conclusions

There were three main purposes of this chapter: 1) to provide an overview of methods used for studying *Pf* SH1 in our laboratory relevant to this thesis, 2) to provide an introduction to native *Pf* SH1, and 3) to study the role of a highly conserved glutamate (E17) of the [NiFe]-H_2ase L0 motif via spectroscopic studies of two enzyme variants, E17Q and E17D.

Regarding native *Pf* SH1, we demonstrated the use of EPR for studying paramagnetic states as well as FTIR and FTIR coupled to equilibrium photochemical reduction for studying oxidized versus reduced states and assigning ν_{CO} peaks to distinct catalytically relevant states. We also showed how CO photolysis could be used to identify/verify the resting state of the enzyme (to which CO binds). Lastly, we also summarized our prior work on hydride photolysis to study PCET, which indicated PCET was observable in a specific pH window that was 1) low enough in pH to have a sufficient population of oxidized electron acceptors (the

electron acceptor well established to be the proximal FeS cluster) and 2) high enough in pH to have a sufficient population of deprotonated proton acceptors. In conjunction with studies from others, we had hypothesized the proton acceptor to be E17.

The most conservative mutation possible with any set of amino acids, E → Q, was our first target mutation of E17. The resultant E17Q variant had ~ 20 % of native enzyme activity and retained overall similar FTIR signatures to native SH1 (with minor blue- and redshifts). FTIR analysis coupled with CO inhibition indicated Ni_a^{2+}-SR and the enzyme resting state, Ni_a^{2+}-S, were severely overlapped. Hydride photolysis and corresponding temperature dependent dynamics indicated that unlike in the native enzyme, hydride recombination was sufficiently faster than proton migration from the active site such that we only observed the Ni_a^{3+}-C ←→ Ni_a^{+}-L(1/2) dynamics and no Ni_a^{+}-L(1/2) ←→ Ni_a^{+}-S dynamics. Based on comparison to native enzyme spectral signatures, slightly elevated hydride recombination barriers in E17Q, and analysis of the E17Q structures from *Ec* Hyd1 and Hyd2, we were able to conclude both photoproducts were essentially similar in native and E17Q, though the hydrogen bonding of the Ni_a^{+}-L1 state was probably different in E17Q, either with the carbonyl group of the glutamine side chain or perhaps a water molecule that could be positioned between C418 and Q17 (based on the Hyd1 E17Q structure). The overall results suggest that E17 is the primary proton donor/acceptor during the Ni_a^{3+}-C ←→ Ni_a^{+}-L(1/2) ←→ Ni_a^{+}-S transition and that the mitigated activity in the E17Q variant and ability to see Ni_a^{2+}-S indicate an alternative proton transfer pathway exists in the mutant (and maybe even in the native enzyme) yet to be identified.

The E → D mutation, which retains side the carboxylic acid side chain of glutamate but is one carbon shorter, resulted in significantly different behavior than native enzyme. The E17D variant in *Pf* SH1 only had 4% activity of native enzyme, drastically less than the same mutations in *Df* and *Ec* Hyd1 which had $\underline{\geq}$ 10 x the activity of the SH1 variant. The spectral signatures as analyzed by FTIR, including with photochemical reduction, indicated the active site is probably somewhat “locked” in oxidized state(s) in

the absence of a driving force for H^+ reduction supplied by an electron donor. Analysis of the E17D structure from Hyd1 indicated the mutation likely perturbs interaction of E17 with the active site and nearby residues. However, most of these residue are not conserved in SH1, which we anticipate is the reason for the low residual activity in E17D from *Pf* SH1 versus E17D in *Df* and Hyd1.

It will be interesting to observe how the infrared signatures of E17D change under different gas compositions (e.g. pure H_2, or CO or other inhibitors) and to see if time-resolved photochemical reduction or cryogenic IR photochemical reduction can show if reductive activation and/or turnover is similar or different from native enzyme, thus providing additional information about how the altered interaction of the E17(D17) position with the protein scaffold directly affects processes at the [NiFe]-core. Similarly, time-resolved IR and cryogenic IR coupled to photochemical reduction with E17Q under properly poised starting redox potentials should provide insight into how the Ni_a^2-S → Ni_a^{3+}-C dynamics are facilitated in the variant, including if a water molecule is a probable donor/acceptor (in accord with the rescue mechanism proposed in *Ec* Hyd1[81]), if the carbonyl group of Q28 is the donor/acceptor, or if proton transfer has changed to a different path altogether.

Together, the E17Q and E17D mutation provide experimental evidence in *Pf* SH1 that the proton donor/acceptor E17 side chain length and side chain functionality are tuned for efficient turnover, probably through fine-tuning of the residue's interaction with both the active site and the outer coordination sphere.

3.4 – References

(1) Armstrong, F. A.; Hirst, J. Reversibility and efficiency in electrocatalytic energy conversion and lessons from enzymes. *Proc. Natl. Acad. Sci. U. S. A.* **2011**, *108*, 14049-14054.

(2) Rees, D. C. Great metalloclusters in enzymology. *Annu. Rev. Biochem.* **2002**, *71*, 221-246.

(3) Vallee, B. L.; Williams, R. J. Metalloenzymes: the entatic nature of their active sites. *Proc. Nat. Acad. Sci. U. S. A.* **1968**, *59*, 498-505.

(4) Wodrich, M. D.; Hu, X. Natural inspirations for metal–ligand cooperative catalysis. *Nat. Rev. Chem.* **2017**, *2*, 0099.

(5) Hemschemeier, A.; Happe, T. The plasticity of redox cofactors: from metalloenzymes to redox-active DNA. *Nat. Rev. Chem.* **2018**, *2*, 231-243.

(6) MacBeth, C. E.; Golombek, A. P.; Young, V. G.; Yang, C.; Kuczera, K.; Hendrich, M. P.; Borovik, A. S. O_2 activation by nonheme iron complexes: A monomeric Fe(III)-oxo complex derived from O_2. *Science* **2000**, *289*, 938.

(7) Reback, M. L.; Ginovska, B.; Buchko, G. W.; Dutta, A.; Priyadarshani, N.; Kier, B. L.; Helm, M. L.; Raugei, S.; Shaw, W. J. Investigating the role of chain and linker length on the catalytic activity of an H_2 production catalyst containing a β-hairpin peptide. *J. Coord. Chem.* **2016**, *69*, 1730-1747.

(8) Geri, J. B.; Shanahan, J. P.; Szymczak, N. K. Testing the push–pull hypothesis: Lewis acid augmented N_2 activation at iron. *J. Am. Chem. Soc.* **2017**, *139*, 5952-5956.

(9) Nichols, E. M.; Derrick, J. S.; Nistanaki, S. K.; Smith, P. T.; Chang, C. J. Positional effects of second-sphere amide pendants on electrochemical CO_2 reduction catalyzed by iron porphyrins. *Chem. Sci.* **2018**, *9*, 2952-2960.

(10) Laureanti, J. A.; O'Hagan, M.; Shaw, W. J. Chicken fat for catalysis: a scaffold is as important for molecular complexes for energy transformations as it is for enzymes in catalytic function. *Sustain. Energy Fuels* **2019**, *3*, 3260-3278.

(11) Yikilmaz, E.; Porta, J.; Grove, L. E.; Vahedi-Faridi, A.; Bronshteyn, Y.; Brunold, T. C.; Borgstahl, G. E. O.; Miller, A.-F. How can a single second sphere amino acid substitution cause reduction midpoint potential changes of hundreds of millivolts? *J. Am. Chem. Soc.* **2007**, *129*, 9927-9940.

(12) Stachura, M.; Chakraborty, S.; Gottberg, A.; Ruckthong, L.; Pecoraro, V. L.; Hemmingsen, L. Direct observation of nanosecond water exchange dynamics at a protein metal site. *J. Am. Chem. Soc.* **2017**, *139*, 79-82.

(13) Ma, K.; Adams, M. W. W.: Hydrogenases I and II from *Pyrococcus furiosus*. In *Method Enzymol.*; Academic Press, 2001; Vol. 331; pp 208-216.

(14) Bryant, F. O.; Adams, M. W. Characterization of hydrogenase from the hyperthermophilic archaebacterium, *Pyrococcus furiosus*. *J. Biol. Chem.* **1989**, *264*, 5070-5079.

(15) Greening, C.; Biswas, A.; Carere, C. R.; Jackson, C. J.; Taylor, M. C.; Stott, M. B.; Cook, G. M.; Morales, S. E. Genomic and metagenomic surveys of hydrogenase distribution indicate H_2 is a widely utilised energy source for microbial growth and survival. *ISME J.* **2016**, *10*, 761-777.

(16) Ma, K.; Zhou, Z. H.; Adams, M. W. W. Hydrogen production from pyruvate by enzymes purified from the hyperthermophilic archaeon, *Pyrococcus furiosus*: A key role for NADPH. *FEMS Microbiol. Lett.* **1994**, *122*, 245-250.

(17) van Haaster, D. J.; Silva, P. J.; Hagedoorn, P.-L.; Jongejan, J. A.; Hagen, W. R. Reinvestigation of the steady-state kinetics and physiological function of the soluble NiFe-hydrogenase I of *Pyrococcus furiosus*. *J. Bacteriol.* **2008**, *190*, 1584-1587.

(18) Vignais, P. M.; Billoud, B.; Meyer, J. Classification and phylogeny of hydrogenases. *FEMS Microbiol. Rev.* **2001**, *25*, 455-501.

(19) Silva, P. J.; De Castro, B.; Hagen, W. R. On the prosthetic groups of the NiFe sulfhydrogenase from *Pyrococcus furiosus*: topology, structure, and temperature-dependent redox chemistry. *J. Biol. Inorg. Chem.* **1999**, *4*, 284-291.

(20) Wang, H.; Ralston, C. Y.; Patil, D. S.; Jones, R. M.; Gu, W.; Verhagen, M.; Adams, M.; Ge, P.; Riordan, C.; Marganian, C. A.; Mascharak, P.; Kovacs, J.; Miller, C. G.; Collins, T. J.; Brooker, S.; Croucher, P. D.; Wang, K.; Steifel, E. I.; Cramer, S. P. Nickel L-edge soft x-ray spectroscopy of nickel-iron hydrogenases

and model compounds-evidence for high-spin nickel(II) in the active enzyme. *J. Am. Chem. Soc.* **2000**, *122*, 10544-10552.

(21) Greene, B. L.; Wu, C.-H.; McTernan, P. M.; Adams, M. W.; Dyer, R. B. Proton-coupled electron transfer dynamics in the catalytic mechanism of a [NiFe]-hydrogenase. *J. Am. Chem. Soc.* **2015**, *137*, 4558-4566.

(22) Greene, B. L.; Wu, C.-H.; Vansuch, G. E.; Adams, M. W.; Dyer, R. B. Proton inventory and dynamics in the Nia-S to Nia-C transition of a [NiFe] hydrogenase. *Biochemistry* **2016**, *55*, 1813-1825.

(23) Chica, B. C. Semiconductor nanoparticle-protein hybrid systems for solar hydrogen production and photo-triggered mechanistic studies. Ph.D. Thesis, Emory University, 2017.

(24) Massanz, C.; Friedrich, B. Amino acid replacements at the H2-activating site of the NAD-reducing hydrogenase from *Alcaligenes eutrophus*. *Biochemistry* **1999**, *38*, 14330-14337.

(25) Burgdorf, T.; De Lacey, A. L.; Friedrich, B. Functional analysis by site-directed mutagenesis of the NAD^+-reducing hydrogenase from *Ralstonia eutropha*. *J. Bacteriol.* **2002**, *184*, 6280-6288.

(26) Dementin, S.; Burlat, B.; De Lacey, A. L.; Pardo, A.; Adryanczyk-Perrier, G.; Guigliarelli, B.; Fernandez, V. M.; Rousset, M. A glutamate is the essential proton transfer gate during the catalytic cycle of the [NiFe] hydrogenase. *J. Biol. Chem.* **2004**, *279*, 10508-10513.

(27) Gebler, A.; Burgdorf, T.; De Lacey, A. L.; Rüdiger, O.; Martinez-Arias, A.; Lenz, O.; Friedrich, B. Impact of alterations near the [NiFe] active site on the function of the H_2 sensor from *Ralstonia eutropha*. *FEBS J.* **2007**, *274*, 74-85.

(28) Szőri-Dorogházi, E.; Maróti, G.; Szőri, M.; Nyilasi, A.; Rákhely, G.; Kovács, K. L. Analyses of the large subunit histidine-rich motif expose an alternative proton transfer pathway in [NiFe] hydrogenases. *PLoS One* **2012**, *7*, e34666.

(29) Bioinformatics Research Centre. https://services.birc.au.dk/hyddb/browser/ (accessed May 2020).

(30) The PyMOL Molecular Graphics System, version 1.3, Schrödinger, LLC: New York 2010.

(31) Tai, H.; Nishikawa, K.; Higuchi, Y.; Mao, Z.-w.; Hirota, S. Cysteine SH and glutamate COOH contributions to [NiFe] hydrogenase proton transfer revealed by highly sensitive FTIR spectroscopy. *Angew. Chem., Int. Ed.* **2019**, *131*, 13419-13424.

(32) Siebert, E.; Horch, M.; Rippers, Y.; Fritsch, J.; Frielingsdorf, S.; Lenz, O.; Velazquez Escobar, F.; Siebert, F.; Paasche, L.; Kuhlmann, U.; Lendzian, F.; Mroginski, M.-A.; Zebger, I.; Hildebrandt, P. Resonance raman spectroscopy as a tool to monitor the active site of hydrogenases. *Angew. Chem., Int. Ed.* **2013**, *52*, 5162-5165.

(33) Kampa, M.; Pandelia, M.-E.; Lubitz, W.; van Gastel, M.; Neese, F. A metal–metal bond in the light-induced state of [NiFe] hydrogenases with relevance to hydrogen evolution. *J. Am. Chem. Soc.* **2013**, *135*, 3915-3925.

(34) Siegbahn, P. E. M. Proton and electron transfers in [NiFe] hydrogenase. *Adv. Inorg. Chem.* **2004**, *56*, 101-125.

(35) Dong, G.; Ryde, U. Protonation states of intermediates in the reaction mechanism of [NiFe] hydrogenase studied by computational methods. *J. Biol. Inorg. Chem.* **2016**, *21*, 383-394.

(36) Ogata, H.; Nishikawa, K.; Lubitz, W. Hydrogens detected by subatomic resolution protein crystallography in a [NiFe] hydrogenase. *Nature* **2015**, *520*, 571-574.

(37) Ogata, H.; Krämer, T.; Wang, H.; Schilter, D.; Pelmenschikov, V.; van Gastel, M.; Neese, F.; Rauchfuss, T. B.; Gee, L. B.; Scott, A. D.; Yoda, Y.; Tanaka, Y.; Lubitz, W.; Cramer, S. P. Hydride bridge in [NiFe]-hydrogenase observed by nuclear resonance vibrational spectroscopy. *Nat. Commun.* **2015**, *6*, 7890.

(38) Smith, D. M. A.; Raugei, S.; Squier, T. C. Modulation of active site electronic structure by the protein matrix to control [NiFe] hydrogenase reactivity. *Phys. Chem. Chem. Phys.* **2014**, *16*, 24026-24033.

(39) Matias, P. M.; Soares, C. M.; Saraiva, L. M.; Coelho, R.; Morais, J.; Le Gall, J.; Carrondo, M. A. [NiFe] hydrogenase from *Desulfovibrio desulfuricans* ATCC 27774: gene sequencing, three-dimensional structure determination and refinement at 1.8 Å and modelling studies of its interaction with the tetrahaem cytochrome c3. *J. Biol. Inorg. Chem.* **2001**, *6*, 63-81.

(40) Volbeda, A.; Charon, M.-H.; Piras, C.; Hatchikian, E. C.; Frey, M.; Fontecilla-Camps, J. C. Crystal structure of the nickel-iron hydrogenase from *Desulfovibrio gigas*. *Nature* **1995**, *373*, 580-587.

(41) Fontecilla-Camps, J. C.; Volbeda, A.; Cavazza, C.; Nicolet, Y. Stucture/Function relationships of [NiFe]- and [FeFe]-hydrogenases *Chem. Rev.* **2007**, *107*, 4273-4303.

(42) Teixeira, V. H.; Soares, C. M.; Baptista, A. M. Proton pathways in a [NiFe]-hydrogenase: a theoretical study. *Proteins: Struct., Funct., Bioinf.* **2008**, *70*, 1010-1022.

(43) Sumner, I.; Voth, G. A. Proton transport pathways in [NiFe]-hydrogenase. *J. Phys. Chem. B* **2012**, *116*, 2917-2926.

(44) Lubitz, W.; Ogata, H.; Rüdiger, O.; Reijerse, E. Hydrogenases. *Chem. Rev.* **2014**, *114*, 4081-4148.

(45) Pierik, A. J.; Roseboom, W.; Happe, R. P.; Bagley, K. A.; Albracht, S. P. J. Carbon monoxide and cyanide as intrinsic ligands to iron in the active site of [NiFe]-hydrogenases. NiFe(CN)2CO, biology's way to activate H2. *J. Biol. Chem.* **1999**, *274*, 3331-3337.

(46) Cotton, F. A.; Wilkinson, G.: *Advanced Inorganic Chemistry*; 5th ed.; John Wiley & Sons, Inc: New York, New York, 1988. pp. 1021 - 1051.

(47) Darensbourg, M. Y.; Lyon, E. J.; Smee, J. J. The bio-organometallic chemistry of active site iron in hydrogenases. *Coord. Chem. Rev.* **2000**, *206-207*, 533-561.

(48) Chica, B.; Wu, C.-H.; Liu, Y.; Adams, M. W. W.; Lian, T.; Dyer, R. B. Balancing electron transfer rate and driving force for efficient photocatalytic hydrogen production in CdSe/CdS nanorod–[NiFe] hydrogenase assemblies. *Energy Environ. Sci.* **2017**, *10*, 2245-2255.

(49) Homer, R. F.; Tomlinson, T. E. Stereochemistry of the bridged quaternary salts of 2,2'-bipyridyl. *J. Chem. Soc.* **1960**, 2498-2503.

(50) El-Sayed, M. A. Small Is different: Shape-, size-, and composition-dependent properties of some colloidal semiconductor nanocrystals. *Acc. Chem. Res.* **2004**, *37*, 326-333.

(51) Zhu, H.; Song, N.; Lv, H.; Hill, C. L.; Lian, T. Near unity quantum yield of light-driven redox mediator reduction and efficient H_2 generation using colloidal nanorod heterostructures. *J. Am. Chem. Soc.* **2012**, *134*, 11701-11708.

(52) de Lacey, A. L.; Hatchikian, E. C.; Volbeda, A.; Frey, M.; Fontecilla-Camps, J. C.; Fernandez, V. M. Infrared-spectroelectrochemical characterization of the [NiFe] hydrogenase of *Desulfovibrio gigas*. *J. Am. Chem. Soc.* **1997**, *119*, 7181-7189.

(53) Bleijlevens, B.; Broekhuizen, F. A.; De Lacey, A. L.; Roseboom, W.; Fernandez, V. M.; Albracht, S. P. J. The activation of the [NiFe]-hydrogenase from *Allochromatium vinosum*. An infrared spectro-electrochemical study. *J. Biol. Inorg. Chem.* **2004**, *9*, 743-752.

(54) Fichtner, C.; Laurich, C.; Bothe, E.; Lubitz, W. Spectroelectrochemical Characterization of the [NiFe] Hydrogenase of Desulfovibrio vulgaris Miyazaki F. *Biochemistry* **2006**, *45*, 9706-9716.

(55) Greene, B. L.; Joseph, C. A.; Maroney, M. J.; Dyer, R. B. Direct evidence of active-aite reduction and photodriven catalysis in sensitized hydrogenase assemblies. *J. Am. Chem. Soc.* **2012**, *134*, 11108-11111.

(56) Ogata, H.; Mizoguchi, Y.; Mizuno, N.; Miki, K.; Adachi, S.-i.; Yasuoka, N.; Yagi, T.; Yamauchi, O.; Hirota, S.; Higuchi, Y. Structural studies of the carbon monoxide complex of [NiFe]hydrogenase from *Desulfovibrio vulgaris* Miyazaki F: Suggestion for the initial activation site for dihydrogen. *J. Am. Chem. Soc.* **2002**, *124*, 11628-11635.

(57) Ilina, Y.; Lorent, C.; Katz, S.; Jeoung, J.-H.; Shima, S.; Horch, M.; Zebger, I.; Dobbek, H. X-ray crystallography and vibrational spectroscopy reveal the key determinants of biocatalytic dihydrogen cycling by [NiFe] hydrogenases. *Angew. Chem., Int. Ed.* **2019**, *58*, 18710-18714.

(58) Bagley, K. A.; Van Garderen, C. J.; Chen, M.; Woodruff, W. H.; Duin, E. C.; Albracht, S. P. J. Infrared studies on the interaction of carbon monoxide with divalent nickel in hydrogenase from *Chromatium vinosum*. *Biochemistry* **1994**, *33*, 9229-9236.

(59) Pandelia, M.-E.; Ogata, H.; Currell, L. J.; Flores, M.; Lubitz, W. Inhibition of the [NiFe] hydrogenase from *Desulfovibrio vulgaris* Miyazaki F by carbon monoxide: an FTIR and EPR spectroscopic study. *Biochim. Biophys. Acta, Bioenerg.* **2010**, *1797*, 304-313.

(60) Pandelia, M.-E.; Infossi, P.; Giudici-Orticoni, M. T.; Lubitz, W. The oxygen-tolerant hydrogenase I from *Aquifex aeolicus* weakly interacts with carbon monoxide: An electrochemical and time-resolved FTIR study. *Biochemistry* **2010**, *49*, 8873-8881.

(61) Sweeney, W. V.; Rabinowitz, J. C. Proteins containing 4Fe-4S clusters: an overview. *Annu. Rev. Biochem.* **1980**, *49*, 139-161.

(62) Ghisla, S.; Massey, V.; Lhoste, J.-M.; Mayhew, S. G. Fluorescence and optical characteristics of reduced flavines and flavoproteins. *Biochemistry* **1974**, *13*, 589-597.

(63) Mirmohades, M.; Adamska-Venkatesh, A.; Sommer, C.; Reijerse, E.; Lomoth, R.; Lubitz, W.; Hammarström, L. Following [FeFe] hydrogenase active site intermediates by time-resolved mid-IR spectroscopy. *J. Phys. Chem. Lett.* **2016**, 3290-3293.

(64) Anfinrud, P. A.; Han, C.; Hochstrasser, R. M. Direct observations of ligand dynamics in hemoglobin by subpicosecond infrared spectroscopy. *Proc. Natl. Acad. Sci. U. S. A.* **1989**, *86*, 8387.

(65) Causgrove, T. P.; Dyer, R. B. Picosecond structural dynamics of myoglobin following photolysis of carbon monoxide. *J. Phys. Chem.* **1996**, *100*, 3273-3277.

(66) Causgrove, T. P.; Dyer, R. B. Protein response to photodissociation of CO from carbonmonoxymyoglobin probed by time-resolved infrared spectroscopy of the amide I band. *Biochemistry* **1993**, *32*, 11985-11991.

(67) Barondeau, D. P.; Roberts, L. M.; Lindahl, P. A. Stability of the Ni-C state and oxidative titrations of *Desulfovibrio gigas* hydrogenase monitored by EPR and electronic absorption spectroscopies. *J. Am. Chem. Soc.* **1994**, *116*, 3442-3448.

(68) Fichtner, C.; Van Gastel, M.; Lubitz, W. Wavelength dependence of the photo-induced conversion of the Ni-C to the Ni-L redox state in the [NiFe] hydrogenase of Desulfovibrio vulgaris Miyazaki F. *Phys. Chem. Chem. Phys.* **2003**, *5*, 5507-5513.

(69) De Lacey, A. L.; Stadler, C.; Fernandez, V. M.; Hatchikian, E. C.; Fan, H.-J.; Li, S.; Hall, M. B. IR spectroelectrochemical study of the binding of carbon monoxide to the active site of *Desulfovibrio fructosovorans* Ni-Fe hydrogenase. *J. Biol. Inorg. Chem.* **2002**, *7*, 318-326.

(70) Fan, C.; Teixeira, M.; Moura, J.; Moura, I.; Huynh, B. H.; Le Gall, J.; Peck, H. D., Jr.; Hoffman, B. M. Detection and characterization of exchangeable protons bound to the hydrogen-activation nickel site of Desulfovibrio gigas hydrogenase: a proton and deuterium Q-band ENDOR study. *J. Am. Chem. Soc.* **1991**, *113*, 20-24.

(71) Brecht, M.; Gastel, M. v.; Buhrke, T.; Barbel, F.; Lubitz, W. Direct detection of a hydrogen ligand in the [NiFe] center of the regulatory H_2 sensing hydrogenase from *Ralstonia eutropha* in its reduced state by HYSCORE and ENDOR spectroscopy. *J. Am. Chem. Soc.* **2003**, *125*, 13075-13083.

(72) Kellers, P.; Pandelia, M.-E.; Currell, L. J.; Goerner, H.; Lubitz, W. FTIR study on the light sensitivity of the [NiFe] hydrogenase from Desulfovibrio vulgaris Miyazaki F: Ni-C to Ni-L photoconversion, kinetics of proton rebinding and H/D isotope effect. *Phys. Chem. Chem. Phys.* **2009**, *11*, 8680-8683.

(73) Van der Zwaan, J. W.; Albracht, S. P. J.; Fontijn, R. D.; Slater, E. C. Monovalent nickel in hydrogenase from *Chromatium vinosum*. Light sensitivity and evidence for direct interaction with hydrogen. *FEBS Lett.* **1985**, *179*, 271-277.

(74) Bagley, K. A.; Duin, E. C.; Roseboom, W.; Albracht, S. P. J.; Woodruff, W. H. Infrared-detectable group senses changes in charge density on the nickel denter in hydrogenase from *Chromatium vinosum*. *Biochemistry* **1995**, *34*, 5527-5535.

(75) Tai, H.; Nishikawa, K.; Suzuki, M.; Higuchi, Y.; Hirota, S. Control of the transition between Ni-C and Ni-Sla states by the redox state of the proximal FeS cluster in the catalytic cycle of [NiFe] hydrogenase. *Angew. Chem., Int. Ed.* **2014**, *53*, 13817-13820.

(76) Foerster, S.; Stein, M.; Brecht, M.; Ogata, H.; Higuchi, Y.; Lubitz, W. Single crystal EPR studies of the reduced active site of [NiFe] hydrogenase from Desulfovibrio vulgaris Miyazaki F. *J. Am. Chem. Soc.* **2003**, *125*, 83-93.

(77) Pardo, A.; De Lacey, A. L.; Fernández, V. M.; Fan, H.-J.; Fan, Y.; Hall, M. B. Density functional study of the catalytic cycle of nickel-iron [NiFe] hydrogenases and the involvement of high-spin nickel(II). *J. Biol. Inorg. Chem.* **2006**, *11*, 286-306.

(78) Volbeda, A.; Montet, Y.; Vernède, X.; Hatchikian, E. C.; Fontecilla-Camps, J. C. High-resolution crystallographic analysis of Desulfovibrio fructosovorans [NiFe] hydrogenase. *Int. J. Hydrog. Energy* **2002**, *27*, 1449-1461.

(79) Duan, J.; Mebs, S.; Laun, K.; Wittkamp, F.; Heberle, J.; Happe, T.; Hofmann, E.; Apfel, U.-P.; Winkler, M.; Senger, M.; Haumann, M.; Stripp, S. T. Geometry of the catalytic active site in [FeFe]-hydrogenase is determined by hydrogen bonding and proton transfer. *ACS Catal.* **2019**, *9*, 9140-9149.

(80) Isom, D. G.; Castañeda, C. A.; Cannon, B. R.; Velu, P. D.; García-Moreno E, B. Charges in the hydrophobic interior of proteins. *Proc. Nat. Acad. Sci. U. S. A.* **2010**, *107*, 16096-16100.

(81) Evans, R. M.; Ash, P. A.; Beaton, S. E.; Brooke, E. J.; Vincent, K. A.; Carr, S. B.; Armstrong, F. A. Mechanistic Exploitation of a Self-Repairing, Blocked Proton Transfer Pathway in an O_2-Tolerant [NiFe]-Hydrogenase. *J. Am. Chem. Soc.* **2018**, *140*, 10208-10220.

(82) Kwon, H.; Basran, J.; Devos, J. M.; Suardíaz, R.; van der Kamp, M. W.; Mulholland, A. J.; Schrader, T. E.; Ostermann, A.; Blakeley, M. P.; Moody, P. C. E.; Raven, E. L. Visualizing the protons in a metalloenzyme electron proton transfer pathway. *Proc. Nat. Acad. Sci. U. S. A.* **2020**, *117*, 6484.

(83) Tai, H.; Nishikawa, K.; Inoue, S.; Higuchi, Y.; Hirota, S. FT-IR characterization of the light-induced Ni-L2 and Ni-L3 states of [NiFe] hydrogenase from *Desulfovibrio vulgaris* Miyazaki F. *J. Phys. Chem. B* **2015**, *119*, 13668-13674.

(84) De Lacey, A. L.; Pardo, A.; Fernández, V. M.; Dementin, S.; Adryanczyk-Perrier, G.; Hatchikian, E. C.; Rousset, M. FTIR spectroelectrochemical study of the activation and inactivation processes of [NiFe] hydrogenases: effects of solvent isotope replacement and site-directed mutagenesis. *J. Biol. Inorg. Chem.* **2004**, *9*, 636-642.

(85) Brooke, E. J. Exploration of proton transfer pathways in the oxygen-tolerant [NiFe]-hydrogenase from *Escherichia coli*. Master of Science by Research, University of Oxford, 2017.

(86) Kwan, P.; McIntosh, C. L.; Jennings, D. P.; Hopkins, R. C.; Chandrayan, S. K.; Wu, C.-H.; Adams, M. W.; Jones, A. K. The [NiFe]-hydrogenase of *Pyrococcus furiosus* exhibits a new type of oxygen tolerance. *J. Am. Chem. Soc.* **2015**, *137*, 13556-13565.

(87) Puustinen, A.; Bailey, J. A.; Dyer, R. B.; Mecklenburg, S. L.; Wikstrom, M.; Woodruff, W. H. Fourier transform infrared evidence for connectivity between CuB and glutamic acid 286 in cytochrome bo3 from Escherichia coli. *Biochemistry* **1997**, *36*, 13195-13200.

(88) Pankhurst, K. L.; Mowat, C. G.; Rothery, E. L.; Hudson, J. M.; Jones, A. K.; Miles, C. S.; Walkinshaw, M. D.; Armstrong, F. A.; Reid, G. A.; Chapman, S. K. A proton delivery pathway in the soluble fumarate reductase from *Shewanella frigidimarina*. *J. Biol. Chem.* **2006**, *281*, 20589-20597.

(89) Abou-Hamdan, A.; Ceccaldi, P.; Lebrette, H.; Gutierrez-Sanz, O.; Richaud, P.; Cournac, L.; Guigliarelli, B.; De Lacey, A. L.; Leger, C.; Volbeda, A.; Burlat, B.; Dementin, S. A threonine stabilizes the NiC and NiR catalytic intermediates of [NiFe]-hydrogenase. *J. Biol. Chem.* **2015**, *290*, 8550-8558.

Chapter 4 – Investigating the R355K Variant

Aspects of this chapter have been reprinted with permission from Vansuch, G. E.; Wu, C.-H.; Haja, D. K.; Blair, S. A.; Chica, B.; Johnson, M. K.; Adams, M. W. W.; Dyer, R. B., *Chem. Sci.* **2020,** *11* (32), 8572-8581. Published by the Royal Society of Chemistry.

Abstract

Facile bond making/breaking and transient stabilization of seemingly high energy intermediates are essential components of bioinorganic enzymes. Achieving the efficiencies and rates of bioinorganic enzymes in artificial systems requires understanding enzyme design principles. Our laboratory focuses on understanding the movement of protons/hydrides, electrons, and hydrogen in the [NiFe]-hydrogenases because all or almost all of these substrates/products are broadly relevant to energy conversion catalysts. In this enzyme, a highly conserved arginine residue (R355) is directly above exogenous ligand binding position of the [NiFe]-catalytic core and is essential for optimal function because mutation to a lysine results in lower catalytic rates. To expand on our studies of soluble hydrogenase-1 from *Pyrococcus furiosus* (*Pf* SH1), we investigated the role of R355 by site-directed-mutagenesis to a lysine (R355K) using infrared and electron paramagnetic resonance spectroscopic probes sensitive to active site redox and protonation events. It was found the mutation resulted in an altered ligand binding environment at the [NiFe] centre. A key observation was destabilization of the Ni_a^{3+}-C state, which contains a bridging hydride. Instead the tautomeric Ni_a^{+}-L states were observed. Overall, the results provided insight into complex metal-ligand cooperativity between the active site protein scaffold regarding the protons/hydrides, notably via electrostatics, which would prove valuable to design principles for efficient bioinspired catalysts.

4.1 – Introduction

Sustainable energy conversion with heterogeneous or homogenous small molecule inorganic catalysts necessitates forming/activating stable small molecules which requires, at a minimum, multi-electron and/or multi-proton processes and the stabilization of otherwise high energy intermediates. To do so with large rates *and* low overpotentials is not easy to achieve. The metal center (active site) is also not the only important component for catalysis: the secondary sphere, outer sphere, and/or solvent environment have

critical roles.[1-7] One subfield of (bio)inorganic energy conversion research focuses on understanding how metalloenzymes are optimally, or near optimally, engineered for the activation and formation of small molecules[8,9] because such information should help develop efficient energy conversion catalysts.

One of the simplest enzymatic reactions is $H_2 \leftrightarrow 2H^+ + 2e^-$ as carried out by the nickel and iron containing hydrogenases (H_2ases). Protons, electrons, and/or hydrogen are elementary substrates in energy conversion reactions, but the details of how enzymes process such substrates (fundamental electron transfer aside) is not well understood. Here, we continue building our model of [NiFe]-hydrogenase catalysis with the soluble hydrogenase-1 from *Pyrococcus furiosus* (*Pf* SH1),[10-12] which belongs the class of H_2ases with the [NiFe] active site depicted in **Figure 4.1a**,[13,14] and more specifically to the group 3b cytoplasmic [NiFe]-H_2ases that use NADP(H) as an external electron donor/acceptor during cellular metabolism.[13] Although various [NiFe]-H_2ases have adopted distinct features for optimal function in particular ecological and cellular environments,[15,16] they share a common set of intermediates that constitute the catalytic cycle,[16,17] and a minimal sketch of turnover is depicted in **Figure 4.1b.**[10,11,18-23]

Various aspects of the primary and secondary coordination sphere fine tune the electronic structure[22,24-28] and further aid catalysis by stabilizing redox/protonation states necessary for turnover[29] and facilitating electrostatic and dynamic processes for efficient substrate processing.[12,30-33] Directly relevant to protons and hydrides, the primary sphere stores one proton and the two electrons of H_2 as a bridging hydride in the Ni_a^{3+}-C and Ni_a^{2+}-SR states.[23,34,35] The Ni_a^{3+}-C state can adopt tautomeric forms that are broadly termed Ni_a^{+}-L (**Figure 4.1b**), and cryogenic FTIR spectroscopy with the *Desulfovibrio vulgaris* Miyazaki F (*Dv* MF) enzyme demonstrated C418 (*Pf* SH1 numbering) is protonated in the Ni_a^{+}-L2 state.[20] An electron transfer from Ni_a^{+}-L1 to an iron-sulphur cluster and a proton transfer to the secondary sphere forms Ni_a^{2+}-S.[10,11,16] The closest ionizable residue to C418 is the highly conserved glutamic acid E17 (**Figure 4.1a**, *Pf* SH1 numbering), which is crucial for the Ni_a^{2+}-S $\leftrightarrow$ Ni_a^{+}-L1 transition because mutation to the non-ionizable amino acid glutamine (E17Q) essentially shuts off the transition in *Pf* SH1[12] and *Escherichia coli*

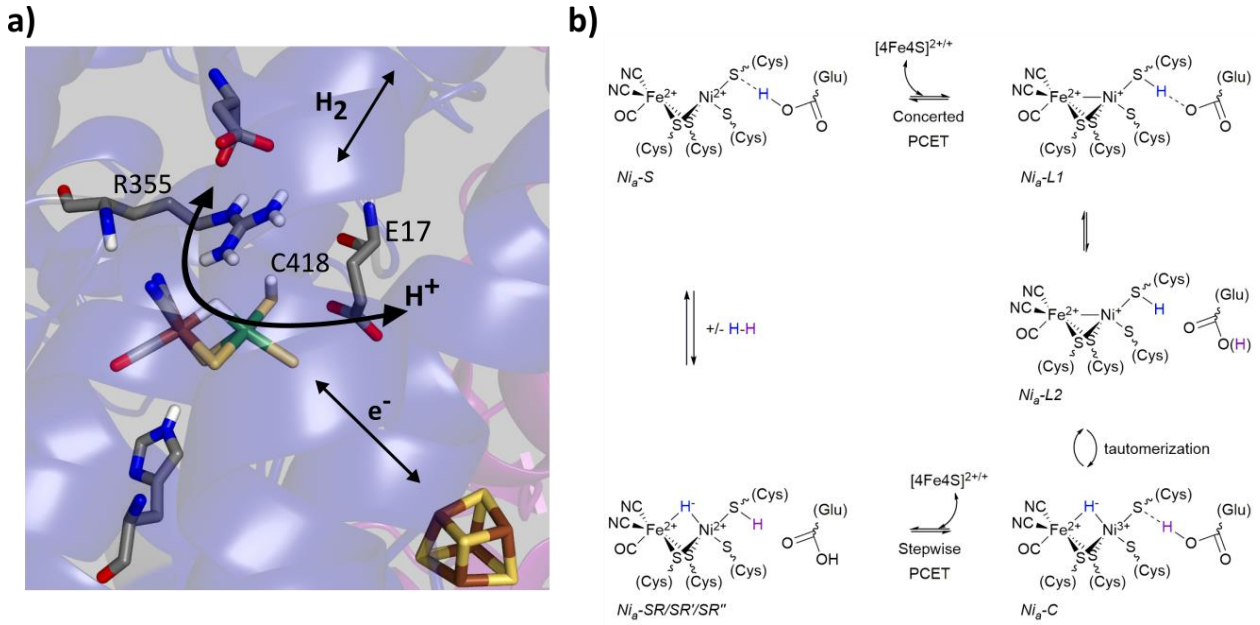

Figure 4.1: a) The [NiFe]-active site based on the Ni_a^{2+}-SR crystal structure from *Desulfovibrio vulgaris* Miyazaki F (PDB code 4U9I). Select conserved amino acid residues in the second coordination sphere are displayed, as well as the iron sulphur cluster proximal to the active site. Colour code: carbon (grey); nitrogen (blue); oxygen (red); hydrogen (white); sulphur (yellow), nickel (green), and iron (brown). **b)** One proposed elementary proton-coupled electron transfer (PCET) mechanism at the [NiFe]-hydrogenase active site that is largely based on mechanistic investigations of Pf SH1. For simplicity, the proton limited Ni_a^{2+}-SR substates are listed with Ni_a^{2+}-SR.

Hyd1 (*Ec* Hyd1).[36] A large H/D kinetic isotope effect observed for the Ni_a^{2+}-S → Ni_a^{3+}-C transition in *Pf* SH1,[10] which requires a Ni_a^{+}-L intermediate, indicated proton tunnelling through a hydrogen bond, meaning that protonated C418 hydrogen bonds to E17 in the Ni_a^{+}-L1 state, and protonated E17 hydrogen-bonds to C418 in the Ni_a^{2+}-S state.[11,20] Thus, C418 and E17 act as a proton donor/acceptor pair during the Ni_a^{2+}-S ↔ Ni_a^{+}-L1 transition as illustrated in **Figure 4.1b**.

Another important residue in the protein scaffold is the highly conserved arginine located above the active site exogenous ligand binding position (R355, **Figure 4.1a**). The conservation of this residue, which

is part of the so-called L4 motif,[37] is demonstrated in the alignment in **Figure 4.2a** (the entire motif is not shown because the other regions are not well conserved or relevant). R355 is known known to be critical for catalysis because mutation to lysine (R355K) in *Ec* Hyd1 and Hyd2 strongly attenuates the enzyme activity.[32,38,39]

There are two main proposals attempt to rationalize how R355 influences turnover. The first is from Evans and co-workers,[32] which suggested the active site and R355 function as a frustrated Lewis pair (FLP)[40] during H_2 activation. Specifically, the [NiFe]-center would behave as a Lewis acid to form a metal hydride, and R355 would function as a Lewis base and become protonated during the Ni_a^{2+}-S → Ni_a^{2+}-SR transition (**Figure 4.2b,** top). Experimental evidence in support of the proposal is the severely mitigated activity of R355K in *Ec* Hyd-1[32,38] and an increased activation entropy for H_2 oxidation.[32,38] These can be explained by lysine being an inherently weaker base than arginine[41] and some of the H-bonds that hold R355 in a moderately rigid position above the active site being absent in the lysine variant.[23,31,32] Thus, the rigidity and strong basicity of R355 should allow it to be an effective Lewis base during H_2 activation. Structural and computational investigations also support the proposal because plausible proton pathway(s) involving R355 have been identified.[31,42,43]

The second proposal was provided in a QM/MM study by Escorcia and co-workers.[33] It was found the chemical behaviour of R355 should be similar to free arginine (pK_a of ~13[41]), and the energetic penalty to deprotonate it in the Ni_a^{2+}-S state was found to be prohibitively large (> 150 kcal/mol). The energetics of H_2 binding was also more favored with a protonated R355, and it was found the protonated arginine helped form the protonic species generated during H_2 heterolysis. The binding of H_2 was less favored in the R355K variant, and formation of the protonic species was not observed in the study. Thus, it was concluded arginine helps position H_2 for activation (need for rigidity) and helps form the protionic species during H_2 for activation with the highly delocalized positive charge of the $[-(NH)C(NH_2)(NH_2]^+$ guanidinum group (**Figure 4.2b,** bottom). The lysine cannot exhibit both of these necessary features. It is more flexible

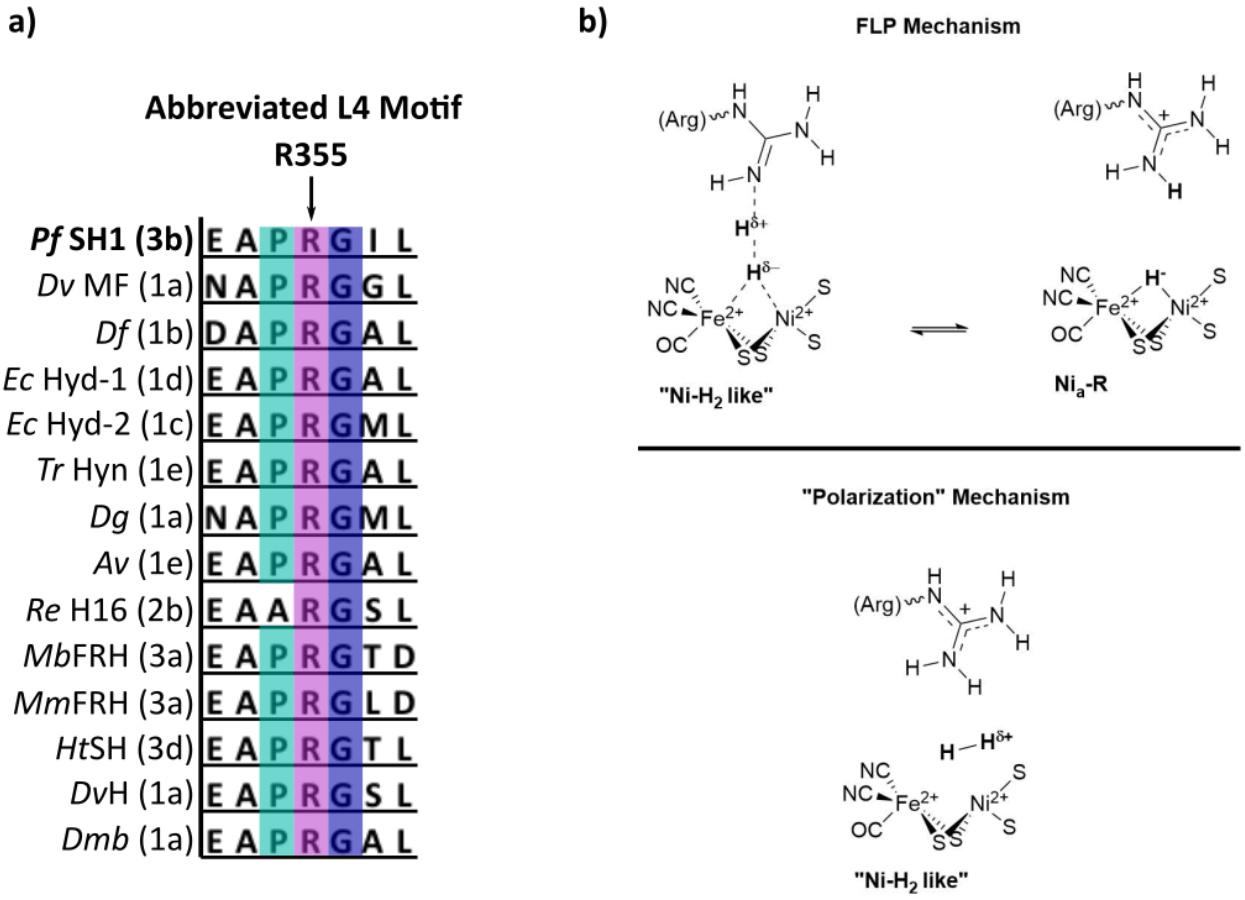

Figure 4.2: a) Sequence alignment of the L4 motif in various [NiFe]-H_2ases, groups/subgroups are in parentheses; only a rather conserved part of the motif is shown to highlight the R355 position. **b)** Schematic of the two proposed roles of R355 during catalysis as studied thus far, which focus specifically on the H_2 activation step of catalysis. In the first (top), a Frusturated-Lewis pair mechanism facilitates hydrogen splitting with arginine acting as a Lewis base and active site as a Lewis acid; see ref 31. The other proposed role is that the delocalized positive charge of arginine helps facilitate formation of the protonic species that results from hydrogen splitting; it was proposed arginine would be unable to reasonably be deprotonated and that the proton acceptor would be a cysteine (one of the terminal cysteines, with C418 being the most likely acceptor); see ref 33.

which does not help position H_2 for activation, and when it occupies a position feasible for H_2 activation, the ε-amino group side chain causes a more localized positive charge that disfavors formation of the protonic species.[33] Such findings and conclusions are consistent with arginine generally maintaining a positive charge in proteins,[44] like in hydrophobic sites of Staphylococcal nuclease.[45] An exception has been experimentally demonstrated recently in ascorbate peroxidase, where neutron scattering indicated the ability of an arginine to undergo deprotonation during proton transfer (probably transiently).[46]

Both proposals are very reasonable, though their fine details are experimentally a major challenge to verify, especially for an enzyme like *Pf* SH1 in which crystallization has remained a challenge. Given its location, R355 is probably also important for other aspects of catalysis beyond just H_2 activation; indeed, computational studies have shown it is important to include R355 when modeling exogenous ligand binding at the [NiFe] center (albeit catalytically irrelevant ligands, e.g. CO and $^-$OH).[47,48] Spectroscopic measurements should be able to provide additional information not readily obtained by crystallography or electrochemical studies alone. Thus far, the only spectroscopic studies that we are aware of are EPR measurements with the R355K variant from *Ec* Hyd1, which were unfortunately somewhat inconclusive: these indicated accessibility of inactive states (which slowly decreased in intensity under H_2) as well as and probable active states that did not correspond to standard native Hyd1 signals (and that were rather difficult to oxidize).[39]

Here, we further expand on our structure-function relationship understand of *Pf* SH1 (see chapter 3) via steady state kinetic and equilibrium studies of the R355K variant in *Pf* SH1. Our results provided insight into possible roles of R355 in catalysis, and also allowed us to study redox states under equilibrium conditions that are not accessible in native SH1. The next section of this chapter is divided into two main parts: first, our results are provided; then, we discuss implications of the results as whole.

4.2 – Results

4.2.1 – Steady State Kinetics

Figure 4.3a shows the steady state H_2 oxidation and H^+ reduction rates of R355K compared to native and E17Q *Pf* SH1 at pH = 8.4 and T = 80 °C. E17Q data is shown because spectroscopic studies have indicated E $\rightarrow$ Q minimally perturbs active site electronics,[12,21,36] making it a useful "baseline" mutation; as indicated earlier, activity of E17Q was 20 – 30% of native SH1 (native and E17Q data are the same data set from Chapter 3). The H_2 oxidation and H^+ reduction activity of R355K was ~ 2% and 16% relative to native SH1, respectively. Native and E17Q SH1 had a clear bias for H_2 oxidation, with the bias defined as the ratio of the H_2 oxidation rate versus the H^+ reduction rate ($k_{H2\ Ox}/k_{H+\ Red}$) at pH = 8.4. R355K had no obvious catalytic bias.

We also measured the H/D exchange rate of D_2 substrate with native and R355K SH1 in H_2O at pH = 6.3 (where it is known *Pf* SH1 has a large H/D exchange rate[49]) and T = 20 °C. Raman spectra of the gas headspace was used to follow the conversion of the D_2 substrate to HD.[49,50] The H/D exchange process is independent of electron transfer because it only requires the Ni_a^{2+}-S $\leftrightarrow$ Ni_a^{2+}-SR interconversion (see Chapter 1, Figure 1.7a), provided the proton transport pathway is in equilibrium with bulk solution. Exponential fits of the kinetics indicated 13% of the exchange rate was retained for R355K (**Figure 4.3b**).

4.2.2 – Electron Paramagnetic Resonance Spectroscopy

We utilized EPR spectroscopy to identify possible paramagnetic intermediates in R355K *Pf* SH1at pH = 6.7 and 9.3 and compared the EPR spectra to native enzyme. The results are shown in **Figure 4.4**. The native enzyme spectra are the same spectra from Chapter 3; briefly, these spectra show native enzyme had g-values that closely corresponded to the Ni_a^{3+}-C feature reported in *Pf* SH1 by Silva and co-workers;[51] the difference between g_y and g_x was not consistent with oxidized/inactive paramagnetic states.[28,51] The R355K spectra were different. The pH = 6.7 sample appeared to have three obvious features, and the pH

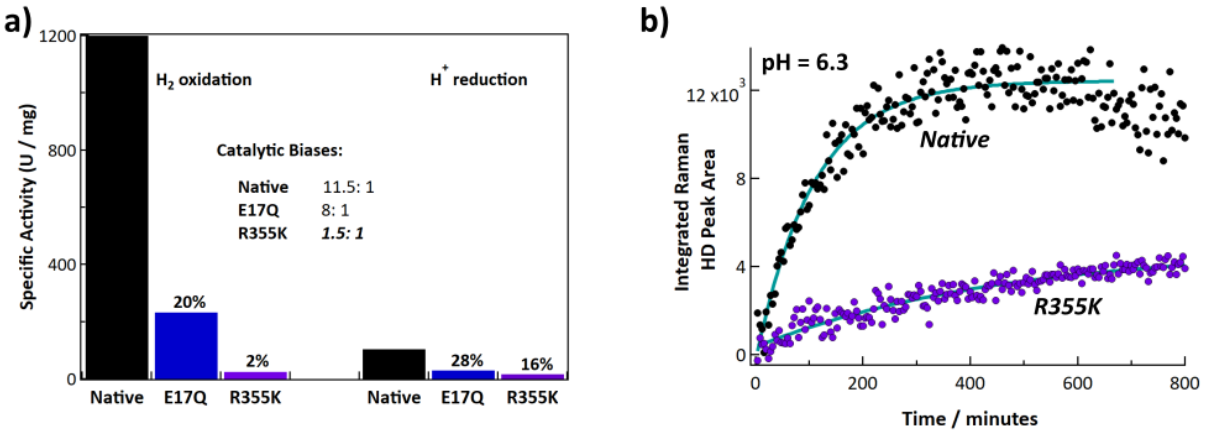

Figure 4.3: a) H_2 oxidation and H^+ reduction activities of native, E17Q, and R355K SH1 at T = 80 °C, pH = 8.4 (100 mM HEPPS buffer). The inset indicates the corresponding catalytic biases of WT, E17Q, and R355K SH1, defined as the ratio of the rate of hydrogen oxidation versus hydrogen production. **b)** Time course of H/D formation for native and R355K SH1 in 50 mM KP_I and 1.5 mM dithionite at pH = 6.3. The R355K data has been scaled to account for concentration differences. Wavenumber calibration and an example workup at a specific time, full point Raman spectra for select time points, and separate plots of native and R355K H/D exchange without scaling are provided in **Appendix D**.

= 9.3 sample one obvious feature. The pH = 9.3 sample feature, g_y ~ 2.11(6) and g_x ~ 2.36, was consistent with Ni_a^+-L, which is clear by computing Δg_y and Δg_x between Ni_a^{3+}-C and Ni_a^+-L in various [NiFe]-hydrogenases (see **Appendix A**) and because the g_y, g_x set is not consistent with inactive paramagnetic states.[28,51] The pH = 6.7 displayed three clear features. One signal assigned as Ni^{3+}-X was similar to an oxidized inactive feature reported by Silva and co-workers.[51] The other two features exhibited a g_y value between what is expected for Ni_a^{3+}-C and Ni_a^+-L (g_y ~ 2.12), and corresponding g_x values that more readily distinguish the two features as Ni_a^{3+}-C (g_x ~ 2.215) and Ni_a^+-L (g_x ~ 2.38, though this signal is overlapped with Ni^{3+}-X and less clear than in the pH = 9.3 sample). Verification of the Ni_a^+-L species was also clear from infrared spectroscopy (see below).

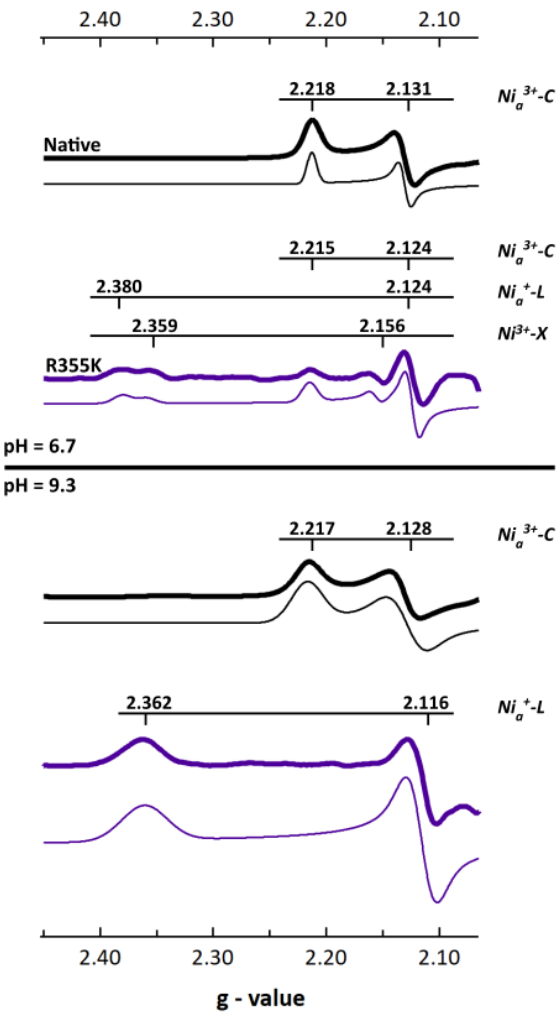

Figure 4.4: X-Band EPR spectra of native and R355K SH1 (microwave power = 10 mW, temperature = 70 K except for the pH = 6.7 R355K sample, which was run at 50 K in order to detect signal). The g_z region is not shown because of an overlapping signal due to other cofactors (see Chapter 3) The maximum value of g_y was normalized to 1 for visual purposes. Fits are located below the data and were scaled by the same factor as the respective spectra. Individual plots of processed spectra and fits are provided in **Appendix A.** The g – values are tabulated in **Appendix A**. The protein was isolated under anaerobic conditions and stored under 3 – 4% hydrogen at least one week prior to sample preparation in 25 mM MOPS (pH = 6.7) or 25 mM glycine (pH = 9.3) buffer.

4.2.3 – Fourier Transform Infrared Spectroscopy

An FTIR spectrum of native SH1 at pH = 7.2 is shown in **Figure 4.5a** (dashed black line). Similar to what we have observed before under a nitrogen or ~4% H_2 atmosphere after anaerobic purification, the spectrum is dominated by a feature near 1967 cm^{-1}, corresponding to Ni_a^{3+}-C.[10,11] Minor features corresponded to Ni_a^{2+}-S (~ 1950 cm^{-1}), and Ni_a^{2+}-SR and subforms[17] Ni_a^{2+}-SR' and Ni_a^{2+}-SR'' (~ 1954, 1940, and 1931 cm^{-1}). Ni_a^{2+}-SR'' probably overlaps with the inactive Ni_r^{2+}-S state,[52] so both features may be present near 1931 cm^{-1}.[10,11,53]

The R355K spectrum at pH = 7.2 is drastically different (**Figure 4.5a**, solid purple line). The 1967 cm^{-1} feature due to Ni_a^{3+}-C was missing. Instead, the tautomeric Ni_a^{+}-L states were observed near 1920 cm^{-1},[10-12] and observation of these states supports the assignment of the R355K Ni_a^{+}-L EPR feature(s). Significant spectral overlap in the region > 1930 cm^{-1} complicated the assignment of other states by direct comparison to native SH1. To aid in the assignments, we generated redox difference spectra using an equilibrium photochemical reduction with CdSe/CdS dot-in-rod nanocrystals and PDQ^{2+}. The spectral changes due to reduction are shown in the (light – dark) difference spectra (**Figure 4.5b**). A strong bleach near 1946 cm^{-1} was assigned to depletion of the enzyme resting state, Ni_a^{2+}-S. The strong induced absorbance near 1936 cm^{-1} was assigned to an increased population of the fully reduced state, Ni_a^{2+}-SR'. There was also a small induced absorbance near 1920 cm^{-1} corresponding to Ni_a^{+}-L. We attributed the very weak induced absorbance near 1965 cm^{-1} to Ni_a^{3+}-C.

FTIR signatures of R355K were further investigated from pH 6.7 to 9.3. The normalized spectra and corresponding multicomponent Voigt fits are shown in **Figure 4.6a**. Peak positions here are provided as the average value and standard deviation from the positions determined by the fits in **Figure 4.6a** as tabulated in **Appendix F**. It is clear in **Figure 4.6a** that the 1944.8 ±0.8 cm^{-1} feature (Ni_a^{2+}-S, red) decreases in relative amplitude with increasing pH, whereas the 1939.0 ±1.42 cm^{-1}[§§] feature (Ni_a^{2+}-SR', light blue)

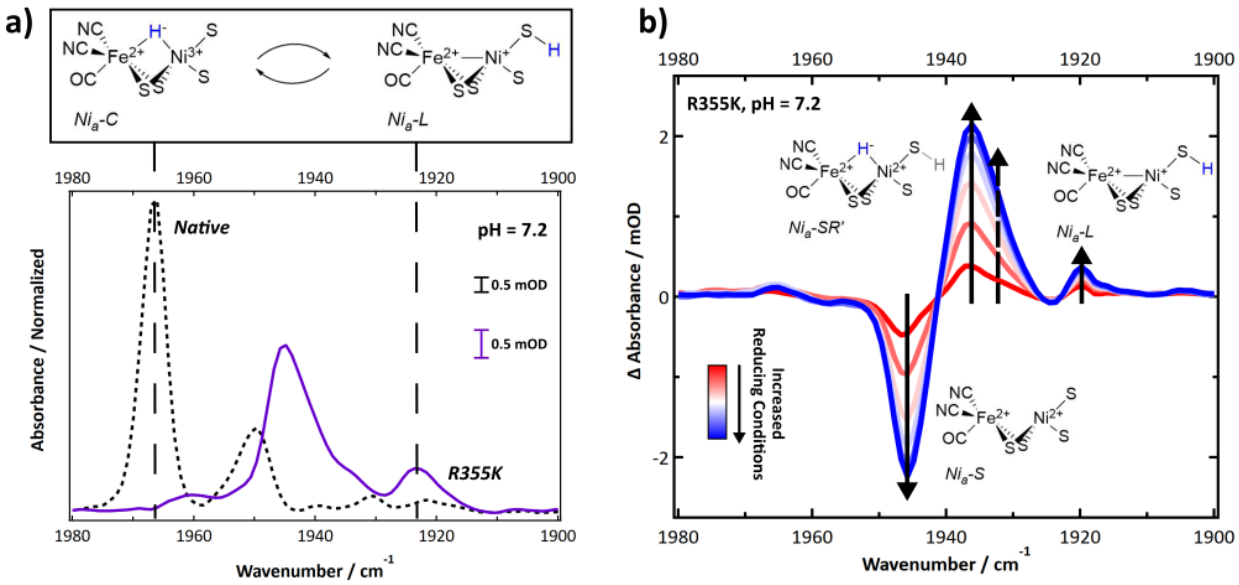

Figure 4.5 a) FTIR spectrum of native and R355K SH1 at pH 7.2, prepared after anaerobic purification of the enzyme and storage under 3 – 4% H_2. Native SH1 displays a dominate peak that corresponds to the Ni_a^{3+}-C state. R355K displays a different distribution of states; unlike native SH1, the Ni_a^{3+}-C state absorbance is not apparent. Instead, the tautomeric Ni_a^{+}-L states are observed. The presented structure of Ni_a^{+}-L assumes identical cysteine based protonation to what has been experimentally demonstrated in Dv MF (see ref 20). **b)** Difference spectra (light – dark) following an equilibrium photochemical reduction of R355K with CdSe/CdS core/shell NCs (OD ~ 0.15 - 0.3) and 30 mM PDQ^{2+} in 30 mM phosphate / 50 mM MPA buffer (pH = 7.2). The illumination wavelength was 405 nm (~ 4 mW). Abbreviated first coordination sphere structures are pictured with the corresponding induced absorbance or bleach. The dashed arrow corresponds to Ni_a-SR''. A weak induced absorbance signal near 1965 cm^{-1} may correspond to Ni_a^{3+}-C. Second derivative (ν_{CO} and ν_{CN} region) and absorbance spectra (ν_{CO} region) and the ν_{CN} region of the difference spectra is shown in **Appendix E.**

increased in relative amplitude with increasing pH. After scaling for oscillator strength differences, the summed area of these two features has no obvious pH dependence and corresponded to 33 – 41 % of the

total peak area at full width half maximum (see **Appendix F**). Plotting the population of these two states versus the estimated H_2/H^+ couple at each pH value shows these features appear in a redox window expected of active states (**Figure 4.6b**),[18,28,54] which further supports their assignments as Ni_a^{2+}-S and Ni_a^{2+}-SR'. In conjunction with our ability to observe R355K turnover from steady state kinetics and even methyl viologen reduction under mild conditions (e.g. 5% H_2 and heat, see **Appendix G**) it is clear active states are accessible between pH = 6.7 and 9.3 under the conditions used.

Ni_a^{2+}-SR''/Ni_r^{2+}-S (pink) are observed near 1933.5 ±0.6 cm^{-1}. Ni_a^{+}-L1 (yellow) is observed at 1917.8 ±1.17 cm^{-1} and Ni_a^{+}-L2 (brown) is observed at 1923.4 ±0.8 cm^{-1}. The weak feature observed near 1952 cm^{-1} may correspond to Ni_a^{2+}-SR (dark blue); however, it did not display an obvious induced absorbance during the photochemical reduction that would be expected for Ni_a^{2+}-SR,[53] so it is likely an inactive state. At least one state was consistently observed > 1955 cm^{-1} (grey). Because the feature did not change significantly during the photochemical (**Figure 4.5b** and **Appendix E**), it likely corresponds to an inactive state that does not reactivate under the experimental conditions.

The summed populations of Ni_a^{+}-L1 and Ni_a^{+}-L2 had no obvious pH dependence and were ~ 5 – 9% of the total peak area (**Appendix F**). However, the equilibrium between Ni_a^{+}-L1 and Ni_a^{+}-L2 exhibited a clear pH dependence (**Figure 4.6b – c**). One possible explanation for the pH dependence would be an acid/base equilibrium involving formation of a hydrogen bond between C418 and the deprotonated form of E17[11] (CysSH + HOGlu ↔ CysSH–OGlu; see **Figure 4.1b**. This assumes *Pf* SH1 exhibits the same type of terminal cysteine protonation observed in *Dv* MF [20]). However, the data do not appear to be a simple monoprotic acid-base equilibrium. This is not surprising since E17 probably interacts with other protein residues, which will affect its interaction with the active site. This has also been noted in native *Ec* Hyd1 which exhibits a pH dependence Ni_a^{+}-L states under ambient condition.[55] We further address this in the discussion section.

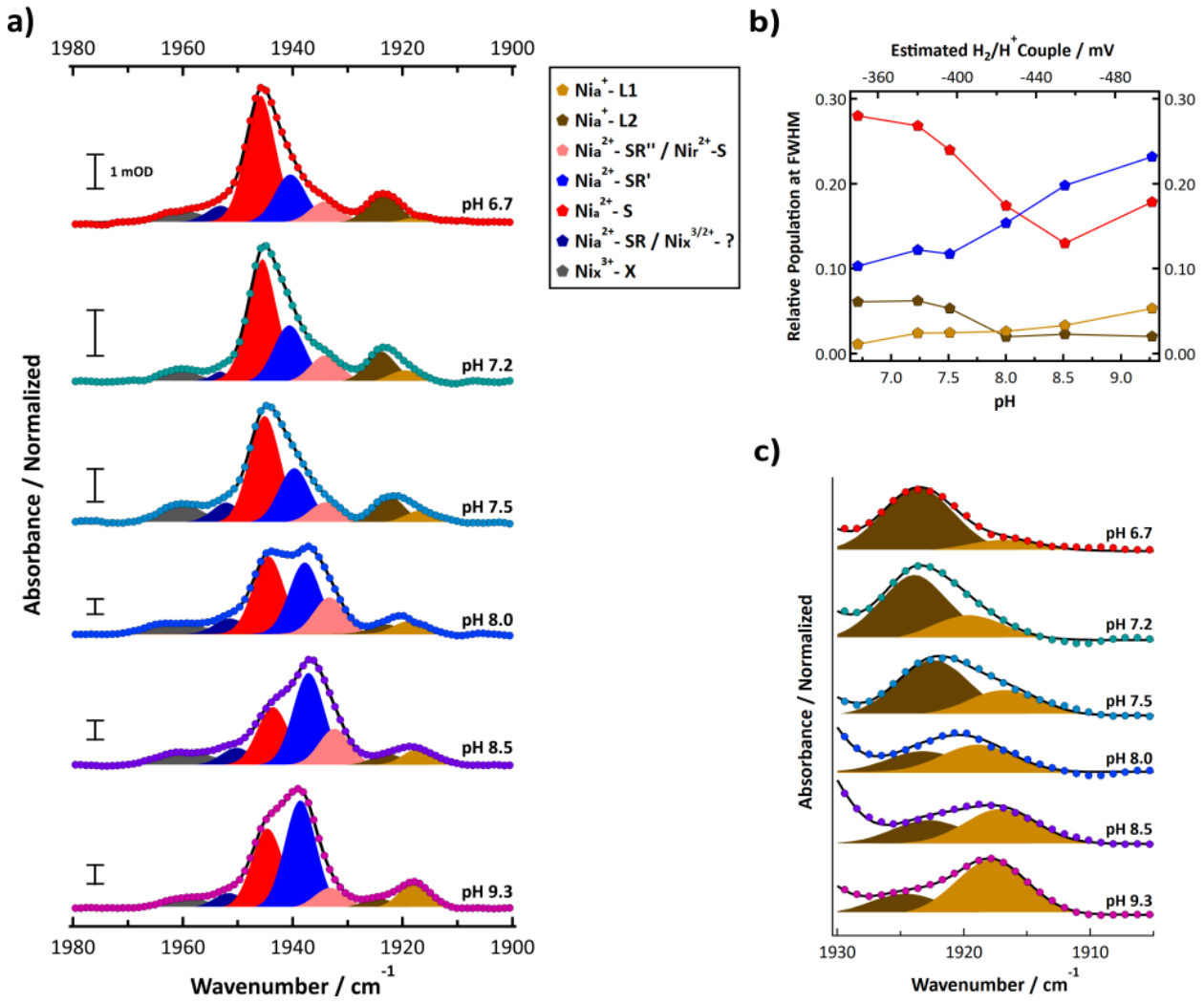

Figure 4.6: **a)** FTIR spectra of R355K SH1 prepared under ~ 4% H_2 after anaerobic purification of the enzyme and storage under a 3 – 4% atmosphere of H_2 for at least one week prior to sample preparation in 25 mM MOPS (pH 6.7), 50 mM Tris (pH 7.5), 50 mM HEPPS (pH 8.0 and 8.5), or 25 mM glycine (pH 9.3) buffer. The pH 7.2 sample the same sample from **Figure 4.5**. Non-normalized spectra and second derivative spectra are presented in **Appendix F**. Peak positions, peak areas at full-width half maximum, and oscillator-strength corrected peak areas from t spectral fits are provided **Appendix F. b)** The pH dependent populations of the Ni_a^{2+}-S, Ni_a^{2+}-SR', Ni_a^{+}-L1, and Ni_a^{+}-L2 states from the oscillator strength corrected peak areas from **Appendix F;** the top axis estimates the H_2/H^+ couple of the cell for a given pH assuming 4% H. **c)** Zoomed in spectra that focuses on the Ni_a^{+}-L states.

Sample oxidation was monitored by two methods, one at pH 8.5 and the other at pH 9.3. In the first method (pH 8.5), the as prepared sample under ~ 4% H_2 was subjected to a temperature ramp between 8 – 70 °C which results in enzyme auto-oxidation through enzyme consumption of the hydrogen and/or loss of H_2 from the infrared cell. As shown in **Figure 4.7**, the feature we have assigned as Ni_a^{2+}-SR' decreased in intensity as the temperature increased, and the Ni_a^{2+}-S feature increased in intensity, which is exactly what is expected during auto-oxidation. In the second method (pH 9.3), the sample cell was stored in the air, which allowed the enzyme to oxidize over time. FTIR spectra were measured periodically over the course of a month (**Figures 4.8** and **Appendix H**). There was a growth of two states between ~1958 – 1970 cm^{-1} as the sample adopted more oxidizing conditions (and perhaps 1950 cm^{-1} as well, see **Figures 4.8** and **Appendix H**). Such peaks are consistent with known inactive states of native *Pf* SH1 near

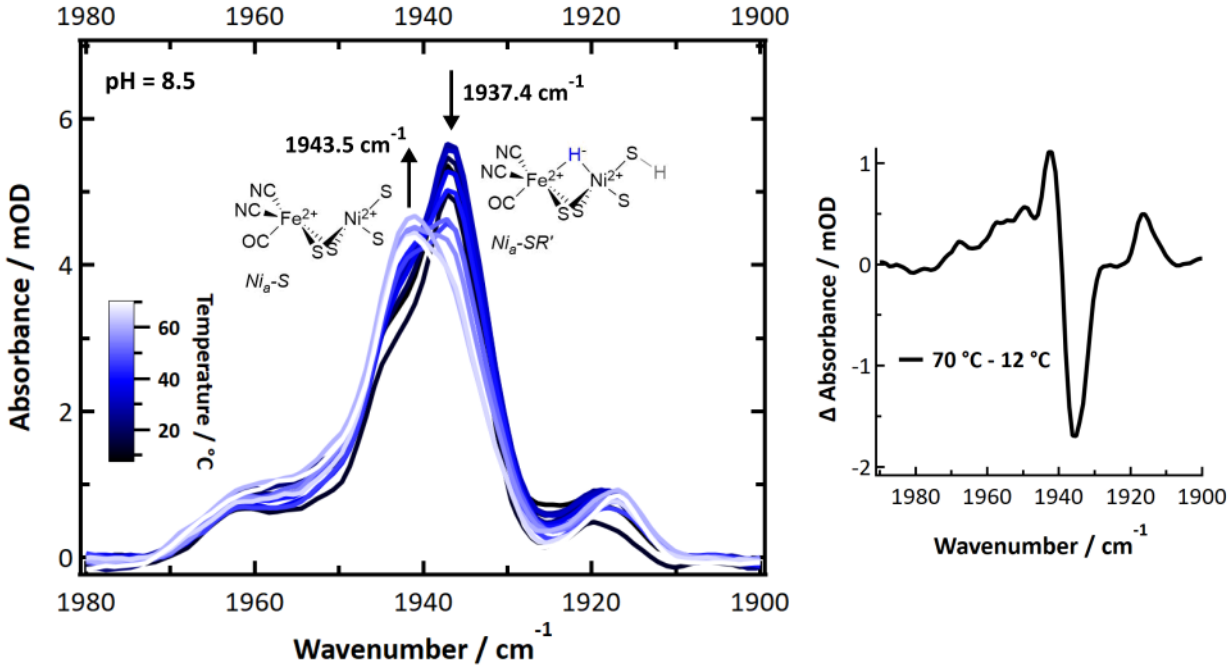

Figure 4.7: Temperature dependent FTIR spectra of R355K at pH = 8.5; the bleach and absorbance that reasonably correspond to NI_a^{2+}-SR and Ni_a^{2+}-S, respectively, are emphasized. The difference spectrum of the 70 ° C and 12° C spectra is shown on the right. The room temperature spectrum is the same spectrum in **Figure 4.6**.

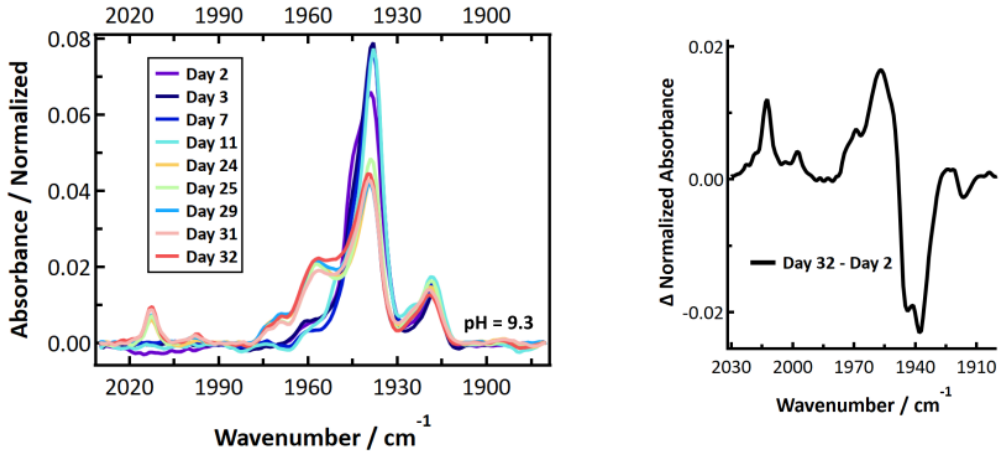

Figure 4.8: Day dependent FTIR spectra of R355K at pH = 9.3. The difference spectrum of the last and first day (Day 2) is shown on the left. Day 2 corresponds to the same spectrum in Figure 4.6 and is the "first day" because more time was required than expected to purge out water vapor from the sample compartment (which took overnight). Second derivative spectra are shown in **Appendix H.**

1948, 1960, and 1963 cm^{-1}.[53] Under highly oxidized conditions, a peak we are unable to assign appeared near 2012 cm^{-1} (and perhaps 1998 cm^{-1}). Interestingly, an unassigned and unusually high frequency state was recently observed at 1993 cm^{-1} in a similar [NiFe]-hydrogenase, *Hydrogenophilus thermoluteolus* TH-1^T, under oxidized (as isolated) conditions.[56]

Exogenous carbon monoxide binding to R355K was also compared to CO binding in native and E17Q *Pf* SH1 at pH 8.0 (**Figure 4.9**; the E17Q spectrum is identical to that used in Chapter 3). Exogenous CO is known to bind terminally to the nickel atom[57,58] and exhibit a distinct ν_{CO} peak around ~ 2050 – 2060 cm^{-1} depending on the exact enzyme.[28,58-61] Both native and E17Q SH1 have exogenous ν_{CO} peaks near 2044 cm^{-1} with a corresponding endogenous ν_{CO} peak near 1946 cm^{-1} that are consistent with a minor redshift of endogenous ν_{CO} relative to Ni_a^{2+}-S (~1950 cm^{-1} in native SH1) and the location of exogenous ν_{CO} in [NiFe]-hydrogenases following CO binding.[28,58-61]

In contrast, the R355K spectrum showed a major endogenous ν_{CO} peak near 1949.5 cm^{-1}, which is blue-shifted from the Ni_a^{2+}-S peak of the variant (~1946 cm^{-1}). Surprisingly, two ν_{co} features were observed near 2013 and 2025 cm^{-1}, likely due to exogenous CO binding. The presence of Fe bound CO would be expected to give a significant trans effect, and the crystal structure of bound CO in the R355K variant from *Ec* Hyd2 showed CO is terminally bound to the nickel atom.[39] Therefore, it is likely these peaks are due to exogenous CO bound to nickel, although we cannot rule out a weak interaction with the iron. The ν_{CN} region also provides evidence for significant alteration of R355K SH1 behaviour in the presence of exogenous CO. A critical observation is shown in the inset of **Figure 4.9**, where a feature near 2100 cm^{-1} is indicative of at least one cyanide frequency being blue-shifted compared to the Ni_a^{2+}-S state, which is not

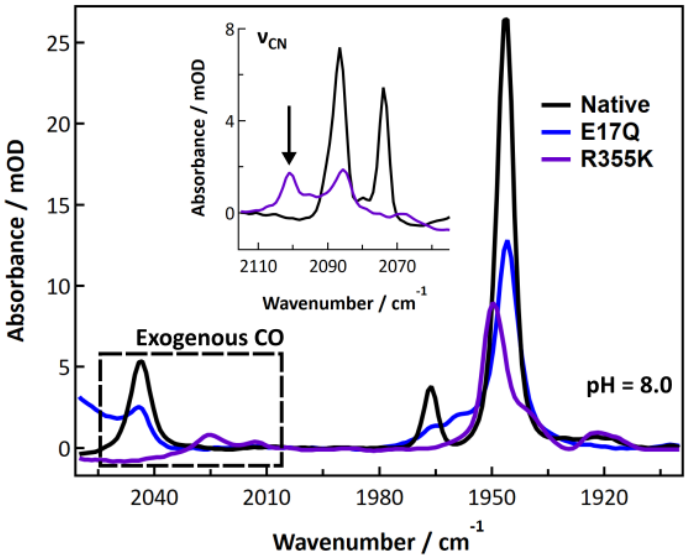

Figure 4.9: FTIR spectra of native, E17Q, and R355K SH1 at pH = 8.0 (50 mM HEPES or HEPPS buffer) after incubation with carbon monoxide. The E17Q spectrum is the same data from Chapter 3. Both native and E17Q displayed similar endogenous and exogenous ν_{CO} peaks. The R355K spectrum displayed a broad distribution of endogenous ν_{CO} peaks, with a major peak located near 1950 cm^{-1}. Two endogenous ν_{CO} peaks were located near 2013 and 2025 cm^{-1}. Individual spectra, the corresponding second derivatives, and tabulated peak positions are provided in **Appendix I**.

seen in native SH1, nor E17Q (see also **Appendix I**). This is an unusually high frequency ν_{CN} feature for almost all known active, inactive, and CO bound enzyme states.[10-12,28,60]

4.3 – Discussion

We have explored the catalytic role of the secondary sphere residue R355 in the soluble [NiFe]-hydrogenase SH1 from the hyperthermophilic organism *Pyrococcus furiosus* by mutating this residue to a lysine. Mutagenesis can sometimes cause dramatic changes to enzyme properties that are not obvious by subtle or even undetectable changes in structure,[62,63] making spectroscopic and kinetic studies necessary for mechanistic information. Here, our steady state kinetic and equilibrium spectroscopic studies of R355K have provided new insight to our understanding of *Pf* SH1 catalysis.[10-12] Important broad considerations to remember in our discussion is we often support conclusions from our FTIR and EPR studies based on structure-function and electronic/computational studies of other [NiFe]-hydrogenases, especially the extensively characterized group 1 *Dv* MF and *Ec* Hyd-1 enzymes. However, the overall conclusions should only be applied to our working model of *Pf* SH1 catalysis.

Our kinetic assays showed R355K exhibits lower H_2 oxidation and H^+ reduction activity than native *Pf* SH1 (**Figure 4.3a**). These results are similar to those for *Ec* Hyd1 and Hyd2,[32,38,39] although the residual activity in SH1 is larger. Attenuated H/D exchange (**Figure 4.3b**) demonstrated the mitigated activity is associated with active site properties. While it is somewhat surprising the H_2 oxidation and H/D exchange rates of R355K are 2% and 13% of native enzyme respectively, the active site transformations of H/D exchange are more limited than what is necessary for H_2 oxidation coupled with reduction of an external redox mediator. H_2 oxidation involves H_2 cleavage, product release, and fundamental active site redox chemistry via formation of Ni_a^{2+}-S, Ni_a^{+}-L, Ni_a^{3+}-C, and Ni_a^{2+}-SR/SR'/SR''. In contrast, the H/D exchange process only involves Ni_a^{2+}-S and Ni_a^{2+}-SR, and simply demonstrates that R355K SH1 can cleave D_2 and H_2, exchange protons and deuterons with bulk solution, and release HD product or the double exchanged H_2

product to solution. These differences make it difficult to compare the H/D exchange rates directly to the proton reduction/hydrogen oxidation rates. Nevertheless, both assays clearly demonstrated mitigated activity of R355K versus native *Pf* SH1; but they do not provide insight into how the R $\rightarrow$ K mutation affects the active site. Thus, we turn to the spectroscopic signatures that directly report on active site chemistry.

We first consider the FTIR spectra of external CO binding. We observed one exogenous ν_{CO} band in native and E17Q SH1, and the endogenous ν_{CO} and ν_{CN} bands were slightly redshifted relative to Ni_a^{2+}-S, as observed for other [NiFe]-hydrogenases.[28,58-60] In contrast, R355K exhibited exogenous ν_{CO} and ν_{CN} bands blueshifted relative to Ni_a^{2+}-S. Furthermore, two exogenous ν_{CO} bands were observed at lower energy compared to the one exogenous band in native and E17Q SH1 (~2013 and 2025 cm^{-1} versus 2046 cm^{-1}; **Figure 4.9**). This shift is indicative of greater π-backbonding to the exogenous CO, and thus stronger binding of CO to the active site relative to native and E17Q SH1. Computational studies have indicated inclusion of R355 is critical for modelling exogenous CO ligand binding in [NiFe]-hydrogenases, which was attributed primarily to steric effects.[47,60] When considering these former computational analyses together with the differences in the FTIR spectrum of exogenous CO bound R355K, it is clear R355 influences binding of the (albeit sterically demanding) external CO ligand.

The importance of R355 for ligand binding extends to the catalytically relevant Ni_a^{3+}-C state and tautomeric Ni_a^{+}-L states. Both here and in other reports, activated native SH1 has clear equilibrium IR and EPR detectable signatures diagnostic of Ni_a^{3+}-C (**Figure 4.4** and **Figure 4.5a**),[10,11,51,64] with minimal to no Ni_a^{+}-L, which is only observed in trace amounts at pH $\geq$ 8.5.[11] In contrast, only a minor amount of Ni_a^{3+}-C was observed for R355K in the EPR spectra and equilibrium photochemical reduction FTIR difference spectra (**Figure 4.4** and **Figure 4.5b**). Although Ni_a^{2+}-S and Ni_a^{2+}-SR' comprised the bulk of the IR detected spectral signatures, we also observed the *Pf* SH1 Ni_a^{3+}-C tautomers, Ni_a^{+}-L(1/2), at room temperature over a broad pH range (**Figure 4.6**). The clear similarity of the IR signatures of Ni_a^{+}-L in native[10,11,53] and R355K highly suggests Ni_a^{+}-C is destabilized relative to Ni_a^{+}-L.

Ni_a^+-L is not observed in most [NiFe]-hydrogenases under ambient conditions, and the same is true for native *Pf* SH1. This state is most commonly observed via photolysis of the Ni_a^{3+}-C hydride under cryogenic conditions to trap the Ni_a^+-L photoproducts.[20,34,65] However, the Ni_a^+-L tautomer has been readily observed under ambient conditions in some [NiFe]-hydrogenases,[18,66] and the pK_a and bond strength of the Ni_a^{3+}-C hydride has been hypothesized to vary through subtle electronic and/or structural changes to partially explain such observations.[17,67] A shift of tautomeric equilibrium to favour base protonation over metal-hydride formation has been demonstrated in a cationic [FeFe] mimic and iron-diphosphine complex via ion-pairing of the protonated base with anionic species such as BF_4^-.[68,69] Furthermore, depending on electronic structure of a nickel atom, there is the possibility of the thermodynamic preference for thiolate protonation over nickel-hydride formation.[70,71] The [NiFe] active site is rather electron rich given the nature of the coordinating ligands,[72] and it is reasonable that R355 would act as a cationic species for an ion pairing like interaction with the hydride ligand in the Ni_a^{3+}-C state, resulting in preferential hydride formation over cysteine base protonation. Thus, R355 modulates the Ni_a^{3+}-C $\leftrightarrow$ Ni_a^+-L tautomeric equilibrium, and the mutation to lysine allows Ni_a^+-L to be trapped under ambient conditions (illustrated in **Figure 4.10**). Interestingly, the inverse situation is observed in [FeFe]-hydrogenases, in which unusual conditions, site-directed mutagenesis,[73,74] or photochemistry at low temperatures[75] is required for trapping the terminal iron-hydride.

The pH dependence of Ni_a^+-L(1/2) (**Figures 4.6**) is rather difficult to understand. It is tempting to think of it as an acid/base equilibrium involving E17, with a hydrogen bond forming between E17 and C418 when E17 is deprotonated (CysSH + HOGlu versus CysSH—OGlu; see also **Figure 4.1b**)[11], and this probably contributes to the pH dependent behaviour. However, the rest of the protein scaffold must be considered because E17 is part of a proton transfer network. Thus, its acid base chemistry and conformation(s) are likely coupled to other components of the network which will affect is general properties and interaction with the active site, which is similar to observations with Ni_a^+-L in native *Ec* Hyd1[55] and would be similar

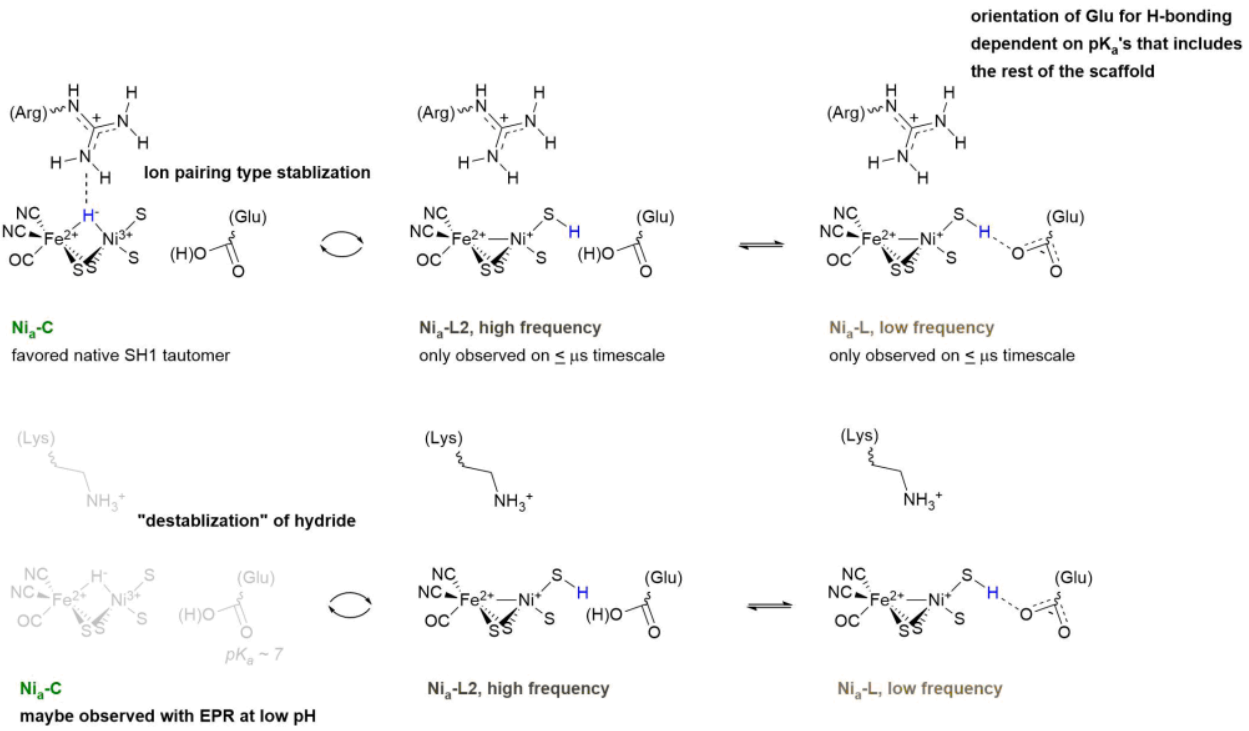

Figure 4.10: Pictorial representation of our overall conclusions regarding how the R355K Pf SH1 variant affects the tautomeric equilibrium between Ni_a^{3+}-C and Ni_a^{+}-L; it is noted that Ni_a^{+}-L is only transiently observed (via time resolved studies) in native enzyme, with exceptions at moderately high pH (see ref 11).

to how the proton transfer pathway residues (and active site) are coupled in [FeFe]-hydrogenases.[76-78] This indicates a complex cooperativity between the primary, secondary, and outer coordination sphere that affect active site properties of *Pf* SH1.

There is a final set of points worth noting about the Ni_a^{+}-L(1/2) states in R355K. In the CO incubated sample in **Figure 4.9**, there was still a presence of Ni_a^{+}-L. This was somewhat surprising to observe because CO is known to bind to the Ni_a^{+}-L state from EPR studies.[61,79] Hidalgo found, similar to us, that CO did not bind to Ni_a^{+}-L in *Ec* Hyd1 under *ambient* conditions; although the reason remains unclear, it was speculated cryogenic versus non-cryogenic temperatures were largely responsible for the observation.[80]

Given that both native and E17Q SH1 could essentially be set entirely in the Ni^{2+}-SCO state, the observation of residual Ni_a^{+}-L (and other states in R355K SH1 suggests) that under equilibrium conditions the interconversion of Ni_a^{+}-L and Ni_a^{2+}-S, with Ni_a^{2+}-S being able to bind CO, is incredibly slow/difficult. On that note, the day dependent pH = 9.3 sample (**Figure 4.8** and **Appendix H**) still displayed a broad distribution of states even after one month; the absorbance spectra and difference spectrum (last – first day) clearly showed changes that corresponded to bleaching out of at least some population of Ni_a^{2+}-S, Ni_a^{2+}-SR', and Ni_a^{+}-L; interestingly, some Ni_a^{+}-L was still present even after one month (some Ni_a^{2+}-S, Ni_a^{2+}-SR' may have been present as well, though that region of the spectrum is congested it is difficult to analyze well). Thus, it would appear Ni_a^{+}-L is difficult to oxidize. This is interesting to note because Beaton had found probable active paramagnetic states in R355K from Hyd1 that were quite difficult oxidize.[39]

Lastly, another intriguing difference between native and R355K *Pf* SH1 is that only the proton limited fully reduced states of R355K, Ni_a^{2+}-SR' and a minor population of Ni_a^{2+}-SR'', were observed in the FTIR spectra (**Figure 4.5b** and **Figure 4.6a**). The proton limited Ni_a^{2+}-SR' state is observed to increase in population (and Ni_a^{2+}-S to decrease) as the pH is raised or as the solution potential is decreased in the photochemical reduction experiment. No obvious IR band for the protonated fully reduced Ni_a^{2+}-SR state was observed at any pH (although the weak inactive state band at 1952 cm^{-1} might mask the presence of a small population) and none was observed to accumulate in the photochemical reduction experiment. This behaviour is in contrast with native *Pf* SH1, for which we observe a strong Ni_a^{2+}-SR band (1954 cm^{-1}) that decreases as the pH is raised from 6.5 to 9.5 and increases as the solution potential is reduced (see also Chapter 2).[10,11,53] While exact differences between sub-forms of Ni_a^{2+}-SR have yet to be determined,[17,52,53] the >10 cm^{-1} redshift of ν_{CO} of Ni_a^{2+}-SR' compared to Ni_a^{2+}-SR is consistent with deprotonation of an active site residue,[81] with the most likely candidate being C418.[23] Both Ni_a^{2+}-SR and Ni_a^{2+}-SR' have bridging hydrides that are likely destabilized in R355K (in the same manner we observe for the Ni_a^{3+}-C state), which would be consistent with the mitigated H/D exchange activity. We postulate that

the destabilized hydride is readily protonated in the Ni_a^{2+}-SR state by a nearby donor (possibly C418) to form H_2, whereas this donor is deprotonated in Ni_a^{2+}-SR', allowing the hydride state to accumulate. Protonation of Ni_a^{2+}-SR to form H_2 would also reform the oxidized Ni_a^{2+}-S state, which would explain the large amount of Ni_a^{2+}-S observed at pH > 8 relative to what would be expected based on an estimated solution potential < -400 mV (**Figure 4.6a-b**).[54] This model is depicted in **Figure 4.11** and is testable using time-resolved potential-jump experiments to observe the transient formation of Ni_a^{2+}-SR prior to protonation of the hydride and formation of H_2.

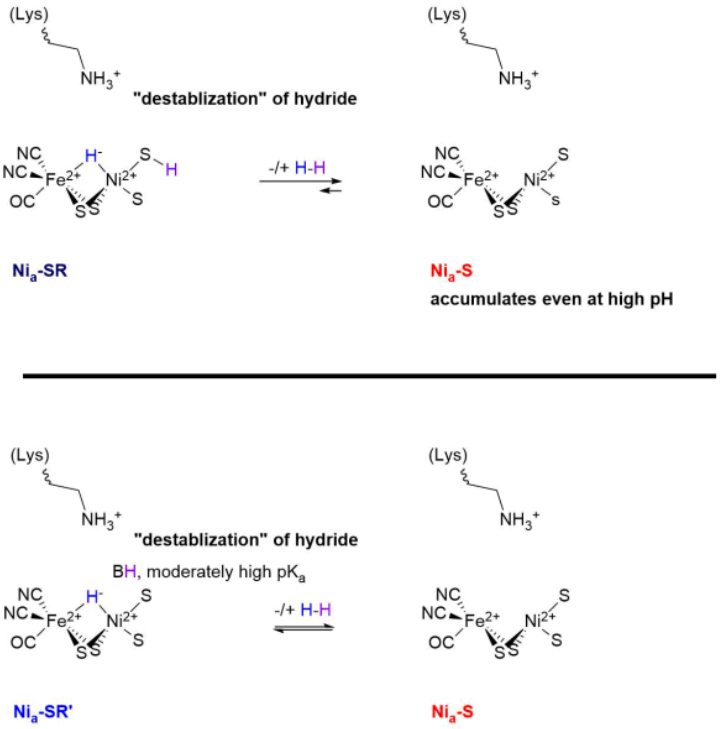

Figure 4.11: Pictorial representation of how R355K may destabilize Ni_a^{2+}-SR (similar to Ni_a^{3+}-C) and how it may cause a large accumulation of Ni_a^{2+}-S even at high pH by simply considering the Ni_a^{2+}-SR'' ←→ Ni_a^{2+}-S equilibrium being "controlled" by a nearby base that is not C418. Although the Ni_a^{2+}-SR'' ←→ Ni_a^{2+}-S model is kept vague, the identity of the base (B) could be the lysine.

4.4 – Conclusions

We have presented an electron paramagnetic and infrared spectroscopic study of the R355K variant in *Pf* SH1. The variant revealed pieces of the complex cooperativity between the active site metal and protein scaffold. Importantly, H/D exchange kinetics indicated R355 is critical for H_2 activation and/or formation, and EPR and FTIR signatures demonstrated it influence exogenous ligand binding at the active site. A key finding was the effect of het mutation on the Ni_a^{3+}-C ←→ Ni_a^{+}-L tautomeric equilibrium, which is relevant to proton/hydride management crucial for substrate processing. Specifically, minimal Ni_a^{3+}-C spectroscopic signatures were detected in R355K, which indicated the mutation alters the thermodynamic landscape and affects hydride reactivity. Observation of Ni_a^{+}-L1 and Ni_a^{+}-L2 signatures over a wide pH range provided a unique opportunity to further explore the communication between the active site, C418, E17, and the larger protein scaffold when the nickel formally adopts a +1 redox state. Unfortunately, no insight was gained regarding the proposed FLP mechanism of hydrogen activation via R355, although given the altered behavior of Ni_a^{2+}-SR versus Ni_a^{2+}-SR', it is possible there is more than one "hydrogen activating" mechanism and that the FLP mechanism operates in one of these mechanisms. The results overall set a foundation for additional studies with R355 and other variants to understand the electrostatic nature of the secondary and even outer sphere for fine tuning [NiFe]-H_2ase catalysis.

4.5 – References

(1) Klug, C. M.; Cardenas, A. J. P.; Bullock, R. M.; O'Hagan, M.; Wiedner, E. S. Reversing the tradeoff between rate and overpotential in molecular electrocatalysts for H_2 production. *ACS Catal.* **2018**, *8*, 3286-3296.

(2) Geri, J. B.; Shanahan, J. P.; Szymczak, N. K. Testing the push–pull hypothesis: Lewis acid augmented N_2 activation at iron. *J. Am. Chem. Soc.* **2017**, *139*, 5952-5956.

(3) Slater, J. W.; Marguet, S. C.; Gray, M. E.; Monaco, H. A.; Sotomayor, M.; Shafaat, H. S. Power of the secondary sphere: modulating hydrogenase activity in nickel-substituted rubredoxin. *ACS Catal.* **2019**, *9*, 8928-8942.

(4) Cronin, S. P.; Strain, J. M.; Mashuta, M. S.; Spurgeon, J. M.; Buchanan, R. M.; Grapperhaus, C. A. Exploiting metal–ligand cooperativity to sequester, activate, and reduce atmospheric carbon dioxide with a neutral zinc complex. *Inorg. Chem.* **2020**, *59*, 4835-4841.

(5) Laureanti, J. A.; Ginovska, B.; Buchko, G. W.; Schenter, G. K.; Hebert, M.; Zadvornyy, O. A.; Peters, J. W.; Shaw, W. J. A positive charge in the outer coordination sphere of an artificial enzyme increases CO_2 hydrogenation. *Organometallics* **2020**, *39*, 1532-1544.

(6) Le, J. M.; Bren, K. L. Engineered enzymes and bioinspired catalysts for energy conversion. *ACS Energy Lett.* **2019**, *4*, 2168-2180.

(7) Laureanti, J. A.; O'Hagan, M.; Shaw, W. J. Chicken fat for catalysis: a scaffold is as important for molecular complexes for energy transformations as it is for enzymes in catalytic function. *Sustain. Energy Fuels* **2019**, *3*, 3260-3278.

(8) Armstrong, F. A.; Hirst, J. Reversibility and efficiency in electrocatalytic energy conversion and lessons from enzymes. *Proc. Natl. Acad. Sci. U. S. A.* **2011**, *108*, 14049-14054.

(9) Evans, R. M.; Siritanaratkul, B.; Megarity, C. F.; Pandey, K.; Esterle, T. F.; Badiani, S.; Armstrong, F. A. The value of enzymes in solar fuels research - efficient electrocatalysts through evolution. *Chem. Soc. Rev.* **2019**, *48*, 2039-2052.

(10) Greene, B. L.; Wu, C.-H.; McTernan, P. M.; Adams, M. W.; Dyer, R. B. Proton-coupled electron transfer dynamics in the catalytic mechanism of a [NiFe]-hydrogenase. *J. Am. Chem. Soc.* **2015**, *137*, 4558-4566.

(11) Greene, B. L.; Wu, C.-H.; Vansuch, G. E.; Adams, M. W.; Dyer, R. B. Proton inventory and dynamics in the Nia-S to Nia-C transition of a [NiFe] hydrogenase. *Biochemistry* **2016**, *55*, 1813-1825.

(12) Greene, B. L.; Vansuch, G. E.; Wu, C.-H.; Adams, M. W. W.; Dyer, R. B. Glutamate gated proton-coupled electron transfer activity of a [NiFe]-hydrogenase. *J. Am. Chem. Soc.* **2016**, *138*, 13013-13021.

(13) Peters, J. W.; Schut, G. J.; Boyd, E. S.; Mulder, D. W.; Shepard, E. M.; Broderick, J. B.; King, P. W.; Adams, M. W. W. [FeFe]- and [NiFe]-hydrogenase diversity, mechanism, and maturation. *Biochim. Biophys. Acta, Mol. Cell Res.* **2015**, *1853*, 1350-1369.

(14) The PyMOL Molecular Graphics System, version 1.3, Schrödinger, LLC: New York 2010.

(15) Shafaat, H. S.; Rüdiger, Olaf; Ogata, H.; Lubitz, W. [NiFe] hydrogenases: A common active site for hydrogen metabolism under diverse conditions. *Biochim. Biophys. Acta, Bioenerg.* **2013**, *1827*, 986-1002.

(16) Tai, H.; Higuchi, Y.; Hirota, S. Comprehensive reaction mechanisms at and near the Ni-Fe active sites of [NiFe] hydrogenases. *Dalton Trans.* **2018**, *47*, 4408-4423.

(17) Ash, P. A.; Hidalgo, R.; Vincent, K. A. Proton transfer in the catalytic cycle of [NiFe] hydrogenases: Insight from vibrational spectroscopy. *ACS Catal.* **2017**, *7*, 2471-2485.

(18) Hidalgo, R.; Ash, P. A.; Healy, A. J.; Vincent, K. A. Infrared spectroscopy during electrocatalytic turnover reveals the Ni-L active site state during H_2 oxidation by a NiFe hydrogenase. *Angew. Chem., Int. Ed.* **2015**, *54*, 7110-7113.

(19) Bagyinka, C.; Whitehead, J. P.; Maroney, M. J. An X-ray absorption spectroscopic study of nickel redox chemistry in hydrogenase. *J. Am. Chem. Soc.* **1993**, *115*, 3576-3585.

(20) Tai, H.; Nishikawa, K.; Higuchi, Y.; Mao, Z.-w.; Hirota, S. Cysteine SH and glutamate COOH contributions to [NiFe] hydrogenase proton transfer revealed by highly sensitive FTIR spectroscopy. *Angew. Chem., Int. Ed.* **2019**, *131*, 13419-13424.

(21) Dementin, S.; Burlat, B.; De Lacey, A. L.; Pardo, A.; Adryanczyk-Perrier, G.; Guigliarelli, B.; Fernandez, V. M.; Rousset, M. A glutamate is the essential proton transfer gate during the catalytic cycle of the [NiFe] hydrogenase. *J. Biol. Chem.* **2004**, *279*, 10508-10513.

(22) Kampa, M.; Pandelia, M.-E.; Lubitz, W.; van Gastel, M.; Neese, F. A metal–metal bond in the light-induced state of [NiFe] hydrogenases with relevance to hydrogen evolution. *J. Am. Chem. Soc.* **2013**, *135*, 3915-3925.

(23) Ogata, H.; Nishikawa, K.; Lubitz, W. Hydrogens detected by subatomic resolution protein crystallography in a [NiFe] hydrogenase. *Nature* **2015**, *520*, 571-574.

(24) De Lacey, A. L.; Fernández, V. M.; Rousset, M.; Cavazza, C.; Hatchikian, E. C. Spectroscopic and kinetic characterization of active site mutants of *Desulfovibrio fructosovorans* Ni-Fe hydrogenase. *J. Biol. Inorg. Chem.* **2003**, *8*, 129-134.

(25) Müller, A.; Tscherny, I.; Kappl, R.; Hatchikian, E. C.; Hüttermann, J.; Cammack, R. Hydrogenases in the "active" state: determination of g-matrix axes and electron spin distribution at the active site by 1H ENDOR spectroscopy. *J. Biol. Inorg. Chem.* **2002**, *7*, 177-194.

(26) Kampa, M.; Lubitz, W.; van Gastel, M.; Neese, F. Computational study of the electronic structure and magnetic properties of the Ni-C state in [NiFe] hydrogenases including the second coordination sphere. *J. Biol. Inorg. Chem.* **2012**, *17*, 1269-1281.

(27) Qiu, S.; Azofra, L. M.; MacFarlane, D. R.; Sun, C. Hydrogen bonding effect between active site and protein environment on catalysis performance in H2-producing [NiFe] hydrogenases. *Phys. Chem. Chem. Phys.* **2018**, *20*, 6735-6743.

(28) Lubitz, W.; Ogata, H.; Rüdiger, O.; Reijerse, E. Hydrogenases. *Chem. Rev.* **2014**, *114*, 4081-4148.

(29) Abou-Hamdan, A.; Ceccaldi, P.; Lebrette, H.; Gutierrez-Sanz, O.; Richaud, P.; Cournac, L.; Guigliarelli, B.; De Lacey, A. L.; Leger, C.; Volbeda, A.; Burlat, B.; Dementin, S. A threonine stabilizes the NiC and NiR catalytic intermediates of [NiFe]-hydrogenase. *J. Biol. Chem.* **2015**, *290*, 8550-8558.

(30) Smith, D. M. A.; Raugei, S.; Squier, T. C. Modulation of active site electronic structure by the protein matrix to control [NiFe] hydrogenase reactivity. *Phys. Chem. Chem. Phys.* **2014**, *16*, 24026-24033.

(31) Fontecilla-Camps, J. C.; Volbeda, A.; Cavazza, C.; Nicolet, Y. Stucture/Function relationships of [NiFe]- and [FeFe]-hydrogenases *Chem. Rev.* **2007**, *107*, 4273-4303.

(32) Evans, R. M.; Brooke, E. J.; Wehlin, S. A.; Nomerotskaia, E.; Sargent, F.; Carr, S. B.; Phillips, S. E.; Armstrong, F. A. Mechanism of hydrogen activation by [NiFe] hydrogenases. *Nat. Chem. Biol.* **2016**, *12*, 46-50.

(33) Escorcia, A. M.; Stein, M. QM/MM investigation of the role of a second coordination shell arginine in [NiFe]-hydrogenases. *Front. Chem.* **2018**, *6*.

(34) Brecht, M.; Gastel, M. v.; Buhrke, T.; Barbel, F.; Lubitz, W. Direct detection of a hydrogen ligand in the [NiFe] center of the regulatory H_2 sensing hydrogenase from *Ralstonia eutropha* in its reduced state by HYSCORE and ENDOR spectroscopy. *J. Am. Chem. Soc.* **2003**, *125*, 13075-13083.

(35) Foerster, S.; van Gastel, M.; Brecht, M.; Lubitz, W. An orientation-selected ENDOR and HYSCORE study of the Ni-C active state of Desulfovibrio vulgaris Miyazaki F hydrogenase. *J. Biol. Inorg. Chem.* **2005**, *10*, 51-62.

(36) Evans, R. M.; Ash, P. A.; Beaton, S. E.; Brooke, E. J.; Vincent, K. A.; Carr, S. B.; Armstrong, F. A. Mechanistic exploitation of a self-repairing, blocked proton transfer pathway in an O2-tolerant [NiFe]-hydrogenase. *J. Am. Chem. Soc.* **2018**, *140*, 10208-10220.

(37) Albracht, S. P. J. Nickel hydrogenases: in search of the active site. *Biochim. Biophys. Acta, Bioenerg.* **1994**, *1188*, 167-204.

(38) Brooke, E. J.; Evans, R. M.; Islam, S. T.; Roberts, G. M.; Wehlin, S. A.; Carr, S. B.; Phillips, S. E.; Armstrong, F. A. Importance of the active site "canopy" residues in an O_2-tolerant [NiFe]-hydrogenase. *Biochemistry* **2017**, *56*, 132-142.

(39) Beaton, S. E. The importance of the active site canopy in [NiFe]-hydrogenases from Escherichia coli. Ph.D. Thesis, University of Oxford, 2018.

(40) Stephan, D. W. The broadening reach of frustrated Lewis pair chemistry. *Science* **2016**, *354*, aaf7229-7221-aaf7229-7228.

(41) Fitch, C. A.; Platzer, G.; Okon, M.; García-Moreno E, B.; McIntosh, L. P. Arginine: Its pK(a) value revisited. *Protein Sci.* **2015**, *24*, 752-761.

(42) Szőri-Dorogházi, E.; Maróti, G.; Szőri, M.; Nyilasi, A.; Rákhely, G.; Kovács, K. L. Analyses of the large subunit histidine-rich motif expose an alternative proton transfer pathway in [NiFe] hydrogenases. *PLoS One* **2012**, *7*, e34666.

(43) Oteri, F.; Baaden, M.; Lojou, E.; Sacquin-Mora, S. Multiscale simulations give insight into the hydrogen in and out pathways of [NiFe]-hydrogenases from *Aquifex aeolicus* and *Desulfovibrio fructosovorans*. *J. Phys. Chem. B* **2014**, *118*, 13800-13811.

(44) Harris, T. K.; Turner, G. J. Structural Basis of Perturbed pKa Values of Catalytic Groups in Enzyme Active Sites. *IUBMB Life* **2002**, *53*, 85-98.

(45) Harms, M. J.; Schlessman, J. L.; Sue, G. R.; García-Moreno E, B. Arginine residues at internal positions in a protein are always charged. *Proc. Natl. Acad. Sci. U. S. A.* **2011**, *108*, 18954-18959.

(46) Kwon, H.; Basran, J.; Devos, J. M.; Suardíaz, R.; van der Kamp, M. W.; Mulholland, A. J.; Schrader, T. E.; Ostermann, A.; Blakeley, M. P.; Moody, P. C. E.; Raven, E. L. Visualizing the protons in a metalloenzyme electron proton transfer pathway. *Proc. Natl. Acad. Sci. U. S. A.* **2020**, *117*, 6484.

(47) Kampa, M. The electronic and geometric structure of [NiFe] hydrogenases studied by theoretical spectroscopy. Technische Universitat Berlin, 2013.

(48) Stadler, C.; de Lacey, A. L.; Montet, Y.; Volbeda, A.; Fontecilla-Camps, J. C.; Conesa, J. C.; Fernandez, V. M. Density functional calculations for modeling the active site of nickel-iron hydrogenases. 2. Predictions for the unready and ready states and the corresponding activation processes. *Inorg. Chem.* **2002**, *41*, 4424-4434.

(49) Greene, B. L. Proton, electron and proton-coupled electron transfer dynamics in the catalytic mechanism of [NiFe] and [FeFe] hydrogenases. Ph.D. Thesis, Emory University, 2015.

(50) Kawahara-Nakagawa, Y.; Nishikawa, K.; Nakashima, S.; Inoue, S.; Ohta, T.; Ogura, T.; Shigeta, Y.; Fukutani, K.; Yagi, T.; Higuchi, Y. New assay method based on Raman spectroscopy for enzymes reacting with gaseous substrates. *Protein Sci.* **2019**, *28*, 663-670.

(51) Silva, P. J.; De Castro, B.; Hagen, W. R. On the prosthetic groups of the NiFe sulfhydrogenase from *Pyrococcus furiosus*: topology, structure, and temperature-dependent redox chemistry. *J. Biol. Inorg. Chem.* **1999**, *4*, 284-291.

(52) Bleijlevens, B.; Broekhuizen, F. A.; De Lacey, A. L.; Roseboom, W.; Fernandez, V. M.; Albracht, S. P. J. The activation of the [NiFe]-hydrogenase from *Allochromatium vinosum*. An infrared spectro-electrochemical study. *J. Biol. Inorg. Chem.* **2004**, *9*, 743-752.

(53) Chica, B. C. Semiconductor nanoparticle-protein hybrid systems for solar hydrogen production and photo-triggered mechanistic studies. Ph.D. Thesis, Emory University, 2017.

(54) Fichtner, C.; Laurich, C.; Bothe, E.; Lubitz, W. Spectroelectrochemical Characterization of the [NiFe] Hydrogenase of Desulfovibrio vulgaris Miyazaki F. *Biochemistry* **2006**, *45*, 9706-9716.

(55) Murphy, B. J.; Hidalgo, R.; Roessler, M. M.; Evans, R. M.; Ash, P. A.; Myers, W. K.; Vincent, K. A.; Armstrong, F. A. Discovery of Dark pH-Dependent H(+) Migration in a [NiFe]-Hydrogenase and Its Mechanistic Relevance: Mobilizing the Hydrido Ligand of the Ni-C Intermediate. *J. Am. Chem. Soc.* **2015**, *137*, 8484-8489.

(56) Preissler, J.; Wahlefeld, S.; Lorent, C.; Teutloff, C.; Horch, M.; Lauterbach, L.; Cramer, S. P.; Zebger, I.; Lenz, O. Enzymatic and spectroscopic properties of a thermostable [NiFe]-hydrogenase performing H2-driven NAD+-reduction in the presence of O2. *Biochim. Biophys. Acta, Bioenerg.* **2018**, *1859*, 8-18.

(57) Ogata, H.; Mizoguchi, Y.; Mizuno, N.; Miki, K.; Adachi, S.-i.; Yasuoka, N.; Yagi, T.; Yamauchi, O.; Hirota, S.; Higuchi, Y. Structural studies of the carbon monoxide complex of [NiFe]hydrogenase from *Desulfovibrio vulgaris* Miyazaki F: Suggestion for the initial activation site for dihydrogen. *J. Am. Chem. Soc.* **2002**, *124*, 11628-11635.

(58) Ilina, Y.; Lorent, C.; Katz, S.; Jeoung, J.-H.; Shima, S.; Horch, M.; Zebger, I.; Dobbek, H. X-ray crystallography and vibrational spectroscopy reveal the key determinants of biocatalytic dihydrogen cycling by [NiFe] hydrogenases. *Angew. Chem., Int. Ed.* **2019**, *58*, 18710-18714.

(59) Bagley, K. A.; Van Garderen, C. J.; Chen, M.; Woodruff, W. H.; Duin, E. C.; Albracht, S. P. J. Infrared studies on the interaction of carbon monoxide with divalent nickel in hydrogenase from *Chromatium vinosum*. *Biochemistry* **1994**, *33*, 9229-9236.

(60) De Lacey, A. L.; Stadler, C.; Fernandez, V. M.; Hatchikian, E. C.; Fan, H.-J.; Li, S.; Hall, M. B. IR spectroelectrochemical study of the binding of carbon monoxide to the active site of *Desulfovibrio fructosovorans* Ni-Fe hydrogenase. *J. Biol. Inorg. Chem.* **2002**, *7*, 318-326.

(61) Pandelia, M.-E.; Infossi, P.; Giudici-Orticoni, M. T.; Lubitz, W. The oxygen-tolerant hydrogenase I from *Aquifex aeolicus* weakly interacts with carbon monoxide: An electrochemical and time-resolved FTIR study. *Biochemistry* **2010**, *49*, 8873-8881.

(62) Yikilmaz, E.; Porta, J.; Grove, L. E.; Vahedi-Faridi, A.; Bronshteyn, Y.; Brunold, T. C.; Borgstahl, G. E. O.; Miller, A.-F. How can a single second sphere amino acid substitution cause reduction midpoint potential changes of hundreds of millivolts? *J. Am. Chem. Soc.* **2007**, *129*, 9927-9940.

(63) Stachura, M.; Chakraborty, S.; Gottberg, A.; Ruckthong, L.; Pecoraro, V. L.; Hemmingsen, L. Direct observation of nanosecond water exchange dynamics at a protein metal site. *J. Am. Chem. Soc.* **2017**, *139*, 79-82.

(64) Wang, H.; Ralston, C. Y.; Patil, D. S.; Jones, R. M.; Gu, W.; Verhagen, M.; Adams, M.; Ge, P.; Riordan, C.; Marganian, C. A.; Mascharak, P.; Kovacs, J.; Miller, C. G.; Collins, T. J.; Brooker, S.; Croucher, P. D.; Wang, K.; Steifel, E. I.; Cramer, S. P. Nickel L-edge soft x-ray spectroscopy of nickel-iron hydrogenases and model compounds-evidence for high-spin nickel(II) in the active enzyme. *J. Am. Chem. Soc.* **2000**, *122*, 10544-10552.

(65) Van der Zwaan, J. W.; Albracht, S. P. J.; Fontijn, R. D.; Slater, E. C. Monovalent nickel in hydrogenase from *Chromatium vinosum*. Light sensitivity and evidence for direct interaction with hydrogen. *FEBS Lett.* **1985**, *179*, 271-277.

(66) Saggu, M.; Zebger, I.; Ludwig, M.; Lenz, O.; Friedrich, B.; Hildebrandt, P.; Lendzian, F. Spectroscopic insights into the oxygen-tolerant membrane-associated [NiFe] hydrogenase of *Ralstonia eutropha* H16. *J. Biol. Chem.* **2009**, *284*, 16264-16276.

(67) Pandelia, M.-E.; Infossi, P.; Stein, M.; Giudici-Orticoni, M.-T.; Lubitz, W. Spectroscopic characterization of the key catalytic intermediate Ni-C in the O2-tolerant [NiFe] hydrogenase I from Aquifex aeolicus: evidence of a weakly bound hydride. *ChemComm* **2012**, *48*, 823-825.

(68) Carroll, M. E.; Barton, B. E.; Rauchfuss, T. B.; Carroll, P. J. Synthetic models for the active site of the [FeFe]-hydrogenase: Catalytic proton reduction and the structure of the doubly protonated intermediate. *J. Am. Chem. Soc.* **2012**, *134*, 18843-18852.

(69) Chambers, G. M.; Johnson, S. I.; Raugei, S.; Bullock, R. M. Anion control of tautomeric equilibria: Fe–H vs. N–H influenced by NH···F hydrogen bonding. *Chem. Sci.* **2019**, *10*, 1410-1418.

(70) Clegg, W.; Henderson, R. A. Kinetic evidence for intramolecular proton transfer between nickel and coordinated thiolate. *Inorg. Chem.* **2002**, *41*, 1128-1135.

(71) Henderson, R. A. Protonation mechanisms of nickel complexes relevant to industrial and biological catalysis. *J. Chem. Res., Synop.* **2002**, 407-411.

(72) Maroney, M. J.; Allan, C. B.; Chohan, B., S.; Choudhury, S. B.; Gu, Z.: Redox metalloenzymes featuring S-donor ligands hydrogenase: A case study. In *Transition Metal Sulfur Chemistry*; ACS Symposium Series 653; American Chemical Society, 1996; Vol. 653; pp 74-100.

(73) Winkler, M.; Duan, J.; Esselborn, J.; Happe, T.; Senger, M.; Stripp, S. T.; Wittkamp, F.; Apfel, U.-P.; Hofmann, E. Accumulating the hydride state in the catalytic cycle of [FeFe]-hydrogenases. *Nat. Commun.* **2017**, *8*, 16115.

(74) Mulder, D. W.; Guo, Y.; Ratzloff, M. W.; King, P. W. Identification of a catalytic iron-hydride at the H-cluster of [FeFe]-hydrogenase. *J. Am. Chem. Soc.* **2017**, *139*, 83-86.

(75) Lorent, C.; Katz, S.; Duan, J.; Kulka, C. J.; Caserta, G.; Teutloff, C.; Yadav, S.; Apfel, U.-P.; Winkler, M.; Happe, T.; Horch, M.; Zebger, I. Shedding light on proton and electron dynamics in [FeFe] hydrogenases. *J. Am. Chem. Soc.* **2020**, *142*, 5493-5497.

(76) Duan, J.; Senger, M.; Esselborn, J.; Engelbrecht, V.; Wittkamp, F.; Apfel, U.-P.; Hofmann, E.; Stripp, S. T.; Happe, T.; Winkler, M. Crystallographic and spectroscopic assignment of the proton transfer pathway in [FeFe]-hydrogenases. *Nat. Commun.* **2018**, *9*, 4726.

(77) Senger, M.; Eichmann, V.; Laun, K.; Duan, J.; Wittkamp, F.; Knör, G.; Apfel, U.-P.; Happe, T.; Winkler, M.; Heberle, J.; Stripp, S. T. How [FeFe]-hydrogenase facilitates bidirectional proton transfer. *J. Am. Chem. Soc.* **2019**, *141*, 17394-17403.

(78) Pham, C. C.; Mulder, D. W.; Pelmenschikov, V.; King, P. W.; Ratzloff, M. W.; Wang, H.; Mishra, N.; Alp, E. E.; Zhao, J.; Hu, M. Y.; Tamasaku, K.; Yoda, Y.; Cramer, S. P. Terminal hydride species in [FeFe]-hydrogenases are vibrationally coupled to the active site environment. *Angew. Chem., Int. Ed.* **2018**, *57*, 10605-10609.

(79) Van der Zwaan, J. W.; Coremans, J. M. C. C.; Bouwens, E. C. M.; Albracht, S. P. J. Effect of oxygen-17 and carbon-13 monoxide on EPR spectra of nickel in hydrogenase from *Chromatium vinosum*. *Biochim. Biophys. Acta, Protein Struct. Mol. Enzymol.* **1990**, *1041*, 101-110.

(80) Hidalgo, R. Infrared spectroelectrochemical study of *E. coli* NiFe hydrogenase 1. Ph.D Thesis, University of Oxford, 2016.

(81) Pardo, A.; De Lacey, A. L.; Fernández, V. M.; Fan, H.-J.; Fan, Y.; Hall, M. B. Density functional study of the catalytic cycle of nickel-iron [NiFe] hydrogenases and the involvement of high-spin nickel(II). *J. Biol. Inorg. Chem.* **2006**, *11*, 286-306.

Appendix

Aspects of the appendix have been reprinted with permission from Vansuch, G. E.; Wu, C.-H.; Haja, D. K.; Blair, S. A.; Chica, B.; Johnson, M. K.; Adams, M. W. W.; Dyer, R. B., *Chem. Sci.* **2020,** *11* (32), 8572-8581. Published by the Royal Society of Chemistry.

Appendix A: Electron Paramagnetic Resonance Spectra and Tabulated Fit Values

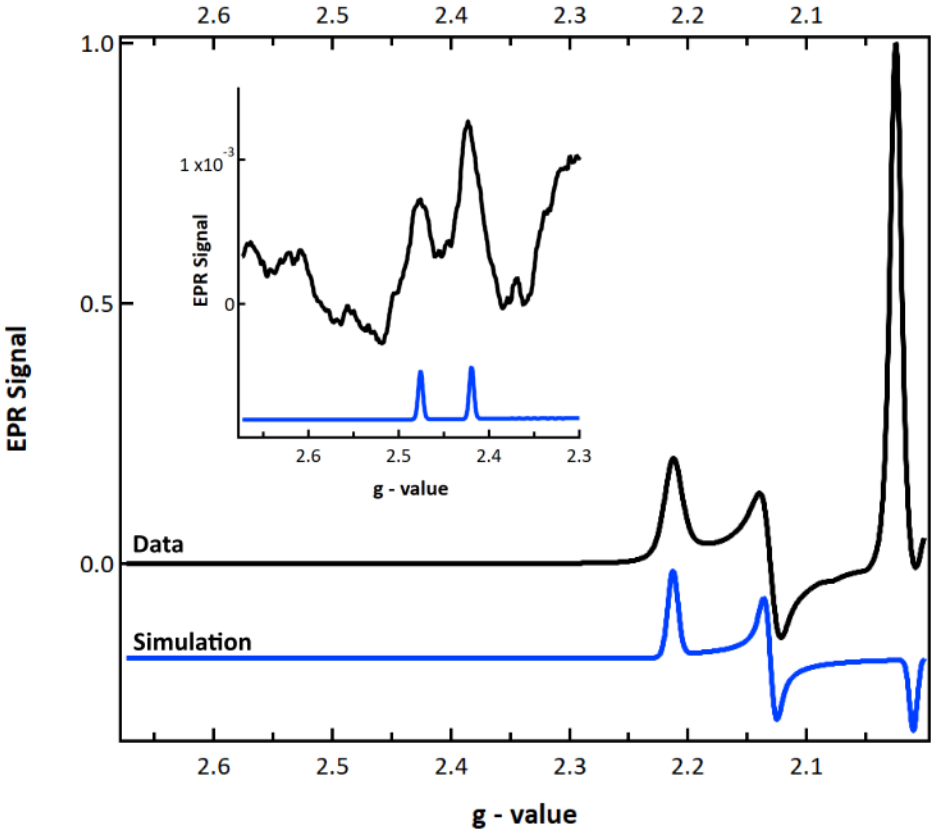

Figure A1: EPR spectrum of ~ 0.13 mM native SH1 at pH = 6.7. The temperature was 70 K. The modulation frequency was 100 kHz, the modulation amplitude was 0.4 mT, and the microwave power was 10 mW. The data represent an average of 100 scans. The inset displays two weak species observed with g_x ~ 2.4 – 2.5. Silva and coworkers previously observed a ready but inactive state with g_x ~ 2.48 in SH1 termed "Ready",[1] and the two very minor states observed here may be similar to these "Ready" states. The simulated data has been offset for clarity.

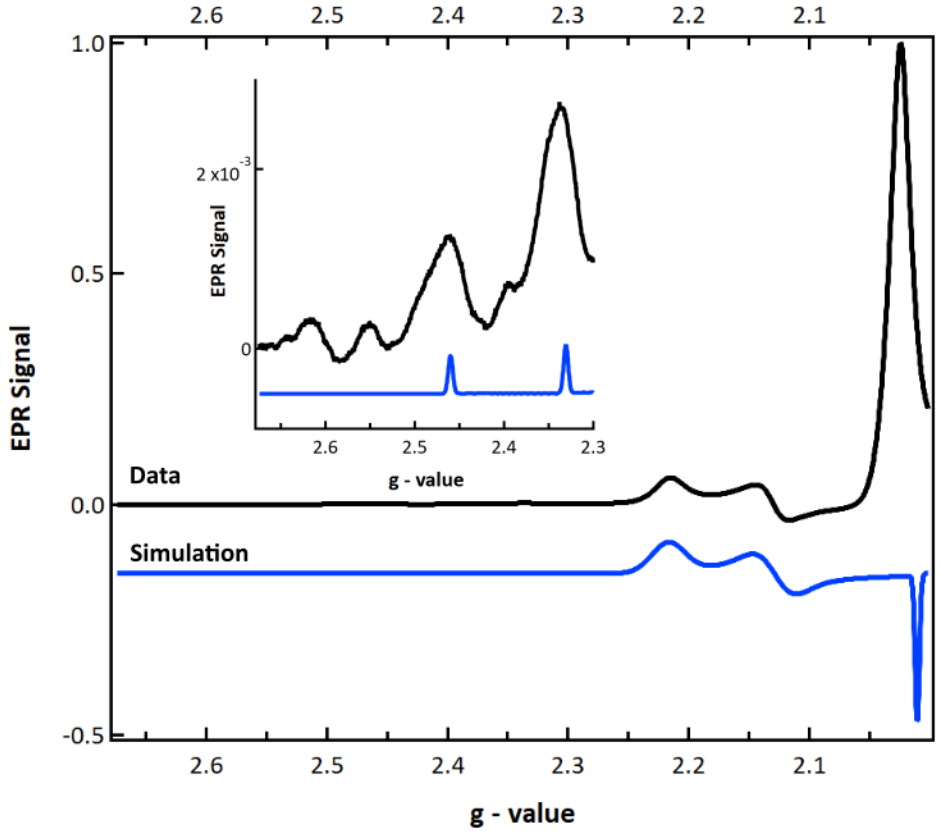

Figure A2: EPR spectrum of ~ 0.13 mM native SH1 at pH = 9.3. The temperature was 70 K. The modulation frequency was 100 kHz, the modulation amplitude was 0.4 mT, and the microwave power was 10 mW. The data represent an average of 500 scans. The inset displays two weak species observed with g_x ~ 2.3 – 2.5, which may be similar to the "Ready" and "Unready" states observed by Silva and co-workers.[1]

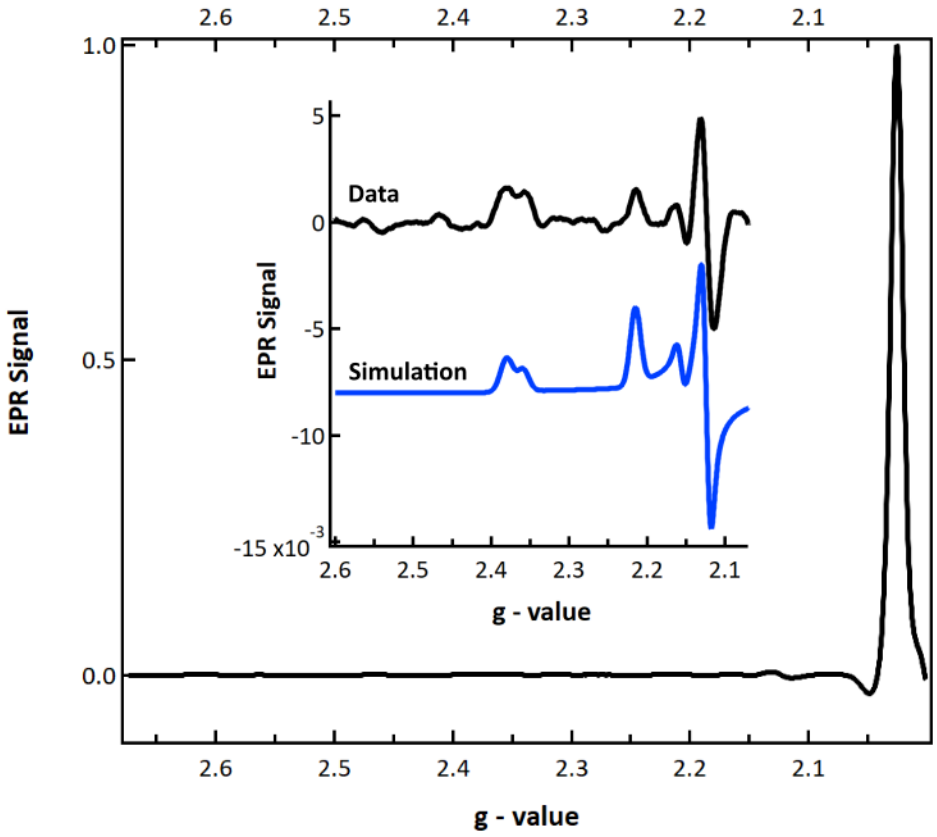

Figure A3: EPR spectrum of ~ 0.8 mM R355K SH1 at pH = 6.7. The temperature was 50 K. The modulation frequency was 100 kHz, the modulation amplitude was 0.4 mT, and the microwave power was 10 mW. The data represent an average of 225 scans. The inset displays the relevant g_y and g_x region and the corresponding three component spectral fit. The simulated data has been offset for clarity.

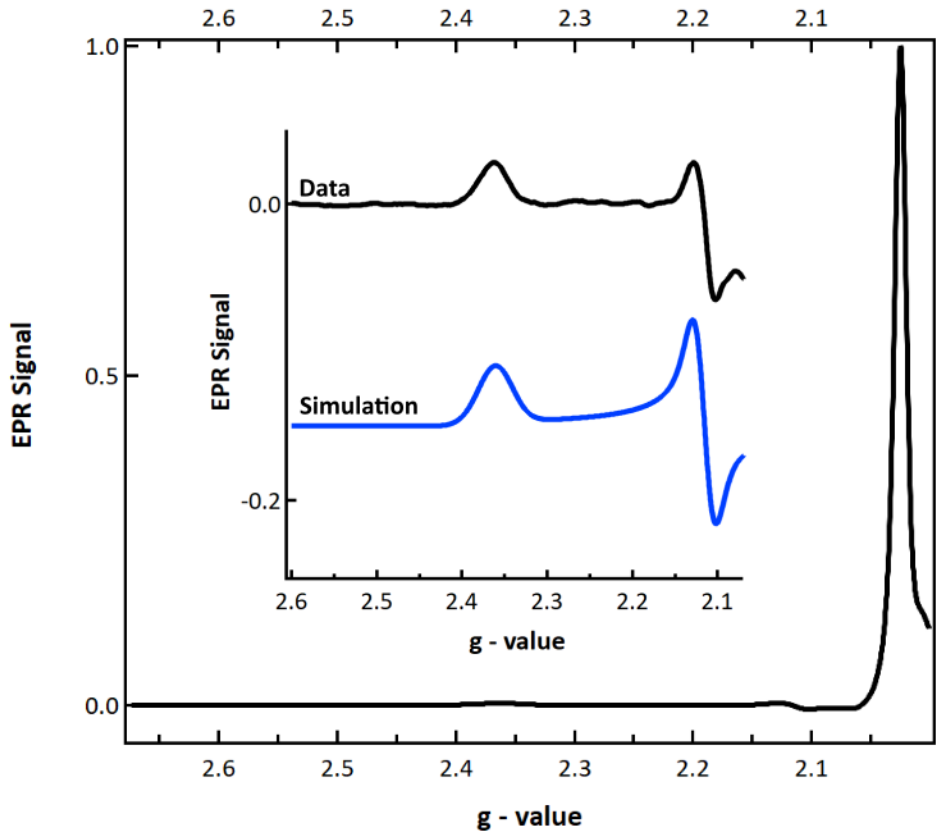

Figure A4: EPR spectrum of ~ 0.8 mM R355K SH1 at pH = 9.3. The temperature was 70 K. The modulation frequency was 100 kHz, the modulation amplitude was 0.4 mT, and the microwave power was 10 mW. The data represent an average of 100 scans. The inset displays the relevant g_y and g_x region and the corresponding minimal one component spectral fit. The simulated data has been offset for clarity.

Table A1. Native *Pf* SH1 at pH = 6.7; g – values determined from a three component rhombic EPR fit. The corresponding g-strains (peak widths) are provided in parenthesis.

State, pH = 6.7	g_z	g_y	g_x
Ni_a^{3+}-C	2.010 (0.0075)	2.131 (0.01)	2.218 (0.01)
Ni_r^{3+}-B like[1]	2.010 (0.0075)	2.131 (0.0095)	2.420 (0.0055)
Ni_r^{3+}-B like[1]	2.010 (0.0075)	2.130 (0.0095)	2.476 (0.0055)

Table A2. Native *Pf* SH1 at pH = 9.3; g – values determined from a three component rhombic EPR fit. The corresponding g-strains (peak widths) are provided in parenthesis.

State, pH = 9.3	g_z	g_y	g_x
Ni_a^{3+}-C	2.010 (0.0035)	2.128 (0.033)	2.217 (0.032)
Ni_u^{3+} - X[1]	2.010 (0.0035)	2.128 (0.032)	2.330 (0.0055)
Ni_r^{3+}-B like[1]	2.010 (0.0035)	2.128 (0.032)	2.456 (0.0055)

[1]Tentative oxidized states observed by our laboratory in native SH1 displayed very weak signals that were only clear in the g_x region (see **Figures A1 – A2**).

Table A3. R355K *Pf* SH1 at pH = 6.7 g – values determined from a three component rhombic EPR fit. The corresponding g-strains (peak widths) are provided in parenthesis.

State, pH = 6.7	g_z	g_y	g_x
Ni_a^{+}-L1	2.045 (0.008)	2.124 (0.0115)	2.380 (0.0189)
Ni^{3+}-X	2.045 (0.008)	2.156 (0.0115)	2.359 (0.0170)
Ni_a^{3+}-C	2.045 (0.008)	2.124 (0.0115)	2.215 (0.0155)

Table A4. R355K *Pf* SH1 at pH = 9.3 g – values determined from a rhombic EPR fit using a minimal one component system. The corresponding g-strains (peak widths) are provided in parenthesis.

State, pH = 9.3	g_z	g_y	g_x
Ni_a^{+}-L	2.045 (0.0025)	2.116 (0.025)	2.362 (0.047)

Table A5: Tabulation of g – values of Ni_a^{3+}-C and Ni_a^{+}-L from various [NiFe]-hydrogenases and the corresponding $g_y(Ni_a^{3+}\text{-C}) - g_y(Ni_a^{+}\text{-L})$ value and $g_x(Ni_a^{3+}\text{-C}) - g_x(Ni_a^{+}\text{-L})$ values, which were used to ultimately identify the paramagnetic state(s) in R355K *Pf* SH1. The g – values are listed in the order of: g_z, g_y, g_x. Each enzyme group and subgroup is also provided.[2,3]

Enzyme source	Group	Ni_a^{3+}-C	Ni_a^{+}-L	g_y (Ni_a^{+}-C) – g_y (Ni_a^{3+}-L)	g_x (Ni_a^{3+}-C) – g_x (Ni_a^{+}-L)	Ref.
Allochromatium vinosum	1e	2.01, 2.15, 2.21	2.05, 2.12, 2.26 2.05, 2.12, 2.28	0.03	- (0.05 - 0.07)	[4,5]
Wolinella succinogenes	1b	2.01, 2.15, 2.195	2.045, 2.125, 2.295 nd, 2.15, 2.265	(0 – 0.025)	-(0.07 – 0.1)	[6]
Thiocapsa roseopersicina	1e	2.02, 2.15, 2.19	2.05, 2.13, 2.29	0.02	- 0.10	[7]
Desulfovibrio vulgaris Miyazaki F	1a	2.01, 2.142, 2.20	2.049, 2.116, 2.30 n.d., n.d., 2.321	0.026	- (0.10 – 0.121)	[5,8-10]
Desulfovibrio gigas	1a	2.009, 2.146, 2.192	2.044, 2.113, 2.264 2.045, 2.124, 2.293 n.d., 2.16, 2.41	(-0.0140 – 0.033)	-(0.072 – 0.218)	[11-13]
Desulfovibrio fructosovorans	1b	2.009, 2.146, 2.192	2.044, 2.113, 2.264 2.045, 2.124, 2.293	(0.022 – 0.033)	- (0.072 – 0.101)	[12]
Aquifex aeolicus hydrogenase-1	1d	2.01, 2.15, 2.21	2.05, 2.15, 2.33 2.05, 2.12, 2.28	(0.00 – 0.03)	- (0.07 – 0.12)	[14]
Escherichia coli hydrogenase-1	1d	2.01, 2.14, 2.21	2.05, 2.14, 2.33	0.00	- 0.12	[15,16]
Ralstonia eutropha H16 trimer[1] (membrane bound hydrogenase)	1d	2.01, 2.14, 2.20	2.05, 2.11, 2.30 2.05, 2.11, 2.27 2.05, 2.11, 2.24	0.03	- (0.04 – 0.10)	[17]
Ralstonia eutropha H16 (cytoplasmic H_2 sensor)	2b	2.015, 2.139, 2.197	2.046, 2.094, 2.251 2.054, 2.077, 2.305	(0.045 – 0.062)	-(0.054 – 0.108)	[18,19]
Ralstonia eutropha H16 (cytoplasmic NAD^+ – linked)	3d	2.016, 2.139, 2.208	2.051, 2.105, 2.281	0.034	-0.073	[20]
Acidithiobacillus ferrooxidans[2]	2a	2.008, 2.150, 2.215	2.038, 2.116, 2.276	0.034	-0.061	[5,21]
Pyrococcus furiosus soluble hydrogenase -1, *prior work*	3b	n.d., 2.137, 2.2185	n.o.	n.d.	n.d.	[1]
			Average	0.025	-0.09	
			Standard Deviation	0.016	0.04	
Pyrococcus furiosus soluble hydrogenase -1[3]	3b	n.d., 2.13, 2.22	n.d., 2.12, 2.36/8	0.01	-(0.14 – 0.16)	This work

n.d. : not determined; n.o: not observed

[1] The trimeric is membrane bound and remains associated with the natural redox partner cytochrome b; when isolated from the membrane, the enzyme is a soluble dimer. For the dimer, the g values are (2.01, 2.14, 2.20) for Ni_a^{3+} - C and (2.05, 2.10, 2.25) for Ni_a^{+} - L.[17]

[2] For the isolated enzyme. Whole cell values are: (2.10, 2.149 and 2.212) for Ni_a^{3+} - C and (2.039, 2.116, 2.275) for Ni_a^{+} - L.[21]

[3] Ni_a^{+} - L signals are from the R355K variant.

Appendix B: Native *Pf* SH1 FTIR Auto-Oxidation Montiored by FTIR and Additional E17Q Auto-Oxidation FTIR Plots

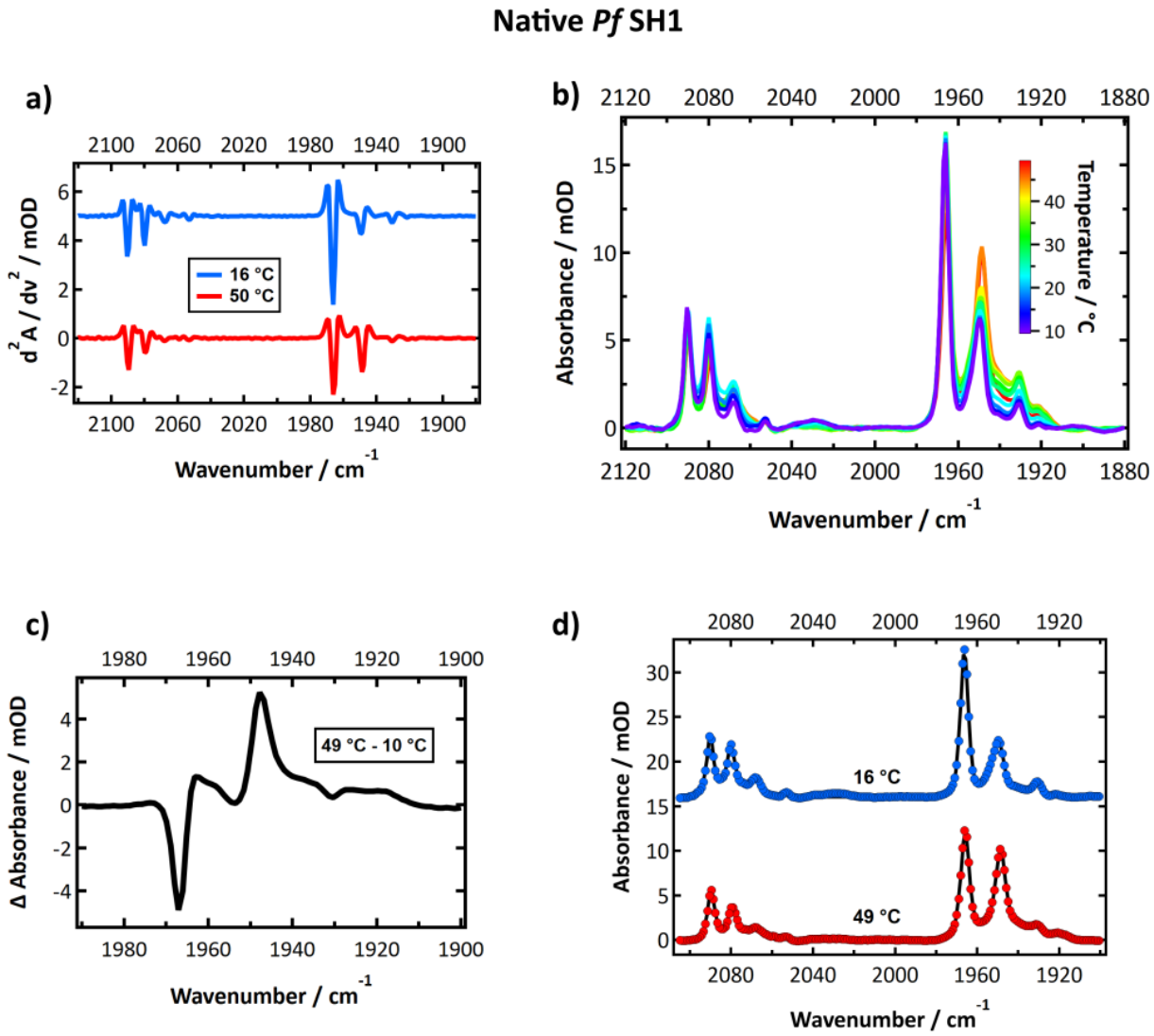

Figure B1: **a)** Select second derivative spectra of native SH1 FTIR absorbance spectra from a temperature ramp (auto-oxidation). **b)** Corresponding from the temperature ramp (~ 10 – 50 °C). **c)** Difference spectrum of the highest minus the lowest temperature. **d)** Select absorbance spectra and corresponding spectral fits. The major changes are the bleach of Ni_a^{3+}-C and Ni_a^{2+}-SR near 1967 and 1954 cm^{-1} and growth of the Ni_a^{2+}-S feature near ~ 1948 cm^{-1}. Conditions: pH = 8.5 (50 mM HEPPS buffer). The enzyme concentration was 300 - 400 µM. Offsets added for clarity.

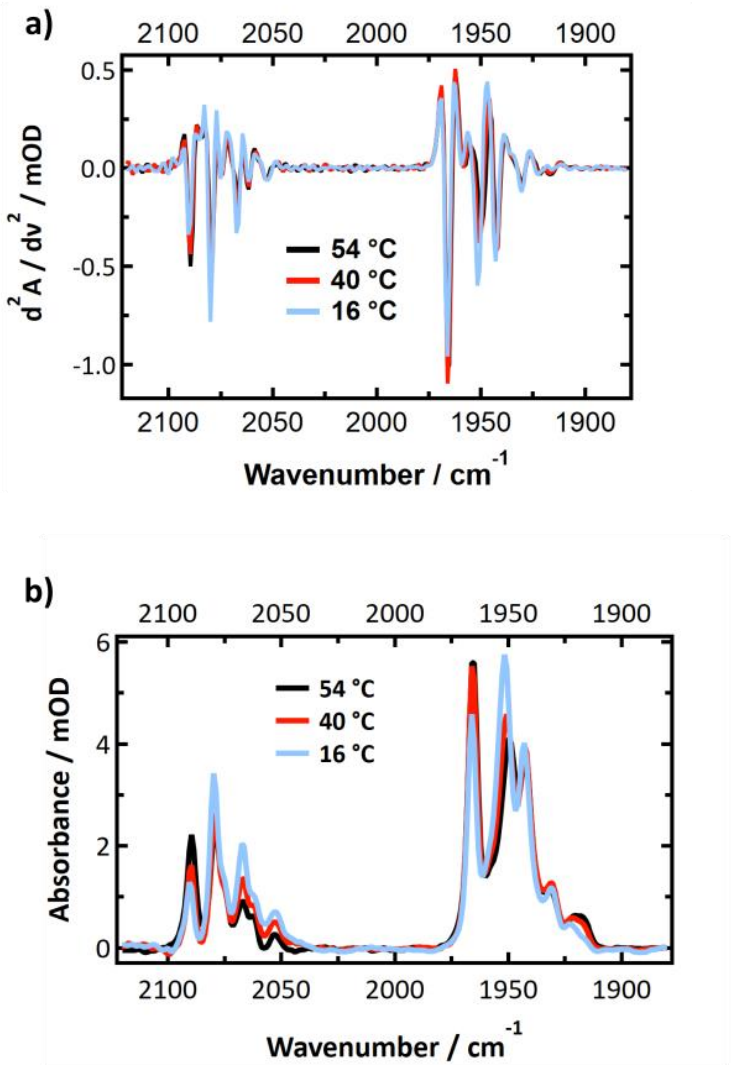

Figure B2: Select second derivative spectra and temperature dependent FTIR spectra from the E17Q temperature ramp (auto-oxidation) for visual clarity.

Appendix C: Second Derivative Spectra, Non-Normalized E17D pH Dependent FTIR Spectra, and the CN Region from the Photochemical Reduction

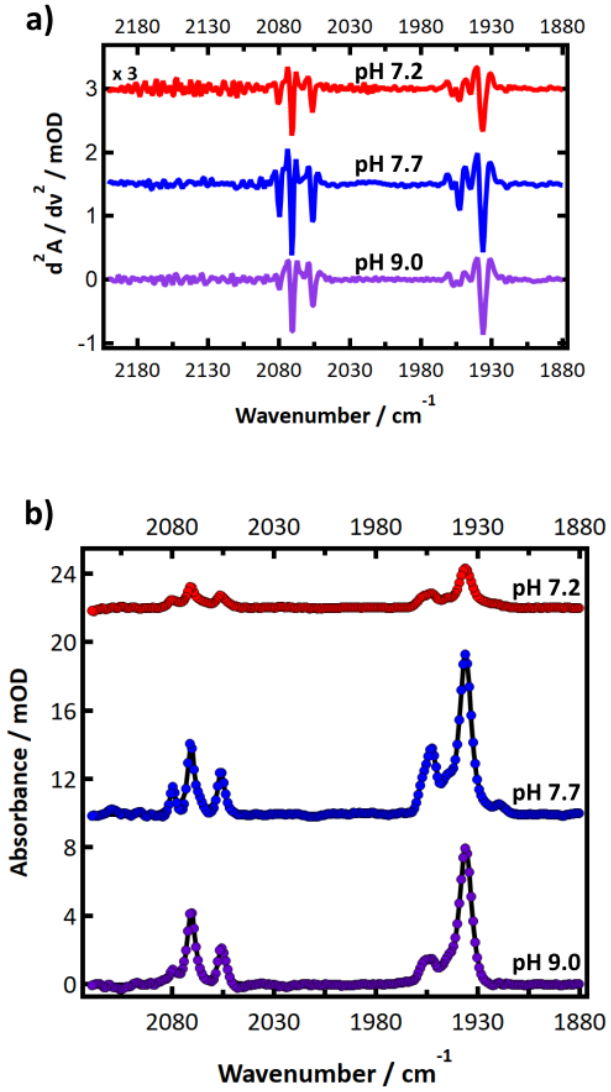

Figure C1: a) Second derivative spectra of the E17D pH dependent samples. **b)** Non-normalized spectra and spectral fits. Offsets added for clarity.

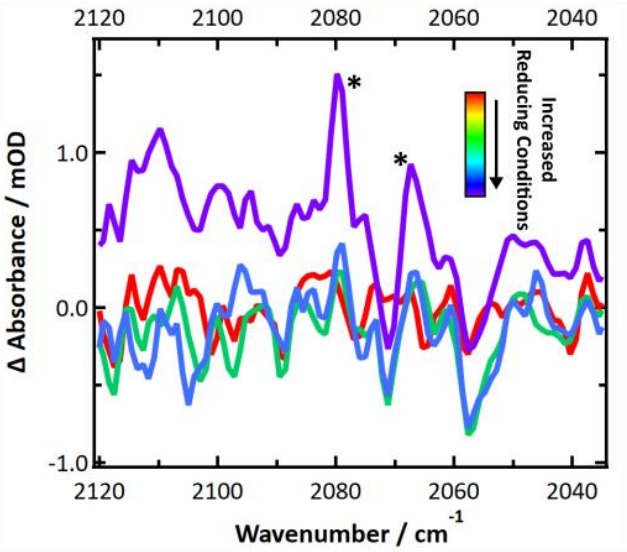

Figure C2: The ν_{CN} region of the E17D photoreduction difference spectra (light – dark). Bolded asterisk correspond to locations where Ni_a^{2+}-SR peaks would be expected based on comparison to native *Pf* SH1 (see **Figure B1** and **B2**).

Appendix D: H/D Exchange Calibration, Data Analysis, and Additional Analysis

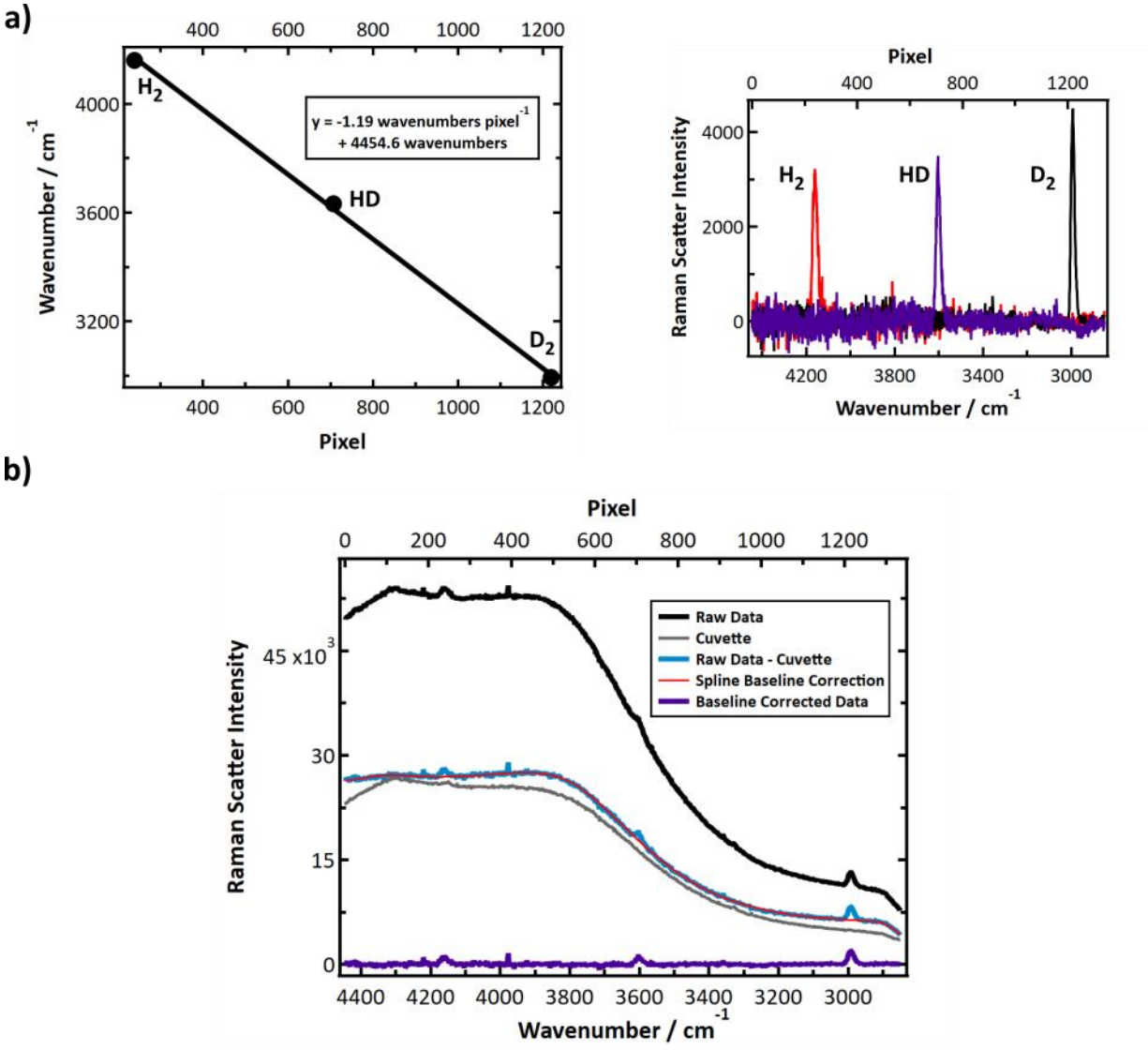

Figure D1: a) Linear relationship obtained for pixel number and Raman scatter position based on the peak position of D_2, HD, and H_2 gas standards. The wavenumber axes of the right hand figure was generated by fixing the center pixel of H_2 as 4160 cm^{-1} and using the slope of calibration curve to assign wavenumber values to the other pixels. **b)** Example analysis of a Raman spectrum from an H/D exchange experiment for native SH1 using the data corresponding to 260 minutes.

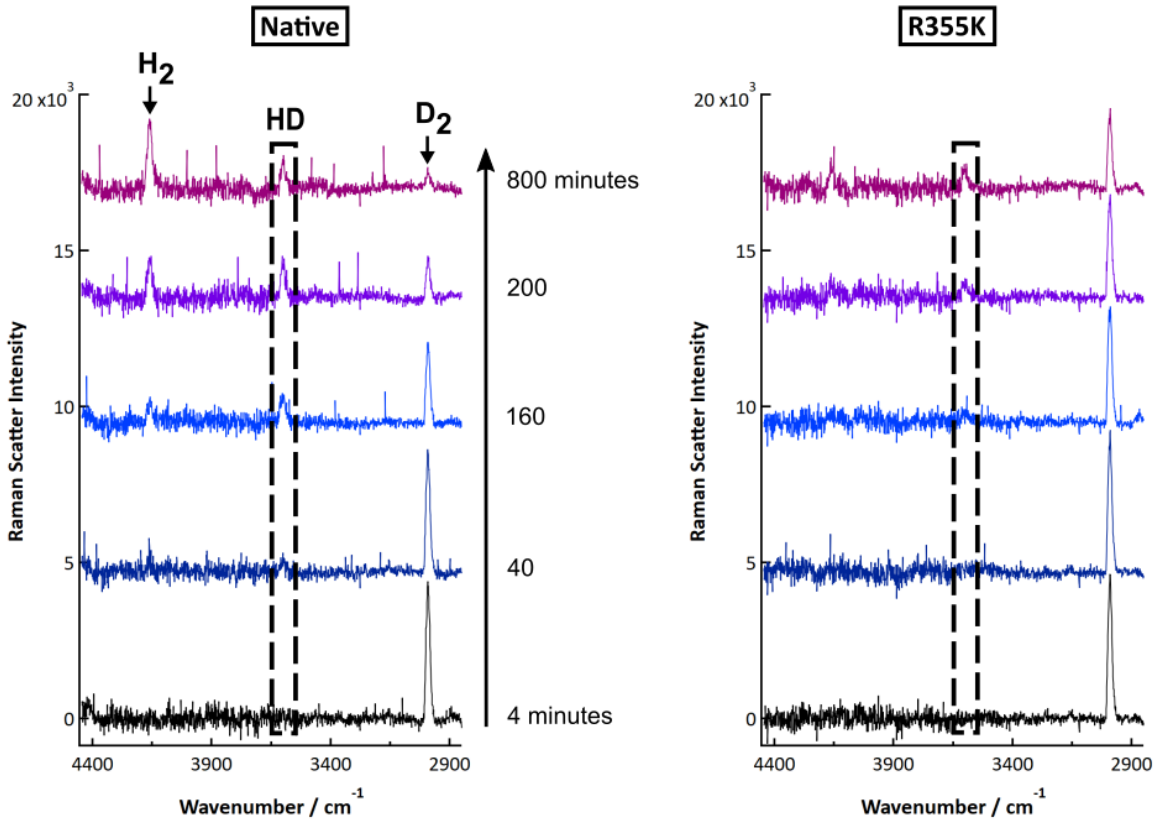

Figure D2: Time dependent Raman spectra of 222 nM native SH1 and 412 nM R355K SH1 during H/D exchange measurements from 4 – 800 minutes in 50 mM KP_i buffer, pH = 6.3, and 1.5 mM dithionite.

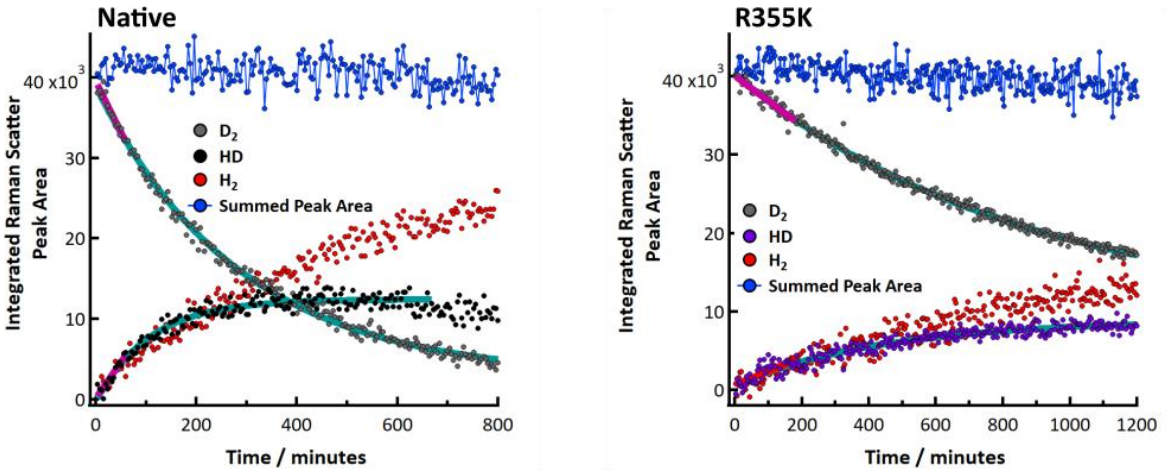

Figure D3: Time course plots of D_2 consumption and HD and H_2 production by native and R355K enzyme from plotting the integrated Raman scatter of the respective peaks at the full width half maximum values obtained from the standards; concentrations were 222 nm native enzyme and 412 nM R355K enzyme. For native enzyme, the linear fits correspond to the first 60 minutes, and the exponential fit to the first 668 minutes of the assay for HD formation and 800 minutes for D_2 consumption. Results of the individual fits are provided in **Table D1**. For R355K enzyme, linear fits correspond to the first 180 minutes, and the exponential fit to 1200 minutes. Results of the individual fits are provided in **Table D1**. Note: because of the small amount of H_2 produced (see **Figure D2**, for example), we anticipate much of the integrated peak area for H_2 at early time is just inherent noise from the measurements, which is why we precluded from quantitatively analyzing the H_2 production. However, as seen in **Figure D2**, H_2 is clearly detected at later time.

Table D1: Linear (method of initial rates for the first 60 minutes of data collection for native SH1 and 180 minutes of data collection for R355K SH1) and exponential fits to the integrated Raman scatter areas of D_2 and HD in **Figures S4 and S5** for native (*222 nM*) and R355K SH1 (*412 nM*). Errors are provided in parenthesis.

Enzyme	Linear (Slope) / Peak Area min^{-1}	Linear Intercept / Peak Area	Exponential rate / min^{-1}	Exponential Amplitude / Peak Area	Exponential Offset / Peak Area
Native, HD	89 (11)	90 (400)	9.2 (0.5) x 10^{-3}	-13,000 (300)	12,000 (100)
R355K, HD	17.1 (3)	600 (300)	2.2 (0.13) x 10^{-3}	-8,000 (200)	9,000 (200)
Native, D_2	-127 (11)	40,000 (400)	3.5 (0.06) x 10^{-3}	36,000 (200)	3,000 (200)
R355K, D_2	-30 (2)	40,000 (200)	1.1 (0.03) x 10^{-3}	30,000 (400)	10,000 (400)

Table D2: Maximum amount of HD produced and the amount of D_2 consumed by native and R355K SH1.

Enzyme	Maximum HD Peak Area	Scaled HD Peak Area	Percentage of Starting D_2 Consumed	Scaled Percentage of D_2 Consumed
Native	12,200	-	90%	-
R355K	8,300 (1200 minutes) 7,700 (800 minutes)	4,500 (1200 minutes) 4,100 (800 minutes)	56% (1200 minutes) 47% (800 minutes)	30% (1200 minutes) 25% (800 minutes)

Appendix E: Second Derivative Spectra, Absorbance Spectra, and the ν_{CN} Region Difference Spectra from R355K Steady State Photochemical Reduction

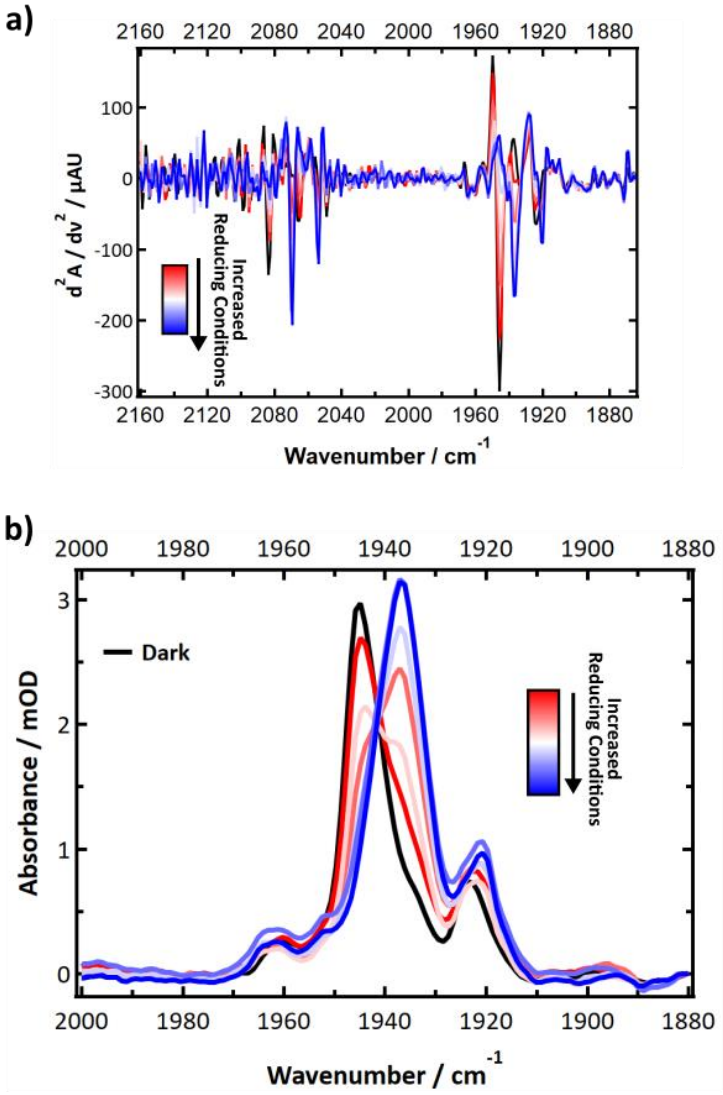

Figure E1: a) Second derivatives of the FTIR absorbance spectra collected during the steady state photochemical reduction of R355K SH1 prior to performing a baseline correction. **b)** FTIR absorbance spectra collected during the steady state photochemical potential reduction of R355K SH1.

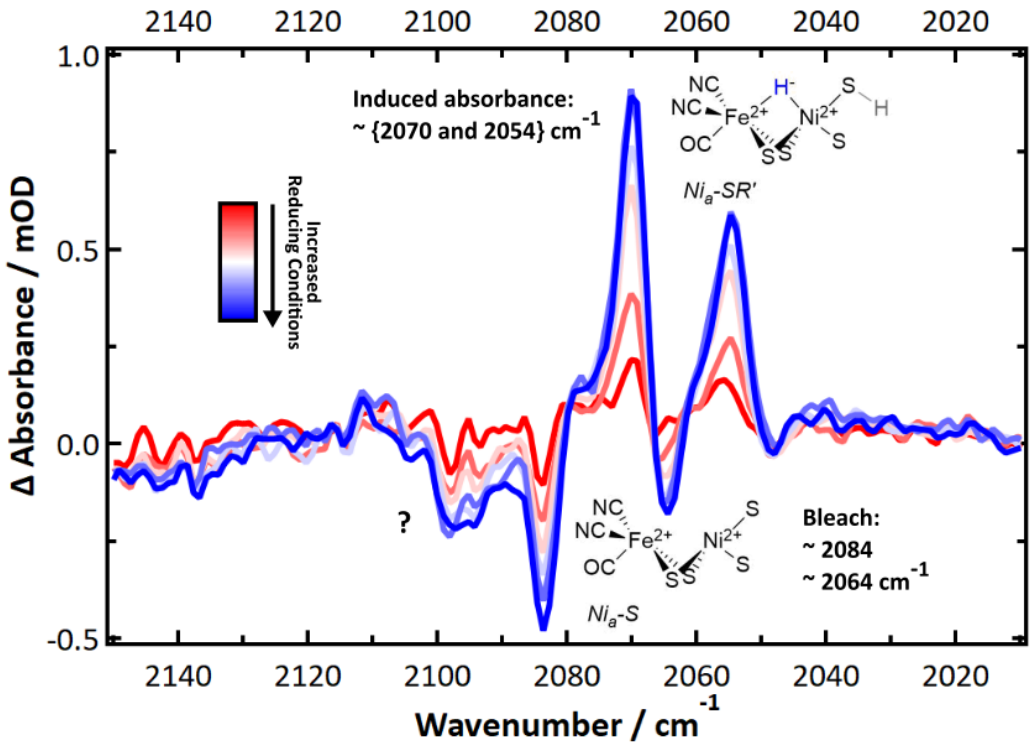

Figure E2: a Difference spectra (light – dark) during the steady state photochemical reduction of R355K in the ν_{CN} region. The spectra are from the data set used in **Figure 4.5b**. The data in **Figure 4.5b** show a clear bleach of Ni_a^{2+}-S and a clear induced absorbance of Ni_a^{2+}-SR'. We accordingly assign the clear bleach at 2084 cm^{-1} to one of the CN stretches for Ni_a^{2+}-S, and the clear absorbances near 2070 and 2054 cm^{-1} to the symmetric and antisymmetric CN stretches for Ni_a^{2+}-SR'. The bleach near 2064 could correspond to Ni_a^{2+}-S (as the antisymmetric CN stretch). The possible bleach(es) near 2090 – 2100 cm^{-1} marked with a "?" could correspond to Ni_a^{2+}-S or signals overlapped with Ni_a^{2+}-S that are not resolved in the difference spectra, absorbance spectra, and ν_{CN} region. Because of the extreme spectral overlap, the ν_{CN} values may be distorted/shifted and are only approximate.

Appendix F: Second Derivative Spectra, Non-normalized Absorbance Spectra, Normalization Values, Peak Positions and Peak Areas Before and After Oscillator Strength Correction of the pH Dependnet R355K FTIR Spectra

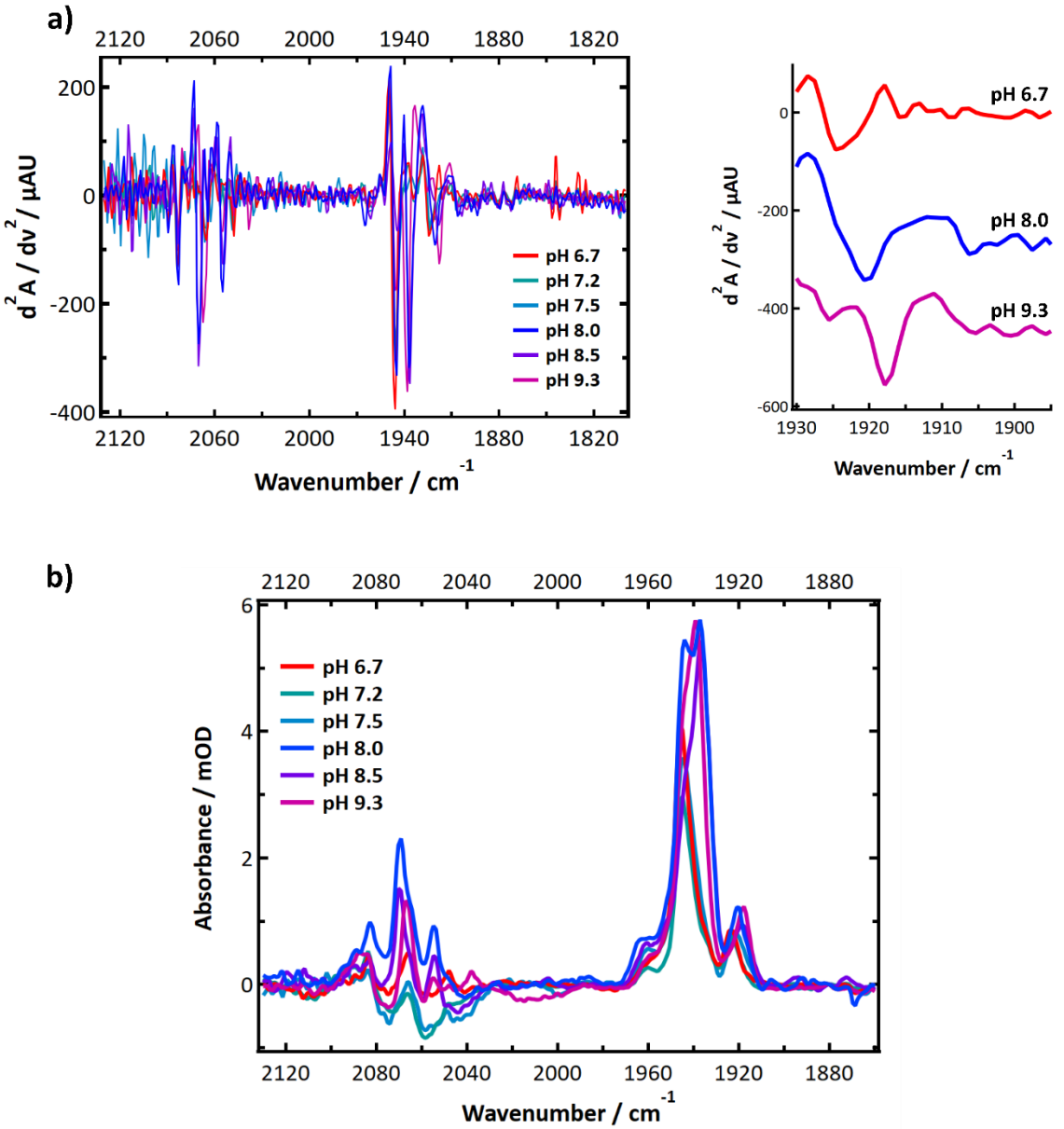

Figure F1: a) Second derivatives of the R355K FTIR spectra and a zoomed in version of the Ni_a^+-L region for pH = 6.7, 8.0, and 9.3; offsets added for clarity. b) Baseline corrected absorbance spectra. *Note:* to be consistent, we applied the baseline spline correction to the same region for each sample. This unfortunately led to negative feature artifacts in the ν_{CN} region of some samples.

Table F1: Area under of curve (AOC) used for normalization for each IR spectrum between 1880 – 2000 cm^{-1} after baseline correction and offset of the absorbance to 0.0 O.D. at 1880 cm^{-1}.

pH	**AOC, 1880 – 2000 cm^{-1}**
6.7	0.0547
7.2	0.0394
7.5	0.0551
8.0	0.117
8.5	0.0921
9.3	0.0871

Table F2: Peak positions from Voigt fits of the pH dependent spectra from pH 6.7 – 9.3. Errors are provided in parenthesis. Units are wavenumbers (cm^{-1}).

pH	**Ni_a^+-L1**	**Ni_a^+-L2**	**Ni_r^{2+}-S / Ni_a^{2+}-SR''**	**Ni_a^{2+}-SR'**	**Ni_a^{2+}-S**	**Ni_x^{2+}- ? / Ni_a^{2+}-SR**	**Ni_x^{3+}-X**
6.7	1916.8 (0.5)	1923.6 (0.098)	1934 (0.19)	1940.4 (0.2)	1945.8 (0.06)	1953.1 (0.3)	1960 (0.7)
7.2	1919.6 (0.8)	1923.9 (0.3)	1934 (0.15)	1940.6 (0.2)	1945.5 (0.08)	1953.2 (0.16)	1960.3 (0.17)
7.5	1916.8 (0.6)	1922.4 (0.3)	1934 (0.4)	1939.7 (0.4)	1945.1 (0.14)	1952.1 (0.3)	1960.2 (0.3)
8.0	1918.9 (0.8)	1923.2 (1.14)	1933.3 (0.4)	1937.8 (0.3)	1944.4 (0.07)	1951.4 (0.2)	1961.1 (0.3)
8.5	1917.1 (0.3)	1922.8 (0.6)	1932.4 (0.4)	1937.1 (0.2)	1943.6 (0.11)	1950.2 (0.3)	1959.2 (0.4)
9.3	1917.8 (0.08)	1924.6 (0.2)	1933.2 (0.3)	1938.6 (0.08)	1944.6 (0.06)	1951.6 (0.2)	1959.3 (0.3)

Table F3: Integrated peak areas at FWHM for the R355K pH dependent spectra (prior to scaling for oscillator strength differences).

pH	Ni_a^{+}-L1	Ni_a^{+}-L2	Ni_r^{2+}-S / Ni_a^{2+}-SR''	Ni_a^{2+}-SR'	Ni_a^{2+}-S	Ni_x^{2+}- ? / Ni_a^{2+}-SR	Ni_x^{3+}-X
6.7	0.011	0.061	0.044	0.0100	0.257	0.034	0.034
7.2	0.024	0.062	0.056	0.117	0.247	0.018	0.040
7.5	0.025	0.053	0.042	0.113	0.220	0.041	0.052
8.0	0.026	0.020	0.076	0.148	0.160	0.032	0.042
8.5	0.033	0.023	0.075	0.190	0.119	0.035	0.048
9.3	0.053	0.020	0.042	0.222	0.164	0.031	0.030

Table F4: Integrated peak areas at FWHM for the R355K pH dependent spectra scaled for oscillator strength differences[22] relative to the Ni_a^{+}-L(1/2) ν_{CO} region.

pH	Ni_a^{+}-L1	Ni_a^{+}-L2	Ni_r^{2+}-S / Ni_a^{2+}-SR''	Ni_a^{2+}-SR'	Ni_a^{2+}-S	Ni_x^{2+}- ? / Ni_a^{2+}-SR	Ni_x^{3+}-X
6.7	0.011	0.061	0.046	0.103	0.280	0.038	0.040
7.2	0.024	0.062	0.058	0.122	0.268	0.022	0.048
7.5	0.025	0.053	0.044	0.117	0.240	0.046	0.062
8.0	0.026	0.020	0.079	0.154	0.174	0.036	0.050
8.5	0.033	0.023	0.078	0.198	0.130	0.040	0.057
9.3	0.053	0.020	0.043	0.232	0.179	0.035	0.036

Appendix G: Methyl Viologen Reduction Under 5% H2 Monitored via UV-Vis Spectroscopy

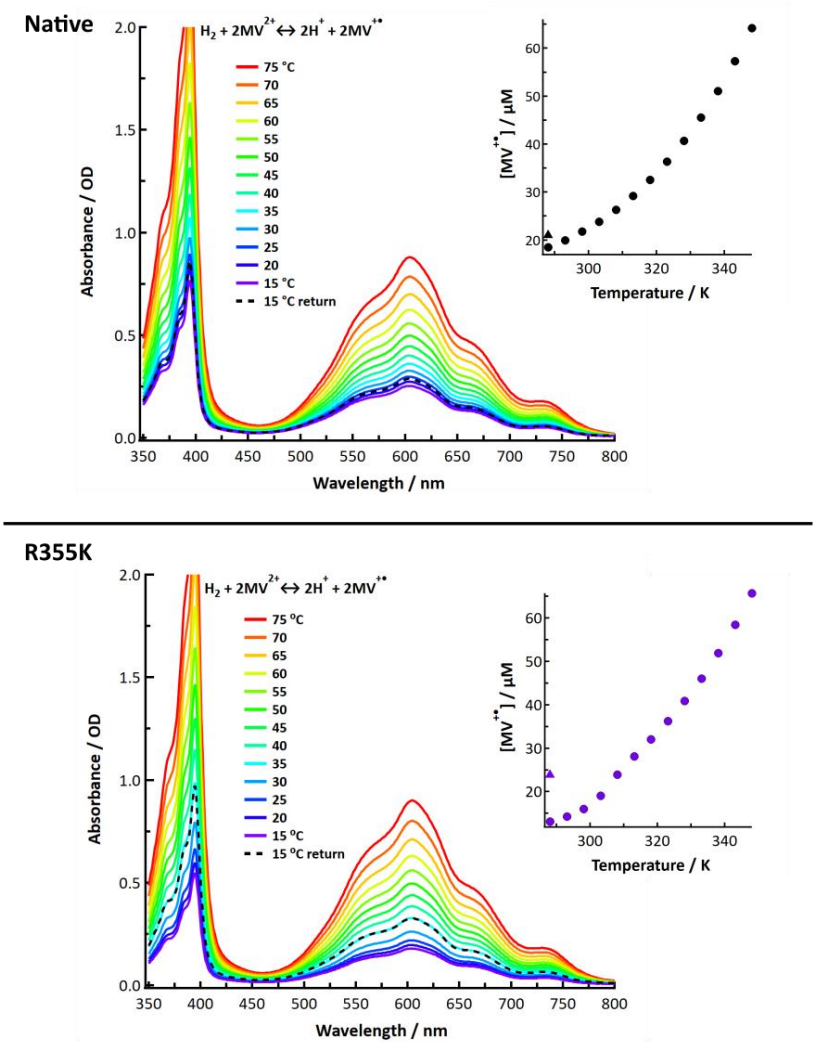

Figure G1: Temperature dependent equilibration of native SH1 with 5% hydrogen and an external electron donor/acceptor, methyl viologen.[23] This is a simple demonstration that native and R355K SH1 undergoes reversible redox behavior over a wide temperature range because the equilibration with the hydrogen and methyl viologen was reversible within reasonable error. Conditions: pH = 7.2, 50 mM KP_I buffer; 50 nM enzyme; 330 µM methyl viologen; and an ~5 % H_2 and 95% N_2 gas composition. Inset: The concentration of methyl viologen radical observed at a given temperature assuming an extinction coefficient of 13,700 $cm^{-1}M^{-1}$ at 605 nm.[24] Triangles are from the return to 15°C.

Appendix H: Second Derivatives of the R355K pH = 9.3 Day Dependent Spectra

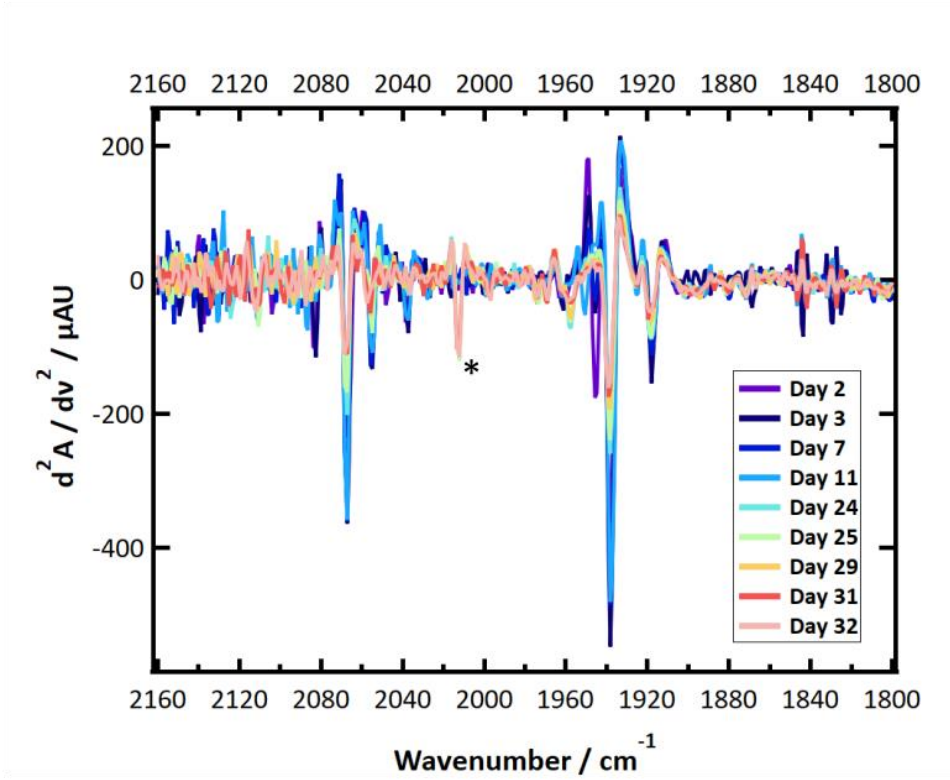

Figure H1: Second derivatives of the pH = 9.3 day dependent FTIR spectra.

Appendix I: Second Derivatives Plot, Individual Absorbance Spectra, and Tabulated Peak Positions of CO Incuabted Native, E17Q, and R355K

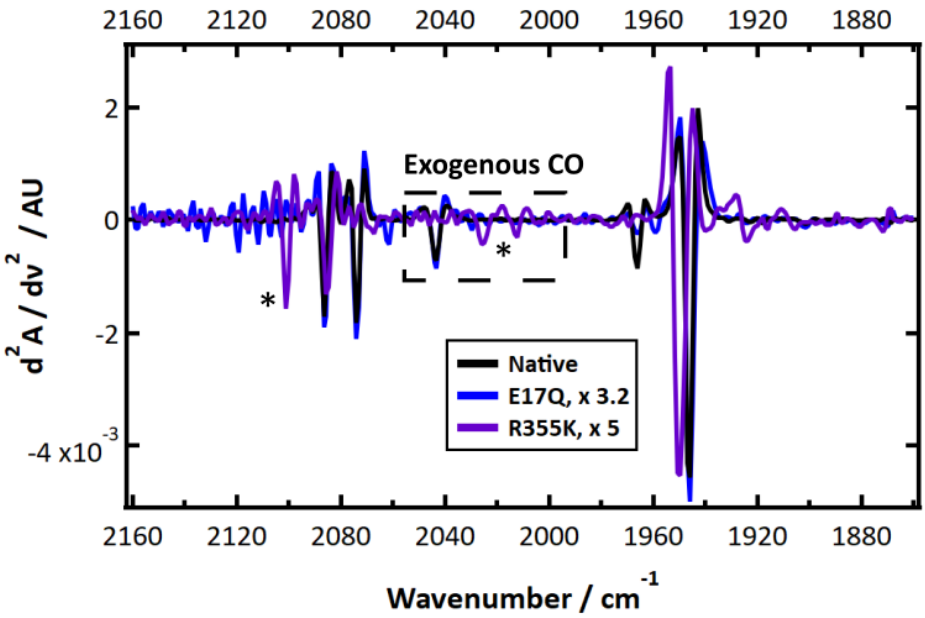

Figure I1: Second derivatives of the pH = 8.0 CO incubated samples; 50 mM HEPES or HEPPS buffer was used for the sample preparation.

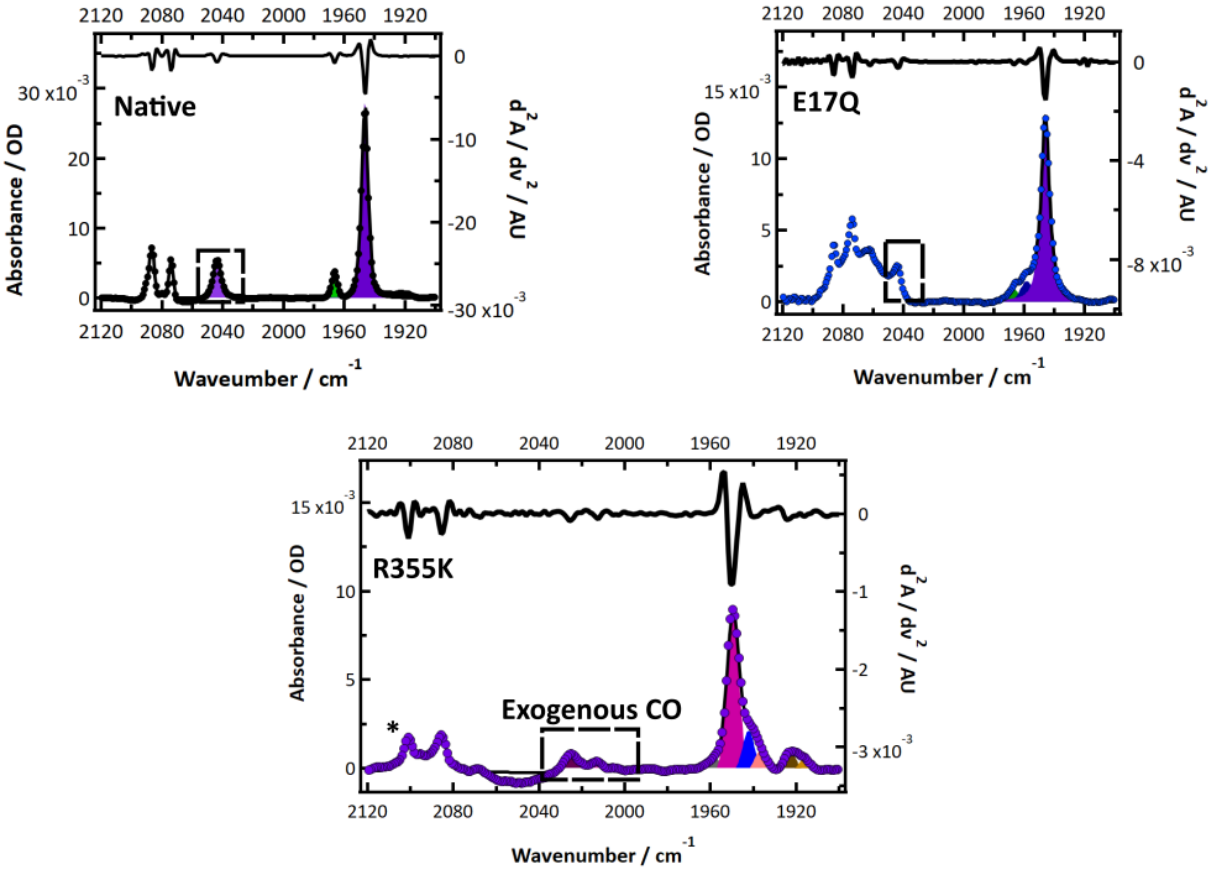

Figure I2: Absorbance spectra and the corresponding second derivative spectra of native, E17Q, and R355K SH1.

Table I1: Endogenous CO frequencies observed for WT, R355K, and E17Q SH1.

Enzyme	**Ni_a^+-L1**	**Ni_a^+-L2**	**Ni^{2+}-X**	**Ni^{2+}-X2**	**Ni^{2+}-CO M-CO**	**Ni^{2+}-X3**	**Ni_a^{3+}-C***
Wild Type	-	-	-	-	1946.4 (0.014)	-	1966.4 (0.095)
R355K	1916.3 (0.7)	1922.7 (0.5)	1936.8 (1.2)	1942.2 (0.8)	1949.5 (0.08)	1958.3 (0.5)	-
E17Q	-	-	-	-	1945.9 (0.02)	1958.2 (0.4)	1966.7 (0.5)

* Varying (minor) amounts to no detectable Ni_a^{3+}-C have been observed between various preparations.

Table I2: Exogenous CO frequencies observed for WT, R355K, and E17Q SH1.

Enzyme	**Ni-CO(1)**	**Ni-CO(2)**	**Ni^{2+}-CO**
Wild Type	-	-	2043.6 (0.08)
R355K	2012.9 (1.03)	2024.9 (0.5)	-
E17Q	-	-	~ 2044*

*visually estimated

Appendix J: References

(1) Silva, P. J.; De Castro, B.; Hagen, W. R. On the prosthetic groups of the NiFe sulfhydrogenase from *Pyrococcus furiosus*: topology, structure, and temperature-dependent redox chemistry. *J. Biol. Inorg. Chem.* **1999**, *4*, 284-291.

(2) Greening, C.; Biswas, A.; Carere, C. R.; Jackson, C. J.; Taylor, M. C.; Stott, M. B.; Cook, G. M.; Morales, S. E. Genomic and metagenomic surveys of hydrogenase distribution indicate H2 is a widely utilised energy source for microbial growth and survival. *ISME J.* **2016**, *10*, 761-777.

(3) Bioinformatics Research Centre. https://services.birc.au.dk/hyddb/browser/ (accessed May 2020).

(4) Van der Zwaan, J. W.; Albracht, S. P. J.; Fontijn, R. D.; Slater, E. C. Monovalent nickel in hydrogenase from *Chromatium vinosum*. Light sensitivity and evidence for direct interaction with hydrogen. *FEBS Lett.* **1985**, *179*, 271-277.

(5) Lubitz, W.; Reijerse, E.; van Gatsel, M. [NiFe] and [FeFe] Hydrogenase Studied by Advanced Magnetic Resonance Techniques. *Chem. Rev.* **2007**, *107*, 4331-4365.

(6) Albracht, S. P. J.; Kröger, A.; Van der Zwaan, J. W.; Unden, G.; Böcher, R.; Mell, H.; Fontijn, R. D. Direct evidence for sulfur as a ligand to nickel in hydrogenase: an EPR study of the enzyme from *Wolinella succinogenes* enriched in sulfur-33. *Biochim. Biophys. Acta, Protein Struct. Mol. Enzymol.* **1986**, *874*, 116-127.

(7) Whitehead, J. P.; Gurbiel, R. J.; Bagyinka, C.; Hoffman, B. M.; Maroney, M. J. The hydrogen binding site in hydrogenase: 35-GHz ENDOR and XAS studies of the nickel-C (reduced and active form) and the Ni-L photoproduct. *J. Am. Chem. Soc.* **1993**, *115*, 5629-5635.

(8) Fichtner, C.; Van Gastel, M.; Lubitz, W. Wavelength dependence of the photo-induced conversion of the Ni-C to the Ni-L redox state in the [NiFe] hydrogenase of *Desulfovibrio vulgaris* Miyazaki F. *Phys. Chem. Chem. Phys.* **2003**, *5*, 5507-5513.

(9) Foerster, S.; Stein, M.; Brecht, M.; Ogata, H.; Higuchi, Y.; Lubitz, W. Single crystal EPR studies of the reduced active site of [NiFe] hydrogenase from *Desulfovibrio vulgaris* Miyazaki F. *J. Am. Chem. Soc.* **2003**, *125*, 83-93.

(10) Tai, H.; Nishikawa, K.; Inoue, S.; Higuchi, Y.; Hirota, S. FT-IR characterization of the light-induced Ni-L2 and Ni-L3 states of [NiFe] hydrogenase from *Desulfovibrio vulgaris* Miyazaki F. *J. Phys. Chem. B* **2015**, *119*, 13668-13674.

(11) Medina, M.; Williams, R.; Cammack, R.; Hatchikian, E. C. Studies of light-induced nickel EPR signals in *Desulfovibrio gigas* hydrogenase. *J. Chem. Soc., Faraday Trans.* **1994**, *90*, 2921-2924.

(12) Medina, M.; Hatchikian, E. C.; Cammack, R. Studies of light-induced nickel EPR signals in hydrogenase: comparison of enzymes with and without selenium. *Biochim. Biophys. Acta, Bioenerg.* **1996**, *1275*, 227-236.

(13) Moura, J. J. G.; Moura, I.; Huynh, B. H.; Krüger, H.-J.; Teixeira, M.; DuVarney, R. C.; DerVartanian, D. V.; Xavier, A. V.; Peck, H. D., Jr.; LeGall, J. Unambiguous identification of the nickel EPR signal in nickel-61 enriched *Desulfovibrio gigas* hydrogenase. *Biochem. Biophys. Res. Commun.* **1982**, *108*, 1388-1393.

(14) Pandelia, M.-E.; Infossi, P.; Stein, M.; Giudici-Orticoni, M.-T.; Lubitz, W. Spectroscopic characterization of the key catalytic intermediate Ni-C in the O_2-tolerant [NiFe] hydrogenase I from *Aquifex aeolicus*: evidence of a weakly bound hydride. *ChemComm* **2012**, *48*, 823-825.

(15) Roessler, M. M.; Evans, R. M.; Davies, R. A.; Harmer, J.; Armstrong, F. A. EPR Spectroscopic Studies of the Fe-S Clusters in the O_2-Tolerant [NiFe]-Hydrogenase Hyd-1 from *Escherichia coli* and Characterization of the Unique [4Fe-3S] Cluster by HYSCORE. *J. Am. Chem. Soc.* **2012**, *134*, 15581-15594.

(16) Murphy, B. J.; Hidalgo, R.; Roessler, M. M.; Evans, R. M.; Ash, P. A.; Myers, W. K.; Vincent, K. A.; Armstrong, F. A. Discovery of Dark pH-Dependent H(+) Migration in a [NiFe]-Hydrogenase and Its Mechanistic Relevance: Mobilizing the Hydrido Ligand of the Ni-C Intermediate. *J. Am. Chem. Soc.* **2015**, *137*, 8484-8489.

(17) Saggu, M.; Zebger, I.; Ludwig, M.; Lenz, O.; Friedrich, B.; Hildebrandt, P.; Lendzian, F. Spectroscopic insights into the oxygen-tolerant membrane-associated [NiFe] hydrogenase of *Ralstonia eutropha* H16. *J. Biol. Chem.* **2009**, *284*, 16264-16276.

(18) Buhrke, T.; Brecht, M.; Lubitz, W.; Friedrich, B. The H2 sensor of *Ralstonia eutropha*: biochemical and spectroscopic analysis of mutant proteins modified at a conserved glutamine residue close to the [NiFe] active site. *J. Biol. Inorg. Chem.* **2002**, *7*, 897-908.

(19) Brecht, M.; Gastel, M. v.; Buhrke, T.; Barbel, F.; Lubitz, W. Direct detection of a hydrogen ligand in the [NiFe] center of the regulatory H_2 sensing hydrogenase from *Ralstonia eutropha* in its reduced state by HYSCORE and ENDOR spectroscopy. *J. Am. Chem. Soc.* **2003**, *125*, 13075-13083.

(20) Lowenstein, J.; Lauterbach, L.; Teutloff, C.; Lenz, O.; Bittl, R. Active Site of the NAD(+)-reducing hydrogenase from *Ralstonia eutropha* studied by EPR spectroscopy. *J. Phys. Chem. B* **2015**, *119*, 13834-13841.

(21) Schroeder, O.; Bleijlevens, B.; Jongh, T. E.; Chen, Z.; Li, T.; Fischer, J.; Foerster, J.; Friedrich, C. G.; Bagley, K. A.; Albracht, S. P. J.; Lubitz, W. Characterization of a cyanobacterial-like uptake [NiFe] hydrogenase: EPR and FTIR spectroscopic studies of the enzyme from *Acidithiobacillus ferrooxidans*. *J. Biol. Inorg. Chem.* **2007**, *12*, 212-233.

(22) Alben, J. O.; Moh, P. P.; Fiamingo, F. G.; Altschuld, R. A. Cytochrome oxidase (a3) heme and copper observed by low-temperature Fourier transform infrared spectroscopy of the carbon monoxide complex. *Proc. Natl. Acad. Sci. U. S. A.* **1981**, *78*, 234-237.

(23) Greene, B. L. Proton, electron and proton-coupled electron transfer dynamics in the catalytic mechanism of [NiFe] and [FeFe] hydrogenases. Ph.D. Thesis, Emory University, 2015.

(24) Watanabe, T.; Honda, K. Measurement of the extinction coefficient of the methyl viologen cation radical and the efficiency of its formation by semiconductor photocatalysis. *J. Phys. Chem.* **1982**, *86*, 2617-2619.